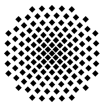

Universität Stuttgart

Collective Effects of Light-Matter Interactions in Rydberg Superatoms

Von der Fakultät Mathematik und Physik der Universität Stuttgart zur Erlangung der Würde eines Doktors der Naturwissenschaften (Dr. rer. nat.) genehmigte Abhandlung

vorgelegt von

Jan Philipp Kumlin

aus Waiblingen

Hauptbericht:	Prof. Dr. Hans Peter Büchler
Mitbericht:	Prof. Dr. Jörg Main
Prüfungsvorsitz:	Prof. Dr. Tilman Pfau

Tag der mündlichen Prüfung: 21. Juli 2021

Institut für Theoretische Physik III
Universität Stuttgart

2021

Meinen Großeltern

Abstract

In this thesis we study collective effects in cold and ultracold atomic ensembles where the atoms interact via the long-range and anisotropic dipole-dipole interaction. These systems have gained a lot of interest both experimentally as well as theoretically over the past years thanks to the increasing experimental control and ability to manipulate these systems for example using external electric and magnetic fields.

The first and main part of this thesis deals with *collective effects of light-matter interactions in Rydberg superatoms*. It is by now a well-known fact that systems in which many emitters are coupled to a common radiation field show collective and cooperative behavior. A Rydberg superatom, which consists of many thousands of individual emitters and is converted into a single, macroscopic two-level system by the Rydberg blockade, represents a particularly interesting system for studying the interaction of light and matter. This thesis focusses on the influence of the resonant dipole-dipole interaction, which is mediated by propagating photons, on the microscopic, internal dynamics of such a Rydberg superatom.

The interaction of a single photon with an individual two-level system is the textbook example of quantum electrodynamics and has interesting applications for quantum information processing. Achieving strong coupling in such a system has so far, however, required confinement of the light field inside resonators or waveguides. In Chapter 3, we discuss the experimental realization of strong coherent coupling between a single Rydberg superatom, consisting of thousands of atoms and turned into a single two-level system using the Rydberg blockade mechanism, and a propagating light pulse containing only a few photons. Using a microscopic description of the system, we show that there is strong and directional emission back in the propagating laser mode and that the system can be modelled as a two-level system with collectively enhanced coupling to a one-dimensional continuum of modes. We discuss the physics of such a system in terms of a master equation and derive a dynamical phase diagram featuring intrinsically damped Rabi oscilla-

tions as a consequence of the collectively enhanced emission. The strong coupling in combination with the nonlinearity of the Rydberg superatom also allows for the observation of two- and non-trivial three-photon correlations imprinted onto initially uncorrelated photons. We find good quantitative agreement between the theory and the experiment by phenomenologically extending the two-level model to a three-level model that also accounts for potential dephasing into dark states due to internal dynamics of the superatom.

For a better understanding of the internal dynamics of the superatom, we study a single collective excitation in a cold ensemble of atoms coupled to a one-dimensional waveguide. The coupling between the matter and the light field gives rise to collective phenomena such as superradiant states with an enhanced initial decay rate, but also to the coherent exchange of the excitation between the atoms. In Chapter 4, we first focus on the coherent exchange interaction and find a remarkable universal dynamics for increasing atom numbers exhibiting several revivals. While this phenomenon provides a limit on the intrinsic dephasing for such a collective excitation, a setup is presented where the universal dynamics can be explored.

In addition to the coherent exchange interaction, in Chapter 5 we include the correlated spontaneous emission. We find that the competition between the two phenomena provides a characteristic dynamics for the decay of the collective excitation and exhibits an algebraic behavior, instead of the expected standard exponential one, for a large number of atoms. The analysis is first performed for a chiral waveguide where the problem can be solved analytically. We demonstrate that, remarkably, a bidirectional waveguide exhibits the same behavior for a large number of atoms and, therefore, it is possible to experimentally access characteristic properties of a chiral waveguide also within a bidirectional waveguide.

In Chapter 6 we discuss experimentally observed collective effects in the decay dynamics of a Rydberg superatom strongly coupled to a propagating light pulse. Instead of observing a constant decay rate determined by the collective coupling strength to the driving field, one finds that the enhanced emission of the single stored photon into the forward direction of the coupled optical mode depends on the dynamics of the superatom before the decay. Based on the findings of Chapters 4 and 5, we motivate an extension of the previously used three-level model of the Rydberg superatom by including an additional subradiant state to which the collectively excited state can coherently couple. We find that this extended model of the superatom well reproduces the observed decay rates providing evidence for the influence of resonant dipole-dipole interactions on the decay dynamics of the superatom.

The second part of this thesis deals with *quantum effects in dipolar Bose gases*.

Recent experiments with ultracold lanthanide atoms which are characterized by a large magnetic moment have revealed the crucial importance of beyond-mean-field corrections in understanding the dynamics of the gas. After a brief review of interactions in ultracold dipolar Bose gases and a brief discussion of how to calculate beyond-mean-field corrections in Chapter 7, we study in Chapter 8 how the presence of an external optical lattice modifies the structure of those corrections. We find that deep in the superfluid regime the equation of state is well described by introducing an anisotropic effective mass. However, for a deep lattice we find terms with anomalous density dependence which do not arise in free space. For a one-dimensional lattice, the relative orientation of the dipole axis with respect to the lattice plays an important role and the beyond-mean-field corrections can either be enhanced or suppressed.

Zusammenfassung

Die vorliegende Dissertation beschäftigt sich mit kollektiven Effekten in kalten und ultrakalten Atomgasen mit langreichweitiger und anisotroper Dipol-Dipol-Wechselwirkung. Aufgrund der zunehmenden experimentellen Kontrolle über diese Systeme und der Möglichkeit sie zum Beispiel mithilfe externer elektrischer und magnetischer Felder zu manipulieren, haben solche Systeme in den letzten Jahren sowohl von experimenteller als auch theoretischer Seite großes Interesse gefunden.

Der erste und größte Teil dieser Arbeit untersucht *kollektive Effekte der Licht-Materie-Wechselwirkung in Rydberg-Superatomen*. Es ist mittlerweile allgemein bekannt, dass Systeme, bei denen viele Emitter an ein gemeinsames Strahlungsfeld gekoppelt sind, ein kollektives und kooperatives Verhalten zeigen. Ein besonders interessantes System zur Untersuchung der Wechselwirkung von Licht und Materie stellt ein Rydberg-Superatom dar, das aus vielen tausend einzelnen Emittern besteht und durch die Rydberg-Blockade in ein einziges, makroskopisches Zwei-Niveau-System umgewandelt wird. Diese Arbeit konzentriert sich auf den Einfluss der resonanten Dipol-Dipol-Wechselwirkung, die durch sich ausbreitende Photonen vermittelt wird, auf die mikroskopische, innere Dynamik eines solchen Rydberg-Superatoms.

Die Wechselwirkung eines einzelnen Photons mit einem einzelnen Zwei-Niveau-System ist das Lehrbuchbeispiel der Quantenelektrodynamik und hat interessante Anwendungen für die Quanteninformationsverarbeitung. Um eine starke Kopplung in einem solchen System zu erreichen, war es jedoch bisher notwendig das Lichtfeld in Resonatoren oder Wellenleitern einzusperren. In Kapitel 3 diskutieren wir daher zunächst die experimentelle Realisierung einer starken kohärenten Kopplung zwischen einem einzelnen Rydberg-Superatom, das aus Tausenden von Atomen besteht und mit Hilfe des Rydberg-Blockade-Mechanismus in ein einzelnes Zwei-Niveau-System umgewandelt wurde, und einem propagierenden Laserpuls, der nur wenige Photonen enthält. Unter Verwendung einer mikrosko-

pischen Beschreibung des Setups zeigen wir, dass es eine starke und gerichtete Emission zurück in die propagierende Lasermode gibt, und das System als Zwei-Niveau-System mit kollektiv verstärkter Kopplung an ein eindimensionales Modenkontinuum beschrieben werden kann. Wir diskutieren die Physik eines solchen Systems in Form einer Mastergleichung und leiten ein dynamisches Phasendiagramm mit intrinsisch gedämpften Rabi-Oszillationen als Folge der kollektiv verstärkten Emission her. Die starke Kopplung in Kombination mit der Nichtlinearität des Rydberg-Superatoms ermöglicht auch die Beobachtung von Zwei- und nichttrivialen Drei-Photonen-Korrelationen, die in die zunächst unkorrelierte Photonen induziert werden. Wir finden eine gute quantitative Übereinstimmung zwischen Theorie und Experiment, indem wir das Zwei-Niveau-Modell phänomenologisch auf ein Drei-Niveau-Modell erweitern, um auch die potenzielle Dephasierung in Zustände, die nicht mehr an das Lichtfeld koppeln, aufgrund der internen Dynamik des Superatoms zu berücksichtigen.

Um die innere Dynamik des Superatoms besser zu verstehen, untersuchen wir eine einzelne kollektive Anregung in einem kalten Ensemble von Atomen, die an einen eindimensionalen Wellenleiter gekoppelt sind. Die Kopplung zwischen den Atomen und dem Lichtfeld führt zu kollektiven Phänomenen wie superradianten Zuständen mit erhöhter Zerfallsrate, aber auch zum kohärenten Austausch einer Anregung zwischen den Atomen. In Kapitel 4 konzentrieren wir uns zunächst auf die kohärente Austauschwechselwirkung und finden eine bemerkenswerte universelle Dynamik für größer werdende Atomzahlen, in der die Besetzung der kollektiven Anregung immer wieder aufs Neue auftritt. Während dieses Phänomen die intrinsische Dephasierung für eine solche kollektive Anregung begrenzt, wird ein experimentelles Setup vorgestellt, mit dem die universelle Dynamik erforscht werden kann.

Neben der kohärenten Austauschwechselwirkung beziehen wir in Kapitel 5 die korrelierte spontane Emission mit ein. Wir finden, dass das Zusammenspiel zwischen beiden Phänomenen eine charakteristische Dynamik für das Abklingen der Anregungen liefert und bemerkenswerterweise ein algebraisches Verhalten anstelle des erwarteten exponentiellen Verhaltens für eine große Anzahl von Atomen zeigt. Die Analyse wird zunächst für einen chiralen Wellenleiter durchgeführt, für den das Problem analytisch gelöst werden kann. Wir zeigen, dass interessanterweise ein bidirektionaler Wellenleiter das gleiche Verhalten für eine große Anzahl von Atomen zeigt und es daher möglich ist, experimentell auf charakteristische Eigenschaften eines chiralen Wellenleiters auch mithilfe eines bidirektionalen Wellenleiters zuzugreifen.

In Kapitel 6 diskutieren wir experimentell beobachtete kollektive Effekte in der Zerfallsdynamik eines Rydberg-Superatoms, das stark an einen propagierenden

Laserpuls gekoppelt ist. Anstatt eine konstante Zerfallsrate zu beobachten, die durch die kollektive Kopplungsstärke zum Lichtfeld, das das Superatom treibt, bestimmt wird, stellt man fest, dass die verstärkte Emission des einzelnen gespeicherten Photons zurück in die gekoppelten optischen Mode von der Dynamik des Superatoms vor dem Zerfall abhängt. Basierend auf den Erkenntnissen der Kapitel 4 und 5 motivieren wir eine Erweiterung des bisher verwendeten Drei-Niveau-Modells des Rydberg-Superatoms um einen zusätzlichen subradianten Zustand, an den der kollektiv angeregte Zustand kohärent koppeln kann. Wir stellen fest, dass dieses erweiterte Modell des Superatoms die beobachteten Zerfallsraten sehr gut reproduziert, was den Einfluss resonanter Dipol-Dipol-Wechselwirkungen auf die Zerfallsdynamik des Superatoms belegt.

Der zweite Teil dieser Arbeit behandelt *Quanteneffekte in dipolaren Bose-Gasen*. Vor kurzem durchgeführte Experimente mit ultrakalten Atomen aus der Gruppe der Lanthanoiden, die durch ein großes magnetisches Dipolmoment charakterisiert sind, haben die wesentliche Bedeutung von Korrekturen zur Molekularfeldnäherung ("beyond-mean-field corrections") für das Verständnis der Dynamik eines solchen Gases aufgedeckt. In Kapitel 8 untersuchen wir daher wie ein externes optisches Gitter die Struktur dieser Korrekturen verändert. Wir zeigen, dass die Zustandsgleichung des Gases tief im suprafluiden Parameterbereich gut durch eine anisotrope effektive Masse beschrieben wird. Für ein tiefes Gitter finden wir jedoch zusätzlich Terme mit einer Dichteabhängigkeit, die von der im freien Raum abweicht. Für ein eindimensionales Gitter spielt die relative Ausrichtung der Dipolachse und des Gitters eine wichtige Rolle und kann die Korrekturen zur Molekularfeldnäherung entweder verstärken oder abschwächen.

Publications

This thesis is based on the following publications:

- *Free-Space Quantum Electrodynamics with a Single Rydberg Superatom*
  Asaf Paris-Mandoki, Christoph Braun, **Jan Kumlin**, Christoph Tresp, Ivan Mirgorodskiy, Florian Christaller, Hans Peter Büchler, and Sebastian Hofferberth
  Physical Review X **7**, 041010 (2017)
  DOI: 10.1103/PhysRevX.7.041010, arXiv: 1705.04128

- *Emergent Universal Dynamics for an Atomic Cloud Coupled to an Optical Waveguide*
  Jan Kumlin, Sebastian Hofferberth, and Hans Peter Büchler
  Physical Review Letters **121**, 013601 (2018)
  DOI: 10.1103/PhysRevLett.121.013601, arXiv: 1803.08837

- *Observation of Three-Body Correlations for Photons Coupled to a Rydberg Superatom*
  Nina Stiesdal, **Jan Kumlin**, Kevin Kleinbeck, Philipp Lunt, Christoph Braun, Asaf Paris-Mandoki, Christoph Tresp, Hans Peter Büchler, and Sebastian Hofferberth
  Physical Review Letters **121**, 103601 (2018)
  DOI: 10.1103/PhysRevLett.121.103601, arXiv: 1806.00062

- *Observation of Collective Decay Dynamics of a Single Rydberg Superatom*
  Nina Stiesdal, Hannes Busche, **Jan Kumlin**, Kevin Kleinbeck, Hans Peter Büchler, and Sebastian Hofferberth
  Physical Review Research **2**, 043339 (2020)
  DOI: 10.1103/PhysRevResearch.2.043339, arXiv: 2005.05089

- *Nonexponential Decay of a Collective Excitation in an Atomic Ensemble Coupled to a One-Dimensional Waveguide*
  Jan Kumlin, Kevin Kleinbeck, Nina Stiesdal, Hannes Busche, Sebastian Hofferberth, and Hans Peter Büchler
  Physical Review A **102**, 063703 (2020)
  DOI: 10.1103/PhysRevA.102.063703, arXiv: 2006.14977

- *Beyond-Mean-Field Corrections for Dipolar Bosons in an Optical Lattice*
  Jan Kumlin, Krzysztof Jachymski, and Hans Peter Büchler
  Physical Review A **99**, 033622 (2019)
  DOI: 10.1103/PhysRevA.99.033622, arXiv: 1901.02829

In the course of this thesis, the following papers have been published in addition:

- *Dimensional Crossover for the Beyond-Mean-Field Correction in Bose Gases*
  Tobias Ilg, **Jan Kumlin**, Luis Santos, Dmitry S. Petrov, and Hans Peter Büchler
  Physical Review A **98**, 051604(R) (2018)
  DOI: 10.1103/PhysRevA.98.051604, arXiv: 1806.01784

- *Controlled Multi-Photon Subtraction with Cascaded Rydberg Superatoms as Single-Photon Absorbers*
  Nina Stiesdal, Hannes Busche, Kevin Kleinbeck, **Jan Kumlin**, Mikkel G. Hansen, Hans Peter Büchler, and Sebastian Hofferberth
  Nature Communications **12**, 4328 (2021)
  DOI: 10.1038/s41467-021-24522-w, arXiv: 2103.15738

Contents

Part I.

Collective Effects of Light-Matter Interactions

Introduction

The interaction of light and matter is essential for many processes in nature. It allows human beings and animals to see and plants to harvest energy by means of photosynthesis. Many modern applications such as imaging, spectroscopy, and optical information processing would be impossible without understanding the fundamental processes that happen when light interacts with matter.

Classically, the interaction of light and matter can be understood by treating the emitters as oscillating dipoles which radiate energy in the form of electromagnetic waves [1]. The emitted radiation can induce oscillations of other dipoles nearby giving rise to induced dynamical dipole-dipole interactions. On the quantum level, emitters are often modelled as two-level systems where the dipole is realized by the dipole moment of the transition between both levels. If all emitters are the same, the frequency of the emitted light from one emitter matches the resonance frequency of another which is why these interactions are also referred to as resonant dipole-dipole interactions; such interactions are interesting for two reasons: First, they are long-range, enabling one emitter to interact with many other emitters at the same time. Second, they include both a dispersive as well as a dissipative component where the first comes from the driving of one dipole by the radiation of another and the latter derives from the fact that the radiation of one dipole can simply dissipate into free space [2]. A more thorough discussion of the microscopic origin of resonant dipole-dipole interactions is presented in Chapter 1 and 2.

Moreover, resonant dipole-dipole interactions can change the optical properties of an ensemble of emitters. In a seminal paper, Dicke showed that emitters that are spaced much closer than their resonance wavelength do not radiate independently but show cooperative behaviour as they are coupled to a common radiation field [3]. The radiation properties of one emitter then strongly depend on the state of others nearby as a consequence of the resonant dipole-dipole interactions between them. This cooperative behavior in dense gases leads to huge level shifts

and correlated spontaneous emission. While the level shifts were identified to lead to the saturation of the refractive index of dense gases and solids [4], the correlated spontaneous emission gives rise to the phenomenon of *superradiance* [3, 5]. Superradiance describes a strongly enhanced emission from a dense ensemble of atoms due to self-stimulated emission. If all emitters are excited, the emitted intensity scales quadratically with the number of emitters (instead of linearly, as in the case of independent emission). In addition also the emission rate varies throughout the emission process and scales quadratically if half of the ensemble is excited [5]. Superradiant properties, including cooperative level shifts, have been observed in a broad range of physical systems ranging from ensembles of nuclei [6] over cold atoms [7–10], ions [11], solid-state systems [12, 13] to more artificial and hybrid light-matter systems like superconducting qubits [14], and atoms coupled to nanophotonic structures [15].

While superradiance was originally discussed in the limit where the emitters are spaced much closer than the resonance wavelength, collective behaviour also appears in extended ensembles. In this regime, a strongly enhanced and even highly directional emission of photons from the ensemble due to constructive interference is achieved for so-called "timed" Dicke states [16] where the phase information of the incoming photon is stored in a collective excitation of the ensemble. In contrast to small ensembles confined within the resonance wavelength, where superradiance is also studied in the multi-excitation case, the theoretical study of superradiance in extended ensembles has so far been mostly limited to the single-excitation limit [16–24], with a few exceptions [25–27], coining the term *single-photon superradiance* [18]. While many aspects of superradiance - such as the quadratic scaling of the emitted intensity or the strongly directional emission of radiation - can be understood classically in terms of dipoles oscillating in phase (in analogy to phased antenna arrays), a quantum-mechanical treatment of the light-matter interaction is necessary for a full understanding of superradiant phenomena [28].

Intimately related to the phenomenon of superradiance is *subradiance* which describes *inhibited* spontaneous emission due to destructive interference. Just as superradiance, subradiance has gained a lot of theoretical interest throughout the years [5, 25, 29–34] but remained elusive in experiments as subradiant states couple only weakly to the electromagnetic field. Most experiments in this direction focussed on two emitters in molecular [35–37] and ion [38] systems and subradiance was only recently observed in atomic ensembles [39–42]. From a practical point of view, subradiant states are appealing for photon storage [43–45] and quantum computation [46] as they are less prone to spontaneous emission, and it was predicted that subradiant states of ordered atomic arrays can lead to a drastic improvement in photon storage fidelities [25].

Collective and cooperative phenomena are common to various systems and interfacing light with atomic ensembles has been shown to find many useful applications [47]. Ensembles of Rydberg atoms, however, provide a particularly interesting systen to harness the collective response of an atomic ensemble interacting with light inspiring the field of *Rydberg quantum optics* [48–50]. The strong van der Waals interaction between Rydberg atoms leads to the phenomenon of *dipole-* or *Rydberg* blockade which was first discussed in the context of quantum information processing [51, 52]. Because of the Rydberg blockade only a single excitation can be present within a certain volume rendering the optical response to incoming photons nonlinear. Using electromagnetically-induced transparency [53], the strong interactions between the Rydberg atoms can be mapped onto the photons [54, 55] realizing cooperative optical nonlinearities [56] and an effective photon-photon interaction [57–60]. Applications of Rydberg-mediated photon-photon interactions include a single-photon switch [61] or -transistor [62, 63], and the realization of quantum gates [64, 65].

Particularly interesting is the concept of a *Rydberg superatom* where all constituents of the ensemble are confined within the blockaded volume and a single photon is sufficient to saturate the medium realizing the most nonlinear response possible [66]. The whole ensemble then behaves similar to a two-level system with collectively enhanced coupling strength which gives rise to collectively enhanced many-body Rabi oscillations [67]. Since the collective excitation of the ensemble encodes the phase information of the incoming light field, there is a strongly directional emission of the excitation in the direction of the propagating photons. The strong coupling of a Rydberg superatom to propagating photons and the resulting forward emission are discussed in Chapter 3 of this thesis. The emitted photons can be analyzed and two- as well as three-body correlations between the photons are observed as a consequence of the effective photon-photon interaction mediated by the Rydberg superatom. The strongly directional emission in combination with the blockade also enables, for example, the realization of a single-photon source in a cold ensemble [68] as well as in a room-temperature vapor cell [69] where a four-wave mixing scheme is employed to first store and subsequently trigger the release of the collective excitation in the forward direction.

Even though the description of the Rydberg superatom as a two-level atom provides a good intuition, the superatom still has an internal structure as it is composed of many emitters that can interact via the resonant dipole-dipole interaction mediated by the propagating light field. In Chapter 6 the influence of such collective effects on the decay dynamics of a Rydberg superatom due to the resonant dipole-dipole interaction is discussed. In setups where the influence of resonant dipole-dipole interactions is obscured by incoherent effects (such as inhomo-

geneous level shifts due to, for example, atomic motion), single-photon subtractors [70–72] can be realized where the dephasing leads to an irreversible transfer of the collective excitation to states decoupled from the light field.

Complementary to disordered ensembles of atoms in free space, over the past years there has also been a rapidly growing interest in the light-matter interaction of low-dimensional and engineered atomic structures [73–77]. The advent of techniques such as optical lattices [78] and optical tweezers [79–81] has enabled the realization of periodic arrangements of atoms in one, two, and even three dimensions. The control of the positions of the atoms allows for a fine-tuning of the optical response of the atomic ensemble [82, 83] with impressive results such as a mirror built from a single layer of atoms [84] which can be functionalized using the Rydberg blockade to create highly entangled photonic states [85]. In addition to periodic arrangements of atoms, the experimental progress in the fabrication of nanostructures and optical nanofibers has paved the way to the new paradigm of *waveguide quantum electrodynamics* where quantum emitters, modelled as two-level systems, are strongly coupled to a one-dimensional continuum of guided modes [66, 86–88]. A brief introduction to waveguide quantum electrodynamics is given in Chapter 1. Waveguide quantum electrodynamics is conveniently realized using atoms coupled to the evanescent field of an optical nanofiber [89–91] or a photonic crystal waveguide [15, 92], quantum dots coupled to photonic nanostructures [93, 94] and superconducting qubits coupled to transmission lines [95]. Recently it was also proposed to realize waveguide quantum electrodynamics with the guided modes of an ordered atomic array [27]. One-dimensional photonic structures and nanofibers offer the possibility to go beyond the long-range resonant dipole-dipole interactions and to realize even *infinite*-range interactions mediated by photons that are tightly confined in two directions but can propagate along the third one [90, 96]. In addition, other types of interactions can be designed by tailoring the environment using, for example, photonic crystals to realize the study of tunable and controlled quantum-many-body systems [97]. These systems allow for the study of strongly correlated photon transport [98–100] and the physics of low-dimensional dissipative systems [101], and facilitate the creation of nonclassical states of light [102–104].

The subwavelength confinement of light in nanophotonic structures like photonic waveguides and nanofibers further opens the possibility to realize exotic *chiral* interactions between the emitters [105]. In such structures the direction of propagation of light is linked to the polarization of the transition dipole moment of the emitter such that the interaction between the atoms and photons becomes nonreciprocal [106, 107]. In extreme cases, absorption and emission of photons become even unidirectional. This special type of interaction allows for the implemen-

tation of cascaded quantum systems [108, 109] where the photons are sent from one emitter to the next without information backflow and can function as a tool for deterministic transfer of quantum information between distant qubits [110]. Other applications include the more robust generation of atom-atom entanglement [101, 111], the optical single-shot read out of the spin state of a single electron in a quantum dot [112], and the implementation of scalable quantum networks [113]. In this thesis, collective effects of chiral and nonchiral light-matter interactions in one-dimensional waveguides are studied in Chapters 4 and 5. The results of these chapters also improve the understanding of the internal dynamics present in the Rydberg superatom discussed in Chapter 6. The experimental setup of a Rydberg superatom strongly coupled to a propagating laser mode discussed in Chapters 3 and 6 further offers the possibility to realize chiral interactions between a chain of multiple Rydberg superatoms as a consequence of the directional emission of photons [72].

1

Basic Concepts

1.1. Rydberg Atoms

Over the last decades Rydberg atoms have developed into a well-established platform to realize strongly interacting and well-controllable systems in the atomic, molecular, and optical physics community. While research initially focussed on spectroscopic and collisional properties of Rydberg atoms [114–116], the huge potential of Rydberg atoms in the emerging field of quantum information processing was realized already two decades ago [51, 52]. In more recent years, the ability to experimentally control and manipulate Rydberg atoms with ever-increasing precision opened the path to high-fidelity quantum simulation of large ensembles of interacting Rydberg atoms [117–121].

In this section, we give a brief overview of the general physics of Rydberg atoms with special focus on their interaction properties. For more details regarding theoretical description and experimental work, we refer the reader to the excellent reviews by Löw [122] and Saffman [123] and the book by Gallagher [124].

1.1.1. General Properties

Rydberg atoms are atoms excited to an electronic state with principal quantum number $n \gg 1$ close to the ionization threshold. The large quantum number leads to exaggerated properties concerning lifetime as well as interactions between each other and with external fields. This makes them prime candidates for many experiments in atomic, molecular and optical physics. In the case of only a single excited electron, a Rydberg atom behaves similar to a hydrogen atom and its energy spec-

trum is well described by

$$E_{nlj} = -\frac{hcR^*}{(n-\delta_{nlj})^2}\,, \tag{1.1}$$

where R^* is the element-specific Rydberg constant and δ_{nlj} is the so-called quantum defect which accounts for the fine structure and the charge distribution of the remaining electrons and the nucleus. The quantum defects decrease with increasing l as the orbitals become more circular and the electron becomes less sensitive to the influence of the non-hydrogenic core. In analogy to the hydrogen atom, the quantum number n and the quantum defect are combined into a renormalized, noninteger quantum number $n^* = n - \delta_{nlj}$ which also determines the scaling properties of Rydberg atoms.

As the valence electron in Rydberg atoms is highly excited and the orbital radius scales as $r \sim (n^*)^2$, Rydberg atoms can extend over micrometer scales. An immediate consequence of being in a highly excited electronic state is the long radiative lifetime of Rydberg atoms. The dominant contribution to the spontaneous emission is given by transition to low-lying states where the transition dipole moment scales as $(n^*)^{-3/2}$. The radiative lifetime of high-lying Rydberg states scales as $(n^*)^3$ and can become on the order of hundred microseconds for principal quantum numbers used in current experiments with cold gases. In room temperature Rydberg gases, however, the lifetime is limited by blackbody radiation for $n \geq 40$ and scales as $(n^*)^2$ [124] being, for example, $42.3\,\mu$s at $300\,\mathrm{K}$ for the $43S$ state in rubidium [122].

In contrast to the small transition dipole moments from Rydberg states to the ground states due to the small spatial overlap, adjacent Rydberg levels can have enormous transition dipole moments orders of magnitude larger than permanent electric dipole moments in polar molecules. The transition from $43P_{3/2}$ to $43S_{1/2}$ in Rb, for example, has a transition dipole moment of $1069\,ea_0$ [122] corresponding to $2741\,\mathrm{D}$ compared to HCN having a permanent electric dipole of $3\,\mathrm{D}$ [125]. Large induced dipole moments in Rydberg atoms also result in an enhanced response to DC and AC electric field with huge polarizabilities scaling as $(n^*)^7$.

1.1.2. Coherent Excitation

In many experimental setups, Rydberg states are excited using a two-photon transition from the ground state $|g\rangle$, which for ^{87}Rb is usually one of the hyperfine states from the $5S_{1/2}$ manifold, via an intermediate state $|e\rangle$ (out of the $5P_{3/2}$ hyperfine manifold) to the Rydberg state $|r\rangle$ which can either be an S-state or a D-state. Compared to the direct excitation of a Rydberg P-state using a direct

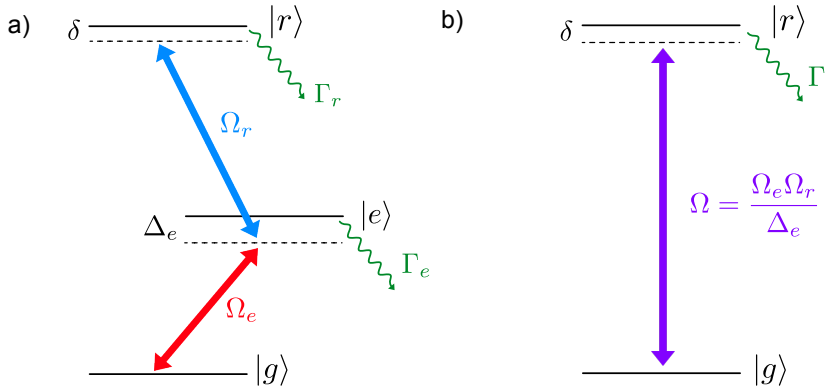

Fig. 1.1.: a) Two-photon transition from ground state $|g\rangle$ via intermediate state $|e\rangle$ with Rabi frequency $2\Omega_e$ to Rydberg state $|r\rangle$ with Rabi frequency $2\Omega_r$. The intermediate state is far detuned, $|\Delta_e| \gg \Omega_r$, Ω_e and the two-photon detuning δ is small. b) Effective two-level system after adiabatic elimination. The ground state and Rydberg state are coupled by the effective coupling strength Ω and the Rydberg state acquires an additional decay from the intermediate state.

transition in the UV-range, the two-photon transition takes advantage of the large dipole moment of the D_2-line in alkali atoms and the availability of high power lasers for larger wavelengths leading to an increased Rabi frequency on the transition from $|e\rangle$ to $|r\rangle$. To avoid the spontaneous decay from the intermediate state, the coupling from the ground state to the intermediate state is far off-resonant. The intermediate state can then be adiabatically eliminated from the dynamics as will be shown in the following. A rigorous treatment of adiabatic elimination in a similar setup is given in [126].

The Hamiltonian of the system shown in Fig. 1.1a) in the rotating frame of the coupling lasers and in the rotating-wave approximation is given by

$$H = \hbar \begin{pmatrix} 0 & \Omega_e & 0 \\ \Omega_e & -\Delta_e & \Omega_r \\ 0 & \Omega_r & \delta \end{pmatrix} , \tag{1.2}$$

where $2\Omega_e$ and $2\Omega_r$ are the Rabi frequencies for the lower transition from $|g\rangle$ to $|e\rangle$ and the upper transition from $|e\rangle$ to $|r\rangle$, respectively. For simplicity, we assume all coupling strengths to be real. The laser for the lower transition is assumed to be red-detuned with $-\Delta_e < 0$ and the two-photon detuning is δ. In a first step, we neglect the spontaneous decay from the intermediate state and the Rydberg state. The time evolution for the state $|\Psi(t)\rangle = c_g(t)\,|g\rangle + c_e(t)\,|e\rangle + c_r(t)\,|r\rangle$ is given

by the coupled differential equations

$$i\partial_t c_g(t) = \Omega_e c_e(t)\,, \tag{1.3}$$
$$i\partial_t c_e(t) = -\Delta_e c_e(t) + \Omega_e c_g(t) + \Omega_r c_r(t)\,, \tag{1.4}$$
$$i\partial_t c_r(t) = \delta c_r(t) + \Omega_r c_e(t)\,. \tag{1.5}$$

If the laser fields are sufficiently far detuned from the intermediate state, $\Delta_e \gg \Omega_e,\ \Omega_r$, and the two-photon detuning δ is small, there is a separation of time scales into fast dynamics given by Δ_e and slow dynamics given by $\Omega_e,\ \Omega_r$ and δ. The fast dynamics of the intermediate state correspond to high-frequency oscillations with small amplitude compared to slow oscillations for the ground state and Rydberg state. The intermediate state can then be eliminated from the dynamics setting $\partial_t c_e(t) = 0$. As a result, the system behaves as a two-level system with equations of motion

$$i\partial_t c_g(t) = \Delta_{\mathrm{AC,e}} c_g(t) + \Omega c_r(t)\,, \tag{1.6}$$
$$i\partial_t c_r(t) = (\Delta_{\mathrm{AC,r}} + \delta) c_r(t) + \Omega c_g(t)\,, \tag{1.7}$$

where $\Omega = \Omega_e\Omega_r/\Delta_e$ is the effective coupling strength between the ground state and the Rydberg state (see Fig. 1.1b)) and $\Delta_{\mathrm{AC,\,i}} = \Omega_i^2/\Delta_e$ are AC Stark shifts which are typically small and can often be neglected.

So far, the lifetimes of the intermediate state and the Rydberg state have been neglected. While the latter is usually large compared to other time scales in the system, the lifetime $1/\Gamma_e$ of the intermediate state cannot be neglected. Even though the population in the intermediate state is small, it contributes to the spontaneous emission from the Rydberg state due to the coupling by Ω_r. The admixture of the intermediate state to the Rydberg state can be calculated within first-order perturbation theory for $\Delta_e \gg \Omega_e,\ \Omega_r$ and gives $|r'\rangle \approx |r\rangle + \frac{\Omega_r}{\Delta_e}|e\rangle$. As a consequence, the effective decay rate of the Rydberg state due to the admixture of the intermediate state is

$$\Gamma = \Gamma_r + \left(\frac{\Omega_r}{\Delta_e}\right)^2 \Gamma_e\,, \tag{1.8}$$

where the first term is the spontaneous decay rate from the Rydberg state and the second term gives the decay rate due to the admixture of the intermediate state and is also referred to as Raman decay. Due to the long Rydberg lifetimes of a several hundred microseconds, the Raman decay often provides the dominant contribution to spontaneous emission.

1.1.3. Interactions

One of the prominent properties of Rydberg atoms is their strong and tunable interaction with each other. In the following, we will elaborate on this.

As Rydberg atoms are many-electron systems, their interaction properties are in principle very complicated to calculate. One huge simplification arises when the separation $|\mathbf{r}|$ between two Rydberg atoms is much larger than the LeRoy radius [127] given by $r_{\mathrm{LR}} \sim (n^*)^2 a_0$, where a_0 is the Bohr radius. In this case, the atomic wave functions of the two atoms do not overlap and the precise form of the charge distribution as well as their statistics can be neglected. The interaction is then calculated considering the electrostatic interaction between two localized charge distributions using a multipole expansion [1]. The leading term in this expansion is the dipole-dipole interaction[1]

$$V_{\mathrm{DDI}}(\mathbf{r}) = \frac{\mathbf{d}_1 \cdot \mathbf{d}_2 - 3(\mathbf{d}_1 \cdot \hat{\mathbf{r}})(\mathbf{d}_2 \cdot \hat{\mathbf{r}})}{|\mathbf{r}|^3}\,, \tag{1.9}$$

where $\mathbf{d}_{1,2}$ are the dipole moments of the two Rydberg atoms. Upon canonical quantization, the dipole moments in Eq. (1.9) are replaced by dipole operators proportional to the position operator. It is important to note that Rydberg atoms do not possess a permanent dipole moment due to the parity of the wave functions unless a strong external electric field is applied and mixes the wave functions. The dipole-dipole interaction is thus realized by transition dipole moments and the Rydberg atoms interact via the exchange of virtual photons (see also Section 1.3).

The interaction between two atoms in generic Rydberg states $|r\rangle = |nljm\rangle$ and $|r'\rangle = |n'l'j'm'\rangle$ is best understood considering a toy model including only the asymptotic pair states $|rr'\rangle$ and $|r''r'''\rangle$, where $|r''\rangle$ and $|r'''\rangle$ are other Rydberg states close in energy. In real systems, the two-channel model is too simplified and the correct calculation of Rydberg interaction potentials requires more levels, in particular in the presence of large electric or magnetic fields or small interatomic separations where several states strongly mix [128]. The restriction to only a few states, however, is possible as the dipole-dipole interaction limits the coupling to energetically close two-atom states for two reasons: First, the energy difference between those states is small and thus less suppressed than transitions to states far away in energy. Second, the transition dipole moments of states with similar principal quantum numbers are the largest and transition dipole moments are strongly suppressed for states with largely different principal quantum numbers.

In the two-channel model, the coupling between the pair states $|rr'\rangle$ and $|r''r'''\rangle$

[1] Throughout this part of the thesis, we use Gauss units. The dipole-dipole interaction in SI units is obtained by multiplying with $1/4\pi\varepsilon_0$.

due to the dipolar interaction leads to the Hamiltonian of the form

$$H = \begin{pmatrix} \Delta_{\mathrm{F}} & V_{\mathrm{DDI}} \\ V_{\mathrm{DDI}} & 0 \end{pmatrix}, \tag{1.10}$$

where $\Delta_{\mathrm{F}} = E_{r''} + E_{r'''} - E_r - E_{r'}$ is the energy defect which is also often referred to as Förster defect [129]. The dipole-dipole interaction takes the form $V_{\mathrm{DDI}}(\mathbf{r}) = C_3/|\mathbf{r}|^3$ where C_3 includes the matrix element of the dipole operators in the numerator of Eq. (1.9). It contains the strength of the transition dipole moments and implies selection rules for dipole-allowed transitions [128]. Note that in general C_3 is complex but here is assumed to be real for simplicity. The eigenenergies of the Hamiltonian are given by[2]

$$V_{\pm}(\mathbf{r}) = \frac{\Delta_{\mathrm{F}}}{2} \pm \mathrm{sign}(\Delta_{\mathrm{F}}) \sqrt{\frac{\Delta_{\mathrm{F}}^2}{4} + (V_{\mathrm{DDI}}(\mathbf{r}))^2}\,. \tag{1.11}$$

One can now distinguish the following cases: If the energy defect Δ_{F} is much larger than the dipole-dipole interaction, for example for large separation between the atoms, the atoms interact via the van der Waals interaction potential

$$V_{\mathrm{vdW}}(\mathbf{r}) = -\frac{C_3^2}{\Delta_{\mathrm{F}}|\mathbf{r}|^6} = -\frac{C_6}{|\mathbf{r}|^6}\,, \tag{1.12}$$

where C_6 is the interaction strength whose sign depends on the sign of the energy defect Δ_{F}. The $1/|\mathbf{r}|^6$ dependence arises from a second-order process via the intermediate pair state $|r''r'''\rangle$. This type of interaction is dominant in real systems when the two atoms are either in the same Rydberg state $|r\rangle = |r'\rangle$, which is the case for the experimental setups discussed in this thesis, or if both states are not directly coupled via a dipole-allowed transition. The interaction between Rydberg atoms in the same S-state is almost isotropic but the angular dependence reminiscent of the dipole-dipole interaction has to be taken into account for states with nonzero orbital angular momentum, for example P- or D-states [130].

In the opposite limit where the dipole-dipole interaction dominates if the atoms are very close ($|\Delta_{\mathrm{F}}| \ll V_{\mathrm{DDI}}(\mathbf{r})$) or if the energy defect vanishes, the interaction potential reduces to the dipole-dipole interaction

$$V_{\pm}(\mathbf{r}) = \pm\frac{C_3}{|\mathbf{r}|^3}\,. \tag{1.13}$$

[2] Note that this expression is only correct if $\Delta_{\mathrm{F}} \neq 0$ and the eigenvalues for $\Delta_{\mathrm{F}} = 0$ read $V_{\pm}(\mathbf{r}) = \pm V_{\mathrm{DDI}}(\mathbf{r})$.

The energy defect can be tuned by means of external electric fields inducing DC Stark shifts [131, 132] and magnetic fields [133] to bring pair states into resonance. By this, the character of the interaction can be changed from a van der Waals type of interaction to a dipolar interaction very similar to Feshbach resonances [134] between ground state atoms, where the scattering length can be tuned by magnetic fields. Förster resonances, where $\Delta_{\mathrm{F}} = 0$, are also discussed in the context of light-harvesting complexes where they underly the non-radiative energy transfer [135–137]. The crossover between the dipolar and the van der Waals interaction takes place at a distance $r_c = |C_3/\Delta_{\mathrm{F}}|^{1/3}$.

A special case occurs when the initial states are dipole-coupled, for example $|r\rangle = \left|nS_{1/2}\right\rangle$ and $|r'\rangle = \left|nP_{3/2}\right\rangle$, such that the pair state $|rr'\rangle$ is resonant with $|r'r\rangle$. Then, one has resonant dipolar exchange interactions in the MHz regime for energetically close states which leads to an excitation hopping over large distances (see also Section 1.3).

The van der Waals interaction (1.12) and the (resonant) dipole-dipole interaction (1.13) are characterized by the coefficients C_6 and C_3, respectively. The coefficient C_3 scales as $(n^*)^4$ with the principal quantum number whereas the van der Waals coefficient C_6 even scales as $(n^*)^{11}$. Typical interaction strengths at a distance of a few micrometers are on the order of a few ten to hundred MHz. These energies are several orders of magnitude larger than the magnetic dipole-dipole interactions or van der Waals interactions for ground state atoms making them suitable candidates to realize strong coherent interactions in combination with their long lifetimes [123].

1.2. Rydberg Superatom

One of the most striking consequences of the huge interactions between Rydberg atoms is the realization of strongly correlated quantum gases leading to the notion of a Rydberg superatom which is at the center of this thesis. In the following, we will outline the basic ingredients behind this concept and what makes Rydberg superatoms so interesting for applications in quantum optics.

1.2.1. Rydberg Blockade

The most important ingredient for Rydberg superatoms is the Rydberg blockade [51, 52] which arises due to the strong interactions between two Rydberg atoms as discussed in Section 1.1.3. As a consequence of the strong mutual interaction between to Rydberg atoms, the excitation of a second or further atoms within a certain distance from the first Rydberg atom is shifted out of resonance and therefore

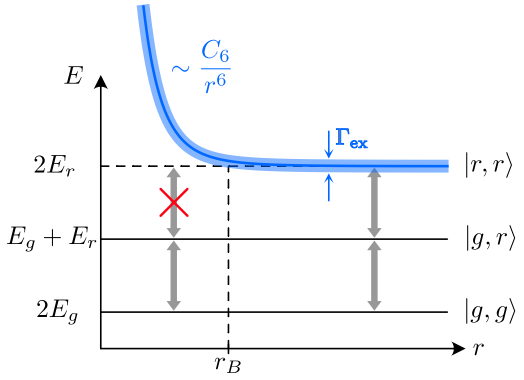

Fig. 1.2.: Sketch of the Rydberg blockade. The strong van der Waals interaction shifts the second excitation out of resonance such that for $r < r_B$ only one atom can be excited. The blockade radius r_B depends on the coefficient C_6 and the excitation linewidth Γ_{ex} which is typically dominated by the laser linewidth Ω.

blocked (see Figure 1.2). The blockade radius r_B depends both on the coefficient C_6 of the interaction as well as the excitation linewidth Γ_{ex}. If one is in the 'frozen gas' regime where Doppler shifts can be neglected, the excitation linewidth is usually dominated by the power broadening of the excitation laser and is given by the Rabi frequency Ω. As soon as the interaction energy shift surpasses this linewidth, the excitation of the second Rydberg atom is out of resonance giving the condition for the blockade radius[3]

$$\frac{C_6}{r_B^6} \stackrel{!}{=} \hbar\Omega\,, \tag{1.14}$$

which can lead to blockade radii on the order of micrometers for highly-excited Rydberg states [71]. The Rydberg blockade mechanism has been exploited to realize atomic two-qubit gates [138–140] and for entanglement generation [141].

It is worth pointing out that the Rydberg blockade is a special case of the more general concept of photon blockade, where the absorption of a second photon is suppressed or even blocked due to a nonlinearity in the excitation spectrum. Here, the position-dependent shift provides this nonlinearity. Other examples include photon blockade in cavities [142] and dense samples [143]. In the first example the resonance is shifted due to the coupling of cavity photons with an atom giving rise to hybridized eigenstates of the Jaynes-Cummings model. In the latter example, the nonlinearity is a consequence of the position-dependent shift induced by resonant dipole-dipole interactions between singly-excited states.

[3] For the sake of clarity, we use a repulsive van der Waals potential ($C_6 > 0$). The definition of the blockade radius for a Rydberg gas interacting via the dipolar potential C_3/r^3 is analogous.

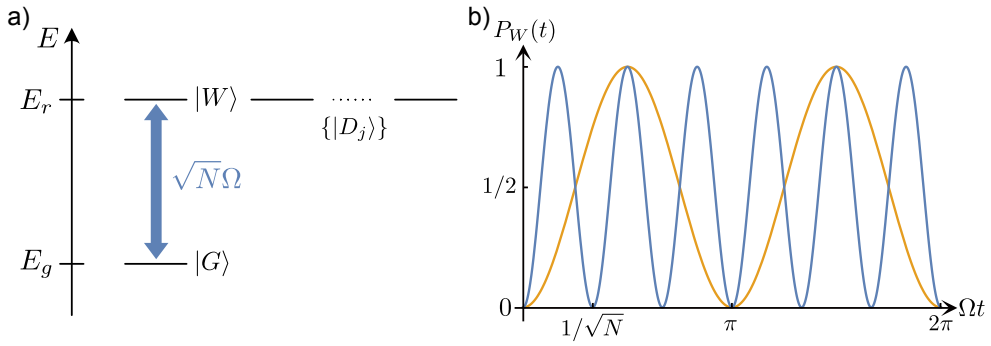

Fig. 1.3.: a) Level structure of the Rydberg superatom. The ground state $|G\rangle$ is coupled to the (collective) bright state $|W\rangle$ with Rabi frequency $2\sqrt{N}\Omega$. The $N-1$ dark states are not coupled to the light field. b) Collectively enhanced Rabi oscillations for the Rydberg superatom (blue) compared to the Rabi oscillations of a single atom (orange).

1.2.2. Collective States

When applied to atomic ensembles, the Rydberg blockade leads to the creation of Rydberg superatoms where a large number of atoms collectively share a single Rydberg excitation. In order to illustrate this concept, we consider N atoms confined to a volume which is smaller than the blockaded volume. As a consequence of the blockade mechanism, all but the singly-excited states are shifted out of resonance and the Hilbert space of the system reduces to the ground state $|G\rangle = |g_1, \ldots, g_N\rangle$ and the excited states $|j\rangle = |g_1, \ldots, r_j, \ldots, g_N\rangle$.

If the ensemble is illuminated by a plane wave of the form $e^{i\mathbf{kr}}$, the dynamics of the system can be reduced to the ground state $|G\rangle$ and the bright state, which the light field excites, given by

$$|W\rangle = \frac{1}{\sqrt{N}} \sum_{j=1}^{N} e^{i\mathbf{kr}_j} |g_1, \ldots, r_j, \ldots, g_N\rangle \ . \tag{1.15}$$

This state is also referred to as a "timed" Dicke state as it contains the information at which time the state $|j\rangle$ has been excited [16]. The Hamiltonian of the ensemble interacting with the light field then reduces to an effective two-level system of the form

$$H = \sqrt{N}\Omega \left(|G\rangle\langle W| + |W\rangle\langle G| \right) \ , \tag{1.16}$$

where the coupling strength is collectively enhanced by the square root of the number of atoms in the ensemble (see Figure 1.3). In addition, there are $N-1$

states $|D_j\rangle$ orthogonal to the bright state which are insensitive to the light field and are called dark states. The collectively enhanced coupling strength implies a collectively enhanced and strongly directed emission of the bright state. The dark states show no directed emission and remain subradiant.

At this point it is important to mention that the plane wave can only be used for pedagogical reasons as it is unphysical in real setups. First, a plane wave extends over the whole space and thus barely interacts with the ensemble. Second, even if one uses the plane wave as an incoming mode, one cannot get the correct collectively enhanced emission as the ensemble cannot emit into plane wave. Including a physical mode $u(\mathbf{r})$, e.g. a Gaussian beam mode, will be part of Chapter 3 where the interaction of a Rydberg superatom with a propagating light mode is studied.

If, however, both the radial as well as the longitudinal variation of the mode function are negligible compared to the length scale of the ensemble, the amplitudes for each atom are the same and the bright state corresponds the well-known symmetric Dicke state

$$|W\rangle = \frac{1}{\sqrt{N}} \sum_{j=1}^{N} |g_1, \ldots, r_j, \ldots, g_N\rangle \ . \tag{1.17}$$

The collective enhancement of the coupling to the light field and the cooperative behaviour of the atoms in a Rydberg superatom was first observed by a density-dependent increase in the excitation rate [144] and nonlinear scaling with density of the optical response [56]. The associated acceleration of coherent dynamics and the characteristic $\sqrt{N}$ scaling of the Rabi frequency were also experimentally verified [67, 145].

1.2.3. Applications of Rydberg Superatoms

The combination of strong light-matter coupling with full blockade of an ensemble in Rydberg superatoms opens the possibility to manipulate light on the single-photon level. Applications that have been demonstrated so far include the on-demand generation [67, 69] and the deterministic absorption [71] of single photons.

The principle of a single-photon source based on a Rydberg superatom was first demonstrated in [67] using a dense and small ensemble of cold rubidium atoms. The single-photon creation is facilitated by a four-wave mixing scheme where the Rydberg state is excited by a two-photon transition and then stored as a collective superposition inside the ensemble. When the photon is retrieved by coupling the Rydberg state to an intermediate state, the mode information stored in the excitation triggers a collective spontaneous emission process on the transition from the

intermediate state to the ground state with enhanced emission rate into the same mode as the stored photon.

The generation of only a single photon during this process strongly depends on the ensemble being fully blockaded. This is shown by measuring the intensity correlations at zero time delay $g^{(2)}(0)$ for the outgoing light as a function of the effective principle quantum number n^* of the Rydberg level. In the experimental setup realized in [67] the ensemble becomes fully blockaded as n^* increases limiting the number of storable photons to one. Consequently, $g^{(2)}(0)$ decreases to a value close to zero for $n^* > 90$ establishing high-quality single-photon statistics.

More recently, a single-photon source based on the same principle was demonstrated in a room-temperature atomic vapor [69], dramatically reducing the complexity of this approach. In the experiment, the vapor was contained in a wedge-shaped glass micro cell which could be translated perpendicular to the excitation beam thereby varying the longitudinal thickness of the atomic ensemble. Upon reducing the size of the cloud, single-photon statistics were demonstrated. Due to the higher temperatures and associated line broadening, the room-temperature approach requires much higher intensities for the excitation lasers resulting in Rabi frequencies on the order of GHz compared to those in the MHz regime for cold gases.

Instead of creating a single photon on demand, taking advantage of Rydberg superatoms as saturable absorbers can be used to deterministically remove single photons from a light field [70, 71]. This enables applications including but not limited to the realization of number-resolved photon detection or the creation of non-classical states of light for quantum-enhanced metrology [146].

Operating a Rydberg superatom as a single-photon absorber relies on engineering fast dephasing of the bright state $|W\rangle$ into subradiant dark states $|D_j\rangle$. As this process is irreversible, the absorbed photon is converted into a stationary Rydberg excitation preventing stimulated emission caused by the propagating light mode. As a consequence, the photon statistics of incoming coherent fields will be altered. The photon statistics of the incoming coherent field follows a Poisson distribution while the mean number of photons for the outgoing field is reduced by one whereas the width of the distribution remains unchanged. This results in super-Poissonian statistics of the outgoing light field, visible in the appearance of bunching features in the intensity correlations.

It is important to note that the deterministic subtraction of a photon is drastically different than applying the photon annihilation operator a, where the amplitude for removing a photon depends on the photon number which leaves a coherent state invariant. The photon subtraction, however, removes a photon independent of the photon number. Very recently, the capability to extend the single-photon

absorber scheme to multiple superatoms in a cascaded setup was demonstrated experimentally [72].

1.3. Resonant Dipole-Dipole Interactions

One of the main themes of this thesis is the resonant dipole-dipole interaction between emitters. In this section, we will briefly discuss the microscopic origin and form of this interaction and also comment on the connection with (resonant) dipole-dipole interactions in Rydberg ensembles as discussed in Section 1.1.3. A more detailed derivation of the resonant dipole-dipole interaction will be given in Chapter 2 in the context of a one-dimensional waveguide, which is conceptually similar to the three-dimensional case considered in this section.

The microscopic origin of the resonant dipole-dipole interaction is most easily understood by considering an ensemble of identical two-level atoms with internal states $|g\rangle$ and $|e\rangle$ dipole-coupled to the vacuum modes of the electromagnetic field. This system is described by the Hamiltonian, using the rotating-wave approximation and within the rotating frame,

$$H = \sum_{\mu} \int \frac{d^3q}{(2\pi)^3} \hbar\omega_{\mathbf{q}} a^{\dagger}_{\mathbf{q}\mu} a_{\mathbf{q}\mu} + \sum_j \left[\sigma_j^- \mathbf{d}\cdot\mathcal{E}^{\dagger}(\mathbf{r}_j) + \mathbf{d}\cdot\mathcal{E}(\mathbf{r}_j)\sigma_j^+\right] . \tag{1.18}$$

Here, the first term corresponds to the quantized free electromagnetic field described by the creation and annihilation operators $a^{\dagger}_{\mathbf{q}\mu}$ and $a_{\mathbf{q}\mu}$, respectively, with polarizations μ. The photons have the dispersion relation $\omega_q = c|\mathbf{q}| - \omega_0$. The second term describes the light-matter coupling of the transition $|g\rangle - |e\rangle$ with resonance requency $\omega_0 = ck = 2\pi c/\lambda$, $\sigma^- = |g\rangle\langle e|$, and the transition dipole moment $\mathbf{d} = d\hat{\mathbf{d}}$, which is assumed to be real for simplicity. The electric field operator in three dimensions reads

$$\mathcal{E}(\mathbf{r}) = \sum_{\mu} \int \frac{d^3q}{(2\pi)^3} c^{\mu}_{\mathbf{q}} a_{\mathbf{q}\mu} e^{i\mathbf{q}\mathbf{r}} , \tag{1.19}$$

with $c^{\mu}_{\mathbf{q}} = i\sqrt{\omega_q 2\pi\hbar}\,\varepsilon^{\mu}_{\mathbf{q}}$, where $\varepsilon^{\mu}_{\mathbf{q}}$ is the polarization vector of the mode with momentum $\mathbf{q}$ and polarization μ.

If one is only interested in the dynamics of the emitters, one can integrate out the photonic degrees of freedom and, when neglecting retardation effects, arrives

at a master equation for the reduced density matrix of the atoms [2]

$$\partial_t \rho(t) = -\frac{i}{\hbar}\left[\frac{1}{2}\sum_{j\neq l}\hbar V(\mathbf{r}_j-\mathbf{r}_l)\sigma_j^+\sigma_l^-,\rho(t)\right] + \sum_{j,l}F(\mathbf{r}_j-\mathbf{r}_l)\left(\sigma_l^-\rho(t)\sigma_j^+ - \frac{1}{2}\left\{\sigma_j^+\sigma_l^-,\rho(t)\right\}\right) \tag{1.20}$$

with the nonradiative (coherent) and radiative (dissipative) part, respectively,

$$V(\mathbf{r}) = \frac{3\Gamma}{2}\left[-\frac{\cos(\eta)}{\eta}(1-\xi^2)+(1-3\xi^2)\left(\frac{\cos(\eta)}{\eta^3}+\frac{\sin(\eta)}{\eta^2}\right)\right], \tag{1.21}$$

$$F(\mathbf{r}) = \frac{3\Gamma}{2}\left[\frac{\sin(\eta)}{\eta}(1-\xi^2)+(1-3\xi^2)\left(\frac{\cos(\eta)}{\eta^2}-\frac{\sin(\eta)}{\eta^3}\right)\right]. \tag{1.22}$$

Here, $\Gamma = 4k^3d^2/3\hbar$ is the single-atom spontaneous decay rate in free space[4], $\eta = k|\mathbf{r}|$ and $\xi = \hat{\mathbf{d}}\cdot\hat{\mathbf{r}}$ denotes the relative orientation of the dipole moment with respect to the distance vector of two atoms. Note that the case $\mathbf{r}_j = \mathbf{r}_l$ is excluded for the coherent part in Eq. (1.20) as this would give rise to a Lamb shift which is already included in the resonance frequency of the atoms. In the dissipative part, $\mathbf{r}_j = \mathbf{r}_l$ corresponds to the single-atom spontaneous decay rate. The position-dependent terms $V(\mathbf{r}_j-\mathbf{r}_l)\sigma_j^+\sigma_l^-$ and $F(\mathbf{r}_j-\mathbf{r}_l)\sigma_j^+\sigma_l^-$ are responsible for the long-range, anisotropic coherent exchange of excitations and correlated spontaneous emission, respectively. The latter are responsible for phenomena like superradiance where cooperative spontaneous emission occurs for dense ensembles with $\eta \ll 1$ for all atoms [3].

It is interesting to note that combining the non-radiative part (1.21) and radiative part (1.22) as $G(\mathbf{r}) = -V(\mathbf{r}) + iF(\mathbf{r})$, one obtains the classical Green's function of an oscillating dipole projected onto the dipole moment.[5] The equivalence to the classical case is a consequence of the Maxwell equations being also valid for the quantized electromagnetic field.

It is important to distinguish two limits determined by the parameter $\eta = k|\mathbf{r}|$. The near-field behaviour is characterized by $\eta \ll 1$. This occurs if the atoms are much closer than the wavelength of the resonant transition. Then the dissipative part approaches the constant Γ while the non-radiative part diverges as $1/\eta^3$ and

[4] We used Gaussian units in the derivation above. In SI units the decay rate is the more familiar $\Gamma = k^3d^2/3\pi\hbar\varepsilon_0$.

[5] The minus sign in front of V depends on the definition of the coherent exchange amplitudes in the Hamiltonian.

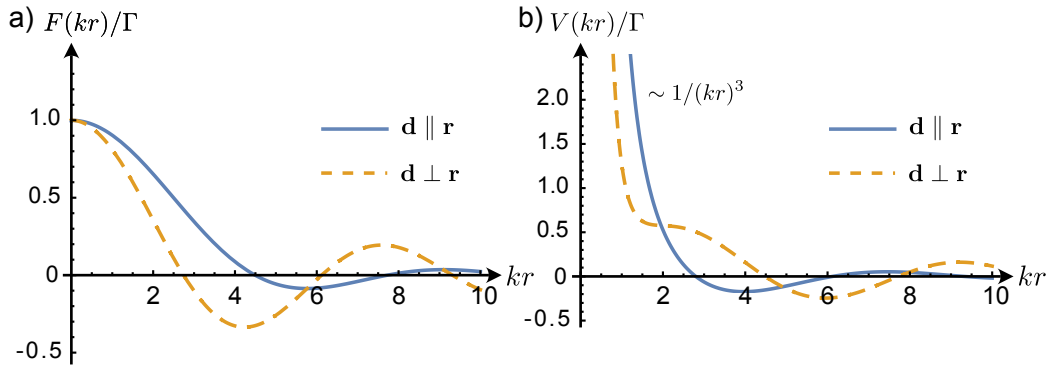

Fig. 1.4.: Radial dependence of the resonant dipole-dipole interaction. a) Radiative/dissipative part for perpendicular (orange dashed) and parallel (blue solid) orientation of the dipole moment to the relative position of the dipoles. The correlated decay approaches a constant for close atoms in both cases and decays as $\sin(kr)/kr$ for perpendicular orientation and $\cos(kr)/(kr)^2$ for parallel orientation. b) Nonradiative part for perpendicular (orange dashed) and parallel (blue solid) orientation of the dipole moment to the relative position of the dipoles. At short distances the coherent interaction diverges as $1/(kr)^3$ and reduces to the static form of the dipole-dipole interaction. At large separations, it scales as $\cos(kr)/kr$ for perpendicular orientation and $\sin(kr)/(kr)^2$ for parallel orientation. Note that the curve for the parallel alignment is multiplied by -1 for better comparison.

becomes dominant. The resonant dipole-dipole interaction reduces to the form of the static dipole-dipole interaction[6]

$$V(\mathbf{r}) = \frac{d^2}{|\mathbf{r}|^3}\left(1 - 3(\hat{\mathbf{d}} \cdot \hat{\mathbf{r}})^2\right) \tag{1.23}$$

between the two transition dipole moments $\mathbf{d}_1 = \mathbf{d}_2 = \mathbf{d}$. Note that, however, the resonant dipole-dipole interaction still is an exchange interaction while the static dipole-dipole has the form of a density-density interaction. The near-field regime is also important for Rydberg atoms where the interaction between transition dipole moments is based on transition frequencies in the microwave regime such that the near-field behaviour is dominant for typical experiments with confined ensembles.

In the far field, where $\eta \gg 1$, corresponding to atoms many wavelengths apart or extended ensembles, both the dissipative part and the non-radiative part become relevant and the behaviour is given by $\sin(\eta)/\eta$ and $\cos(\eta)/\eta$, respectively, with an additional geometric factor depending on the relative orientation between the dipole moment and the vector $\mathbf{r}$ between the dipoles. The full dipole-dipole interaction takes the form $\sim e^{i\eta}/\eta$ which has the same form as a spherical wave. The full dependence of $V(\mathbf{r})$ and $F(\mathbf{r})$ on η for parallel and perpendicular orientation of the dipole moment with respect to the relative distance between the emitters is shown in Fig. 1.4.

1.4. Waveguide Quantum Electrodynamics

In this section, we briefly discuss the main properties and features of low-dimensional waveguide systems giving rise to the new paradigm of waveguide quantum electrodynamics where atom-like quantum emitters are coupled to the electromagnetic field of a one-dimensional waveguide. Particular emphasis will be put on the appearance of nonreciprocal and chiral light-matter interactions, which we will make use of for parts of this thesis. Commonly used implementation of waveguide systems are optical nanofibers and photonic crystal waveguides, and superconducting qubits coupled to transmission lines operating in the microwave regime. A more detailed overview for optical nanofibers is given in [147] and in [94] for photonic nanostructures such as photonic crystal waveguides. An extensive review of superconducting qubits coupled to transmission lines is given in [148].

[6] In order to obtain the dipole-dipole interaction in SI units, one has to multiply the expression by $1/4\pi\varepsilon_0$.

Waveguides are characterized by a set of guided modes that propagate with very low losses along a one-dimensional channel. One way to realize guided modes in optical nanofibers is by tightly confining light along two directions, while allowing it to freely propagate along the third one. Optical nanofibers have a tapered structure such that the light can be efficiently coupled into the nanofiber but is still mode-matched to the thinned part. A second approach is to use structures such as photonic crystals, where the guided modes along one direction are the consequence of band gaps opening in the other direction because of periodic modulations of the structure or the refractive index [149]. Waveguide quantum electrodynamics in those systems is then realized by coupling to atoms via the evanescent field of the guided modes. Another possibility is, instead of using real atoms, to use artificial atoms composed of quantum dots or superconducting qubits which are then coupled to photonic structures or to the continuum of an open transmission line realized by a microwave LC circuit, respectively.

Important parameters in all waveguide quantum electrodynamics implementations are the emission rate into the guided modes of the waveguide $\Gamma_{1\mathrm{D}}$ and the emission rate into free space Γ. These parameters constitute the two figures of merit: The emission probability into the waveguide given by $\Gamma_{1\mathrm{D}}/(\Gamma_{1\mathrm{D}}+\Gamma)$, also called β-factor, and the optical depth $OD = N\Gamma_{1\mathrm{D}}/\Gamma$, which includes the number of emitters N coupled to the waveguide. While the β-factor accounts for the efficiency of the coupling to the waveguide modes for a single atom, the optical depth is the determining quantity for collective effects such as super- and subradiance to be observed. Setups with atoms coupled to optical nanofibers and photonic crystal waveguides only offer coupling efficiencies on the order of a few to a few ten percent [90–92] whereas solid-state implementations using quantum dots and superconducting qubits achieve couplings which are one or two orders of magnitude larger owing to the larger transition dipole moment of the artificial atoms [93, 95]. On the other hand, current solid-state implementations of waveguide quantum electrodynamics have only been realized with around ten superconducting qubits [150, 151], while for atom-based setups with optical nanofibers a few hundred to thousand atoms have been trapped [89] enabling the observation of strongly correlated photon transport through the waveguide [100].

In contrast to free space setups, where the amplitude of the electromagnetic field decays with distance, one-dimensional or quasi-one-dimensional system have fields propagating with almost nondecaying amplitude along the waveguide axis. This leads to infinite-ranged[7] resonant dipole-dipole interactions which have been

[7] Strictly speaking, infinite-ranged interactions are only possible for purely one-dimensional systems. In a broader sense, infinite-ranged here means that all atoms of an ensemble are interacting with the same strength albeit with different phase factors.

observed experimentally for atoms trapped close to optical nanofibers [90] but also in optical cavities, where self-organization due to infinite-ranged interactions was observed in a quantum degenerate Bose gas [152]. For purely one-dimensional systems, the exchange interaction strengths and correlated emission rates in Eq. (1.20) take the form

$$V_{1\mathrm{D}}(z) = \Gamma_{1\mathrm{D}} \sin(k|z|)\,, \tag{1.24}$$
$$F_{1\mathrm{D}}(z) = 2\Gamma_{1\mathrm{D}} \cos(k|z|)\,, \tag{1.25}$$

respectively, where $2\Gamma_{1\mathrm{D}}$ is the emission rate of a single atom into the waveguide. In addition, there is an uncorrelated decay into nonguided modes. Note that the detailed derivation of the dynamics of a one-dimensional system is presented in Chapter 2.

Another interesting prospect of low-dimensional artificial photonic structures is to realize non-Markovian dynamics in photonic crystal waveguides [153, 154]. In these systems, a band gap opens around a certain frequency and changes the dispersion relation around the band gap strongly reducing the group velocity of the photons close to the edge of the band gap [155, 156]. Then, non-Markovian effects can appear either due to the deviation from the linear dispersion relation or due to the stronger influence of retardation effects coming from the slowed down propagation velocity of the photons mediating the interaction. Examples of non-Markovian effects include the appearance of atom-photon bound states [157, 158], deviations from the exponential decay of an excitation [159], and super-superradiant behavior beyond the collective enhancement of the emission due to time-delayed feedback [160, 161]

1.4.1. Chiral Light-Matter Interactions

A very intriguing feature of quasi-one-dimensional systems where the light is strongly confined in the transversal direction is the appearance of nonreciprocal or chiral light-matter interactions. This is a consequence of a spin-momentum locking of light which we will briefly discuss in the following. A very good account on the physics of chiral light-matter interactions is given in [105] while the angular momentum of light and spin-momentum locking are discussed in depth in [107]. In the remainder of this section, we will closely follow the arguments presented in those works.

In order to understand nonreciprocal or chiral light-matter interaction, we consider a focused light beam propagating along the z-axis inside a waveguide. The electric field is given by $\mathbf{E}_{\pm}(\mathbf{r},t) = (\boldsymbol{\mathcal{E}}_{\pm}(\mathbf{r})e^{-i(\omega t \mp kz)} + \mathrm{c.c})/2$, where $\boldsymbol{\mathcal{E}}_{\pm}$ is the field amplitude, $k = 2\pi/\lambda$ is the wave vector and ω the angular frequency. The

positive and negative signs denote the direction of propagation of the field along the z-axis. Assuming no charges inside the waveguide, we can apply Gauss' law $\nabla \cdot \mathbf{E}_\pm = 0$ and get

$$\partial_x \mathcal{E}_\pm^x(\mathbf{r}) + \partial_y \mathcal{E}_\pm^y(\mathbf{r}) + \partial_z \mathcal{E}_\pm^z(\mathbf{r}) \pm ik\mathcal{E}_\pm^z = 0\,. \tag{1.26}$$

If the field amplitude $\mathcal{E}$ is slowly varying along the z-direction, we can set $\partial_z \mathcal{E}_\pm^z(\mathbf{r}) \approx 0$ and obtain an expression for the longitudinal component of the field amplitude

$$\mathcal{E}_\pm^z(\mathbf{r}) = \mp \frac{i}{k}\left(\partial_x \mathcal{E}_\pm^x(\mathbf{r}) + \partial_y \mathcal{E}_\pm^y(\mathbf{r})\right)\,. \tag{1.27}$$

Consequently, there is a longitudinal component of the electric field if there is a strong gradient in the transverse direction of the electric field which happens if the light field is strongly focused or is confined within the order of a wavelength λ as, for example, in photonic nanostructures. At the same time, the electric field becomes elliptically polarized as a consequence of the phase factor in front. Even more important, however, is that the direction of polarization depends on the direction of propagation as indicated by the $\mp$ sign in front of Eq. (1.27). Note that a longitudinal component of the electric field also appears for evanescent waves [107] to which atoms close to optical waveguides or nanofibers are coupled.

In order to illustrate the appearance of spin-momentum locking, we consider the electric field component of the spin angular momentum density [107, 162]

$$\mathbf{S}_{\mathrm{el}} = \frac{1}{16\pi\omega}\mathrm{Im}\left(\boldsymbol{\mathcal{E}}^* \times \boldsymbol{\mathcal{E}}\right)\,. \tag{1.28}$$

Note that there is an analogous definition for the magnetic field which gives rise to the magnetic field component of the spin angular momentum density. The combination of both contributions gives the (total) spin angular momentum of light $\mathbf{S}$. The spin angular momentum density of light is an intrinsic property of the electromagnetic field and has to be considered as an independent dynamical property of the field which is related to the polarization degrees of freedom. Other independent dynamical properties include the energy density of the field, the momentum density, and the helicity density [107].

Because the electric field acquires a longitudinal component, the spin angular momentum density has a non-zero transversal component whose sign depends on the direction of propagation of the light mode. This link between the direction of propagation and the sign of the transverse spin is known as spin-momentum locking and is a consequence of time-reversal symmetry of Maxwell's equations [163].

The spin-momentum locking directly leads to nonreciprocal couplings to confined propagating light fields as can be seen by the following arguments. Considering modes propagating into the positive and negative z-direction in a waveguide, the emission rates into the respective modes are given by $\Gamma_\pm \propto |\mathbf{d}^* \cdot \boldsymbol{\mathcal{E}}_\pm|^2$ with the complex transition dipole moment $\mathbf{d}$ and field amplitudes $\boldsymbol{\mathcal{E}}_\pm$. From the time-reversal symmetry of Maxwell's equation it follows that $\boldsymbol{\mathcal{E}}_+ = \boldsymbol{\mathcal{E}}_-^*$. If the transverse component of the spin angular momentum is nonzero, the fields cannot be real and $\boldsymbol{\mathcal{E}}_- \neq \boldsymbol{\mathcal{E}}_+$ implying that $\Gamma_- \neq \Gamma_+$. Thus, the absorption from and emission into a propagating mode depends on the direction of propagation of this mode and the light-matter interaction becomes nonreciprocal.

In the extreme case, one of the rates vanishes, for example $\Gamma_- = 0$, and the light-matter interaction becomes unidirectional or chiral. This can be achieved if the polarization of the light field is circular at the position of the emitters and opposite directions of propagation have orthogonal circular polarization. One way to realize this, for example, is to place atoms in the evanescent field at certain positions close to a nanofiber [106]. Matching the polarization of the atomic transition to which the light field couples with the polarization of the light field, the atom can only emit into or absorb light from one direction but not the other. It is important to note that the chirality of the light-matter interaction is only a consequence of the spin-momentum locking. The waveguide can still support modes propagating in both directions. Nonreciprocal and chiral light-matter interactions have been realized, for example, in solid-state systems by coupling quantum dots to a photonic crystal waveguide [164] and with atoms trapped close to an optical nanofiber [106], where in both systems a directionality of around 90% was observed.

2

Microscopic Description of Light-Matter Interaction: Master Equation and Input-Output Formalism

In this chapter, we discuss the microscopic description of light-matter interaction in ensembles of two-level atoms. By integrating out the photonic degrees of freedom we end up with an effective description of the matter degrees of freedom in terms of a master equation. This master equation is characterized by the propagator of the electric field which depends on the particular setup at hand and we will discuss different cases. To illustrate an application of the derived model, we discuss the propagation of a light pulse through an atomic medium under conditions of electromagnetically induced transparency.

2.1. Master Equation

We consider a system of N noninteracting two-level atoms at positions $\mathbf{r}_j$, where each atom has a ground state $|g\rangle$ and an excited state $|e\rangle$ which are separated by the energy $\hbar\omega_0 = \hbar ck$ as shown in Figure 2.1a). The Hamiltonian describing the system in the rotating-wave approximation[1] and within the rotating frame of the

[1] Since we are mostly interested in optical setups, where the transition frequency is on the order of a few hundred THz and coupling constant γ is in the MHz regime, this approximation is well satisfied for our purposes.

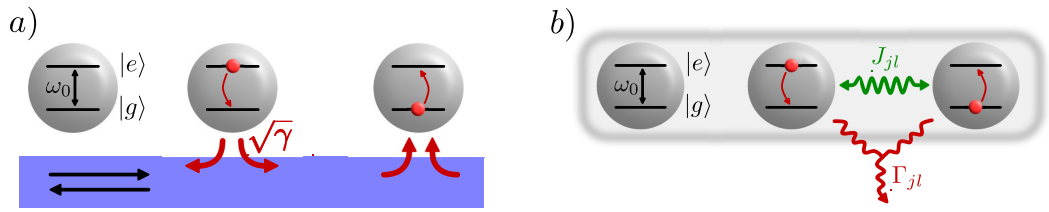

Fig. 2.1.: a) Two-level atoms coupled to a one-dimensional waveguide. The waveguide supports (in general) left- and right-propagating modes and the atoms can emit (absorb) photons into (from) both modes with single-atom coupling strength $\sqrt{\gamma}$. b) Effective system after the elimination of the waveguide photons. The atoms interact via an (infinite-ranged) exchange interaction J_{jl} and have a correlated decay Γ_{jl}.

atoms takes the form

$$H = H_0 - \hbar\sqrt{\gamma}\sum_{j=1}^{N}\left[\mathcal{E}^+(\mathbf{r}_j)\sigma_j^- + \sigma_j^+\mathcal{E}^-(\mathbf{r}_j)\right] . \tag{2.1}$$

The first term, H_0, characterizes the free evolution of the electromagnetic field and depends on the geometry of the system. The second part describes the coupling of the atoms to the electromagnetic field with coupling strength $\sqrt{\gamma}$ and the raising (lowering) operators $\sigma^+ = |e\rangle\langle g|$ ($\sigma^- = |g\rangle\langle e|$) for the atomic transition, respectively. The operator $\mathcal{E}^-$ ($\mathcal{E}^+$) denotes the positive (negative) frequency component of the electromagnetic field operator, respectively. Note that the scalar product of the polarization with the dipole transition moment is included in the definition of $\mathcal{E}^\pm$.

The electric field at any time t can be decomposed into the field radiated by spontaneous emission of the atoms and the free field which accounts for the quantized field of the incoming photons and reads [2, 96, 105, 165–169]

$$\mathcal{E}^-(\mathbf{r},t) = \mathcal{E}_0^-(\mathbf{r},t) + \sqrt{\gamma}\sum_{j=1}^{N} G(\mathbf{r},\mathbf{r}_j,\omega_0)\sigma_j^-(t) . \tag{2.2}$$

In this expression, $G(\mathbf{r},\mathbf{r}_j,\omega_0)$ is the propagator of the electric field whose precise form is determined by H_0 and we will show explicit forms for different setups in Section 2.2. The relation in Eq. (2.2) is peculiar in the sense that the propagator is local in time, which is only correct if the dispersion relation of the photons around the resonance frequency is linear for all relevant modes within the bandwidth of

the system and if retardation effects due to the propagation of photons through the ensemble can be neglected. These approximations are usually well satisfied in quantum optical experiments with (cold) atoms on which we focus in this thesis. The approximations will be reviewed and discussed in more detail in the following section where we explicitly calculate the propagator for one-dimensional setups.

The expression of the electric field operator, Eq. (2.2), then serves as the starting point to derive the master equation that describes the dynamics of the atoms alone. This derivation has been performed for a general setup in three dimensions [2] as well as for one-dimensional chiral and nonchiral waveguides [96, 105, 165–169]. For the sake of completeness, we will review this derivation here.

For an arbitrary operator O that acts only on the atomic degrees of freedom, the Heisenberg equation of motion reads

$$\begin{aligned}\partial_t O(t) &= -i\sqrt{\gamma}\sum_{j=1}^{N} \mathcal{E}^{+}(\mathbf{r}_j,t)[\sigma_j^{-}(t),O(t)] + [\sigma_j^{+}(t),O(t)]\mathcal{E}^{-}(\mathbf{r}_j,t)\\ &= -i\sqrt{\gamma}\sum_{j=1}^{N} \mathcal{E}_0^{+}(\mathbf{r}_j,t)[\sigma_j^{-}(t),O(t)] + [\sigma_j^{+}(t),O(t)]\mathcal{E}_0^{-}(\mathbf{r}_j,t)\\ &\quad - i\gamma\sum_{j,l=1}^{N} G^{*}(\mathbf{r}_j,\mathbf{r}_l,\omega_0)\sigma_l^{+}(t)[\sigma_j^{-}(t),O(t)]\\ &\quad + G(\mathbf{r}_j,\mathbf{r}_l,\omega_0)[\sigma_j^{+}(t),O(t)]\sigma_l^{-}(t)\,. \end{aligned} \tag{2.3}$$

Note that here $\mathcal{E}_0^{\pm}$ describes the free evolution of the incoming field and does not depend on any emitter operators. If we only consider coherent input fields such as a laser field, this contribution can be added to H_0 as a classical driving field using the Mollow transformation [170]. Consequently, we will ignore this contribution in the following.

Next, we use that $\partial_t\langle O(t)\rangle = \mathrm{tr}(\partial_t O(t)R(0)) = \mathrm{tr}(O\partial_t R(t))$, where $R(t)$ is the density matrix of the full system including photonic and atomic degrees of freedom. We assume the system to be in the initial state $R(0) = |0\rangle\langle 0|\otimes\rho(0)$, where $|0\rangle$ denotes the photonic vacuum and $\rho(0)$ is the initial density matrix of the atomic subsystem[2]. Furthermore, we are only concerned with atomic operators and can thus write $\mathrm{tr}(R(t)O) = \mathrm{tr}_S(\rho(t)O)$ where the trace in the second expression only

[2]Note that we can safely assume the photon field to be in the vacuum initially as we have already separated the contribution coming from the incoming field given by $\mathcal{E}_0$ for a coherent input. Equivalently, we can assume the photon field to be in a coherent state with field amplitude $\langle\mathcal{E}_0\rangle$ initially. In general, a non-coherent input can be included using the corresponding initial photonic state.

runs over the atomic degrees of freedom. It then follows

$$\begin{aligned}\partial_t\langle O(t)\rangle &= \mathrm{tr}_S(O\partial_t\rho(t))\\ &= -i\gamma\sum_{j,l=1}^{N} G^*(\mathbf{r}_j,\mathbf{r}_l,\omega_0)\mathrm{tr}_S(\sigma_l^+[\sigma_j^-,O]\rho(t))\\ &\quad + G(\mathbf{r}_j,\mathbf{r}_l,\omega_0)\mathrm{tr}_S([\sigma_j^+,O]\sigma_l^-\rho(t))\\ &= -i\gamma\sum_{j,l=1}^{N} G^*(\mathbf{r}_j,\mathbf{r}_l,\omega_0)\mathrm{tr}_S\left[O(\rho(t)\sigma_l^+\sigma_j^- - \sigma_j^-\rho(t)\sigma_l^+)\right]\\ &\quad + G(\mathbf{r}_j,\mathbf{r}_l,\omega_0)\mathrm{tr}_S\left[O(\sigma_l^-\rho(t)\sigma_j^+ - \sigma_j^+\sigma_l^-\rho(t))\right]\,. \end{aligned} \tag{2.4}$$

Since the operator O is arbitrary, we can infer the equation of motion for the density matrix ρ, which reads

$$\begin{aligned}\partial_t\rho(t) &= -i\gamma\sum_{j,l=1}^{N} G^*(\mathbf{r}_j,\mathbf{r}_l,\omega_0)(\rho(t)\sigma_l^+\sigma_j^- - \sigma_j^-\rho(t)\sigma_l^+)\\ &\quad + G(\mathbf{r}_j,\mathbf{r}_l,\omega_0)(\sigma_l^-\rho(t)\sigma_j^+ - \sigma_j^+\sigma_l^-\rho(t))\\ &= -\frac{i}{\hbar}\left[\hbar\sum_{j,l=1}^{N} J_{jl}\sigma_j^+\sigma_l^-,\rho(t)\right]\\ &\quad + \sum_{j,l=1}^{N}\Gamma_{jl}\left(\sigma_l^-\rho(t)\sigma_j^+ - \frac{1}{2}\{\sigma_j^+\sigma_l^-,\rho(t)\}\right)\,. \end{aligned} \tag{2.5}$$

The first term describes the coherent interaction induced by the virtual exchange of photons between the atoms, while the second term accounts for the correlated spontaneous emission (see Figure 2.1b)). The exchange interaction strengths and decay rates are related to the propagator via

$$J_{jl} = -\gamma\frac{G^*(\mathbf{r}_l,\mathbf{r}_j,\omega_0)+G(\mathbf{r}_j,\mathbf{r}_l,\omega_0)}{2}\,, \tag{2.6}$$

$$\Gamma_{jl} = i\gamma(G^*(\mathbf{r}_l,\mathbf{r}_j,\omega_0) - G(\mathbf{r}_j,\mathbf{r}_l,\omega_0))\,. \tag{2.7}$$

Here, the term J_{jj} accounts for a single-atom Lamb shift and is usually dropped as the Lamb shift is already included in the resonance frequency of a single emitter. In turn, Γ_{jj} gives the single-emitter decay rate. Note that the above expressions are general and do not assume any symmetry of the photon propagator. This becomes crucial when one considers a one-dimensional chiral waveguide where the propagator is not symmetric under the exchange of two atoms.

2.2. Propagator of the Electromagnetic Field

In the previous section we have derived the general master equation that describes the dynamics of an ensemble of atoms which is coupled to a continuum of photonic modes. In this section we specify the nature of the photonic modes and focus on one-dimensional systems which are of interest for the remainder of this thesis. Of particular interest will be the difference between bidirectional and chiral one-dimensional waveguides. While the former supports modes that can propagate in both directions, the latter breaks time-reversal symmetry and the symmetry under exchange of two atoms which leads to the interesting phenomena at the core of this thesis.

For simplicity, we assume the atoms to be at positions $\mathbf{r}_j = (x_j, 0, 0)^T$ along the waveguide which extends in x-direction and consider the coupling strengths of all atoms to be equal.

2.2.1. One-Dimensional Chiral Waveguide

In the following, we outline the derivation of the propagator of the photon field for a one-dimensional waveguide focussing first on the chiral setup and then extending this to the bidirectional case. The Hamiltonian for the photons in the rotating frame of the atoms for the chiral waveguide reads

$$H_0 = \int_{k-q_c}^{k+q_c} \frac{dq}{2\pi} \hbar\omega_q a_q^\dagger a_q \,, \tag{2.8}$$

where $\omega_q = c|q| - \omega_0$ is the dispersion relation for the photons which is assumed to be linear around the resonance frequency ω_0 of the atoms. The range of momenta for which the dispersion relation is linear is characterized by the cutoff momentum q_c. The bosonic operators $a_q^\dagger$ (a_q) describe the creation (annihilation) of a photon with momentum q. The electric field operator takes the form

$$\mathcal{E}^-(x) = i\sqrt{c} \int_{k-q_c}^{k+q_c} \frac{dq}{2\pi} a_q e^{iqx} \,. \tag{2.9}$$

In order to derive the propagator of the photon field, we start with the time evolution of the electric field which is obtained by formally integrating the Heisenberg equation of motion

$$\partial_t a_q(t) = \frac{i}{\hbar}[H, a_q(t)] = -i\omega_q a_q(t) + \sqrt{\gamma\, c} \sum_{j=1}^{N} e^{-iqx_j} \sigma_j^-(t) \tag{2.10}$$

which gives

$$a_q(t) = e^{-i\omega_q t} a_q(0) + \sqrt{\gamma\, c} \sum_{j=1}^{N} \int_0^t ds\, e^{-iqx_j} e^{-i\omega_q(t-s)} \sigma_j^-(s)\,. \tag{2.11}$$

Plugging this expression back into the mode expansion of the electric field, Eq. (2.9), results in

$$\mathcal{E}^-(x,t) = \mathcal{E}_0^-(x,t) + ic\sqrt{\gamma} \sum_{j=1}^{N} \int_{k-q_c}^{k+q_c} \frac{dq}{2\pi} \int_0^t ds\, e^{-i\omega_q(t-s)+iq(x-x_j)} \sigma_j^-(s)\,, \tag{2.12}$$

where $\mathcal{E}_0^-(x,t) = i\sqrt{c}\int_{k-q_c}^{k+q_c} \frac{dq}{2\pi} a_q(0) e^{-i\omega_q t + iqx}$ is the noninteracting component of the electric field. Since the dispersion relation is linear, we can easily convert the integration over the momentum to an integration over the frequency using $\omega = cq$ and $\omega_c = cq_c$ such that we can simplify the second term in Eq. (2.12) to

$$\begin{aligned}
&ic\sqrt{\gamma} \sum_{j=1}^{N} \int_{k-q_c}^{k+q_c} \frac{dq}{2\pi} e^{iq(x-x_j)} \int_0^t ds\, e^{-i\omega_q(t-s)} \sigma_j^-(s) \\
&= i\sqrt{\gamma} \sum_{j=1}^{N} e^{i\omega_0(x-x_j)/c} \int_{\omega_0-\omega_c}^{\omega_0+\omega_c} \frac{d\omega}{2\pi} \int_0^t ds\, e^{-i(\omega-\omega_0)[t-s-(x-x_j)/c]} \sigma_j^-(s) \\
&= i\sqrt{\gamma} \sum_{j=1}^{N} e^{i\omega_0(x-x_j)/c} \int_0^t ds\, \frac{\sin\left[\omega_c(t-s-(x-x_j)/c)\right]}{\pi(t-s-(x-x_j)/c)} \sigma_j^-(s)\,.
\end{aligned} \tag{2.13}$$

In order to simplify the last expression, we assume that the atomic operators σ_j^- only slowly vary on a time scale $1/N\gamma$ with $N\gamma \ll \omega_c \ll \omega_0$. The main contribution to the integral then comes from values around $s = t - (x - x_j)/c$ as long as $x \geq x_j$ and we can approximate the integration over time as $\theta(x - x_j)\sigma_j^-(t - (x - x_j)/c)$, where $\theta(x)$ is the Heaviside function with $\theta(x > 0) = 1$, $\theta(x < 0) = 0$ and $\theta(0) = 1/2$. This approximation is known as *narrow-bandwidth approximation* (or *Weisskopf-Wigner approximation* [171]) and is closely connected to the Markov approximation [172]. It relies on a continuum of modes and a linear spectrum and allows to replace the frequency integration by a δ-function at the retarded time $t - (x - x_j)/c$ as long as $x \geq x_j$. The latter condition is reminiscent of the chirality of the system.

The electric field then takes the form

$$\mathcal{E}^-(x,t) = \mathcal{E}_0^-(x,t) + i\sqrt{\gamma} \sum_{j=1}^{N} \theta(x - x_j) e^{ik(x-x_j)} \sigma_j^-(t - (x - x_j)/c)\,. \tag{2.14}$$

Note that this expression still includes retardation effects. These can be neglected if the time scale for a photon to propagate through the ensemble of atoms is much smaller than the time scale on which the atomic operators evolve, that is $L/c \ll 1/N\gamma$, where L is the width of the system. For typical quantum optical setups with coupling strengths on the order of a few MHz and atom numbers of a few thousands to ten thousands, this corresponds to a maximum width on the order of a few millimeters to centimeters. This is well beyond the length scales of micrometers of those systems we are interested in.

Neglecting retardation effects, we can approximate $\sigma_j^-(t-(x-x_j)/c) \approx \sigma_j^-(t)$ and the expression for the electric field becomes local in time, that is

$$\mathcal{E}^-(x,t) = \mathcal{E}_0^-(x,t) + i\sqrt{\gamma}\sum_{j=1}^{N}\theta(x-x_j)e^{ik(x-x_j)}\sigma_j^-(t)\,. \tag{2.15}$$

Comparing this with Eq. (2.2), we can infer the propagator for a one-dimensional chiral waveguide which reads

$$G_{\text{chiral}}(x,x_j,\omega_0) = i\theta(x-x_j)e^{ik(x-x_j)} = i\theta(x-x_j)e^{i\omega_0(x-x_j)/c}\,. \tag{2.16}$$

It is important to note that this propagator is not symmetric under the exchange of two atoms, that is $G_{\text{chiral}}(x_j,x_l) \neq G_{\text{chiral}}(x_l,x_j)$ and the coherent exchange terms and decay rates read

$$J_{jl} = \frac{\gamma}{2i}\text{sign}(x_j-x_l)e^{ik(x_j-x_l)}\,, \tag{2.17}$$

$$\Gamma_{jl} = \gamma e^{ik(x_j-x_l)}\,, \tag{2.18}$$

where $\text{sign}(x \lessgtr 0) = \mp 1$ and $\Gamma_{jj} = \gamma$ is the single-atom decay rate.

2.2.2. One-Dimensional Bidirectional Waveguide

In contrast to the chiral waveguide where the atoms are only coupled to modes propagating into one direction, that is for example only modes having positive momentum, we turn to the situation where the atoms are coupled to modes having both positive and negative momenta. In this case, the Hamiltonian that describes the waveguide photons reads

$$H_0 = \int_{k-q_c}^{k+q_c}\frac{dq}{2\pi}\hbar\omega_q a_q^\dagger a_q + \int_{-k-q_c}^{-k+q_c}\frac{dq}{2\pi}\hbar\omega_q a_q^\dagger a_q\,, \tag{2.19}$$

where the first term is the same as in the chiral case and the second one accounts for modes propagating with negative momentum. Analogously, the electric field operator is

$$\mathcal{E}^-(x) = i\sqrt{c}\left(\int_{k-q_c}^{k+q_c}\frac{dq}{2\pi} + \int_{-k-q_c}^{-k+q_c}\frac{dq}{2\pi}\right)e^{iqx}a_q\,. \tag{2.20}$$

Similar to the chiral waveguide, the Heisenberg equation of motion for the photonic operator a_q can be formally integrated and plugged into the expression for the electric field, Eq. (2.20). The interacting part of the electric field then has the form

$$\begin{aligned} &ic\sqrt{\gamma}\sum_{j=1}^{N}\left(\int_{k-q_c}^{k+q_c} + \int_{-k-q_c}^{-k+q_c}\right)\frac{dq}{2\pi}e^{iq(x-x_j)}\int_0^t ds\, e^{-i\omega_q(t-s)}\sigma_j^-(s) \\ &= i\sqrt{\gamma}\sum_{j=1}^{N}\sum_{\lambda=\pm}\int_{\omega_0-\omega_c}^{\omega_0+\omega_c}\frac{d\omega}{2\pi}e^{i\lambda\omega(x-x_j)/c}\int_0^t ds\, e^{-i(\omega-\omega_0)(t-s)}\sigma_j^-(s)\,. \end{aligned} \tag{2.21}$$

Here, the sum over $\lambda = \pm$ accounts for the fact that we now couple to two different modes. Performing the narrow-bandwidth approximation as well as neglecting retardation effects, we arrive at

$$\begin{aligned} &i\sqrt{\gamma}\sum_{j=1}^{N}\sum_{\lambda=\pm}\int_{\omega_0-\omega_c}^{\omega_0+\omega_c}\frac{d\omega}{2\pi}e^{i\lambda\omega(x-x_j)/c}\int_0^t ds\, e^{-i(\omega-\omega_0)(t-s)}\sigma_j^-(s) \\ &\approx i\sqrt{\gamma}\sum_{j=1}^{N}\sum_{\lambda=\pm}\theta(\lambda(x-x_j))e^{i\lambda k(x-x_j)}\sigma_j^-(t) \\ &= i\sqrt{\gamma}\sum_{j=1}^{N}e^{ik|x-x_j|}\sigma_j^-(t)\,. \end{aligned} \tag{2.22}$$

From the last expression, we obtain the propagator of the photon field for a bidirectional waveguide, which is

$$G(x, x_j, \omega_0) = ie^{i\omega_0|x-x_j|/c} = ie^{ik|x-x_j|}\,. \tag{2.23}$$

In contrast to the propagator in the chiral case, this propagator is symmetric under the exchange of two atoms, that is $G(x_j, x_l) = G(x_l, x_j)$. The coherent exchange terms and decay rates are, respectively,

$$J_{jl} = \gamma\sin(k|x_j - x_l|)\,, \tag{2.24}$$

$$\Gamma_{jl} = 2\gamma\cos(k|x_j - x_l|)\,. \tag{2.25}$$

The single-atom decay rate $\Gamma_{jj} = 2\gamma$ is twice as large as for the chiral waveguide as the atom can now emit a photon in the forward and backward direction.

2.3. Propagation through an EIT Medium

As an application of the theoretical foundations we have laid in the previous section, we turn to the propagation of a light pulse through an atomic medium under conditions of electromagnetically induced transparency (EIT) [53]. In such a setup, the dissipative response of a two-level system to incoming light is changed to being absorptive by strongly coupling the excited state $|e\rangle$ to another metastable state $|r\rangle$ by means of an additional classical light field on two-photon resonance.

Typically, the single-photon propagation is studied by means of the Maxwell-Bloch equations in the paraxial equation [57, 173] where the atomic medium is assumed to be homogeneous and the photons propagate as so-called dark state polaritons through the ensemble. In the following, we present an alternative way to describe the single-photon propagation which uses the master equation (2.5) to calculate the dynamics of the individual atoms and the input-output relation (2.2) to reconstruct the outgoing electric field. We want to point out that a similar treatment using the same method is given in [174] where the propagation is solved numerically and higher input intensities are treated using matrix product states. Here, we only consider a single excitation and solve the propagation analytically for a setup which can be modelled as atoms coupled to a chiral waveguide.

2.3.1. Setup

In order to microscopically describe the propagation of a light pulse through an EIT medium, we consider an ensemble of N three-level atoms with ground state $|g\rangle$, an intermediate state $|e\rangle$, and a metastable state $|r\rangle$ (see Fig. 2.2a)). The state $|g\rangle$ is coupled to $|e\rangle$ by a weak, quantized propagating light field. For simplicity, we assume that the light field, which propagates along the z-direction, is characterized by a single transverse mode of transverse width ξ, which is much larger than the resonance wavelength λ of the $|g\rangle$-$|e\rangle$ transition but much smaller than the radial size of the medium $L_\perp$ (see Fig. 2.2b)). The transition between the intermediate state $|e\rangle$ and the metastable state $|r\rangle$ is driven by a classical light field with Rabi frequency 2Ω and detuning δ. The coupling laser is assumed to be homogenous over the whole ensemble both in radial as well as in longitudinal direction and the two-photon transition from $|g\rangle$ to $|r\rangle$ is resonant.

Even though the system is three-dimensional, one can go over to a one-dimensional description if the longitudinal extent of the medium is much larger than the transverse size of the light mode, that is $L \gg \xi$. In this scenario, the field emitted by the atoms has mostly wave vectors which point along the direction of propagation of the incoming light field and the radiated field only varies along the

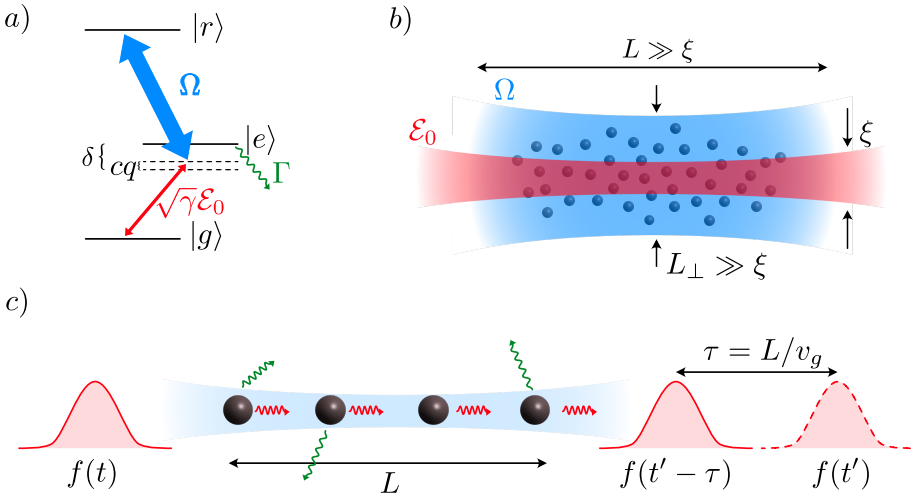

Fig. 2.2.: a) EIT setup in ladder scheme. A weak (quantized) probe field $\mathcal{E}_0$ couples to the transition between the ground state $|g\rangle$ and the intermediate state $|e\rangle$ with single-atom coupling strength $\sqrt{\gamma}$. A strong coupling laser drives the transition from $|e\rangle$ to a metastable state $|r\rangle$ with Rabi frequency 2Ω and detuning δ. The intermediate state decays with a rate Γ. b) Three-dimensional setup for the propagation. The incoming probe field is characterized by a single transverse mode of size ξ. If the transverse mode size is much smaller than the radial extent $L_\perp$ of the medium and also much smaller than its length L, the system can be treated as being one-dimensional. The coupling laser is assumed to be homogenous over the whole ensemble both in radial as well as in longitudinal direction. c) Propagation through the EIT medium in the one-dimensional approximation and slow light. The incoming coherent state with temporal mode $f(t)$ propagates through a one-dimensional chiral system with N atoms of length L. Due to the coupling to the metastable state the group velocity inside the medium is reduced, $v_g \ll c$, and the outgoing photon field is delayed by $\tau = L/v_g$. For long pulses, the propagation is lossless and the temporal shape is preserved.

longitudinal axis if the number of atoms is large enough [5] [3]. Emission into other modes can then be neglected with respect to the collective emission in the forward (and backward direction) and might well be treated as a spontaneous single-atom decay rate Γ accounting for uncorrelated emission into other directions. Note that this is only an approximation and it has been shown that keeping the correlated emission into other modes can lead to interesting physical effects [25]. While this reasoning still allows emission in the backward direction as well, we emphasize that backscattering is strongly suppressed for a smooth distribution of the atoms. This can be intuitively understood by the fact that the incoming field imprints a phase e^{ikz} on the atoms, while a backscattered field has the phase e^{-ikz}. If the characteristic size of the ensemble is on a scale $L \gg \lambda$, then the backscattered field is strongly suppressed in L/λ.

2.3.2. Model and Master Equation

In the one-dimensional approximation, the Hamiltonian within the rotating frame of the atoms[4] is given by

$$H_{\mathrm{1D}} = \int_{k-q_c}^{k+q_c} \frac{dq}{2\pi} \hbar\omega_q a_q^\dagger a_g - \sqrt{\gamma} \sum_{j=1}^{N} \left[\mathcal{E}^+(z_j)\sigma_j^- + \sigma_j^+ \mathcal{E}^-(z_j)\right] + \sum_{j=1}^{N} \hbar\delta\sigma_j^+\sigma_j^- + \sum_{j=1}^{N} \hbar\Omega(\sigma_j^+\tau_j^- + \tau_j^+\sigma_j^-)\,. \tag{2.26}$$

The first term represents the photonic field propagating from left to right, the second term accounts for the coupling to the quantized light field, the third term is the atomic Hamiltonian, and the last term gives the coupling of the intermediate state to the metastable state $|r\rangle$. The transition from $|g\rangle$ to $|e\rangle$ is described by the operator $\sigma^+ = |e\rangle\langle g|$ and the transition from $|e\rangle$ to $|r\rangle$ by $\tau^+ = |r\rangle\langle e|$. Note that unlike other approaches, we still retain the granularity of the system in the direction of propagation and do not assume a homogeneous distribution along this direction.

Similar to the previous sections, we can integrate out the quantized light field

[3] The important quantity in this context is the Fresnel number $F = \pi\xi^2/L\lambda$ which in fact should be on the order of one to treat the problem as being one-dimensional [5].

[4] And of course within the rotating-wave approximation and the dipole approximation.

which leads to the master equation for the atoms

$$\partial_t \rho(t) = -\frac{i}{\hbar}[H, \rho(t)] + \gamma \sum_{j,l=1}^{N} e^{ik(z_j - z_l)} \left(\sigma_l^- \rho(t) \sigma_j^+ - \frac{1}{2}\{\sigma_j^+ \sigma_l^-, \rho(t)\} \right) + \Gamma \sum_{j=1}^{N} \left(\sigma_j^- \rho(t) \sigma_j^+ - \frac{1}{2}\{\sigma_j^+ \sigma_j^-, \rho(t)\} \right) , \tag{2.27}$$

where $H = H_{\text{drive}} + H_{\text{chiral}} + H_{\text{sys}}$ is the Hamiltonian of the system with

$$H_{\text{drive}} = \hbar\sqrt{\gamma} \sum_{j=1}^{N} \left(f(t) e^{ikz_j} \sigma_j^+ + f^*(t) e^{-ikz_j} \sigma_j^- \right) , \tag{2.28}$$

$$H_{\text{chiral}} = \sum_{j,l=1}^{N} \frac{\hbar\gamma}{2i} \text{sign}(z_j - z_l) e^{ik(z_j - z_l)} \sigma_j^+ \sigma_l^- , \tag{2.29}$$

$$H_{\text{sys}} = \sum_{j=1}^{N} \left(\hbar\delta \sigma_j^- \sigma_j^+ + \hbar\Omega(\sigma_j^+ \tau_j^- + \tau_j^+ \sigma_j^-) \right) . \tag{2.30}$$

The Hamiltonian H_{drive} describes the driving due to the incoming propagating coherent light field with spatio-temporal mode $\langle \mathcal{E}_0(z,t) \rangle = f(t) e^{ikz}$, the Hamiltonian H_{chiral} accounts for the photon-mediated chiral interactions between the atoms and H_{sys} describes the pure system Hamiltonian taking into account the detuning from the intermediate state and the coupling between $|e\rangle$ and $|r\rangle$. The second term in Eq. (2.27) gives the correlated emission into the forward direction and the last term accounts for residual decay of the intermediate state in other directions which we assume is the same for all the atoms and that emission into other directions than the forward direction is uncorrelated.

2.3.3. Collective Operators and Equations of Motion

The master equation can be slightly simplified by introducing the collective operators $S^+ = 1/\sqrt{N} \sum_j e^{ikz_j} \sigma_j^+$ and $T^+ = 1/\sqrt{N} \sum_j e^{ikz_j} \tau_j^+$. Then, the incoming field couples to the collective excitation $S^+ |g_1, \cdots, g_N\rangle$ with collectively enhanced coupling strength $\sqrt{N\gamma} = \sqrt{\kappa}$ described by the Hamiltonian

$$H_{\text{drive}} = \hbar\sqrt{\kappa} (f(t) S^+ + f^*(t) S^-) . \tag{2.31}$$

In addition, the emission into the forward direction is collectively enhanced and described by

$$\gamma \sum_{j,l=1}^{N} e^{ik(z_j - z_l)} \left(\sigma_l^- \rho(t) \sigma_j^+ - \frac{1}{2}\{\sigma_j^+ \sigma_l^-, \rho(t)\} \right) = \kappa \Bigg(S^- \rho(t) S^+ - \frac{1}{2}\{S^+ S^-, \rho(t)\} \Bigg) . \tag{2.32}$$

The outgoing electric field can be calculated using the input-output relation (2.2) and reads

$$\mathcal{E}^-(z > z_N, t) = f(t - z/c) - i\sqrt{\kappa} S^-(t - z/c) . \tag{2.33}$$

Introducing the collective operators

$$S_\alpha^\pm = \frac{1}{\sqrt{N}} \sum_{j=1}^{N} e^{\mp i \frac{\pi \alpha j}{N}} e^{\pm i k z_j} \sigma_j^\pm \tag{2.34}$$

where α is an odd number with $-N \leq \alpha < N$, one can write the Hamiltonian that mediates the chiral atom-atom interactions as

$$H_{\text{chiral}} = \frac{\hbar \gamma}{2} \sum_\alpha \cot\left(\frac{\pi \alpha}{2N}\right) S_\alpha^+ S_\alpha^- . \tag{2.35}$$

The collective operator S^- can be expressed in terms of S_α^- as $S^- = \sum_\alpha a_\alpha S_\alpha^-$ with $a_\alpha = 2/[N(e^{-i\pi\alpha/N} - 1)]$ and similarly for S^+. The properties of the operators $S_\alpha^\pm$ and the diagonalization of the Hamiltonian will be discussed in more detail in Chapter 4 of this thesis.

Using an analogous definition for the operators T_α, the coherent part of the master equation then takes the form

$$H = \sum_\alpha \begin{pmatrix} S_\alpha^+ \\ T_\alpha^+ \end{pmatrix}^T \begin{pmatrix} E_\alpha + \hbar\delta & \hbar\Omega \\ \hbar\Omega & 0 \end{pmatrix} \begin{pmatrix} S_\alpha^- \\ T_\alpha^- \end{pmatrix} + \hbar\sqrt{\kappa}(f(t) S^+ + f^*(t) S^-) , \tag{2.36}$$

with $E_\alpha = \frac{\hbar\gamma}{2} \cot(\frac{\pi\alpha}{2N})$.

As we are only interested in weak input fields, we work in the low-excitation regime, where the collective operators $S_\alpha^\pm$ and $T_\alpha^\pm$ can be treated as bosonic with the commutation relations $[S_\alpha^-, S_\beta^+] \approx \delta_{\alpha\beta}$ and $[T_\alpha^-, T_\beta^+] \approx \delta_{\alpha\beta}$, respectively. This approximation neglects the fact that every atom can only carry one excitation and

introduces errors on the order of $1/N$. For the sake of clarity, we make the replacement $S^- \to S$ and $S^+ \to S^\dagger$ for all collective operators and similarly for T whenever we use the bosonic approximation. The equations of motion for the collective (bosonic) operators read

$$\partial_t S_\alpha(t) = -i(E_\alpha/\hbar + \Delta)S_\alpha(t) - i\Omega T_\alpha - i\sqrt{\kappa} f(t) a_\alpha^* - \frac{\kappa}{2} a_\alpha^* S(t)\,, \tag{2.37}$$

$$\partial_t T_\alpha(t) = -i\Omega S_\alpha(t)\,, \tag{2.38}$$

where $\Delta = \delta - i\Gamma/2$ is a complex detuning that also accounts for the uncorrelated single-atom decay. Going over to frequency space, we get $\tilde{T}(\omega) = \frac{\Omega}{\omega}\tilde{S}(\omega)$ leading to

$$\omega \tilde{S}_\alpha(\omega) = \left(\frac{E_\alpha}{\hbar} + \Delta + \frac{\Omega^2}{\omega}\right)\tilde{S}_\alpha(\omega) + a_\alpha^*\left(\sqrt{\kappa}\tilde{f}(\omega) - i\frac{\kappa}{2}\tilde{S}(\omega)\right). \tag{2.39}$$

Solving this equation for $\tilde{S}_\alpha(\omega)$ and plugging the result into $\tilde{S} = \sum_\alpha a_\alpha \tilde{S}_\alpha$ results in

$$\tilde{S}(\omega) = \sum_\alpha |a_\alpha|^2 \frac{\sqrt{\kappa}\tilde{f}(\omega) - i\frac{\kappa}{2}\tilde{S}(\omega)}{\omega - (E_\alpha/\hbar + \Delta + \Omega^2/\omega)}\,. \tag{2.40}$$

This equation only depends on the collective operator $\tilde{S}(\omega)$ and is solved by

$$\tilde{S}(\omega) = \frac{1}{\kappa}\frac{\sqrt{\kappa}\tilde{f}(\omega)\mu(\omega)}{1 + i\frac{\mu(\omega)}{2}} \tag{2.41}$$

with $\mu(\omega) = \kappa\sum_\alpha |a_\alpha|^2/(\omega - (E_\alpha/\hbar + \Delta + \Omega^2/\omega))$. This result can now be used to directly relate the outgoing photon field to the incoming one using Eq. (2.33) and gives

$$\tilde{\mathcal{E}}^-(z > z_N, \omega) = \frac{1 - i\frac{\mu(\omega)}{2}}{1 + i\frac{\mu(\omega)}{2}}\tilde{f}(\omega)e^{i\frac{z}{c}\omega}\,. \tag{2.42}$$

The physical interpretation of Eq. (2.42) is that the prefactor in front of the incoming field $\tilde{f}(\omega)$ plays the role of a transmission coefficient which reduces to a phase factor if $\Gamma = 0$ and includes absorption of photons for $\Gamma \neq 0$. Going to the limit where $N \to \infty$, the analytic form of $\mu(\omega)$ is

$$\mu(\omega) \approx \kappa \sum_\alpha \frac{4}{\pi^2\alpha^2}\frac{1}{\omega - (\frac{\kappa}{\pi\alpha} + \Delta + \frac{\Omega^2}{\omega})} = 2\tan\left(\frac{\kappa/2}{\omega - \Delta - \frac{\Omega^2}{\omega}}\right). \tag{2.43}$$

Plugging this back into Eq. (2.42) and using $\frac{1-i\tan(1/2x)}{1+i\tan(1/2x)} = e^{-i/x}$ leads to

$$\tilde{\mathcal{E}}^{-}(z > z_N, \omega) = \exp\left(i\frac{\kappa\,\omega}{(\Delta-\omega)\omega+\Omega^2}\right)\tilde{f}(\omega)e^{i\frac{z}{c}\omega}\,. \tag{2.44}$$

The above formula encodes all information for the propagation of the light pulse through the medium in the limit of weak intensity where the medium is far below saturation and the bosonic approximation is valid. It was already derived in the context of photons propagating through a Rydberg medium under conditions of electromagnetically induced transparency by approximating the medium as being continuous [57]. We want to stress that this assumption was not necessary here and Eq. (2.42) gives the result when retaining the granularity of the system. It is, however, important to note that in the derivation of Eq. (2.44) we used that $N \to \infty$ in order to arrive at the continuum limit. This in turn means that also $\kappa \to \infty$ which is unphysical when compared to real media that always have a finite number of particles. The relevant quantity for the linear optical response is the (resonant) optical depth OD in the absence of the coupling laser Ω. For the setup discussed here, it is given by $\mathrm{OD} = 2\kappa/\Gamma = 2N\gamma/\Gamma$ and is assumed to be finite such that we have to keep $\kappa = N\gamma$ constant when going over to the continuum limit.

The approach discussed above in principle offers the possibility to include backscattering in the one-dimensional channel, which is neglected in the standard approach considering a continuous medium. To this end, the coherent exchange interactions and correlated emission rates of a bidirectional waveguide given in Eqs. (2.24) and (2.25), respectively, have to be used in Eq. (2.27). This, however, is beyond the scope of this thesis.

2.3.4. Slow Light

In the low-energy regime where $\omega \ll \Omega, |\Delta|, \kappa$, meaning only slowly varying pulses, the phase factor in Eq. (2.44) can be simplified leading to

$$\tilde{\mathcal{E}}^{-}(L, \omega) \approx e^{i\omega\tau}\tilde{f}(\omega) \tag{2.45}$$

with $\tau = \kappa/\Omega^2 + L/c$. This results in an outgoing field delayed by τ after transforming back into the time domain (see Fig. 2.2c)). Due to the coupling to the metastable state $|r\rangle$, the group velocity of the light inside the medium is

$$v_g = \frac{L}{\tau} = \frac{\Omega^2}{g^2+\Omega^2}c \tag{2.46}$$

with $g^2 = c\kappa/L = cn\gamma$ and the density $n = N/L$. If the density of the medium is sufficiently high, the collective coupling strength g can become much larger than Ω and $v_g \ll c$.

This phenomenon is known as *slow light* and has been demonstrated experimentally by slowing down light to a few metres per second in an optically thick medium [175]. Using a time-dependent coupling laser with $\Omega(t)$, it is also possible to stop the light, store it in the medium and release it on demand [176].

The physical picture behind slow light is that inside the medium, the photons propagate as dark-state polaritons [173] (or in the slow-light regime also called slow-light polaritons). They are quasiparticles having both a photonic as well as a matter component whose relative contribution depends on the ratio Ω/g where $\Omega \gg g$ corresponds to a more photon-like polariton and in the opposite limit $\Omega \ll g$ the matter part is dominant. As long as the spectral width of the incoming probe field is much narrower than the EIT linewidth given by $\Gamma_{\text{EIT}} = \Omega^2/|\delta - i\Gamma/2|$, the dispersion relation of the polaritons is linear with $\omega_q = v_g q$ and they propagate through the medium without losses and without disturbing the pulse shape.

3

Free-Space Quantum Electrodynamics with a Single Rydberg Superatom

This chapter deals with the strong coupling of a single emitter to a propagating light mode. The experimental implementation of the strong coupling is realized by means of a so-called Rydberg superatom and the microscopic description of this system is based on the theory discussed in Chapter 2. One consequence of the strong coupling is the observation of two- and three-body correlations of outgoing photons which is discussed in the second part of this chapter.

In order to present a coherent story, we will also review relevant experimental details which are discussed in more depth in Refs. [177] and [178].

3.1. Introduction

The interaction between a single emitter and individual photons is a fundamental process in nature [179] which underlies many phenomena such as vision and photosynthesis as well as applications including imaging, spectroscopy or optical information processing and communication. In the strong coupling limit, where the coherent interaction between a single photon and an individual emitter exceeds all decoherence and loss rates, a single emitter can serve as an interface between stationary and flying qubits, a central building block for future quantum networks [180, 181]. Such a quantum optical node is able to mediate effective photon-photon interactions enabling deterministic all-optical quantum gates [182–184].

One groundbreaking scheme to achieve strong coupling is the use of electromagnetic cavities, where the photons are trapped within the finite volume of a high-finesse resonator. The physics of these systems is captured by the seminal Jaynes-Cummings model [185], which has been experimentally realized and extensively studied in atomic cavity quantum electrodynamics (QED) [186] and more recently in circuit QED systems combining on-chip microwave resonators with superconducting two-level systems [187, 188]. Achieving a strong interaction between propagating photons and a single emitter opens the possibility to realize novel quantum-optical devices where atoms process photonic qubits on the fly and facilitate the preparation of nonclassical states of light [167]. However, mode matching between the input field and the dipolar emission pattern of the quantum emitter in free space is challenging and has so far limited the achievable coupling strength [189–191]. Waveguide QED systems seek to overcome this limitation by transversely confining the propagating electromagnetic mode coupled to one or more emitters [94, 106, 192–196].

Another approach to achieve strong coupling is to use atomic ensembles and in this chapter we discuss the theoretical and experimental realization of coherent coupling between a propagating few-photon optical field and a single Rydberg superatom in free space. By exploiting the Rydberg blockade effect in an atomic ensemble [52, 67, 197, 198], which allows at most a single excitation shared among all N constituents, ten thousands of individual ultracold atoms are transformed into a single effective two-level quantum system. The collective nature of this excitation enhances the coupling of the light field to the superatom by a factor of $\sqrt{N}$ compared to the single-atom coupling strength and guarantees an enhanced directed emission in the forward direction [16, 52]. The resulting large coupling enables the driving of Rabi oscillations of the single superatom with a few-photon probe pulse and the observation of the effects of the coherent emitter-photon interaction on the photon-photon correlations of the outgoing field for the first time. We show that our system is well described by the theory of a single quantum emitter strongly coupled to a one-dimensional quantized light mode and that the light-matter coupling that is achieved in the experimental setup in free space is competitive to state-of-the-art optical waveguide QED systems [94, 195, 196].

3.2. Setup

The single Rydberg superatom is experimentally implemented by focusing a weak probe field together with a strong counterpropagating control field onto an optically trapped ensemble of ultracold ^{87}Rb atoms (see Fig. 3.1). The few-photon co-

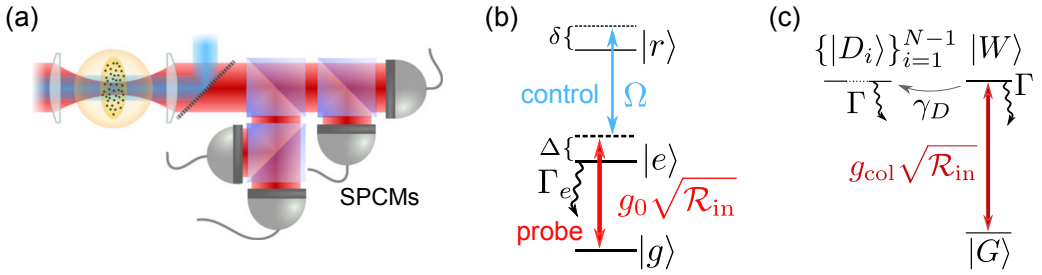

Fig. 3.1.: Sketch of the experimental setup and level scheme. (a) An ensemble of N atoms is laser-cooled and confined within the blockade volume using an optical dipole trap. The light that interacts with the atoms is detected by single-photon counting modules (SPCM). Using beam splitters, the setup is also capable of measuring two- and three-photon correlations. (b) For a single atom, the ground state $|g\rangle$ is coupled to the Rydberg state $|r\rangle$ via a few-photon probe field (red) and a strong control field (blue). Their Rabi frequencies are $g_0\sqrt{\mathcal{R}_{\rm in}}$ and Ω, respectively, where g_0 is the single-atom coupling constant for the probe field and $\mathcal{R}_{\rm in}$ is the photon rate. (c) The Rydberg blockade turns the whole ensemble into an effective two-level system with ground state $|G\rangle$ and collectively excited state $|W\rangle$. In addition to the spontaneous Raman decay Γ, the collective state $|W\rangle$ can dephase into the manifold of dark states, $\{|D_i\rangle\}_{i=1}^{N-1}$. Figure taken and adapted from [178]

herent probe pulse couples the ground state $|g\rangle = \left|S_{1/2},\, F=2,\, m_F=2\right\rangle$ to the intermediate state $|e\rangle = |P_{3/2},\, F=3,\, m_F=3\rangle$ with a Rabi frequency $g_0\sqrt{\mathcal{R}_{\rm in}}$, where g_0 is the single-atom-single-photon coupling constant, determined by the geometry of the setup, and $\mathcal{R}_{\rm in}$ is the photon rate of the incoming probe field. The control field couples the intermediate state $|e\rangle$ and the metastable Rydberg state $|r\rangle = \left|111S_{1/2},\, m_J=1/2\right\rangle$ with Rabi frequency Ω. Using a large intermediate-state detuning Δ which is much larger than the inverse lifetime of the intermediate state $\Gamma_{\rm e}$ and the Rabi freqeuency Ω, the intermediate state can be adiabatically eliminated. Setting the two-photon detuning δ to Raman resonance, the dynamics for each atom simplifies to those of a resonantly coupled two-level system between $|g\rangle$ and $|r\rangle$ with an effective Rabi frequency $g_0\sqrt{\mathcal{R}_{\rm in}}\Omega/2\Delta$. In the effective two-level system, the decay of the Rydberg state is dominated by the spontaneous Raman decay via the intermediate state $|e\rangle$ with rate $\Gamma = \Omega^2/(2\Delta)^2\Gamma_e$.

The strong interaction between the Rydberg atoms results in a blockade volume which only supports a single excitation [52, 67, 197, 198]. Reducing both the transverse probe beam diameter and the longitudinal extent of the atomic cloud to values smaller than the radius of the blockaded volume results in a collective coupling of all N atoms within this volume to the propagating light mode. In the experimental setup described above, a few ten thousand atoms are confined within

this volume. In this case, the N-body ground state $|G\rangle = |g_1, \ldots, g_N\rangle$ couples only to one many-body excited state

$$|W\rangle = \frac{1}{\sqrt{N}} \sum_{j=1}^{N} e^{i\mathbf{k}\mathbf{x}_j} |j\rangle \ , \tag{3.1}$$

where $|j\rangle = |g_1, \ldots, r_j, \ldots, g_N\rangle$ is the state with the jth atom in the Rydberg state and all others in $|g\rangle$, $\mathbf{k}$ is the sum of the wave vectors of the probe and control field, and $\mathbf{r}_j$ denotes the position of the jth atom. Thus, the ensemble of N atoms acts as a single two-level superatom coupled to a probe light with the collective coupling $g_{\text{col}} = \sqrt{N} g_0 \Omega/(2\Delta)$. In addition to the ground state $|G\rangle$ and the singly-excited state $|W\rangle$, there are $N-1$ so-called dark states $\{|D_i\rangle \ , \ i = 1, N-1\}$ which also carry a single excitation but are orthogonal to $|W\rangle$ and do therefore not couple to the light field. It has been shown that the exchange of virtual photons between atoms provides a coupling between $|W\rangle$ and the dark states [2, 20, 199, 200], which can alter the decay rate of the state $|W\rangle$ [201, 202]. This will also be discussed in more detail in Chapters 4 and 5. In addition to that, inhomogeneous dephasing acting on individual atoms can irreversibly drive the ensemble from $|W\rangle$ into the manifold of dark states $\{|D_i\rangle \ , \ i = 1, N-1\}$, which enables the system to function as a single-photon absorber [70, 71].

3.3. Theoretical Description

In this section, we present the theoretical description of the experimental setup based on a microscopic model and show that the interaction of the Rydberg superatom with a propagating light mode results in a collectively enhanced decay into the same mode. This enables treating the light-matter interaction as a one-dimensional problem.

We start with a microscopic setup as realized in the experiment, where a large number of atoms N is harmonically trapped. The density distribution of the ground-state atoms is given by a Gaussian profile with widths σ_z along the direction of the incoming light field and σ_r in the transverse direction with peak density n_0. As discussed above, each individual atom is well described by a two-level atom with ground state $|g\rangle$ and the excited Rydberg state $|r\rangle$ with an optical transition frequency $\omega = 2\pi c/\lambda$ and the wavelength λ.

In the following, we describe the two states of the atoms by the bosonic field operators $\psi_g^\dagger(\mathbf{r})$ for the ground state and $\psi_r^\dagger(\mathbf{r})$ for the Rydberg state, respectively. In terms of these operators, the ground state density is defined as the expectation

value

$$n(\mathbf{r}) = \langle \psi_g^\dagger(\mathbf{r})\psi_g(\mathbf{r})\rangle = n_0 e^{-z^2/2\sigma_z^2} e^{-(x^2+y^2)/2\sigma_r^2}. \tag{3.2}$$

It is important to stress that for a thermal gas above quantum degeneracy the statistics of the operator $\psi_g^\dagger(\mathbf{r})$ are irrelevant, but the correlations exhibit the fundamental property

$$\langle \psi_g^\dagger(\mathbf{r})\psi_g(\mathbf{r})\psi_g^\dagger(\mathbf{r}')\psi_g(\mathbf{r}')\rangle = g^{(2)}(\mathbf{r},\mathbf{r}')n(\mathbf{r})n(\mathbf{r}') + n(\mathbf{r})\delta(\mathbf{r}-\mathbf{r}') \tag{3.3}$$

with the two-body correlation function $g^{(2)}(\mathbf{r},\mathbf{r}')$. In the present system, the atoms are randomly distributed within the trap and no correlations appear on length scales comparable to the wavelength λ, i.e., $g_2 = 1$. Next, we introduce the operators $S^+(\mathbf{r}) = \psi_r^\dagger(\mathbf{r})\psi_g(\mathbf{r})$ creating a Rydberg excitation from the ground state and $S^-(\mathbf{r}) = \psi_g^\dagger(\mathbf{r})\psi_r(\mathbf{r})$ for a transition from the Rydberg state to the ground state. These operators satisfy the commutation relation

$$[S^-(\mathbf{r}), S^+(\mathbf{r}')] = \left(\psi_g^\dagger(\mathbf{r})\psi_g(\mathbf{r}) - \psi_r^\dagger(\mathbf{r})\psi_r(\mathbf{r})\right)\delta(\mathbf{r}-\mathbf{r}'). \tag{3.4}$$

Then, the Hamiltonian describing the coupling between the light and the atomic ensemble within the rotating frame and using the rotating-wave approximation reduces to

$$H = \sum_\mu \int \frac{d^3q}{(2\pi)^3}\hbar\omega_{\mathbf{q}} a_{\mathbf{q}\mu}^\dagger a_{\mathbf{q}\mu} + g\int d^3r \left[S^-(\mathbf{r})\mathcal{E}^\dagger(\mathbf{r}) + \mathcal{E}(\mathbf{r})S^+(\mathbf{r})\right], \tag{3.5}$$

where the first term describes the quantized electromagnetic field with creation and annihilation operators $a_{\mathbf{q}\mu}^\dagger$ and $a_{\mathbf{q}\mu}$, respectively, for a photon with momentum $\mathbf{q}$ and polarization μ. The photons have the dispersion relation $\omega_{\mathbf{q}} = c|\mathbf{q}| - \omega$. The second term describes the light-matter coupling where g is the dipole matrix element for the optical transition. In the following, we assume a polarization $\mathbf{p}$ of the dipole transition along the x-direction. The electric field operator in three dimensions takes the form

$$\mathcal{E}(\mathbf{r}) = \sum_\mu \int \frac{d^3q}{(2\pi)^3}\, c_{\mathbf{q}}^\mu\, a_{\mathbf{q}\mu}\, e^{i\mathbf{q}\mathbf{r}}, \tag{3.6}$$

where $c_{\mathbf{q}}^\mu = i\sqrt{\omega_{\mathbf{q}} 2\pi\hbar}\ \mathbf{p}\cdot\varepsilon_{\mathbf{q}}^\mu$ accounts for the normalization and the influence of the polarization $\varepsilon_{\mathbf{q}}^\mu$. The incoming electric field is characterized by a Gaussian beam propagating along the z-direction with width w_0 and polarization parallel to $\mathbf{p}$. The precise mode function is denoted as $u(\mathbf{r})$ and gives rise to the transverse

mode area $A = \pi w_0^2/2$. This incoming field then couples coherently to the W-state of the superatom

$$|W\rangle = \frac{1}{\sqrt{N}} \int d^3r \, u(\mathbf{r}) \, S^+(\mathbf{r})|G\rangle \tag{3.7}$$

with the ground state $|G\rangle = \sqrt{1/N!} \prod_{i=1}^{N} \psi_g^\dagger(\mathbf{r}_i) \, |0\rangle$ of the many-body system. Here, N denotes the relevant number of particles overlapping with the incoming mode of the photonic state, i.e.,

$$N = \int d^3r |u(\mathbf{r})|^2 \langle G|\psi_g^\dagger(\mathbf{r})\psi_g(\mathbf{r})|G\rangle. \tag{3.8}$$

In general, this quantity varies within each shot of the experiment as the positions of the atoms are randomly distributed. However, its fluctuations are suppressed by $\Delta N/\bar{N} \sim 1/\sqrt{\bar{N}}$ and can be safely ignored for 10^4 particles participating in the superatom. Here, $\bar{N}$ is the mean of the contributing atom number after averaging over many realizations. In the experimentally relevant regime with $\lambda \ll w_0, \sigma_z$ and $w_0 \ll \sigma_r$, one gets

$$\bar{N} = \int d^3r |u(\mathbf{r})|^2 n(\mathbf{r}) = \frac{(2\pi)^{3/2}}{4} \, w_0^2 \sigma_z n_0 = (2\pi)^{1/2} \sigma_z A \, n_0 \, . \tag{3.9}$$

In order to understand the collective enhancement of the decay of the superatom state $|W\rangle$, we determine its decay rate within Fermi's Golden Rule. The averaged decay rate into a photonic mode $\mathbf{q}$ with polarization μ takes the form

$$\begin{aligned} \bar{\Gamma}_{\mathbf{q},\mu} &= \frac{2\pi g^2}{\hbar^2} \delta(\omega - c|\mathbf{q}|) \, |c_{\mathbf{q}}^{\mu}|^2 \int d^3r' \, d^3r e^{i\mathbf{q}(\mathbf{r}-\mathbf{r}')} \left\langle \frac{\psi_g^\dagger(\mathbf{r})\psi_g(\mathbf{r})\psi_g^\dagger(\mathbf{r}')\psi_g(\mathbf{r}')}{N} \right\rangle \\ &\quad \times u^*(\mathbf{r}')u(\mathbf{r}) \\ &= \frac{2\pi g^2}{\hbar^2} \delta(\omega - c|\mathbf{q}|) \, |c_{\mathbf{q}}^{\mu}|^2 \left[1 + \frac{1}{\bar{N}} \left| \int d^3r e^{-i\mathbf{q}\mathbf{r}} u(\mathbf{r}) n(\mathbf{r}) \right|^2 + \mathcal{O}\left(\frac{\Delta N}{\bar{N}} \right) \right] \end{aligned} \tag{3.10}$$

and ω denotes the optical frequency of the transition. The first term in the square brackets gives rise to the standard spontaneous decay rate $\Gamma = 4g^2\omega^3/3\hbar c^3$ for a single atom. We therefore conclude that the superatom exhibits an incoherent decay process into an arbitrary photon mode $\mathbf{q}$ giving rise to the conventional spontaneous decay rate. In turn, the second term characterizes the possibility for collective enhancement of the decay into a specific mode. In the experimental

parameter regime with $w(\sigma_z) < \sigma_r$, however, this collective decay only provides a significant contribution for modes in the forward direction with an opening angle

$$\sin^2\theta \lesssim \frac{\lambda^2}{\pi^2 w_0^2}\,. \tag{3.11}$$

These angles are, however, on the same order as the angular spread of the incoming Gaussian beam. Moreover, the backscattering is suppressed by $\exp(-8\pi^2\sigma_z^2/\lambda^2)$.

Thus, it is possible to restrict the analysis to modes that predominantly propagate into the forward direction with momentum k, still allowing for residual propagation into angles comparable to those in Eq. (3.11). This corresponds to the paraxial approximation of wave propagation and one can calculate the spontaneous emission of the superatom state into the forward propagating Gaussian beam with mode $u(\mathbf{r})$ and polarization $\varepsilon^\mu = \mathbf{p}$ which gives

$$\kappa = \frac{2\pi g^2}{\hbar^2}\int \frac{dk}{2\pi}\delta(\omega - ck)\frac{|c_k^\mu|^2}{A}\left[1 + \frac{1}{\bar{N}}\left|\int d\mathbf{r}|u(\mathbf{r})|^2 n(\mathbf{r})\right|^2\right] = \frac{2\pi(\bar{N}+1)g^2}{A}\frac{\omega}{\hbar c}\,. \tag{3.12}$$

Here, $A = \pi w_0^2/2$ denotes the transverse mode volume of the Gaussian beam and in the following discussion we can well approximate $\bar{N}+1 \approx \bar{N}$. For a transverse width of the atomic density distribution $\sigma_r \lesssim w_0$, scattering into higher Gaussian modes is possible and the determination of the decay rates into these modes can straightforwardly be derived within Fermi's Golden Rule (see Appendix 3.A). These terms describe the fact that a narrow atomic medium in free space acts as a lens for the incoming photons.

We conclude from this analysis that the superatom state $|W\rangle$ collectively couples to a one-dimensional channel of forward propagating modes. The latter are described by the Gaussian beam of the incoming probe field, and the collective coupling strength takes the form

$$g_{\mathrm{col}} = 2\sqrt{\kappa} = \sqrt{\frac{8\pi\bar{N}g^2\omega}{A\hbar c}} = \sqrt{\frac{3\bar{N}\,\Gamma\,\lambda^2}{2\pi A}}\,. \tag{3.13}$$

This coupling strength and the associated emission rate κ account for two effects: The first is the enhancement by a factor $\bar{N}$ due to the collective behavior of the superatom. The second is the scattering probability $\sim \lambda^2/A$ well known from the scattering of a focussed beam off a single atom. Here, the scattering cross section of a single atom is proportional to the square of its resonance wavelength and the incoming beam realizes an effective mode area A.

For the narrow bandwidth pulses used in the experiment, the variation in momentum of the electric field is small and one can safely ignore any changes in the transverse wave function of the Gaussian beam. Furthermore, the incoherent spontaneous emission into the transverse channels as well as backscattering is well accounted for by the single atom decay rate Γ.

3.4. Master Equation

As shown in the previous section, the Rydberg superatom predominantly emits back into the probe field mode and we can describe the dynamics of the system in terms of the Hamiltonian of a single two-level system coupled to a quantized light field in one dimension[1]

$$H = \int \frac{dk}{2\pi} \hbar c k \, a_k^\dagger a_k + \frac{\hbar g_{\mathrm{col}}}{2} \left(E^\dagger(0)\sigma_{\mathrm{GW}} + E(0)\sigma_{\mathrm{GW}}^\dagger \right) , \tag{3.14}$$

where a_k and $a_k^\dagger$ are photon annihilation and creation operators, $E(x) = \frac{\sqrt{c}}{2\pi} \int e^{ikx} a_k \, dk$ is the electric field operator measured in $\sqrt{\mathrm{photons/time}}$ and $\sigma_{\alpha\beta} = |\alpha\rangle\langle\beta|$. Since the probe photons irreversibly leave after a single pass through the system, we can solve and trace out the time-dependence of the photonic part (see Appendix 3.B). For a coherent input state, we obtain a master equation for the atomic density matrix [166, 167]

$$\partial_t \rho(t) = -\frac{i}{\hbar} \left[H_0(t), \rho(t) \right] + \kappa \, \mathcal{D} \left[\sigma_{\mathrm{GW}} \right] \rho(t), \tag{3.15}$$

where the Hamiltonian

$$H_0(t) = \hbar \sqrt{\kappa} \left(\alpha^*(t)\sigma_{\mathrm{GW}} + \alpha(t)\sigma_{\mathrm{GW}}^\dagger \right) , \tag{3.16}$$

accounts for the driving by the coherent probe beam with field amplitude $\alpha(t)$ and collective coupling strength $\sqrt{\kappa}$. The coherent field amplitude $\alpha(t)$ is related to the time-dependent mean photon rate by $|\alpha(t)|^2 = \mathcal{R}_{\mathrm{in}}(t)$. The dissipative terms are described by the Lindblad dissipator $\mathcal{D}[\sigma]\rho = \sigma\rho\sigma^\dagger - (\sigma^\dagger\sigma\rho + \rho\sigma^\dagger\sigma)/2$ and the emission rate $\kappa = g_{\mathrm{col}}^2/4$ of the two-level system into the strongly coupled mode.

[1] Note that to connect the two-level model derived from the microscopic model in Section 3.3 with the experiment, one must consider the adiabatic elimination of the intermediate state. In this case, the effective coupling strength is $g_{\mathrm{col}}^{\mathrm{eff}} = g_{\mathrm{col}}\Omega/2\Delta$. For simplicity, further theoretical analysis will only make use of $g_{\mathrm{col}} = 2\sqrt{\kappa}$ and use κ as a free parameter which later will be fit to the experimental results.

In addition to this intrinsic decay channel which is derived from the Hamiltonian in Eq. (3.14), we phenomenologically add the spontaneous Rydberg atom decay rate Γ of the excited state and the dephasing rate γ_{D} of the superatom state $|W\rangle$ into the manifold of dark states $|D\rangle$. The resulting master equation then reads

$$\begin{aligned}\partial_t \rho(t) = &-\frac{i}{\hbar}\left[H_0(t), \rho(t)\right] + (\kappa+\Gamma)\mathcal{D}\left[\sigma_{\mathrm{GW}}\right]\rho(t) \\ &+ \gamma_{\mathrm{D}}\mathcal{D}\left[\sigma_{\mathrm{DW}}\right]\rho(t) + \Gamma\mathcal{D}\left[\sigma_{\mathrm{GD}}\right]\rho(t)\,. \end{aligned} \tag{3.17}$$

The Rydberg population is given by $\rho_{\mathrm{WW}} + \rho_{\mathrm{DD}}$, while the outgoing electric field is

$$E(t) = \alpha(t) - i\sqrt{\kappa}\sigma_{\mathrm{GW}}(t)\,. \tag{3.18}$$

As a consequence, the equal-time expectation values for the electric field operator reduce to the determination of equal-time correlations of the operator $\sigma^{\dagger}_{\mathrm{GW}}(t)$ which are obtained from the numerical solution of Eq. (3.17). In particular, the expectation value of the photon flux at retarded time $s = t - x/c$ is given by

$$\begin{aligned}\langle E^{\dagger}(s)E(s)\rangle = &|\alpha(s)|^2 + \kappa\langle\sigma^{\dagger}_{\mathrm{GW}}(s)\sigma_{\mathrm{GW}}(s)\rangle \\ &- i\sqrt{\kappa}\left[\alpha^*(s)\langle\sigma_{\mathrm{GW}}(s)\rangle - \alpha(s)\langle\sigma^{\dagger}_{\mathrm{GW}}(s)\rangle\right]\,. \end{aligned} \tag{3.19}$$

The first term on the right-hand side of this expression is the noninteracting component of the intensity, the second part corresponds to the signal coming from the collective emission of the state $|W\rangle$ into the propagating mode, and the last term accounts for the interferences between the propagating light mode and the dynamics of the superatom.

The intensity calculated using Eqs. (3.19) and (3.17) can now be fitted to the experimental data which is shown in Fig. 3.2 as solid lines and results in the parameters $\kappa = 0.428\,\mu\mathrm{s}^{-1}$, $\Gamma = 0.069\,\mu\mathrm{s}^{-1}$, and $\gamma_{\mathrm{D}} = 1.397\,\mu\mathrm{s}^{-1}$. The agreement between theory and experiment is very good over the whole range of input photon rates based on a single set of parameters. This clearly shows that the single-emitter model is capable of reproducing the observed damped Rabi oscillations which can be understood on a microscopic level.

For a single atom in free space, the coupling to a photon quantified by κ is naturally bounded by the spontaneous decay rate Γ of the bare atom in the case of perfect mode matching [203]. For a superatom both the coupling $g_{\mathrm{col}} \sim \sqrt{\kappa}$ and the decay κ into a specific mode are increased solely through the collective enhancement of the atom-light interaction and the collective spontaneous emission without any confinement of the propagating light. Consequently, the superatom

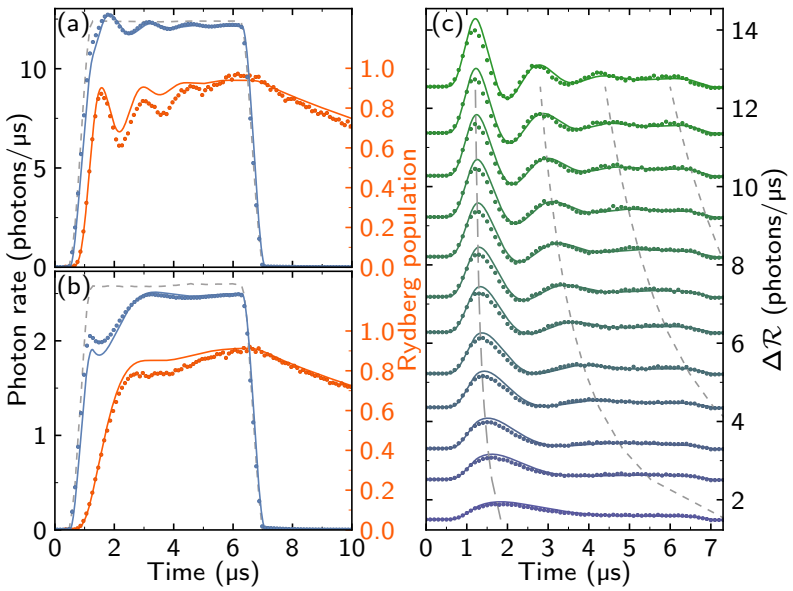

Fig. 3.2.: Time evolution of the photon signal and the Rydberg population. (a,b) Time traces of the outgoing photon rate (blue points) and Rydberg population (orange points) for input pulses (dashed gray line) with peak photon rates $\mathcal{R}_{\mathrm{in}} = 12.4\,\mu\mathrm{s}^{-1}$ (a) and $\mathcal{R}_{\mathrm{in}} = 2.6\,\mu\mathrm{s}^{-1}$ (b), corresponding to a mean number $\bar{N}_{\mathrm{ph}}$ of 71.6 and 15.1 photons in the pulse. The Rabi oscillation of the single superatom is visible both in the Rydberg state population and the modulation of the outgoing probe light. (c) Difference signal $\Delta\mathcal{R}(t)$ between the incoming and the outgoing probe light for different input photon rates $\mathcal{R}_{\mathrm{in}}$. Each time trace is vertically shifted by the corresponding $\mathcal{R}_{\mathrm{in}}$. Dashed lines indicate the expected positions of the Rabi oscillation peaks based on the fitted parameters, showing the scaling of the Rabi period with $1/\sqrt{\bar{N}_{\mathrm{ph}}}$. Solid lines in all panels are fits to the data with the theoretical model described in the text using only a single set of fit parameters for all time traces. Error bars in all panels are SEM and are smaller than the data points. Figure taken and adapted from [177].

spontaneously emits into the forward direction of the strongly coupled mode with probability[2] $\beta = \kappa/(\kappa + \Gamma) = 0.86$, while loss of photons due to scattering out of the propagating mode with rate Γ is minimal as shown in Section 3.3. The main source of decoherence in the experimental setup is the superatom dephasing γ_{D}, which is expected to be dominated by the thermal motion of the atoms and could be reduced by further cooling the atoms. However, a coherent virtual exchange of photons can also provide an additional coherent dynamics of the superatom [2, 20, 199, 200], which will be discussed in more detail in Chapter 4. Given the excellent agreement between the experimental data and the theoretical model, we conclude that in the present experimental regime, the potential influence of this coherent term is well accounted for by the phenomenological dephasing rate γ_{D}.

3.5. Dynamical Phase Diagram

After having derived the master equation (3.17) and the input-output relation (3.18) that describe the dynamics of the system, we discuss the implications for the physics.

3.5.1. Analytical Solution of the Master Equation

In order to get more insight into the physics of the free-space setup, we analytically solve Eq. (3.17) for a constant driving field $\alpha(t) = \alpha$ in the absence of spontaneous decay Γ and internal dephasing γ_{D}. Note that for simplicity we take α to be real. For a two-level system, the density matrix can be written as

$$\rho = \begin{pmatrix} \rho_{\mathrm{GG}} & \rho_{\mathrm{GW}} \\ \rho_{\mathrm{WG}} & \rho_{\mathrm{WW}} \end{pmatrix} \tag{3.20}$$

and the resulting equations of motion for its components ρ_{ij} read

$$\partial_t \rho_{\mathrm{GG}} = i\sqrt{\kappa}\alpha(\rho_{\mathrm{WG}} - \rho_{\mathrm{GW}}) + \kappa\rho_{\mathrm{WW}}\,, \tag{3.21}$$

$$\partial_t \rho_{\mathrm{GW}} = i\sqrt{\kappa}\alpha(\rho_{\mathrm{WW}} - \rho_{\mathrm{GG}}) - \frac{\kappa}{2}\rho_{\mathrm{GW}}\,, \tag{3.22}$$

$$\partial_t \rho_{\mathrm{WG}} = -i\sqrt{\kappa}\alpha(\rho_{\mathrm{WW}} - \rho_{\mathrm{GG}}) - \frac{\kappa}{2}\rho_{\mathrm{WG}}\,, \tag{3.23}$$

$$\partial_t \rho_{\mathrm{WW}} = -i\sqrt{\kappa}\alpha(\rho_{\mathrm{WG}} - \rho_{\mathrm{GW}}) - \kappa\rho_{\mathrm{WW}}\,. \tag{3.24}$$

[2] Note that the definition here does not include the nonradiative contribution coming from the dephasing γ_{D}. Including this contribution leads to $\beta' = \kappa/(\kappa + \Gamma + \gamma_{\mathrm{D}}) = 0.26$.

One can reduce the set of four equations to two by first introducing

$$\rho_x = \rho_{\mathrm{GW}} + \rho_{\mathrm{WG}}\,, \tag{3.25}$$
$$\rho_y = i(\rho_{\mathrm{GW}} - \rho_{\mathrm{WG}}) \tag{3.26}$$

and replacing $\rho_{\mathrm{GG}} = 1 - \rho_{WW}$ since the trace of ρ is preserved. Then, Eqs. (3.21)-(3.24) reduce to

$$\partial_t \rho_x = -\kappa \rho_x\,, \tag{3.27}$$
$$\partial_t \rho_y = -\frac{\kappa}{2}\rho_y - 4\sqrt{\kappa}\alpha\rho_{\mathrm{WW}} + 2\sqrt{\kappa}\alpha\,, \tag{3.28}$$
$$\partial_t \rho_{\mathrm{WW}} = -\sqrt{\kappa}\alpha\rho_y - \kappa\rho_{\mathrm{WW}}\,. \tag{3.29}$$

The first equation is independent of the other two and can be solved directly. Since we assume that there are no initial coherences between the light field and the atom, we get

$$\rho_x(t) = \rho_x(0)e^{-\kappa t/2} = 0. \tag{3.30}$$

The remaining two equations can be cast into the form

$$\partial_t \begin{pmatrix} \rho_y \\ \rho_{\mathrm{WW}} \end{pmatrix} = \begin{pmatrix} -\kappa/2 & -4\sqrt{\kappa}\alpha \\ -\sqrt{\kappa}\alpha & -\kappa \end{pmatrix} \begin{pmatrix} \rho_y \\ \rho_{\mathrm{WW}} \end{pmatrix} + \begin{pmatrix} 2\sqrt{\kappa}\alpha \\ 0 \end{pmatrix}\,. \tag{3.31}$$

The homogeneous part of this differential equation is solved by diagonalizing the coupling matrix which has eigenvalues

$$\mu_\pm = -\frac{3}{4}\kappa \pm i\sqrt{4\alpha^2\kappa - \left(\frac{\kappa}{4}\right)^2} = -\frac{3}{4}\kappa \pm i\Omega_{\mathrm{eff}}\,, \tag{3.32}$$

where Ω_{eff} is an effective Rabi frequency.

The probability to be in the collective state $|W\rangle$ is given by

$$\rho_{\mathrm{WW}}(t) = \frac{4\kappa\alpha^2}{\kappa^2 + 8\kappa\alpha^2}\left[1 - \left(\cos(\Omega_{\mathrm{eff}}t) + \frac{3\kappa}{4\Omega_{\mathrm{eff}}}\sin(\Omega_{\mathrm{eff}}t)\right)e^{-3\kappa t/4}\right]\,. \tag{3.33}$$

3.5.2. Different Coupling Regimes

As can already be seen from Eqs. (3.32) and (3.33), the system behaves qualitatively different depending on the parameters α and κ. To illustrate this point, we show in Fig. 3.3 the visibility of Rabi oscillations, defined as

$$\mathrm{max}_{0\le t\le\tau}[\rho_{\mathrm{WW}}(t)] - \rho^{\mathrm{ss}}_{\mathrm{WW}}\,, \tag{3.34}$$

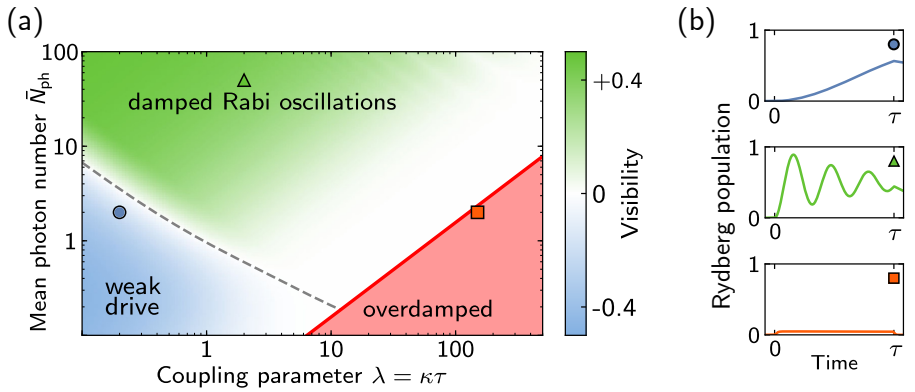

Fig. 3.3.: Dynamical phase diagram of a driven atom in free space. (a) Visibility of Rabi oscillations, defined as $\max_{0\leq t\leq\tau}[\rho_{\mathrm{WW}}(t)]-\rho^{\mathrm{ss}}_{\mathrm{WW}}$ of an ideal ($\Gamma = \gamma_{\mathrm{D}} = 0$) atom driven by a propagating field. For large coupling strengths ($\lambda \gg 1$), the system becomes overdamped and a minimal number of photons is required to observe Rabi oscillations and increases with coupling strength. For $\lambda \ll 1$, a large number of photons is required to drive the system with a π pulse, defining a crossover (dashed line) between the weak driving regime and the regime where intrinsically damped Rabi oscillations can be observed. The experiment operates at $\lambda = 2.2$ such that Rabi oscillations are visible even for low photon numbers. (b) Examples of the time evolution of the Rydberg population ($\rho_{\mathrm{WW}} + \rho_{\mathrm{DD}}$) for the points indicated in (a). Figure taken and adapted from [177].

for a constant pulse of length τ as a function of the dimensionless coupling parameter $\lambda = \kappa\tau$ and the mean number of photons in the pulse $\bar{N}_{\mathrm{ph}} = \alpha^2\tau$. In Eq. (3.34) $\rho^{\mathrm{ss}}_{\mathrm{WW}}$ denotes the steady state value of the bright state population for an infinitely long pulse. It is important to note that in contrast to cavity QED, in free-space and waveguide QED an increase in the coupling g_{col} necessarily increases the decay rate κ resulting in an intrinsic damping in these systems preventing prefect transfer of a photonic qubit to a matter qubit within a finite time [203–205].

For $\lambda \gg 1$, the atom decays very quickly and photons exhibit correlations on a time scale $1/\kappa$. This results in an *overdamped* regime, where the system settles to a nonzero probability to find the superatom in its excited state without undergoing Rabi oscillations. This can also be inferred from Eq. (3.32) noting that for $\alpha^2 < \kappa/64$ the effective Rabi frequency becomes imaginary and we are in the overdamped regime of a damped harmonic oscillator. This condition can be recast in the form $\bar{N}_{\mathrm{ph}} < \lambda/64$ which gives a critical photon number $\bar{N}^c_{\mathrm{ph}} = \lambda/64$ for the transition into the overdamped regime.

In the opposite limit, $\lambda \ll 1$, the interaction between photons and the atoms is very weak and there are no correlations. Thus, a minimum number of photons

is required to drive a π pulse which defines a crossover (dashed line in Fig. 3.3) between the regime of Rabi oscillations and the *weak driving* regime where the excitation probability remains below its steady-state value during the pulse duration τ. The crossover line can be determined by the condition

$$\Omega_{\text{eff}}\tau = \pi \tag{3.35}$$

in analogy to the π pulse in an ideal two-level system. In the limit $\lambda \ll 1$, the critical photon number for the crossover is

$$\bar{N}_{\text{ph}}^{c,\text{weak}} = \frac{\pi^2}{4\lambda}\,. \tag{3.36}$$

In between those regions, there is a regime where *intrinsically damped Rabi oscillations* occur.

Including the Dark State Subspace

Due to inhomogeneous dephasing, the $|W\rangle$ state eventually decays into the dark state manifold. This decay is modelled by introducing a dummy state $|D\rangle$ which represents the dark state manifold and is populated from the $|W\rangle$ state with a rate γ_{D}. If we neglect the Raman decay, that is $\Gamma = 0$, the dark state dephasing can be included as an additional decay channel in the calculation above. The effective Rabi frequency then takes the form

$$\tilde{\Omega}_{\text{eff}} = \sqrt{4\alpha^2\kappa - \left(\frac{\kappa+\gamma_{\text{D}}}{4}\right)^2}\,. \tag{3.37}$$

The inclusion of the dark state manifold by $|D\rangle$ influences the dynamical phase diagram in Fig. 3.3 in the following way: The critical photon number for the overdamped regime does not decrease linearly with λ but rather exhibits a minimum since now

$$\bar{N}_{\text{ph}}^{c} = \frac{(\lambda+\bar{\gamma}_{\text{D}})^2}{64\lambda} \tag{3.38}$$

with $\bar{\gamma}_{\text{D}} = \gamma_{\text{D}}\tau$. For $\lambda \to 0$ this increases as

$$\bar{N}_{\text{ph}}^{c} \approx \frac{\bar{\gamma}_{\text{D}}^2}{64\lambda} + \frac{\bar{\gamma}_{\text{D}}}{32}\,. \tag{3.39}$$

In the limit $\lambda \gg 1$, the critical photon number again increases linearly with λ but is shifted by a constant towards larger $\bar{N}_{\text{ph}}$ and reads

$$\bar{N}_{\text{ph}}^{c} \approx \frac{\lambda}{64} + \frac{\bar{\gamma}_{\text{D}}}{32}\,. \tag{3.40}$$

The critical photon number for the crossover from the weak driving regime to the regime of damped Rabi oscillations also exhibits a shift towards larger photon numbers and, for $\lambda \ll 1$, reads

$$\bar{N}_{\mathrm{ph}}^{\mathrm{c,weak}} \approx \frac{\pi^2 + \bar{\gamma}_{\mathrm{D}}^2}{64\lambda} + \frac{\bar{\gamma}_{\mathrm{D}}}{32} \,. \tag{3.41}$$

Due to the modified scaling of the critical line of the overdamped regime, the weak drive regime occupies less space in the phase diagram and eventually vanishes for large dephasing rates.

3.6. Two- and Three Photon Correlation Functions

A central concept for quantifying the effective photon-photon interaction mediated by the Rydberg superatom is to study the intensity correlations imprinted by the interaction onto the initially uncorrelated photons in terms of n-body correlation functions

$$g^{(n)}(s_1, \ldots, s_n) = \frac{\langle E^\dagger(s_1) \cdots E^\dagger(s_n) E(s_n) \cdots E(s_1) \rangle}{\prod_{i=1}^{n} \langle E^\dagger(s_i) E(s_i) \rangle} \,. \tag{3.42}$$

Here, the operators $E^\dagger(s)$ and $E(s)$ describe the creation and annihilation, respectively, of a photon at time s and are in our system given by Eq. (3.18). The evaluation of n-body correlation functions, in contrast to the intensity expectation value, requires the determination of correlations of the operator $\sigma_{\mathrm{GW}}^\dagger(t)$ at different times. Within the theoretical model described above any multi-time correlation function for a coherent input pulse is conveniently calculated using the quantum regression theorem [172, 206] while alternative approaches using Keldysh formalism have also been developed [207].

It is a remarkable property of a single atom coupled to a single photonic mode that these expectation values can be determined by the quantum regression theorem without involving any additional approximations. While in general the quantum regression theorem relies on the Born approximation quenching the correlations between the bath and the system, here, the emitted photons never interact with the superatom again which is exactly the requirement of the quantum regression theorem [166]. For more details on the derivation of the quantum regression theorem see Appendix 3.C.

3.6.1. Two-Photon Correlations

Figure 3.4 compares the results for the two-photon correlation function obtained from the numerical solution of Eq. (3.18) in combination with the quantum regres-

sion theorem (panels 3.4(c) and 3.4(d)) with the correlation functions measured in the experiment (panels 3.4(a) and 3.4(b)) for two different incoming photon rates $\mathcal{R}_{\text{in}} = 12.4\,\mu\text{s}^{-1}$ ((a), (c)) and $\mathcal{R}_{\text{in}} = 2.5\,\mu\text{s}^{-1}$ ((b),(d)). The parameters used for the theoretical calculations are based on the fits of the measured intensity given by $\kappa = 0.428\,\mu\text{s}^{-1}$, $\Gamma = 0.069\,\mu\text{s}^{-1}$, and $\gamma_D = 1.397\,\mu\text{s}^{-1}$.

The theory results are in excellent agreement with the experimental data, including correlations beyond the duration of the pulse. These originate from collective spontaneous emission of single photons after the input pulse has left the sample which can only occur if the superatom is in state $|W\rangle$ at the end of the driving pulse. The observed correlations indicate that photons separated by up to $5\,\mu\text{s}$ become entangled [208] because of the effective photon-photon interaction mediated by the single superatom. This can be understood considering two incoming photons: The first photon passing the atom results in a superposition of the photon either being absorbed and the superatom excited or the photon having passed the superatom without exciting it [20]. The second photon following has now restricted options depending on whether the first photon has been absorbed or not and the superatom state is already occupied, that is the second photon can only be absorbed if the first one was not. This results in a spatial entanglement between the two photons mediated by their subsequent interaction with a single two-level system.

3.6.2. Three-Photon Correlations

A natural extension to studying two-photon correlations is to study the interaction between three photons using three-photon correlations $g^{(3)}$ [209–211]. To visualize these correlations, it is convenient to transform to Jacobi coordinates

$$R = \frac{s_1 + s_2 + s_3}{\sqrt{3}}\,, \tag{3.43}$$

$$\eta = \frac{s_1 - s_2}{\sqrt{2}}\,, \tag{3.44}$$

$$\zeta = \sqrt{\frac{2}{3}}\left(\frac{s_1 + s_2}{2} - s_3\right)\,, \tag{3.45}$$

where R is to be interpreted as center-of-mass coordinate, while η and ζ play the role of relative coordinates between two photons and a pair of two photons and a third one, respectively.

Since the experiment naturally uses pulses of finite length, the correlation function is not stationary and thus depends on the center-of-mass value R as well as on the relative coordinates η and ζ. In Fig. 3.5 we show the third-order correlation

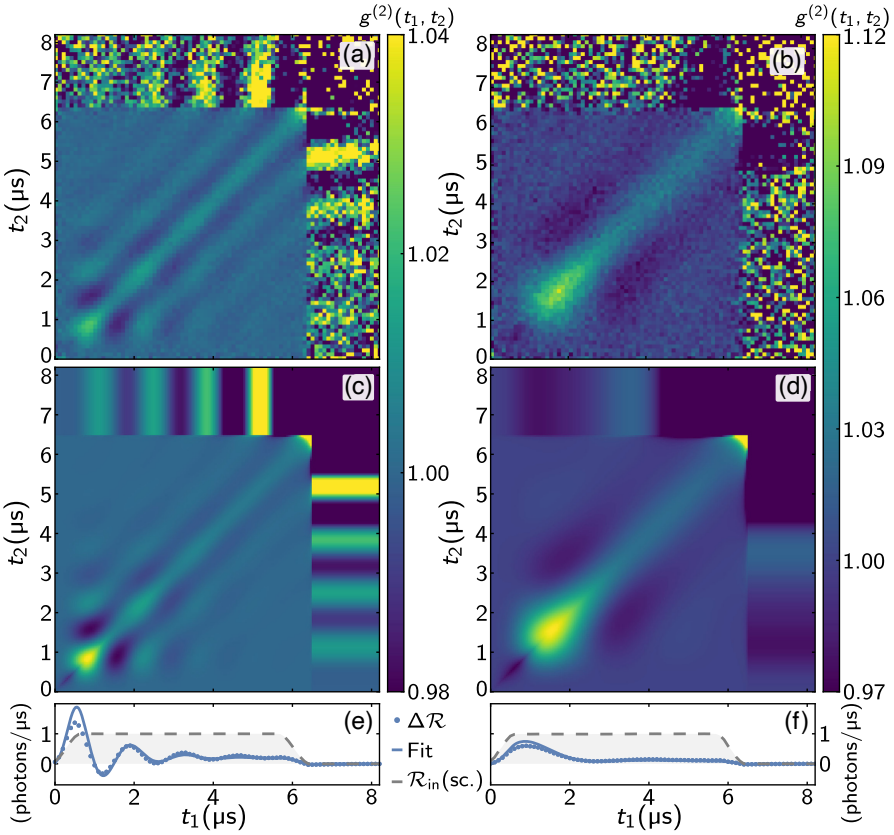

Fig. 3.4.: Two-photon correlation functions of the outgoing probe field. (a,b) Measured two-photon correlations $g^{(2)}(t_1, t_2)$ for probe pulses with $\mathcal{R}_{\text{in}} = 12.4\,\mu\text{s}^{-1}$ and $\mathcal{R}_{\text{in}} = 2.5\,\mu\text{s}^{-1}$. (c,d) Corresponding calculated two-photon correlation function using the values κ, Γ, and γ_D obtained by fitting the time traces in Fig. 3.2. (e,f,) Measured (dotted line) and simulated (solid line) $\Delta\mathcal{R}_{\text{in}}$ together with scaled input pulses (dashed gray) for reference. Figure taken and adapted from [177].

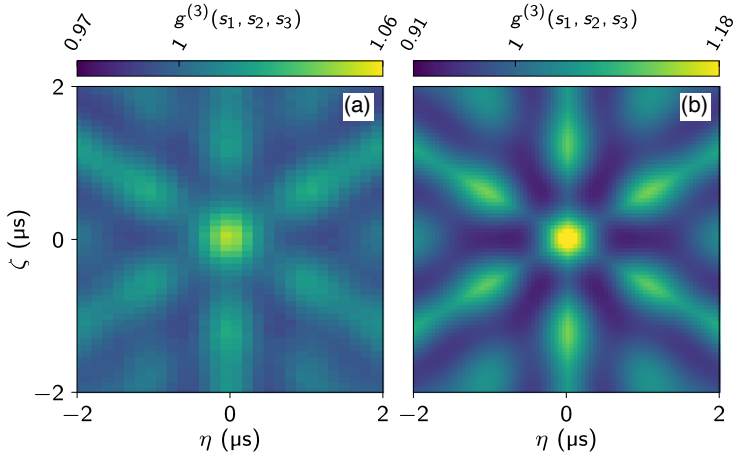

Fig. 3.5.: Cut through the (a) experimentally measured and (b) calculated third-order correlation function $g^{(3)}(s_1, s_2, s_3)$ along the relative Jacobi coordinates η and ζ. Both cuts are averaged over the center-of-mass coordinate range $R_{\text{range}} = \sqrt{3} \times (2.5 \ldots 3.5)\,\mu\text{s}^{-1}$. The photon rate of the probe field is $\mathcal{R}_{\text{in}} = 6.7\,\mu\text{s}^{-1}$ and the parameters for the theoretical calculations are $\kappa = 0.55\,\mu\text{s}^{-1}$, $\Gamma = 0.14\,\mu\text{s}^{-1}$, $\gamma_D = 1.49\,\mu\text{s}^{-1}$. Note the different scalings of the colorbars and that the contrast of the experimentally observed correlations is reduced due to finite detection efficiency (for more details, see [178].) Figure taken and adapted from [178].

function $g^{(3)}(\eta, \zeta)$ for an input rate $\mathcal{R}_{\text{in}} = 6.7\,\mu\text{s}^{-1}$. It is averaged over the time range $R_{\text{range}} = \sqrt{3} \times (2.5 \ldots 3.5)\,\mu\text{s}$ for the experimental data (panel (a)) and the theoretical calculations based on the single-emitter model in Eq. (3.17) (panel (b)). The average over R is necessary for the experiment to extract a significant signal from the few-photon data for a realistic number of repetitions of the experiment. The theoretical third-order correlations are calculated based on the parameters extracted from fits to the intensity ($\kappa = 0.55\,\mu\text{s}^{-1}$, $\Gamma = 0.14\,\mu\text{s}^{-1}$, $\gamma_D = 1.49\,\mu\text{s}^{-1}$)[3] and very well reproduce the bunching and antibunching features.

Since any two-body correlation will also induce a signal in the three-body correlation function, a natural approach is to subtract these contributions via the cumulant expansion to identify genuine three-body correlations. This approach leads to the connected three-body correlation function

$$g_c^{(3)}(s_1, s_2, s_3) = 2 + g^{(3)}(s_1, s_2, s_3) - \sum_{i<j} g^{(2)}(s_i, s_j)\,. \tag{3.46}$$

[3] The fits to the intensity were obtained based on a different data set compared to the two-photon correlations.

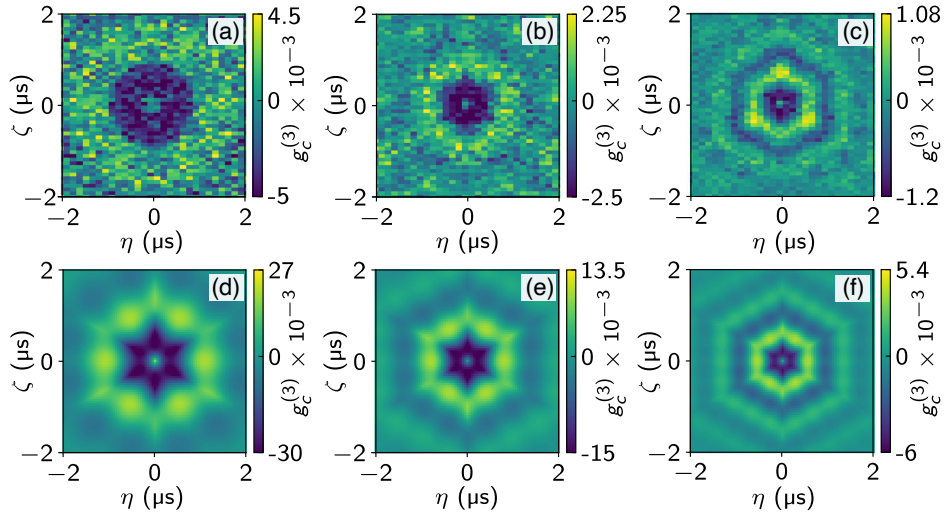

Fig. 3.6.: Connected part of the three-photon correlation function $g_c^{(3)}$ in the relative Jacobi coordinates η and ζ. Panels (a)-(c) show the experimental results and panels (d)-(f) the corresponding theoretical calculations. The photon rates are (from left to right) $\mathcal{R}_{\text{in}} = 3.4\,\mu\text{s}^{-1}$, $\mathcal{R}_{\text{in}} = 6.7\,\mu\text{s}^{-1}$, and $\mathcal{R}_{\text{in}} = 15.2\,\mu\text{s}^{-1}$. The parameters for the theoretical calculations are the same as in Fig. 3.5. Figure taken and adapted from [178].

Note that $g_c^{(3)}$ vanishes if one photon is separated from the other two. In additon, the connected three-body correlation function for any classical Gaussian state of photons is zero. Figure 3.6 shows cuts $g_c^{(3)}(\eta, \zeta)$ through the calculated connected three-photon correlation function for three different photon input rates $\mathcal{R}_{\text{in}} = 3.4\,\mu\text{s}^{-1}$, $\mathcal{R}_{\text{in}} = 6.7\,\mu\text{s}^{-1}$, and $\mathcal{R}_{\text{in}} = 15.2\,\mu\text{s}^{-1}$ averaged over R_{range}. The theoretical calculations based on the single-emitter model, shown in Figs. 3.6(d)-(f), well reproduce the observed structure in the measured data shown in Figs. 3.6(a)-(c). Even for low photon numbers, the connected part of $g^{(3)}$ shows a clear signal of three-photon correlations with three-photon bunching at small distances, accompanied by an antibunching at intermediate separations, following another ring of bunching. This sequence of bunching and antibunching features increases with increasing photon number. Note that $g^{(3)}$ for a translationally invariant system has a sixfold symmetry in Jacobi coordinates which is reduced to a threefold symmetry in our case due to the finite length of the incoming probe pulse.

Microscopic Theory of Three-Body Correlations

The very good agreement between the experimental data and the theoretical calculations suggests that the single-emitter model very well captures the physics of

the interaction of the superatom with the propagating light field and the effective photon-photon interaction mediated by the superatom. Nevertheless, it is not straightforward to understand the microscopic origin of the three-body correlations within this model. It turns out that the idealized model given by the Hamiltonian in Eq. (3.14), where both the dephasing and the spontaneous Raman decay are neglected, allows for an analytical solution in terms of the Bethe ansatz [212, 213]. In the following, we will briefly outline the most important results coming from that idealized model in order to give a more conclusive picture, whereas more details, in particular on the analytical calculations, can be found in [213].

Studying the eigenstates of Eq. (3.14), it turns out that the exact eigenstates for three photons can be characterized as a three-photon bound state, a combination of a two-photon bound state with an additional scattering photon, and finally pure scattering states. The three-photon bound state in particular provides a nontrivial contribution to the connected part of the correlation function. For three photons in an incoming state of the form $\psi_{\mathrm{in}}^{(3)} = \psi(s_1)\psi(s_2)\psi(s_3)$ with a single photon mode ψ with width τ and $\kappa\tau \gg 1$, the outgoing wave function in the center of the pulse reduces to (for $s_1 \geq s_2 \geq s_3$)

$$\psi_{\mathrm{out}}^{(3)} = 1 + 12e^{-\kappa(s_1-s_3)/2} - 4\left(e^{-\kappa(s_1-s_2)/2} + e^{-\kappa(s_2-s_3)/2}\right) . \tag{3.47}$$

The contribution of the three-body bound state to the three-photon correlation function can be inferred from the decomposition $\psi_{\mathrm{out}}^{(3)} = 4e^{-\kappa(s_1-s_3)} + \psi_{\mathrm{sc}}$, where the first term describes the three-photon bound state and ψ_{sc} accounts for the contributions of the scattering states and the two-photon bound state. Since $\psi_{\mathrm{sc}} = 1$ for $s_1 = s_2 = s_3$, the three-body bound state provides the dominant contribution to the three-photon bunching in the center of the pulse but contributions of the remaining states are still significant. Thus, based on this microscopic understanding of the three-photon correlations, the three-photon bunching signal cannot purely attributed to a three-photon bound state in contrast to recent observations on Rydberg polaritons [211].

3.7. Conclusion and Outlook

Concluding, the experimental measurements demonstrate the realization of strong light-matter coupling in free space through collective enhancement of the coupling strength without any confining structures for the propagating light mode. The tunable dephasing of the superatom into dark states creates additional functionality beyond the conventional two-level system [70, 71]. The strong coupling furthermore enables the observation of two- and three-body correlations imprinted by

the Rydberg superatom on initially uncorrelated photons.

These findings are very well captured by an effective three-level model of a single atom which includes the collectively enhanced coupling to the collective bright state as well as a phenomenological dephasing to uncoupled dark states. The effective model is based on a microscopic analysis of the full three-dimensional geometry and shows that for the experimental parameters a simpler effective one-dimensional model can be employed. Since the enhanced coupling implies an enhanced emission rate, the observed Rabi oscillations are intrinsically damped and there is very good agreement between a numerical solution of the master equation and the measurements.

The realization of strong coupling and the observation of three-body correlations imprinted by a single two-level system shed light on the fundamental processes of absorption and emission at the quantum level and highlight the potential for experimentally realizing strongly correlated photonic many-body systems in quantum nonlinear optical systems [184]. The directionality of the superatom emission can in addition be used to implement a cascaded quantum system for dissipative entanglement generation [101, 105] and to build quantum optical networks [180, 181].

Appendix

3.A. Scattering into Higher Modes

In this section, we provide some details for the derivation of Eq. (3.12) and give estimates for the scattering into higher-order Gaussian modes and the corresponding decay rates.

Based on the analysis of decay rates into photonic modes with momentum $\mathbf{q}$ using Fermi's Golden Rule in Eq. (3.10), we identified modes with positive momentum k and small angles $\theta \ll \lambda/\pi w_0$ as the dominant contributions to the scattering. Consequently, it is possible to restrict the further analysis only to those modes, which corresponds to the paraxial approximation for wave propagation.

For simplicity, we only consider scalar fields $u(\mathbf{r})$ which obey the Helmholtz equation[4]

$$\left[\nabla^2 + k^2\right] u(\mathbf{r}) = 0\,, \tag{3.48}$$

where $k = 2\pi/\lambda$ is the wave number. In order to perform the paraxial approximation, we make the ansatz $u(\mathbf{r}) = \tilde{u}(\mathbf{r})e^{ikz}$, where $\tilde{u}(\mathbf{r})$ is a slowly varying function in the coordinates x, y, and z and the fast oscillation along the direction of propagation z is given by e^{ikz}. Assuming that $|\partial_z^2\tilde{u}| \ll |k\partial_z\tilde{u}|\,, |\partial_x^2\tilde{u}|,\ |\partial_y^2\tilde{u}|$, we arrive at the paraxial wave equation

$$(\partial_x^2 + \partial_y^2 + 2ik)\tilde{u}(\mathbf{r}) = 0\,. \tag{3.49}$$

The solutions to this differential equation are given by the Fresnel diffraction integral or (in closed form) by Gaussian beams or paraxial modes $\tilde{u}_n(\mathbf{r})$ with $n \geq 0$ [214]. The lowest mode with $n = 0$ corresponds to the incoming Gaussian beam considered in our theoretical analysis. Examples of Gaussian modes are

[4] Note that this is only an approximation as Gauss' law $\nabla \cdot \mathbf{E} = 0$ can also introduce field components in other directions.

the Laguerre-Gauss modes in cylindrical coordinates which are parametrized by a beam waist w_0 and a focal point z_0 which we take to be zero for simplicity. We will not give the full expression for the Laguerre-Gauss modes here, but they can be found in [214]. Gaussian modes obey the orthogonality condition

$$\int d^2\rho\, \tilde{u}_n^*(\boldsymbol{\rho}, z)\tilde{u}_m(\boldsymbol{\rho}, z) = A\delta_{nm}\,, \tag{3.50}$$

where $A = \pi w_0^2/2$ is the effective mode area of the beam.

Only considering the paraxial modes, we can rewrite the electric field operator as

$$\mathcal{E}(\mathbf{r}) = \sum_n \int \frac{dk}{2\pi} i\sqrt{\omega_k 2\pi\hbar}\, \frac{\tilde{u}_n(\mathbf{r})e^{ikz}}{\sqrt{A}} a_{nk}\,. \tag{3.51}$$

As a consequence, we can also split the total decay rate of the ensemble into

$$\Gamma_{\mathrm{tot}} = \sum_n \Gamma_n + \Gamma'\,, \tag{3.52}$$

where Γ_n denotes the decay rate into the paraxial mode $\tilde{u}_n$ and Γ' accounts for the decay into all remaining modes of the solid angle 4π which are not captured by the paraxial modes. The decay rates into the paraxial modes can be calculated using Fermi's Golden Rule as

$$\begin{aligned}\Gamma_n &= \frac{2\pi g^2}{\hbar}\int \frac{dk}{2\pi}\delta(\hbar\omega - \hbar ck)\frac{2\pi\hbar\omega_k}{A}\frac{1}{\bar{N}}\left|\int d^3r\, n(\mathbf{r})\tilde{u}_n^*(\mathbf{r})u(\mathbf{r})\right|^2 \\ &= \frac{2\pi g^2\omega}{\hbar A c}\left|\frac{1}{\sqrt{\bar{N}}}\int d^3r\, n(\mathbf{r})\tilde{u}_n^*(\mathbf{r})u(\mathbf{r})\right|^2\,,\end{aligned} \tag{3.53}$$

where $u(\mathbf{r}) = u_0(\mathbf{r})$ is the Gaussian mode of the incoming beam. The prefactor in Eq. (3.53) corresponds to $\kappa/\bar{N}$, while the integral gives the probability of scattering into higher Gaussian modes. If the density is smooth over the region where the mode functions are nonvanishing, these transitions are strongly suppressed and the scattering into those modes as well as the remaining solid angle is then well accounted for by a phenomenological incoherent decay rate Γ. If, however, the beam size is larger than the atomic density distribution, transitions into higher modes are possible and lensing effects can occur. The reduction to an effective one-dimensional model then breaks down.

3.B. Derivation of the Master Equation

We start with the Hamiltonian Eq. (3.14), which describes the coherent coupling of the superatom to the optical mode of the incoming laser field. The derivation of the master equation closely follows the methods described in standard textbooks [172], and recent publications on atom-light coupling in one-dimensional waveguides [166, 167] (see also Chapter 2). The first step is to derive the Heisenberg equation of motion for the photonic field operators

$$\partial_t a_k(t) = -\frac{i}{\hbar}\left[a_k, H\right] = -ick a_k(t) - i\sqrt{\kappa c}\,\sigma_{\mathrm{GW}}(t) \tag{3.54}$$

with $\sigma_{\mathrm{GW}} = |G\rangle\langle W|$ and the coupling strength $\sqrt{\kappa} = g_{\mathrm{col}}/2$. This equation can be formally integrated which leads to a connection between the outgoing electric field and the operator σ_{GW}, which describes the coherences in the superatom,

$$a_k(t) = e^{-ick(t-t_0)}a_k(t_0) - i\sqrt{\kappa c}e^{-ick(t-t_0)}\int_{t_0}^{t} ds\, e^{ick(s-t_0)}\sigma_{\mathrm{GW}}(s)\,. \tag{3.55}$$

Here, t_0 denotes the initial time with the condition that the incoming photon field has not yet reached the superatom. Without loss of generality we set $t_0 = 0$. Then, the electric field operator reduces to

$$\begin{aligned} E(x,t) &= \bar{E}(ct-x) - i\sqrt{\kappa}c\int_0^t ds \int \frac{dk}{2\pi}\, e^{-ick(t-s)+ikx}\sigma_{\mathrm{GW}}(s) \\ &= \bar{E}(ct-x) - i\sqrt{\kappa}\sigma_{\mathrm{GW}}(t-x/c)\theta(x)\theta(ct-x)\,, \end{aligned} \tag{3.56}$$

where $\bar{E}$ denotes the noninteracting electric field operator and $\theta(x)$ is the Heaviside function with the definition that $\theta(0) = 1/2$. For an incoming coherent state, the noninteracting electric field $\bar{E}(ct)$ can be replaced by the amplitude of the coherent field $\alpha(t) \equiv \langle \bar{E}(ct)\rangle$, which characterizes the incoming photon rate by $|\alpha(t)|^2 = \mathcal{R}_{\mathrm{in}}$. Alternatively, it would be possible to apply the well-established Mollow transformation [170] leading to the same final result for the master equation.

For an arbitary operator A acting on the superatom alone, its Heisenberg equation of motion reduces to

$$\begin{aligned} \partial_t A(t) = &-i\sqrt{\kappa}\left[A(t), \sigma_{\mathrm{GW}}^\dagger(t)\right]\alpha(t) - \frac{\kappa}{2}\left[A(t), \sigma_{\mathrm{GW}}^\dagger(t)\right]\sigma_{\mathrm{GW}}(t) \\ &- i\sqrt{\kappa}\,\alpha^*(t)\left[A(t), \sigma_{\mathrm{GW}}(t)\right] + \frac{\kappa}{2}\sigma_{\mathrm{GW}}^\dagger(t)\left[A(t), \sigma_{\mathrm{GW}}(t)\right]\,. \end{aligned} \tag{3.57}$$

The right-hand side can be split into a coherent part given by

$$-i\sqrt{\kappa}\left[A(t),\sigma_{\mathrm{GW}}^{\dagger}(t)\right]\alpha(t)-i\sqrt{\kappa}\alpha^{*}(t)\left[A(t),\sigma_{\mathrm{GW}}(t)\right]=-\frac{i}{\hbar}\left[A(t),H_{0}(t)\right] \tag{3.58}$$

with the Hamiltonian $H_0(t)$ in Eq. (3.16) while the remaining terms describe the spontaneous emission into the photonic mode.

Using the relation $\partial_t\langle A\rangle = \mathrm{tr}\left(A\partial_t\rho(t)\right)$ with the reduced density matrix for the atomic system alone $\rho(t)$, the dissipative part reduces to the well-established Lindblad form

$$\kappa\,\mathcal{D}[\sigma_{\mathrm{GW}}]\rho(t)=\kappa\left(\sigma_{\mathrm{GW}}\rho(t)\sigma_{\mathrm{GW}}^{\dagger}(t)-\frac{1}{2}\{\sigma_{\mathrm{GW}}^{\dagger}\sigma_{\mathrm{GW}}(t),\rho(t)\}\right). \tag{3.59}$$

This term describes the enhanced spontaneous emission into the forward direction due to the collective character of the superatom. In addition, the superatom can also decay into transverse photonic modes, which is still determined by the standard single atom spontaneous emission rate Γ. Finally, we can add the dephasing into the dark states $\{|D_i\rangle\}_{i=1}^{N-1}$ as well as the decay by spontaneous emission of these dark states. The analysis is independent of the specific dark state the system dephases into and therefore we can account for the dephasing by losses into a single dark state $|D\rangle$ with a phenomenological dephasing rate γ_{D}. The microscopic mechanisms for the dephasing are Doppler shifts of the atoms, as well as inhomogeneous shifts of the Rydberg state level, and residual interactions between the individual atoms by resonant exchange interactions [2, 20, 167, 174, 199].

3.C. Quantum Regression Theorem

In this appendix, we briefly review the quantum regression theorem which was first introduced by Lax [206] and show how it can be used to calculate multi-time correlation functions which appear in the calculation of second- and third-order correlation functions as mentioned in Section 3.6. We will closely follow [172] where we refer to for more details.

Single-time expectation values for a system operator A evaluated at some time t are given by

$$\langle A(t)\rangle=\mathrm{tr}_{\mathrm{S}}(A\rho(t))\,, \tag{3.60}$$

where $\rho(t)$ is the reduced density matrix of the system alone. The time evolution of ρ is given by the master equation

$$\partial_t\rho(t)=\mathcal{L}(t)\rho(t) \tag{3.61}$$

with some Lindblad (super-)operator $\mathcal{L}$ that may depend on time. Formally, the solution of Eq. (3.61) is given by

$$\rho(t) = \mathcal{T} \exp\left(\int_{t_0}^{t} dt' \, \mathcal{L}(t')\right) \rho(t_0) \equiv \mathcal{V}(t, t_0)\rho(t_0) \tag{3.62}$$

for some initial $\rho(t_0)$. In this expression, $\mathcal{T}$ denotes the time-ordering operator and $\mathcal{V}(t, t_0)$ is the time evolution operator of the density matrix and satisfies the equation of motion

$$\partial_t \mathcal{V}(t, t_0) = \mathcal{L}(t)\mathcal{V}(t, t_0) \tag{3.63}$$

with the initial condition $\mathcal{V}(t_0, t_0) = 1$. It follows from Eq. (3.63) that $\mathcal{V}(t, t_0)$ fulfills the semigroup property

$$\mathcal{V}(t, t')\mathcal{V}(t', t_0) = \mathcal{V}(t, t_0) \, . \tag{3.64}$$

Multi-time correlation functions of two system operators A and B evaluated at times $t + \tau$ and t with $\tau > 0$ are given by

$$\langle A(t + \tau)B(t)\rangle = \mathrm{tr}(A(t + \tau)B(t)R(t_0)) \tag{3.65}$$

with $\mathrm{tr}()$ being the trace over the full system, that is system and bath, and $R(t_0)$ being the density matrix of the full system at some time t_0. This expression can be rewritten in the Schrödinger picture as

$$\begin{aligned}
\langle A(t + \tau)B(t)\rangle &= \mathrm{tr}\left(U^\dagger(t + \tau, t_0)AU(t + \tau, t_0)U^\dagger(t, t_0)BU(t, t_0)R(t_0)\right) \\
&= \mathrm{tr}\left(AU(t + \tau, t)BR(t)U^\dagger(t + \tau, t)\right) \\
&= \mathrm{tr}_\mathrm{S}\left(A \, \mathrm{tr}_\mathrm{B}\left(U(t + \tau, t)R(t)U^\dagger(t + \tau, t)\right)\right) \, .
\end{aligned} \tag{3.66}$$

where $R(t) = U(t, t_0)R(t_0)U^\dagger(t, t_0)$ and $U(t, t_0)$ is the time evolution operator for the dynamics of the full system. The final result is very appealing since we are now dealing with the expectation value of the operator A for a state with some generalized density operator $BR(t)$ that is time evolved up to some time $t + \tau$. Note that BR is not a real density operator since, for example, the trace may not be equal to one in general. Nevertheless, the operator

$$X(\tau, t) = U(t + \tau)BR(t)U^\dagger(t + \tau, t) \, , \tag{3.67}$$

as a function of τ obeys the same equation of motion as the density matrix R

$$i\hbar\partial_t X(\tau, t) = [H, X(\tau, t)] \, , \tag{3.68}$$

where H is the Hamiltonian of the full system.

Using both the Markov approximation as well as the Born approximation[5], that is $R(t) = \rho(t) \otimes \rho_{\mathrm{B}}$ with ρ_{B} being the density matrix of the bath, one can show that $X_{\mathrm{S}}(\tau, t) = \mathrm{tr}_{\mathrm{B}}\left(X(\tau, t)\right) = B\rho(t)$ follows the same dynamics as $\rho(t)$, that is

$$X_{\mathrm{S}}(\tau, t) = \mathcal{V}(t+\tau)X(t, t)\,. \tag{3.69}$$

The multi-time correlation function can then be calculated as

$$\langle A(t+\tau)B(t)\rangle = \mathrm{tr}_{\mathrm{S}}\left(A\mathcal{V}(t+\tau, t)\left[B\rho(t)\right]\right)\,. \tag{3.70}$$

Note that $\mathcal{V}(t+\tau, t)$ is a super-operator that acts on the space of operators and therefore the order of the operators matters and $\mathcal{V}$ directly acts on $B\rho$.

In the same manner it is possible to derive multi-time correlation functions for more than two operators and more than two times. For our purposes, we are interested in correlators with four operators at two times and six operators at three times. For these cases, the general formulae read (for $t_0 \leq t_1 \leq t_2$)

$$\langle A(t_0)B(t_1)C(t_1)D(t_0)\rangle = \mathrm{tr}_{\mathrm{S}}\left(BC\mathcal{V}(t_1, t)[D\rho(t_0)A]\right)\,, \tag{3.71}$$

$$\langle A(t_0)B(t_1)C(t_2)D(t_2)E(t_1)F(t_0)\rangle = \mathrm{tr}_{\mathrm{S}}(CD\mathcal{V}(t_2, t_1)[E\mathcal{V}(t_1, t_0)[F\rho(t_0)A]B])\,. \tag{3.72}$$

[5]Not performing the Born approximation leads to corrections in the master equation that depend on the difference $R - \rho(t) \otimes \rho_{\mathrm{B}}$ [215].

4

Emergent Universal Dynamics for an Atomic Cloud Coupled to a One-Dimensional Optical Waveguide

In this chapter, we study the influence of the virtual exchange of photons on the properties of a single collective excitation, focusing on a setup described by an ensemble of atoms coupled to a one-dimensional wave guide. In Chapter 2 we have seen that the time evolution of the collectively excited state is governed by two competing terms: first, the spontaneous and strongly directed emission into the wave guide, and second an intrinsic coherent exchange interaction. We find that the coherent part gives rise to a universal dynamics of the collective excitation for increasing particle numbers and exhibits several revivals until it eventually saturates at a universal value. While this phenomenon provides an intrinsic limit on the dephasing in a superatom, we also present a setup where this universal dynamics can be explored. This chapter is based on Ref. [216].

4.1. Introduction

The collective interaction between an ensemble of emitters and photons is at the heart of many fascinating phenomena in quantum optics [3, 5]. For a single coherent excitation of such an ensemble, the direction as well as the rate of spontaneous emission are strongly modified and can either be enhanced or suppressed, which

has been experimentally observed recently [39, 67]. For these effects to be observable, it is crucial that the coherence between the atoms within the ensemble is maintained. While the influence of thermal motion of the atoms has been investigated [217], an ensemble of atoms with a single excitation also exhibits an interaction induced by virtual exchange of photons [2], which might provide an intrinsic dephasing inherent to any ensemble of emitters. In this chapter, we study within a microscopic analysis whether there is a fundamental limit on this intrinsic dephasing.

Signatures of the coherent interaction by virtual exchange of photons in an ensemble of atoms with several excitations have been discussed in terms of a collective Lamb shift [2, 218], and have been observed in various physical systems ranging from an ensemble of nuclei [6] over solid-state systems [12, 13] to ions [11] and atoms [8, 9]. On the theoretical side, recent research has focused on the understanding of transmission of photons and the appearance of correlations in one-dimensional wave guides [15, 90, 105, 166–168], as well as the appearance of superradiance and a collective Lamb shift in the single-excitation manifold [16, 18, 20, 21, 25, 219]. In order to guarantee a single excitation in an ensemble of scatterers, the notion of superatom has emerged as a powerful concept, where a strong interaction between the excited states suppresses multiple excitations in the ensemble and is conveniently realized with Rydberg atoms [51, 52, 68, 118, 123, 145, 177, 220].

4.2. Setup and Hamiltonian

In our setup, each atom is well described by a two-level system with the ground state $|g\rangle$ and an excited state $|e\rangle$, see Fig. 4.1. The optical transition frequency between the two states is given by $\omega_0 = 2\pi c/\lambda$ with the wavelength λ and the corresponding wave vector $k = 2\pi/\lambda$. In the following, we describe the two states of an atom at position x by the bosonic field operators $\psi_g(x)$ and $\psi_e(x)$ for the ground and excited state, respectively. Then, the initial state with all N atoms in the ground state takes the form $|G\rangle = \sqrt{1/N!}\prod_{i=1}^{N}\psi_g^\dagger(x_i)\,|0\rangle$. The atomic positions x_i are randomly distributed with a distribution function giving rise to the averaged atomic ground state density $n(x) = \big\langle\langle G|\psi_g^\dagger(x)\psi_g(x)|G\rangle\big\rangle_{\text{dis}}$; here, $\langle\cdots\rangle_{\text{dis}}$ denotes the ensemble average over many experimental realizations. Furthermore, we introduce the operators $S^+(x) = \psi_e^\dagger(x)\psi_g(x)$ creating an excitation from the ground state to the excited state and $S^-(x) = \psi_g^\dagger(x)\psi_e(x)$ for a transition from the excited state to the ground state. These operators satisfy the commutation relation

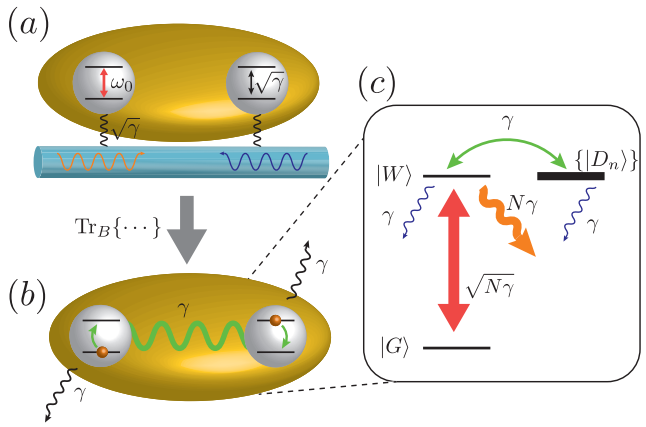

Fig. 4.1.: (a) Two-level atoms coupled to a one-dimensional wave guide with left- and right-moving modes. (b) After integrating out the photonic degrees of freedom, the system exhibits spontaneous emission and an infinite-ranged exchange interaction between the atoms. (c) In the presence of a blockade mechanism, the superatom state $|W\rangle$ is collectively coupled to the ground state with coupling strength $\sqrt{N\gamma}$ giving rise to an enhanced spontaneous emission $N\gamma$ into the forward direction, while the coherent exchange interaction leads to a coupling between this bright state and the manifold of dark states.

$$[S^+(x), S^-(y)] = \delta(x-y)\,[\hat{n}_g(x) - \hat{n}_e(x)] \tag{4.1}$$

with $\hat{n}_\nu(x) = \psi_\nu^\dagger(x)\psi_\nu(x)$ for $\nu \in \{g, e\}$. Then, the microscopic Hamiltonian describing the coupling of the atoms to a one-dimensional waveguide within the rotating-wave approximation takes the form

$$\begin{aligned} H = &\int \frac{dq}{2\pi}\hbar\omega_q a_q^\dagger a_q + \hbar\omega_0 \int dx\, \psi_e^\dagger(x)\psi_e(x) \\ &- \hbar\sqrt{\gamma}\int dx\, \left[\mathcal{E}^\dagger(x)S^-(x) + S^+(x)\mathcal{E}(x)\right] , \end{aligned} \tag{4.2}$$

where $\sqrt{\gamma}$ characterizes the effective mode coupling giving rise to the rate γ for spontaneous emission of a left- or right-moving photon into the waveguide [15, 90, 105, 166–168]. Furthermore, the electric field operator within the waveguide reduces to

$$\mathcal{E}^\dagger(x) = -i\sqrt{c}\int \frac{dq}{2\pi}\, a_q^\dagger e^{-iqx} . \tag{4.3}$$

The bosonic operators $a_q^\dagger$ account for the creation of a waveguide photon with momentum q, while $\omega_q = c|q|$ denotes the dispersion relation for the relevant photon modes.

Starting from the microscopic Hamiltonian (4.2) and integrating out the electric field, the effective dynamics for the atoms alone is governed by a master equation [2, 167] and takes the form

$$\partial_t \rho = -\frac{i}{\hbar}[H_s, \rho] + \mathcal{D}_{\mathrm{F}}[\rho] + \mathcal{D}_{\mathrm{B}}[\rho]\,. \tag{4.4}$$

The first term describes a coherent interaction between the atoms by the exchange of virtual photons,

$$H_s = \hbar\gamma \int dx\, dy\, \sin(k|x-y|)\, S^+(x) S^-(y)\,. \tag{4.5}$$

The term $\mathcal{D}_{\mathrm{F}}$ ($\mathcal{D}_{\mathrm{B}}$) describes the spontaneous emission of a photon in the forward (backward) propagating mode, respectively.

In the following, the main analysis focuses on the superatom state

$$|W\rangle = \frac{1}{\sqrt{N}} \int dx\, e^{ikx} S^+(x)\, |G\rangle \tag{4.6}$$

which couples to the incoming light field with the collectively enhanced coupling strength $\sqrt{N}\gamma$. In addition, there are $N-1$ "dark" states

$$|D_n\rangle = \int dx\, D_n(x) S^+(x)\, |G\rangle \tag{4.7}$$

with the wave functions $D_n(x)$ defined by the orthogonality conditions $\langle W|D_n\rangle = 0$ and $\langle D_m|D_n\rangle = \delta_{nm}$.

4.3. Coherent Dynamics

First, we study the *coherent dynamics* of the state $|W\rangle$ under the Hamiltonian H_s alone. This Hamilton gives rise to a coupling between $|W\rangle$ and the dark states $|D_n\rangle$. Therefore, the quantity of interest is the probability $P(t)$ to stay in the superatom state $|W\rangle$ under the coherent time evolution after averaging over many experimental realizations, i.e., $P(t) = \left\langle |\langle W| e^{-\frac{i}{\hbar}H_s t} |W\rangle|^2 \right\rangle_{\mathrm{dis}}$. This probability can be evaluated numerically using exact diagonalization and averaging over different disorder realizations and is shown in Fig. 4.2. Remarkably, the dynamics features robust revivals on the characteristic time scale $\tau = \pi/N\gamma$, which only damp out on the slower time scale $\tau_{\mathrm{dp}} = \sqrt{N}\tau$. Therefore, for increasing particle number the amount of observable coherent oscillations increases. Finally, $P(t)$

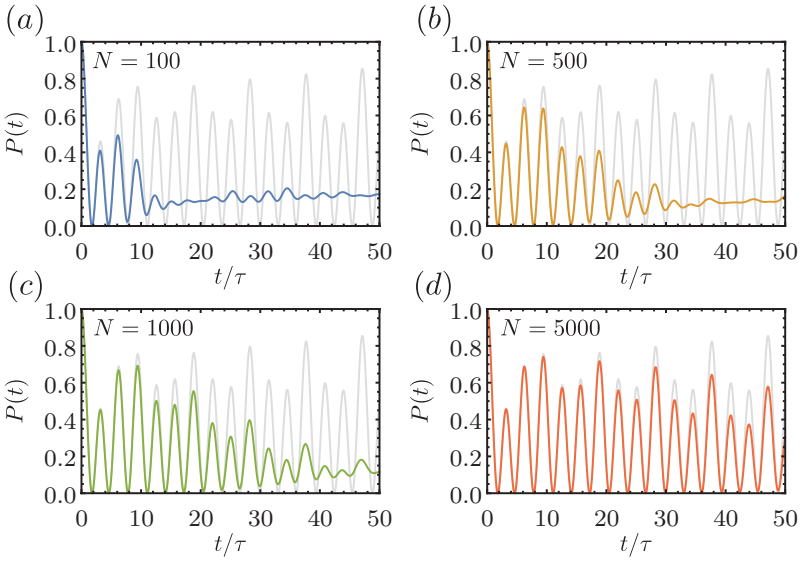

Fig. 4.2.: Time evolution of the state $|W\rangle$ under the Hamiltonian H_s for (a) $N = 100$, (b) $N = 500$, (c) $N = 1000$ and (d) $N = 5000$ particles after averaging over 10^5 realizations with a Gaussian distribution and $k\sigma = 100$. The gray curve indicates the universal dynamics given by Eq. (4.11).

saturates at a finite value $\sim 1/6$ for long times $t \gg \tau_{\text{dp}}$. Note that in Fig. 4.2 we chose a Gaussian density distribution $n(x) = N \exp(-x^2/\sigma^2)/\sqrt{\pi\sigma^2}$. However, the above observations are independent of the atomic density profile as long as the atomic cloud is smooth on distances comparable to the optical wavelength λ.

In the following, we provide an analytical analysis of this universal dynamics for the superatom state $|W\rangle$. It turns out to be convenient to split the Hamiltonian $H_s = H_{\text{F}} + H_{\text{B}}$ into two parts, where H_{F} (H_{B}) describes the virtual exchange of forward (backward) propagating photons, respectively. The part describing the interaction between the atoms due to forward propagating photons is given by

$$H_{\text{F}} = \frac{\hbar\gamma}{2i} \int dx\, dy\, \text{sign}(x-y)\, e^{ik(x-y)} S^+(x) S^-(y)\,, \tag{4.8}$$

and the backward-propagating part reads

$$H_{\text{B}} = -\frac{\hbar\gamma}{2i} \int dx\, dy\, \text{sign}(x-y)\, e^{-ik(x-y)} S^+(x) S^-(y)\,. \tag{4.9}$$

These Hamiltonians are exactly solvable individually (see Appendix 4.A) and the spectrum takes the form $E_\alpha = \frac{\hbar\gamma}{2} \cot\left(\frac{\alpha\pi}{2N}\right)$ with α an odd integer and $-N \leq \alpha <$

N. Furthermore, the eigenstates are

$$|\alpha, \mathrm{F}\rangle = \frac{1}{\sqrt{N}} \int dx\, e^{ikx} S^+(x) \exp\left(-i\frac{\pi\alpha}{N} F(x)\right) |G\rangle \tag{4.10}$$

with the operator $F(x) = \int_{-\infty}^{x} dz\, \hat{n}_g(z)$ counting the number of ground state atoms on the left of position x; similar for $|\alpha, \mathrm{B}\rangle$.

For a large atom number $N \gg 1$, only states with $|\alpha| \ll N$ have significant overlap with the superatom state with $|W\rangle = \sum_\alpha 2i/(\pi\alpha)\, |\alpha, \mathrm{F}\rangle$ and the energies reduce to $E_\alpha = N\hbar\gamma/\pi\alpha$. As a result, the probability to remain in the bright state given only the forward-propagating part of the Hamiltonian is given by $[\chi(t/\tau)]^2$ with $\tau = \pi/N\gamma$ and

$$\chi(s) = \frac{8}{\pi^2} \sum_{n=0}^{\infty} \frac{1}{(1+2n)^2} \cos\left(\frac{s}{1+2n}\right) . \tag{4.11}$$

It is this universal function which $P(t)$ approaches for increasing number of atoms, see Fig. 4.2. In order to understand this observation, there are two important points to notice: First, only those states $|\alpha, \mathrm{F}\rangle$ with small values of $|\alpha|$ have a significant overlap with $|W\rangle$. In addition, these states dominate the fast dynamical behavior with the characteristic energy scale $E_1 = \hbar\gamma N/\pi$. It is therefore sufficient to restrict the analysis to low values of $|\alpha|$. Second, the states $|\alpha, \mathrm{F}\rangle$ with low values of $|\alpha|$ become exact eigenstates of the full Hamiltonian H_s with energy E_α in the limit of a large particle number $N \to \infty$ and a smooth atomic density distribution with $\sigma \gg \lambda$. Then, the universal dynamics $P(t) = [\chi(t/\tau)]^2$ is the asymptotic dynamical behavior for large particle numbers. Note that the precise condition of low values of α reduces to $|\alpha| < \sigma/\lambda$ as will be shown below.

4.3.1. Emergent Universal Dynamics

Here, we prove the statement that the states $|\alpha, \mathrm{F/B}\rangle$ with low values of α become exact eigenstates in the limit $N \to \infty$ and $\lambda/\sigma \to 0$. More details on the calculations can be found in Appendix 4.C. First, we analyze the wave function overlap between eigenstates of H_F and the eigenstates of H_B, i.e., $h_{\alpha\beta} = \langle\beta, \mathrm{B}|H_\mathrm{B}|\alpha, \mathrm{F}\rangle/E_1 = \langle\beta, \mathrm{B}|\alpha, \mathrm{F}\rangle/\beta$, and the matrix element $\delta_\alpha = \langle\alpha, \mathrm{F}|H_\mathrm{B}|\alpha, \mathrm{F}\rangle/E_1$. These dimensionless parameters take the form

$$h_{\alpha\beta} = \frac{1}{\beta} \int \frac{dx}{N} e^{2ikx} \langle G|\, \hat{n}_g(x) e^{-i\frac{\pi(\alpha+\beta)}{N}F(x)} |G\rangle \ , \tag{4.12}$$

$$\delta_\alpha = \int \frac{dx\, dy}{2iN^2} \operatorname{sign}(x-y)\, e^{2ik(x-y)} \langle G|\, \hat{n}_g(x)\hat{n}_g(y) e^{-i\frac{\pi\alpha}{N}(F(x)-F(y))} |G\rangle \, . \tag{4.13}$$

In the limit $N \to \infty$, we can replace the atomic density operator by its averaged expectation value $n(x)$ as the fluctuations in the density vanish with $1/\sqrt{N}$. Then, the overlaps in $h_{\alpha\beta}$ reduce to the Fourier transform of a smoothly varying function. Therefore, the overlap between states with low numbers of α, β, i.e., $2|k| \gg \pi|\alpha+\beta|/\sigma$, vanishes for $\lambda/\sigma \to 0$; here, σ denotes the characteristic size of the atomic cloud in general. For example, it vanishes exponentially for a Gaussian density distribution, while for a stepwise atomic distribution it vanishes as $(\lambda/\sigma)^2$. On the other hand, overlaps with $|\beta| \gtrsim \sigma/\lambda$ are suppressed by the factor $1/\beta$ in Eq. (4.12). Similarly, the expression for δ_α reduces to $\delta_\alpha = c_0\frac{\lambda}{\sigma} + c_1\alpha\frac{\lambda^2}{\sigma^2} + \mathcal{O}((\lambda/\sigma)^3)$ with dimensionless parameters c_0 and c_1 of order one, which only depend on the atomic density distribution $n(x)$. The first term is an irrelevant shift in energy, while the second correction again vanishes as $(\lambda/\sigma)^2$. In conclusion, we have demonstrated that the eigenstates $|\alpha, \mathrm{F}\rangle$ with energy E_α become exact eigenstates of the full Hamiltonian H_s for $|\alpha| < \sigma/\lambda$ in the limit $N \to \infty$ and $\lambda/\sigma \to 0$.

Next, we analyze the leading correction due to a finite number of particles N in the regime $\lambda \ll \sigma$. The main influence are deviations from the mean density distribution $n(x)$ due to the random distribution of the particles within each experimental realization which leads to fluctuations of $h_{\alpha\beta}$ and δ_α. We illustrate this behavior for the overlap $w_\alpha = \langle\alpha, \mathrm{B}|\alpha, \mathrm{F}\rangle$. The important quantity is the variance of these fluctuations, i.e., $\Delta w_\alpha = \sqrt{\langle|w_\alpha|^2\rangle_{\mathrm{dis}} - \langle|w_\alpha|\rangle_{\mathrm{dis}}^2}$. Using the general relation

$$\langle\hat{n}_g(x)\hat{n}_g(y)\rangle_{\mathrm{dis}} = \frac{N-1}{N}n(x)n(y) + n(x)\delta(x-y) \tag{4.14}$$

valid for a thermal gas on distances studied in the present setup, the full distribution function for $|w_\alpha|^2$ can be derived (see Appendix 4.C). In the limit $k\sigma \gg \pi|\alpha|$ it follows an exponential distribution with mean $1/N$ such that the leading contribution to the fluctuations takes the form $\Delta w_\alpha = 1/\sqrt{N}$.

The last step to understand the behavior of $P(t)$ is to derive the leading correction to the energies E_α using perturbation theory in the small parameter w_α,

$$\frac{E_\alpha^\pm}{E_\alpha} = 1 \pm |w_\alpha| \quad \text{with} \quad |\alpha, \pm\rangle = \frac{1}{\sqrt{2}}\left(|\alpha, \mathrm{F}\rangle \pm e^{i\phi_\alpha}|\alpha, \mathrm{B}\rangle\right)$$

and $w_\alpha = |w_\alpha|e^{i\phi_\alpha}$. Therefore, the relevant energies of the Hamiltonian H_s fluctuate within each experimental realization with a variance $\Delta E_\alpha = E_\alpha/\sqrt{N}$ giving rise to a characteristic dephasing rate $\tau_{\mathrm{dp}} = \pi/\sqrt{N}\gamma$. This observation allows us to derive the leading dynamical behavior $P(t)$ for the superatom states $|W\rangle$ by performing the average over many different experimental realizations using the knowledge on the distribution function of $|w_\alpha|^2$ (for more details see Ap-

pendix 4.D),

$$P(t) = \left\{ \frac{8}{\pi^2} \sum_{n\geq 0} \frac{2}{(2n+1)^2} \cos\left(\frac{t/\tau}{2n+1}\right) \left[1 - 2f\left(\frac{t}{2\tau_{\rm dp}(2n+1)}\right)\right] \right\}^2 - \frac{16}{\pi^4} \sum_{n\geq 0} \left\{ \frac{2}{(2n+1)^4} \left(\left[1 - 2f\left(\frac{t}{2\tau_{\rm dp}(2n+1)}\right)\right]^2 - \left[1 - f\left(\frac{t}{\tau_{\rm dp}(2n+1)}\right)\right] \right) \right\} \tag{4.15}$$

with $f(x) = xD(x)$ and the Dawson function $D(x) = e^{-x^2} \int_0^x dt\, e^{t^2}$ with the limit $f(x \to \infty) = 1/2$. The first term in Eq. (4.15) is a modification of the universal function Eq. (4.11) which now includes damping on a time scale $\tau_{\rm dp}$. For long times $t \gg \tau_{\rm dp}$, the dynamics saturates at

$$P(t) \xrightarrow[t\gg\tau_{\rm dp}]{} \sum_{n=0}^{\infty} \left(\frac{2}{\pi(2n+1)}\right)^4 = \frac{1}{6}. \tag{4.16}$$

In Fig. 4.3, we compare the numerically calculated $P(t)$ for $N = 1000$ averaged over 10^5 realizations with a Gaussian density distribution with $k\sigma = 100$ and $P(t)$ given in Eq. (4.15), and find excellent agreement.

4.4. Dissipative Dynamics

Finally, we analyze the *dissipative dynamics*. The collective enhancement of the coupling between the forward-propagating waveguide mode and the $|W\rangle$ state also implies an enhanced spontaneous emission rate $\Gamma_{\rm F} = N\gamma$ into the forward direction. By contrast, the spontaneous emission $\Gamma_{\rm B}$ into the backward-propagating mode depends on the details of the atomic distribution within each experimental realization and is given by

$$\Gamma_{\rm B} = \frac{\gamma}{N} \int dx\, dy\, e^{2ik(x-y)} \langle G| \hat{n}_g(x) \hat{n}_g(y) |G\rangle \ . \tag{4.17}$$

Its average value can be obtained using Eq. (4.30) and as a result, we get

$$\bar{\Gamma}_{\rm B} = \gamma(N-1)\frac{|n_{2k}|^2}{N^2} + \gamma\,, \tag{4.18}$$

where n_{2k} is the Fourier transform of the density distribution $n(x)$. For a smooth density distribution with variations large compared to the optical wavelength λ,

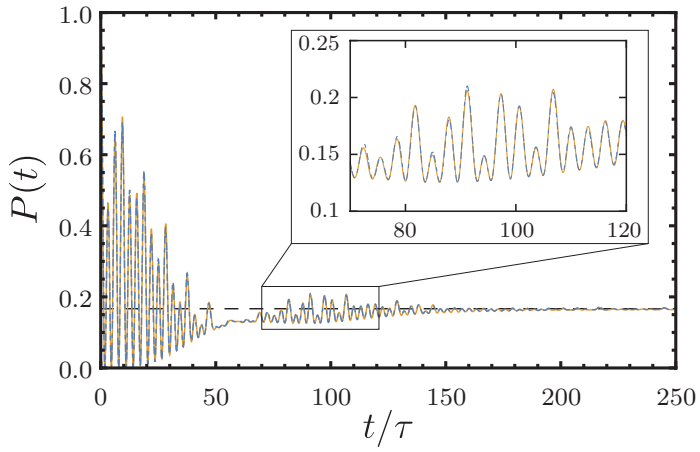

Fig. 4.3.: Comparison between the numerically and analytically calculated time evolution of $|W\rangle$ under H_s. Blue (dashed) curve: Numerically calculated time evolution for $N = 1000$ particles averaged over 10^5 realizations with a Gaussian distribution and $k\sigma = 100$. Orange (solid) curve: Analytical prediction for $\lambda/\sigma \ll 1$ and large N. (Inset:) Zoomed image of the dynamics for better comparison between numerically and analytically calculated time evolution. Note that there is hardly any visible difference.

this contribution is strongly suppressed. Considering, for example, a Gaussian distribution $n(x) = Ne^{-x^2/2\sigma^2}/\sqrt{2\pi\sigma^2}$ with width σ, we get $n_{2k}/N = e^{-8\pi^2\sigma^2/\lambda^2}$ which is exponentially suppressed for $\lambda \ll \sigma$. Thus, the back scattering is not enhanced and is dominated by the incoherent contribution γ.

4.5. Experimental Implementation

It is important to point out that the characteristic time scales for the revivals in the coherent dynamics and the dissipative part are of the same order. On one hand, we conclude that the coherent part always provides an intrinsic contribution to the dephasing of a superatom state. On the other hand, it is important to disentangle the dissipative dynamics and the coherent part for the experimental observation of the revivals. This goal can be achieved by quenching the spontaneous emission by tailoring the waveguide.

This approach is described in the following for an experimentally realistic setup. Such a setup exhibits, in addition to the coupling to the waveguide, naturally also a spontaneous emission into free space with rate γ_0. As a first requirement, this decay must be comparable or smaller than the decay into the wave guide, i.e., $\gamma \gtrsim \gamma_0$, which can be achieved in current experimental setups [15, 89]. Then, the

coherent dynamics as well as the dephasing are collectively enhanced and appear on a time scale much faster than residual losses, $N\gamma \gg \sqrt{N}\gamma \gg \gamma_0$. Second, the initial preparation of the setup in the superatom state $|W\rangle$ is achieved using a π pulse with a time scale fast compared to the characteristic dynamics τ. As the Rabi frequency is also collectively enhanced, this condition reduces to $\Omega \gg \gamma\sqrt{N}$ with Ω the single atom Rabi frequency. To reveal the effect of the coherent dynamics, we propose an experimental setup where the atoms are coupled to a one-dimensional photonic crystal or Bragg grating such that the emission process is strongly suppressed due to the opening of a band gap whereas the virtual photons mediating the exchange interaction can still propagate outside the photonic band gap. To satisfy this condition, the size of the photonic band gap Δ is required to be in the range $\Gamma_{\mathrm{F}} \ll \Delta \ll 2\pi c/\sigma$, where σ is the characteristic size of the system. The lower bound results from the fact that the emitted photon has a Lorentzian spectrum. The upper bound derives from the condition that the virtual photons should be able to propagate with a linear dispersion such that the initial form of the exchange Hamiltonian is unaffected.

For typical quantum optics experiments the system size is in the micrometer regime which relates to a mode spacing of the virtual photons of a few THz. In addition, the decay into the waveguide is typically in the range of MHz providing the enhanced decay rate $\Gamma_{\mathrm{F}} = N\gamma$ in the lower GHz regime for $N \sim 10^4$ atoms. This requires the width of the gap to be of the size of a few ten to hundred GHz. Such gratings have been produced for example in germanosilicate optical fibers [221] and specifically designed for quantum optics experiments [222].

4.6. Conclusion

In conclusion, we demonstrated that the nonequilibrium dynamics of a quantum many-body system consisting of atoms coupled to a one-dimensional waveguide can exhibit a highly nontrivial universal dynamics characterized by revivals and eventually a saturation on $1/6$. This observation is independent of the averaged atomic distribution $n(x)$ and becomes more pronounced for increasing particle number. In the present analysis, we chose a fixed number of atoms within each experimental realization. However, it is straightforward to derive that for a Poisson distributed number of atoms, the only modification in the dynamics is the enhancement of the dephasing rate by a factor $\sqrt{2}$, while the revivals and the saturation remain unaffected. One expects that similar phenomena can also appear in free space for two-level systems strongly coupled to a single highly focused light mode.

Appendix

4.A. Spectrum and Eigenstates

In this section, we show that the eigenenergies of the forward-propagating part H_F of the exchange Hamiltonian are given by

$$E_\alpha = \frac{\hbar\gamma}{2}\cot\left(\frac{\pi\alpha}{2N}\right) \tag{4.19}$$

with an odd integer $-N \leq \alpha < N$ and that the eigenstates are given by

$$|\alpha, \mathrm{F}\rangle = \frac{1}{\sqrt{N}}\int dx\, e^{ikx} S^+(x) \exp\left(-i\frac{\pi\alpha}{N}F(x)\right)|G\rangle \tag{4.20}$$

with $F(x) = \int_{-\infty}^{x} dz\, \hat{n}_g(z)$. To do so we apply the Hamiltonia H_F onto the state (4.20) and recall the definition of the state $|G\rangle = 1/\sqrt{N!}\prod_i \psi_g^\dagger(x_i)\,|0\rangle$ and the operators $S^+(x) = \psi_e^\dagger(x)\psi_g(x)$ and $S^-(x) = \psi_g^\dagger(x)\psi_e(x)$. We then rewrite Eq. (4.20) as

$$|\alpha, \mathrm{F}\rangle = \frac{1}{\sqrt{N}}\sum_{n=1}^{N} e^{ikx_n} S^+(x_n) e^{-i\frac{\pi\alpha n}{N}}\,|G\rangle\,, \tag{4.21}$$

and the Hamiltonian as

$$H_\mathrm{F} = \frac{\hbar\gamma}{2i}\sum_{n=1}^{N}\sum_{l=1}^{N} \mathrm{sign}(x_n - x_l) e^{ik(x_n - x_l)} S^+(x_n) S^-(x_l)\,. \tag{4.22}$$

Note that in the following, we always assume the positions of the atoms to be ordered, that is $x_1 \leq x_2 \leq \ldots \leq x_N$. Using that $S^-(x_n)S^+(x_l)\,|G\rangle = \delta_{nl}\,|G\rangle$, we

get

$$\begin{aligned} H_{\mathrm{F}}\left|\alpha,\mathrm{F}\right\rangle &= \frac{\hbar\gamma}{2i\sqrt{N}}\sum_{n,l,m=1}^{N} e^{ikx_m}e^{-i\frac{\pi\alpha m}{N}}\,\mathrm{sign}(x_n-x_l)e^{ik(x_n-x_l)} \\ &\quad\times S^+(x_n)S^-(x_l)S^+(x_m)\left|G\right\rangle \\ &= \frac{\hbar\gamma}{2i\sqrt{N}}\sum_{n,l=1}^{N} e^{ikx_n}e^{-i\frac{\pi\alpha l}{N}}\,\mathrm{sign}(x_n-x_l)S^+(x_n)\left|G\right\rangle \\ &= \frac{\hbar\gamma}{2i\sqrt{N}}\sum_{n=1}^{N} e^{ikx_n}\left(\sum_{l=1}^{n-1}e^{-i\frac{\pi\alpha l}{N}}-\sum_{l=n+1}^{N}e^{-i\frac{\pi\alpha l}{N}}\right)S^+(x_n)\left|G\right\rangle \\ &= \frac{\hbar\gamma}{2i\sqrt{N}}\sum_{n=1}^{N} e^{ikx_n}S^+(x_n)\left|G\right\rangle\frac{e^{-i\frac{\pi\alpha n}{N}}(1+e^{-i\frac{\pi\alpha}{N}})-e^{-i\frac{\pi\alpha}{N}}(1+e^{-i\pi\alpha})}{e^{-i\frac{\pi\alpha}{N}}-1}\,. \end{aligned} \tag{4.23}$$

From the last line, it is clear that if α is an odd integer, the second term in the numerator vanishes and $\left|\alpha,\mathrm{F}\right\rangle$ is indeed an eigenstate of H_{F}. The corresponding eigenvalue is then

$$E_\alpha = \frac{\hbar\gamma}{2i}\frac{e^{-i\frac{\pi\alpha}{N}}+1}{e^{-i\frac{\pi\alpha}{N}}-1} = \frac{\hbar\gamma}{2}\cot\left(\frac{\pi\alpha}{2N}\right)\,. \tag{4.24}$$

From Eq. (4.24) it is also clear that α is limited to $-N \leq \alpha < N$ due to the periodicity of the eigenvalues.

For the left-moving part $H_{\mathrm{B}} = -\frac{\hbar\gamma}{2i}\sum_{n,l}\mathrm{sign}(x_n-x_l)e^{-ik(x_n-x_l)}S^+(x_n)S^-(x_l)$, we make the ansatz

$$\left|\alpha,\mathrm{B}\right\rangle = \frac{1}{\sqrt{N}}\sum_{n=1}^{N} e^{-ikx_n}S^+(x_n)e^{i\frac{\pi\alpha n}{N}}\left|G\right\rangle\,. \tag{4.25}$$

The proof that this state is an eigenstate of H_{B} follows along the same lines as above and the eigenvalue is also given by $E_\alpha = \hbar\gamma\cot(\pi\alpha/2N)/2$.

4.B. Universal Dynamics

In order to derive the universal dynamics given by Eq. (4.11), we consider the Hamiltonian H_{F} with its eigenstates $\left|\alpha,\mathrm{F}\right\rangle$ and -energies E_α only. Using that α is an odd integer, the overlap with $\left|W\right\rangle$ is given by

$$\left\langle W|\alpha,\mathrm{F}\right\rangle = \frac{1}{N}\sum_{j=1}^{N} e^{-i\pi\alpha j/N} = -\frac{2}{N}\frac{e^{-i\pi\alpha}}{e^{i\pi\alpha/N}-1} \approx -\frac{2i}{\pi\alpha}\,. \tag{4.26}$$

The time evolution $P(t)$ in the limit $N \to \infty$ can then be calculated as

$$\begin{aligned} P(t) &= \left| \sum_\alpha e^{-iE_\alpha t} |\langle W|\alpha, \mathrm{F}\rangle|^2 \right|^2 \\ &\approx \left| \sum_\alpha e^{-i\frac{\gamma N t}{\pi\alpha}} \left(\frac{2}{\pi\alpha}\right)^2 \right|^2 \\ &= \left| \sum_{j=0}^{\infty} \left(\frac{2}{\pi(2j+1)}\right)^2 \cos\left(\frac{\gamma N t}{\pi(2j+1)}\right) \right|^2 , \end{aligned} \tag{4.27}$$

which is the universal function given in Eq. (4.11) describing the dynamics in the presence of only forward scattering. The time scale of the dynamics is given by $\tau = \pi/N\gamma$.

4.C. Perturbation Theory

As mentioned in Section 4.3.1, we define two dimensionless variables

$$h_{\alpha\beta} = \frac{\langle \beta, \mathrm{B}|\alpha, \mathrm{F}\rangle}{\beta} = \frac{1}{N\beta} \int dx\, e^{2ikx} \langle G|\, \hat{n}_g(x) e^{-i\frac{\pi(\alpha+\beta)}{N}F(x)} |G\rangle , \tag{4.28}$$

$$\begin{aligned} \delta_\alpha &= \frac{\langle \alpha, \mathrm{F}|\, H_\mathrm{B} |\alpha, \mathrm{F}\rangle}{E_1} \\ &= -\frac{1}{2iN^2} \int dx\, dy\, e^{2ik(x-y)} \mathrm{sign}(x-y) \\ &\qquad \times \langle G|\, \hat{n}_g(x)\hat{n}_g(y) e^{-i\frac{2\pi\alpha}{N}(F(x)-F(y))} |G\rangle . \end{aligned} \tag{4.29}$$

Since the positions of the atoms are randomly distributed in each experimental realization, the ground state density distribution $\hat{n}_g(x)$ and consequently the variables $h_{\alpha\beta}$ and δ_α will fluctuate. In the following, we will calculate the leading order behavior of the mean values and the fluctuations of these variables in the limits $k\sigma \to \infty$ and $N \to \infty$. To this end, we split the density distribution as $\hat{n}_g(x) = n(x) + \delta\hat{n}_g(x)$ where $n(x) = \langle \hat{n}_g(x)\rangle_\mathrm{dis}$ is the mean density distribution and thus $\langle \delta\hat{n}_g(x)\rangle_\mathrm{dis} = 0$. Further, we will make use of

$$\langle \hat{n}_g(x)\hat{n}_g(y)\rangle_\mathrm{dis} = g^{(2)}(x,y)n(x)n(y) + \delta(x-y)n(x) \tag{4.30}$$

with the two-body correlation function $g^{(2)}(x,y)$. Since the atoms are uncorrelated on distances comparable to the optical wavelength λ, we have $g^{(2)} = 1 - 1/N$ for

a fixed atom number N. Similarly, we get

$$\begin{aligned}\langle \delta\hat{n}_g(x)\delta\hat{n}_g(y)\rangle_{\text{dis}} &= (g^{(2)}(x,y)-1)n(x)n(y)+\delta(x-y)n(x)\\ &= -\frac{n(x)n(y)}{N}+\delta(x-y)n(x)\end{aligned} \tag{4.31}$$

for the correlations in the fluctuations of the density. Equations (4.30) and (4.31) will be used in the following to simplify the variables $h_{\alpha\beta}$ and δ_α given in Eqs. (4.28) and (4.29), respectively.

4.C.1. Mean Values

We start by calculating the mean value of $h_{\alpha\beta}$. Therefore, we note that we can write

$$\begin{aligned}\overline{h_{\alpha\beta}} &= \frac{1}{N\beta}\int dx\, e^{2ikx}\left\langle \hat{n}_g(x)e^{-i\frac{\pi(\alpha+\beta)}{N}\int_{-\infty}^{x}dz\,\hat{n}_g(z)}\right\rangle_{\text{dis}}\\ &= \frac{1}{N\beta}\int dx\, e^{2ikx}\left(\frac{iN}{\pi(\alpha+\beta)}\right)\partial_x\left\langle e^{-i\frac{\pi(\alpha+\beta)}{N}\int_{-\infty}^{x}dz\,\hat{n}_g(z)}\right\rangle_{\text{dis}},\end{aligned} \tag{4.32}$$

where we assume that $\hat{n}_g(-\infty)=0$. Using $\hat{n}_g(x)=n(x)+\delta\hat{n}_g(x)$, we can rewrite

$$\begin{aligned}\left\langle e^{-i\frac{\pi(\alpha+\beta)}{N}\int_{-\infty}^{x}dz\,\hat{n}_g(z)}\right\rangle_{\text{dis}} &= e^{-i\frac{\pi(\alpha+\beta)}{N}N(x)}\sum_{m=0}^{\infty}\frac{(i\pi(\alpha+\beta))^m}{N^m m!}\\ &\quad\times\prod_{i=1}^{m}\left[\int dz_i\theta(x-z_i)\right]\langle\delta\hat{n}_g(z_1)\cdots\delta\hat{n}_g(z_m)\rangle_{\text{dis}},\end{aligned} \tag{4.33}$$

where we defined $N(x)=\int_{-\infty}^{x}dz\,n(z)$ and $\theta(x)$ is the Heaviside function. The correlator can now be evaluated using Isserlis' theorem (in quantum field theory also known as Wick's theorem) which states that each m-point correlator of a normally distributed variable with zero mean can be written as a sum over a product of all possible combinations of two-point correlators for even m. Since the total number of terms in the sum is given by $(m-1)!!=(2n-1)!!=(2n)!/(2^n n!)$, we can write

$$\sum_{n=0}^{\infty}\frac{(i\pi(\alpha+\beta))^{2n}}{N^{2n}2^n n!}\left[\int_{-\infty}^{x}dz_1\,dz_2\,\langle\delta\hat{n}_g(z_1)\delta\hat{n}_g(z_2)\rangle\right]^n = e^{-\frac{1}{2}\left(\frac{\pi(\alpha+\beta)}{N}\right)^2\left(N(x)-\frac{N(x)^2}{N}\right)}. \tag{4.34}$$

Such that finally we have

$$\overline{h_{\alpha\beta}} = \frac{1}{N\beta}\int dx\, e^{2ikx}\left(\frac{iN}{\pi(\alpha+\beta)}\right)\partial_x e^{-i\frac{\pi(\alpha+\beta)}{N}N(x)-\frac{1}{2}\left(\frac{\pi(\alpha+\beta)}{N}\right)^2\left(N(x)-\frac{N(x)^2}{N}\right)}. \tag{4.35}$$

Performing the derivative, we finally get

$$\begin{aligned}\overline{h_{\alpha\beta}} = \frac{1}{N\beta}\int dx\, e^{2ikx}n(x)\left[1-\frac{i\pi(\alpha+\beta)}{2N}\left(1-\frac{2N(x)}{N}\right)\right]\\ \times e^{-i\frac{\pi(\alpha+\beta)}{N}N(x)-\frac{1}{2}\left(\frac{\pi(\alpha+\beta)}{N}\right)^2\left(N(x)-\frac{N(x)^2}{N}\right)}.\end{aligned} \tag{4.36}$$

This expression is now simply the Fourier transform of a (in principle very complicated) function. If however $n(x)$ and $N(x)$ are smooth functions and $2k\sigma \gg \pi|\alpha+\beta|$, the mean value $\overline{h_{\alpha\beta}}$ is strongly suppressed. As an example, we consider a Gaussian distribution of the particles with $n(x) = N/\sqrt{2\pi\sigma^2}e^{-x^2/2\sigma^2}$ and $N(x) = N/2(1+\mathrm{erf}(x/\sqrt{2}\sigma))$, where $\mathrm{erf}(x)$ is the error function. Focusing on the limit $N\to\infty$ (where we can safely neglect terms of order $1/N$) we get

$$\overline{h_{\alpha\beta}} = \frac{1}{\beta}\int dx\, e^{2ikx}\frac{e^{-x^2/2\sigma^2}}{\sqrt{2\pi\sigma^2}}e^{-i\frac{\pi(\alpha+\beta)}{2}(1+\mathrm{erf}(x/\sqrt{2}\sigma))}, \tag{4.37}$$

which vanishes exponentially in the limit $2k\sigma \gg \pi|\alpha+\beta|$. On the other hand, for $|\beta| \geqslant \sigma/\lambda$, this value is suppressed by the factor $1/\beta$.

For the mean value of δ_α, we write

$$\begin{aligned}\overline{\delta_\alpha} &= -\frac{1}{2iN^2}\int dx\, dy\, e^{2ik(x-y)}\mathrm{sign}(x-y)\frac{N^2}{(2\pi\alpha)^2}\\ &\quad\times\partial_x\partial_y\left\langle e^{-i\frac{2\pi\alpha}{N}\int dz\,\hat{n}_g(z)(\theta(x-z)-\theta(y-z))}\right\rangle_{\mathrm{dis}}\\ &= -\frac{1}{2iN^2}\int dx\, dy\, e^{2ik(x-y)}\mathrm{sign}(x-y)\frac{N^2}{(2\pi\alpha)^2}\\ &\quad\times\partial_x\partial_y e^{-i\frac{2\pi\alpha}{N}(N(x)-N(y))}e^{-\frac{1}{2}\left(\frac{2\pi\alpha}{N}\right)^2\left[\int dz(\theta(x-z)-\theta(y-z))^2 n(z)-\frac{1}{N}(N(x)-N(y))^2\right]}.\end{aligned} \tag{4.38}$$

Since we are again only interested in the limit $N\to\infty$, the expression reduces to

$$\begin{aligned}\overline{\delta_\alpha} &\approx -\frac{1}{2i}\int dx\, dy\, e^{2ik(x-y)}\mathrm{sign}(x-y)\frac{n(x)n(y)}{N^2}e^{-i\frac{2\pi\alpha}{N}(N(x)-N(y))}\\ &= -\int_{-\infty}^{\infty}dx\int_{-\infty}^{x}dy\,\sin\left[2k(x-y)-2\pi\alpha(N(x)-N(y))/N\right]\frac{n(x)n(y)}{N^2},\end{aligned} \tag{4.39}$$

where we assumed that $n(-x) = n(x)$ and consequently $N(-x) = N - N(x)$. Given a characteristic length σ of the atomic distribution and the condition $k\sigma \gg \pi|\alpha|$, we may neglect the second term in the phase of the sine and write

$$\overline{\delta_\alpha} \approx -\int_{-\infty}^{\infty} dx \int_{-\infty}^{x} dy \sin\left[2k(x-y)\right] \frac{n(x)n(y)}{N^2} \,. \tag{4.40}$$

In the following, we will estimate the value of this integral and derive the behavior in leading order for $k\sigma \gg 1$. Since we are only interested in realistic density distributions, we may estimate the integral by an exponential distribution $f(x) \sim e^{-x^2/2\sigma^2}$ which we make broad and large enough such that $f(x) > n(x)$ for all x. Note that the width of the exponential distribution is assumed to be some multiple of the width of the original distribution. Then, the integral can be calculated analytically as

$$\begin{aligned}
\int_{-\infty}^{\infty} dx\, dy \sin\left[2k(x-y)\right] \frac{n(x)n(y)}{N^2} &< \int_{-\infty}^{\infty} dx \int_{-\infty}^{x} dy \sin\left[2k(x-y)\right] \frac{e^{-(x^2+y^2)/2\sigma^2}}{2\pi\sigma^2} \\
&= \int_0^{\infty} dR \frac{e^{-R^2/2}}{\sqrt{2\pi}} \int_0^{\infty} dr\, \sin(\sqrt{2}k\sigma r) \frac{e^{-r^2/2}}{\sqrt{2\pi}} \\
&= \sqrt{2} D(k\sigma) \sim \frac{1}{\sqrt{2}\, k\sigma} \,,
\end{aligned} \tag{4.41}$$

where $D(x) = e^{-x^2} \int_0^x dt\, e^{t^2}$ is the Dawson function with the asymptotic expansion for $x \to \infty$

$$D(x) = \sum_{n=0}^{\infty} \frac{(2n-1)!!}{2^{n+1} x^{2n+1}} = \frac{1}{2x} + \mathcal{O}(x^{-3}) \,. \tag{4.42}$$

Thus, the leading order behavior of $\overline{\delta_\alpha}$ in the limit $N \to \infty$ and $k\sigma \gg \pi|\alpha|$ is bounded by

$$\overline{\delta_\alpha} \sim -\frac{1}{\sqrt{2}\, k\sigma} \tag{4.43}$$

and consequently vanishes in the limit $k\sigma \to \infty$.

4.C.2. Fluctuations

Distribution of $|w_\alpha|^2$

Here, we prove that in the limit $k\sigma \gg \pi|\alpha|$, $X = |w_\alpha|^2$ follows an exponential distribution $p(X) = \lambda e^{-\lambda X}$ with mean $\bar{X} = 1/\lambda$. The exponential distribution

can be characterized by its moments $\bar{X}^n = n!/\lambda^n$. The n-th moment of $|w_\alpha|^2$ is given by

$$\begin{aligned}\overline{|w_\alpha|^{2n}} &= \frac{1}{N^{2n}} \int dx_1 \cdots dx_{2n}\, e^{-2ik(x_1-x_2)} \cdots e^{-2ik(x_{2n-1}-x_{2n})} \\ &\quad \times \left\langle \hat{n}_g(x_1) \cdots \hat{n}_g(x_{2n}) e^{-i\frac{\pi\alpha}{N}(F(x_1)-F(x_2)+\cdots+F(x_{2n-1})-F(x_{2n}))} \right\rangle_{\text{dis}} \\ &= \frac{1}{N^{2n}} \int dx_1 \cdots dx_{2n}\, e^{-2ik(x_1-x_2)} \cdots e^{-2ik(x_{2n-1}-x_{2n})} \\ &\quad \times \sum_{m=0}^{\infty} \frac{(-i\pi\alpha)^m}{N^m m!} \int dz_1 \cdots dz_m h(\mathbf{x}, z_1) \cdots h(\mathbf{x}, z_m) \\ &\quad \times \left\langle \hat{n}_g(x_1) \cdots \hat{n}_g(x_{2n}) \hat{n}_g(z_1) \cdots \hat{n}_g(z_m) \right\rangle_{\text{dis}} , \end{aligned} \tag{4.44}$$

where we defined $h(\mathbf{x}, z) = \theta(x_1 - z) - \theta(x_2 - z) + \cdots + \theta(x_{2n-1} - z) - \theta(x_{2n} - z)$. In the next step, we express the density operator using $\hat{n}_g(x) = n(x) + \delta\hat{n}_g(x)$ in order to apply Isserlis' theorem. Further, we point out that whenever we pair operators with variables x and z, some phase factor e^{ikx} remains and this term is strongly suppressed in the limit $k\sigma \gg \pi|\alpha|$. Thus, the only contribution with no phase factors comes from the terms where only x variables are paired, that is

$$\begin{aligned}\overline{|w_\alpha|^{2n}} &= \frac{1}{N^{2n}} \int dx_1 \cdots dx_{2n}\, e^{-2ik(x_1-x_2)} \cdots e^{-2ik(x_{2n-1}-x_{2n})} \\ &\quad \times e^{-i\frac{\pi\alpha}{N}[N(x_1)-N(x_2)+\cdots N(x_{2n-1})-N(x_{2n})]} \\ &\quad \times \left\langle \delta\hat{n}_g(x_1) \cdots \delta\hat{n}_g(x_{2n}) \right\rangle_{\text{dis}} . \end{aligned} \tag{4.45}$$

In this expression, only those terms where odd indices are paired with even ones do not have a phase factor. For $2n$ indices, there are in total $n!$ possibilities for this kind of pairing and we are left with

$$\overline{|w_\alpha|^{2n}} = \frac{n!}{N^{2n}} \int dx_1 \cdots dx_n\, n(x_1) \cdots n(x_n) = \frac{n!}{N^{2n}} \left(\int dx\, n(x) \right)^n = \frac{n!}{N^n} , \tag{4.46}$$

which shows that indeed $|w_\alpha|^2$ follows an exponential distribution with mean $\overline{|w_\alpha|^2} = 1/N$. Consequently, the variance of the complex variable w_α is given by

$$(\Delta w_\alpha)^2 = \langle |w_\alpha|^2 \rangle_{\text{dis}} - \langle |w_\alpha| \rangle_{\text{dis}}^2 = \frac{1}{N} . \tag{4.47}$$

Fluctuations in δ_α

In a next step, we calculate the fluctuations in the variable δ_α. Since this variable is real, the variance is given by

$$(\Delta\delta_\alpha)^2 = \langle\delta_\alpha^2\rangle_{\text{dis}} - \langle\delta_\alpha\rangle_{\text{dis}}^2 \,, \tag{4.48}$$

where

$$\begin{aligned}\langle\delta_\alpha^2\rangle_{\text{dis}} = -\frac{1}{4N^4}\int dx\, dy\, dx'\, dy'\, \text{sign}(x-y)\text{sign}(x'-y')e^{2ik(x-y)}e^{2ik(x'-y')} \\ \times\left\langle \hat{n}_g(x)\hat{n}_g(y)\hat{n}_g(x')\hat{n}_g(y')e^{-i\frac{\pi\alpha}{N}(F(x)-F(y)+F(x')-F(y'))}\right\rangle_{\text{dis}} .\end{aligned} \tag{4.49}$$

Similar to the previous case where we studied the fluctuations of w, the only non-vanishing contribution after applying Isserlis' theorem in the limit $k\sigma \gg \pi|\alpha|$ comes from the term with the pairing

$$\begin{aligned}\langle\delta\hat{n}_g(x)\delta\hat{n}_g(y')\rangle_{\text{dis}}\langle\delta\hat{n}_g(y)\delta\hat{n}_g(x')\rangle_{\text{dis}} = \left(\delta(x-y)n(x) - \frac{1}{N}n(x)n(y')\right) \\ \times\left(\delta(y-x')n(y) - \frac{1}{N}n(y)n(x')\right) .\end{aligned} \tag{4.50}$$

From these four terms, only the term $\delta(x-y')\delta(y-x')n(x)n(y)$ survives in the limit of interest and we are left with

$$\begin{aligned}\langle\delta_\alpha^2\rangle_{\text{dis}} &= -\frac{1}{4N^4}\int dx\, dy\, \text{sign}(x-y)\text{sign}(y-x)n(x)n(y) \\ &= \frac{1}{4N^4}\left(\int dx\, n(x)\right)^2 = \frac{1}{4N^2} .\end{aligned} \tag{4.51}$$

Thus, the fluctuations of δ_α are given by

$$(\Delta\delta_\alpha)^2 \sim \frac{1}{N^2} \tag{4.52}$$

and hence vanish faster than those of w_α.

4.C.3. Spectrum in Perturbation Theory

As shown in Appendix 4.C.2, the states $|\alpha, \text{F}\rangle$ and $|\alpha, \text{B}\rangle$ have vanishing overlap in the limit $k\sigma \gg \pi|\alpha|$ on average while the fluctuations of this quantity behave

as $1/N$ in the limit $N \to \infty$. Further, we know that the matrix element δ_α also vanishes on average while having fluctuations on the order of $1/N^2$. In the derivation of the universal dynamics in Section 4.C, we have shown that the dominant contribution comes from those states with small values of α where the overlap to the state $|W\rangle$ is large. Hence, we restrict our analysis to those values of α and aim at calculating the eigenenergies and -states of the full Hamiltonian in perturbation theory to derive an analytic formula for $P(t)$ in the presence of disorder.

For the perturbation theory, we assume that the unperturbed basis is given by $|\alpha, \mathrm{F/B}\rangle$ and the perturbation is given by both H_F and H_B. This can be justified by noting that, for example, the matrix element δ_α vanishes on average and has only small fluctuations for small $|\alpha|$ and large N. The same applies for the matrix element $\langle \alpha, \mathrm{B}| H_\mathrm{F} |\alpha, \mathrm{B}\rangle$ and all off-diagonal elements. Since we are only interested in leading order effects in N, we apply degenerate perturbation theory in the subspace $\{|\alpha, \mathrm{F}\rangle, |\alpha, \mathrm{B}\rangle\}$ for fixed α. Note, however, that these states are not orthogonal in general but only on average with fluctuations on the order of $1/N$ such that we have to orthogonalize this subspace artificially using

$$|\psi_1\rangle = |\alpha, \mathrm{F}\rangle \tag{4.53}$$

$$|\psi_2\rangle = \frac{1}{\sqrt{1-|w_\alpha|^2}} \left(|\alpha, \mathrm{B}\rangle - w_\alpha^* |\alpha, \mathrm{F}\rangle\right) . \tag{4.54}$$

In order to simplify the calculations, we neglect δ_α since its fluctuations are much smaller than those of w_α. The corresponding Hamiltonian in the subspace spanned by $|\psi_1\rangle$ and $|\psi_2\rangle$ then reads

$$H = E_\alpha \begin{pmatrix} 1 & \frac{w_\alpha^*}{\sqrt{1-|w_\alpha|^2}} \\ \frac{w_\alpha}{\sqrt{1-|w_\alpha|^2}} & \frac{1-3|w_\alpha|^2}{1-|w_\alpha|^2} \end{pmatrix} . \tag{4.55}$$

Its eigenvalues are given by

$$E_\pm = \frac{E_\alpha}{1-|w_\alpha|^2} \left(1 - 2|w_\alpha|^2 \pm |w_\alpha|\right) \approx E_\alpha (1 \pm |w_\alpha|) \tag{4.56}$$

to leading order in w_α. The corresponding eigenstates are to leading order in w_α given by

$$|\alpha, +\rangle = \frac{1}{\sqrt{2}} \left(|\psi_1\rangle + \frac{w_\alpha^*}{|w_\alpha|} |\psi_2\rangle\right) \approx \frac{1}{\sqrt{2}} \left[\left(1 - \frac{w_\alpha^{*\,2}}{|w_\alpha|}\right) |\alpha, \mathrm{F}\rangle + \frac{w_\alpha^*}{|w_\alpha|} |\alpha, \mathrm{B}\rangle\right] , \tag{4.57}$$

$$|\alpha, -\rangle = \frac{1}{\sqrt{2}} \left(|\psi_1\rangle - \frac{w_\alpha^*}{|w_\alpha|} |\psi_2\rangle\right) \approx \frac{1}{\sqrt{2}} \left[\left(1 + \frac{w_\alpha^{*\,2}}{|w_\alpha|}\right) |\alpha, \mathrm{F}\rangle - \frac{w_\alpha^*}{|w_\alpha|} |\alpha, \mathrm{B}\rangle\right] . \tag{4.58}$$

In conclusion, the degenerate eigenenergies E_α split to first order in w_α with the splitting

$$\frac{\Delta E_\alpha}{E_\alpha} = 2|w_\alpha| \sim \frac{d_\alpha}{\sqrt{N}} \tag{4.59}$$

where d_α is of order unity and depends on each single realization of the experiment. These fluctuating energies then set a time scale for the dephasing

$$\tau_{\text{dp}} \sim \frac{\hbar}{\Delta E_\alpha} \sim \frac{1}{\sqrt{N}\gamma}\,. \tag{4.60}$$

In terms of the time scale $\tau^{-1} \sim N\gamma$ given by the universal dynamics, we have

$$\tau_{dp} \sim \sqrt{N}\tau \tag{4.61}$$

such that relative to τ, τ_{dp} even grows with the particle number and the universal dynamics persists for longer times.

4.D. Analytic Expression of $P(t)$ in the Large-N limit

Using the results calculated in Appendices 4.C.2 and 4.C.3, we are now able to derive analytically an approximate expression for $P(t)$ in the limit of large N and $k\sigma \gg 1$. We start by writing

$$\begin{aligned}
P(t) &= \left|\langle W|\, e^{-\frac{i}{\hbar}Ht}\, |W\rangle\right|^2 \\
&\approx \left|\sum_\alpha e^{-i\frac{E_\alpha}{\hbar}t(1+|w_\alpha|)}\, |\langle W|\alpha,+\rangle|^2 + e^{-i\frac{E_\alpha}{\hbar}t(1-|w_\alpha|)}\, |\langle W|\alpha,-\rangle|^2\right|^2 \\
&= \left|\sum_\alpha e^{-i\frac{E_\alpha}{\hbar}t}\left(e^{-i\frac{E_\alpha|w_\alpha|}{\hbar}t}\, |\langle W|\alpha,+\rangle|^2 + e^{i\frac{E_\alpha|w_\alpha|}{\hbar}t}\, |\langle W|\alpha,-\rangle|^2\right)\right|^2 \\
&= \sum_{\alpha\neq\beta} e^{-i\frac{E_\alpha}{\hbar}t} e^{i\frac{E_\beta}{\hbar}t}\left(e^{-i\frac{E_\alpha|w_\alpha|}{\hbar}t}|\, \langle W|\alpha,+\rangle\, |^2 + e^{i\frac{E_\alpha|w_\alpha|}{\hbar}t}\, |\langle W|\alpha,-\rangle|^2\right) \\
&\qquad \times \left(e^{-i\frac{E_\beta|w_\beta|}{\hbar}t}\, |\langle W|\beta,+\rangle|^2 + e^{i\frac{E_\beta|w_\beta|}{\hbar}t}\, |\langle W|\beta,-\rangle|^2\right) \\
&\qquad + \sum_\alpha \left|e^{-i\frac{E_\alpha|w_\alpha|}{\hbar}t}\, |\langle W|\alpha,+\rangle|^2 + e^{i\frac{E_\alpha|w_\alpha|}{\hbar}t}\, |\langle W|\alpha,-\rangle|^2\right|^2 \\
&= (\mathrm{A}) + (\mathrm{B})
\end{aligned} \tag{4.62}$$

where (A) contains the sum where $\alpha \neq \beta$ and (B) contains the sum with $\alpha = \beta$. The overlap of the eigenstates $|\alpha, \pm\rangle$ with $|W\rangle$ is given by

$$|\langle W|\alpha,\pm\rangle|^2 = \frac{1}{2}\left[\left(\frac{2}{\pi\alpha}\right)^2 + |\langle W|\psi_2\rangle|^2 \mp \frac{2}{\pi\alpha}\left(e^{-i\phi_\alpha}\langle W|\psi_2\rangle + e^{i\phi_\alpha}\langle\psi_2|W\rangle\right)\right], \tag{4.63}$$

where we set $w_\alpha = |w_\alpha|e^{i\phi_\alpha}$. Further, we have

$$\langle W|\psi_2\rangle = \langle W|\alpha, \mathrm{B}\rangle + |w_\alpha|e^{-i\phi_\alpha}\frac{2}{\pi\alpha} \tag{4.64}$$

and

$$|\langle W|\psi_2\rangle|^2 = |\langle W|\alpha,\mathrm{B}\rangle|^2 + |w_\alpha|^2\left(\frac{2}{\pi\alpha}\right)^2 + \frac{2}{\pi\alpha}2|w_\alpha|\cos(\phi_\alpha)\,. \tag{4.65}$$

The overlap of the state $|W\rangle$ and the state $|\alpha,\mathrm{B}\rangle$ is given by

$$\langle W|\alpha,\mathrm{B}\rangle = \frac{1}{N}\int dx\, e^{-2ikx}\langle G|\,\hat{n}_g(x)e^{i\frac{\pi\alpha}{N}F(x)}\,|G\rangle \tag{4.66}$$

and has the same distribution as w_α^* in the limits we are interested in. Thus, to leading order in w_α, we can write

$$|\langle W|\alpha,\pm\rangle|^2 = \frac{1}{2}\left\{\left(\frac{2}{\pi\alpha}\right)^2 + \frac{2}{\pi\alpha}|w_\alpha|\left[2\cos(\phi_\alpha) \mp \left(1+\frac{2}{\pi\alpha}\right)2\cos(2\phi_\alpha)\right]\right\}. \tag{4.67}$$

Let us now focus on the second term in Eq. (4.62), where the sum runs only over α. We can write

$$\begin{aligned}(\mathrm{B}) = \sum_\alpha\, &|\langle W|\alpha,+\rangle|^4 + |\langle W|\alpha,-\rangle|^4 \\ &+ 2\,|\langle W|\alpha,+\rangle|^2\,|\langle W|\alpha,-\rangle|^2\cos\left(\frac{2E_\alpha|w_\alpha|}{\hbar}t\right).\end{aligned} \tag{4.68}$$

Next, we insert the result obtained in Eq. (4.67) and neglect all terms of order w_α^2. For the linear terms, we point out that they are all accompanied by a factor $\cos(\phi_\alpha)$ or $\cos(2\phi_\alpha)$. One can verify numerically that the complex random variable w_α follows a Gaussian distribution which is spherically symmetric such that $|w_\alpha|$ and ϕ_α

are independent random variables. The random phase ϕ_α is uniformly distributed in the interval $[-\pi, \pi]$ and hence the cosine terms vanish after averaging over different realizations. Thus, we are left with

$$\text{Eq. (4.68)} = \frac{16}{4\pi^4} \sum_\alpha \frac{2}{\alpha^4} \left(1 + \cos\left(\frac{2E_\alpha |w_\alpha|}{\hbar} t\right)\right) . \tag{4.69}$$

In addition, the averaging over $|w_\alpha|$ can be carried out by noting that $|w_\alpha|^2$ follows an exponential distribution with mean $1/N$ such that

$$\begin{aligned}\overline{\text{Eq. (4.69)}} &= \frac{16}{2\pi^4} \sum_\alpha \frac{1}{\alpha^4} \int_0^\infty d|w_\alpha|^2 N e^{-N|w_\alpha|^2} \left[1 + \cos\left(\frac{2E_\alpha \sqrt{|w_\alpha|^2}}{\hbar} t\right)\right] \\ &= \frac{16}{\pi^4} \sum_\alpha \frac{1}{\alpha^4} \left[1 - \frac{E_\alpha t\, D\left(\frac{E_\alpha t}{\hbar\sqrt{N}}\right)}{\hbar\sqrt{N}}\right] ,\end{aligned} \tag{4.70}$$

with the Dawson function $D(x)$ as defined below Eq. (4.41).

In a similar way, we can treat the first term in Eq. (4.62) which leads to

$$\overline{(\mathrm{A})} = \frac{16}{\pi^4} \sum_{\alpha\neq\beta} e^{-i\frac{E_\alpha}{\hbar}t} e^{i\frac{E_\beta}{\hbar}t} \frac{1}{\alpha^2}\frac{1}{\beta^2} \left[1 - \frac{E_\alpha t D\left(\frac{E_\alpha t}{2\hbar\sqrt{N}}\right)}{\hbar\sqrt{N}}\right] \left[1 - \frac{E_\beta t D\left(\frac{E_\beta t}{2\hbar\sqrt{N}}\right)}{\hbar\sqrt{N}}\right] . \tag{4.71}$$

Since $E_{-\alpha} = -E_\alpha$, we can restrict the sum over positive α and then replace $\alpha = 2n+1$ where $n = 0, 1, 2, \ldots$ Note that now we let the sum run over infinitely many integers even though we only have a finite number of states for finite N. The contributions from large n give only small contributions such that we can safely neglect them. Further, we introduce $\tau = \pi/N\gamma$ such that finally the disorder-averaged dynamics of the state $|W\rangle$ is given by

$$\begin{aligned}P(t) = \frac{16}{\pi^4} \sum_{n\neq m\geq 0} &\frac{2}{(2n+1)^2}\frac{2}{(2m+1)^2} \cos\left(\frac{t/\tau}{2n+1}\right) \cos\left(\frac{t/\tau}{2m+1}\right) \\ &\times \left[1 - \frac{t/\tau_{\mathrm{dp}}\, D\left(\frac{t/2\tau_{\mathrm{dp}}}{2n+1}\right)}{2n+1}\right] \left[1 - \frac{t/\tau_{\mathrm{dp}}\, D\left(\frac{t/2\tau_{\mathrm{dp}}}{2m+1}\right)}{2m+1}\right] \\ &- \frac{16}{\pi^4} \sum_n \frac{2}{(2n+1)^4} \left[\left(1 - \frac{t/\tau_{\mathrm{dp}}\, D\left(\frac{t/2\tau_{\mathrm{dp}}}{2n+1}\right)}{2n+1}\right)^2 - \left(1 - \frac{t/\tau_{\mathrm{dp}} D\left(\frac{t/\tau_{\mathrm{dp}}}{2n+1}\right)}{2n+1}\right)\right] .\end{aligned} \tag{4.72}$$

In this expression, the first term is reminiscent of the universal dynamics showing oscillatory behavior which then is damped out on a time scale $\tau_{\text{dp}} = \sqrt{N}\tau$, while for times $t \gg \tau_{\text{dp}}$, the last term reduces to

$$\frac{16}{\pi^4}\sum_n \frac{2}{(2n+1)^4}\left[1 - \frac{t/\tau_{\text{dp}} D\left(\frac{t/\tau_{\text{dp}}}{2n+1}\right)}{2n+1}\right] \;\to\; \frac{16}{\pi^4}\sum_{n=0}^{\infty}\frac{1}{(2n+1)^4} = \frac{1}{6} \tag{4.73}$$

which gives the universal saturation value different from zero.

5

Decay Dynamics of a Collective Excitation

In this chapter, we extend the findings of Chapter 4 and study the influence of the coherent exchange of photons in an ensemble on the decay dynamics of a single collective excitation. In particular, we focus on one-dimensional systems and distinguish between chiral and bidirectional waveguides. We find that, for a chiral waveguide, the probability of having a collective excitation decays with an algebraic power law instead of the conventional exponential decay. Remarkably, this characteristic algebraic behavior remains present even for the bidirectional waveguide in the limit of large particle number and extended sample size. This observation suggests that some characteristic properties of chiral waveguides are also experimentally accessible in bidirectional waveguides. This chapter is based on Ref. [223].

5.1. Introduction

Coupling light to an ensemble of emitters is one of the paradigmatic models in quantum optics and gives rise to interesting collective and cooperative effects [224]. The most prominent example is superradiance [3, 5] where ensembles of many excited emitters emit at higher intensities if they are excited collectively rather than independently. Superradiance and other cooperative effects have been observed in a broad spectrum of physical systems ranging from ensembles of nuclei [6] over cold atoms [8–10], ions [11], solid-state systems [12, 13] to more artificial and hybrid light-matter systems like superconducting qubits [14, 225] or atoms

coupled to nanophotonic structures [194]. Intimately connected to the appearance of superradiant properties of an ensemble is the existence of subradiant states with a strongly quenched emission. These subradiant states find potential applications, for example, in photon storage [25] or quantum computing [46]. However, interesting phenomena appear even in a very weakly excited system with only a single excitation coherently shared among all emitters [16, 18, 19, 21–24]. Due to the collective light-matter coupling, for example, the emission rate from the sample is still enhanced compared to an independent emission and scales linearly with the number of emitters. Here, we study the emission dynamics of a single coherent excitation in a superradiant state from an ensemble of emitters coupled to a one-dimensional waveguide.

The influence of collective effects is two-fold. On one hand, the coupling of the ensemble to an external light field is collectively enhanced which can be used to strongly couple a propagating light pulse to an ensemble of many atoms in order to drive Rabi oscillations with only a few photons [177]. This collective coupling also leads to a strongly enhanced emission rate and the emission becomes highly directional [16, 39, 226]. On the other hand, coherent interactions mediated by the exchange of virtual photons between the emitters were shown to give rise to a collective Lamb shift [2, 23], universal internal dynamics of the ensemble [216] but also strongly influence the decay dynamics of single photon superradiance in three dimensions [19, 21, 227]. Moreover, coherent interactions can be used to create quantum antennas [228], cavities built from only two atoms [165] or mirrors built from a single layer of atoms [75, 83, 84]. Recently, the efficient coupling of atoms to nanophotonic structures in low dimensions [89] has enabled the study of almost perfectly one-dimensional systems that show infinite-range interactions [90] but also exotic chiral, coherent light-matter interactions which depend on the polarisation of the incoming light [105]. Such waveguides have a high potential to generate nonclassical states of light [99, 102, 104].

5.2. Setup and Model

Similar to Chapter 4 we consider a system of N noninteracting two-level atoms at positions x_j where each atom has a ground state $|g\rangle$ and an excited state $|e\rangle$ separated by the transition frequency $\omega_0 = ck$ (see Fig. 5.1). The atoms are coupled to a one-dimensional waveguide and the coupling is described within the rotating frame and applying the rotating-wave approximation. The Hamiltonian takes the

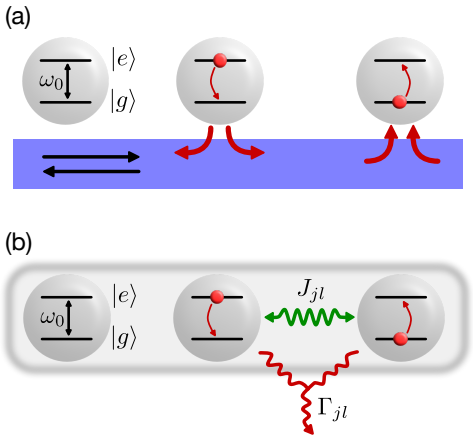

Fig. 5.1.: (a) Two-level atoms coupled to a one-dimensional waveguide. The waveguide supports (in general) left- and right-propagating modes and the atoms can emit (absorb) photons into (from) both modes. (b) Effective system after the elimination of the waveguide photons. The atoms interact via an (infinite-ranged) exchange interaction J_{jl} and have a correlated decay Γ_{jl}.

form

$$H = \int \frac{dq}{2\pi} \hbar\omega_q a_a^\dagger a_q - \hbar\sqrt{\gamma} \sum_{j=1}^{N} \left[\mathcal{E}^-(x_j)\sigma_j^+ + \mathcal{E}^+(x_j)\sigma_j^-\right] . \tag{5.1}$$

The first term describes the photons in the waveguide with linear dispersion $\omega_q = c|q| - \omega_0$ around the resonance frequency and annihilation (creation) operators $a_q^{(\dagger)}$ of photons with momentum q. The second term accounts for the coupling of the atoms to the electromagnetic field with strength $\sqrt{\gamma}$. Here, $\sigma_j^+ = |e\rangle\langle g|_j$ and $\sigma_j^- = |g\rangle\langle e|_j$ are the raising and lowering operators for the atomic transition, respectively. The positive frequency component of the electric field operator $\mathcal{E}^-$ is given by

$$\mathcal{E}^-(x) = i\sqrt{c} \int \frac{dq}{2\pi} a_q e^{iqx} , \tag{5.2}$$

and analogously for the negative frequency component $\mathcal{E}^+$. Note that the scalar product of the polarization with the transition dipole moment is already included in the definition of $\mathcal{E}^\pm$.

As discussed in Chapter 2, the photonic degrees of freedom can be integrated out leaving us with an effective description of the dynamics of the atoms in terms

of a master equation of the form

$$\partial_t \rho(t) = -\frac{i}{\hbar}\left[\sum_{j,l} \hbar J_{jl} \sigma_j^+ \sigma_l^-, \rho(t)\right] + \sum_{j,l} \Gamma_{jl}\left(\sigma_l^- \rho(t) \sigma_j^+ - \frac{1}{2}\left\{\sigma_j^+ \sigma_l^-, \rho(t)\right\}\right). \tag{5.3}$$

The first term accounts for the coherent exchange interaction mediated by virtual photons and the second one gives rise to correlated spontaneous emission. In general, J_{jl} and Γ_{jl} are related to the propagator of the electromagnetic field (2.7). The term J_{jj} accounts for a Lamb shift and is usually dropped as it is already included in the resonance frequency of a single emitter, while Γ_{jj} describes the single-emitter decay rate.

In this chapter, we focus on chiral and bidirectional waveguides. For a chiral waveguide, where the atoms only couple to modes with either positive or negative momentum, the coherent exchange terms and decay rates read

$$J_{jl} = \frac{\gamma}{2i}\text{sign}(x_j - x_l) e^{ik(x_j - x_l)}\,, \tag{5.4}$$

$$\Gamma_{jl} = \gamma e^{ik(x_j - x_l)}\,, \tag{5.5}$$

respectively, where the single-atom decay rate is $\Gamma_{jj} = \gamma$. Here, $\text{sign}(x-y) = \mp 1$ if $x \lessgtr y$ and $\text{sign}(x-y) = 0$ if $x = y$.

For the bidirectional waveguide, where the atoms couple to both forward- and backward-propagating modes, the coherent exchange terms and decay rates are given by

$$J_{jl} = \gamma\, \sin(k|x_j - x_l|)\,, \tag{5.6}$$

$$\Gamma_{jl} = 2\gamma\, \cos(k|x_j - x_l|)\,, \tag{5.7}$$

respectively, with the single-atom decay rate $\Gamma_{jj} = 2\gamma$. Note that the single-atom decay rate is twice as large for the bidirectional waveguide as the photon can be emitted into the forward- and the backward-propagating modes.

5.3. Two-Atom Solution

As an illustrative example that already contains the important physics, we review the case of only two atoms, which has also been studied extensively in previous works [229, 230]. Consider the generic master equation for a system of only two

identical atoms at positions x_1 and x_2 given by

$$\partial_t \rho = -i\left[J_{12}\sigma_1^+\sigma_2^- + J_{12}^*\sigma_2^+\sigma_1^-, \rho\right] + \Gamma\Bigg(\mathcal{D}[\sigma_1^-]\rho + \mathcal{D}[\sigma_2^-]\rho + F_{12}\left(\sigma_2^-\rho\sigma_1^+ - \frac{1}{2}\{\sigma_1^+\sigma_2^-, \rho\}\right) + F_{12}^*\left(\sigma_1^-\rho\sigma_2^+ - \frac{1}{2}\{\sigma_2^+\sigma_1^-, \rho\}\right)\Bigg), \tag{5.8}$$

where $J_{12} \in \mathbb{C}$ is the coherent coupling between the atoms, $\mathcal{D}[\sigma^-]\rho = \sigma^-\rho\sigma^+ - \{\sigma^+\sigma^-, \rho\}/2$ is the Lindblad dissipator and Γ is the single-atom emission rate into the waveguide. In a chiral waveguide there is only a coupling to the forward propagating modes and the single-atom emission rate is $\Gamma = \gamma$, whereas for a bidirectional waveguide, the atom can emit into forward- and backward-propagating modes and the emission rate is $\Gamma = 2\gamma$ (see Fig. 5.2(a)).

The dimensionless factor $F_{12} \in \mathbb{C}$ is a measure for the correlated decay of both atoms in terms of Γ. If $F_{12} = 0$, the atoms decay independently of each other with the single-atom decay rate Γ. If F_{12} is different from zero, the decay rates are modified in general and in the single-excitation subspace, there is one superradiant state which decays faster than Γ and one subradiant state which decays slower than Γ. The super- and subradiant states read

$$|\pm\rangle = \frac{1}{\sqrt{2}}\left(\sigma_1^+ \pm e^{-i\phi}\sigma_2^+\right)|G\rangle \equiv \frac{1}{\sqrt{2}}S_\pm^\dagger|G\rangle \tag{5.9}$$

where $\phi = \arg(F_{12})$ and $|G\rangle$ is the ground state of the atomic system where all atoms are in their respective ground state. The corresponding decay rates are $\Gamma_\pm = \Gamma(1 \pm |F_{12}|)$. Note that the decay rates depend on the distance between the emitters.

While the super- and subradiant states provide an elegant way to describe the decay dynamics of a single excitation, for actual experiments another type of state is of importance. Assume that in a one-dimensional setup the system is excited by means of a plane wave e^{ikx}. In the single-excitation sector the light field couples to the so-called bright state

$$|W\rangle = \frac{1}{\sqrt{2}}(\sigma_1^+ + e^{-ik(x_1-x_2)}\sigma_2^+)|G\rangle \equiv \frac{1}{\sqrt{2}}S_W^\dagger|G\rangle\ . \tag{5.10}$$

The orthogonal state

$$|D\rangle = \frac{1}{\sqrt{2}}(\sigma_1^+ - e^{-ik(x_1-x_2)}\sigma_2^+)|G\rangle \equiv \frac{1}{\sqrt{2}}S_D^\dagger|G\rangle \tag{5.11}$$

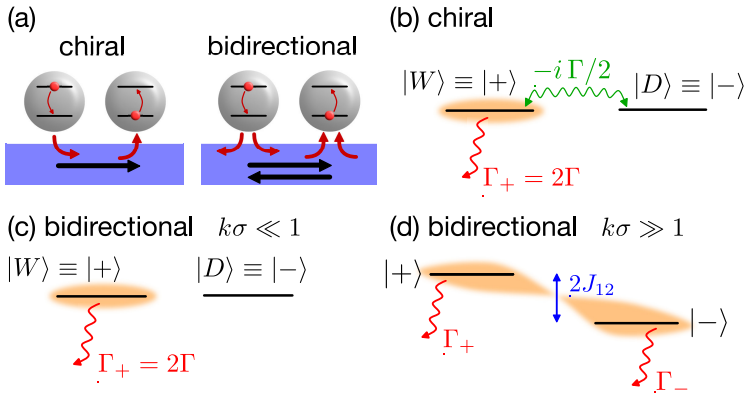

Fig. 5.2.: Setup for two atoms coupled to a one-dimensional waveguide. (a) In a chiral setup (left) the atom can only emit into the forward-propagating mode with rate γ, while in the bidirectional setup (right) the atoms can emit into forward- and backward-propagating mode with rate γ for each mode. (b) For a chiral waveguide, the subradiant and superradiant states correspond to the bright and dark state, respectively. The bright and dark state are coupled and the bright state decays with a collectively enhanced decay rate $\Gamma_+ = 2\Gamma$ and the single-atom emission rate $\Gamma = \gamma$. Initially, the system is prepared in the bright state. (c) In the bidirectional case, when the atoms are on average very close to each other compared to the wavelength, there is no coupling and the bright (dark) state corresponds to the superradiant (subradiant) state. A system that is initially prepared in the bright state decays with the collectively enhanced decay rate 2Γ, where the single-atom decay rate is $\Gamma = 2\gamma$. (d) In the case where the interatomic distance is on average much greater than the wavelength, the superradiant and subradiant state are shifted with respect to each other (depending on the distance between the atoms) and emit with rates Γ_+ and Γ_-, respectively. Since the bright state is now a superposition of the super- and subradiant state, these two states are coupled by the initial condition.

is called the dark state and is decoupled from the incoming light field. It is important to note that while the bright and dark state look similar to the super- and subradiant state defined in Eq. (5.9), they coincide only in very special cases as we will show in the following.

5.3.1. Bidirectional Waveguide

First, we focus on the bidirectional waveguide for which $\Gamma = 2\gamma$, $F_{12} = \cos(k|x_1 - x_2|)$ and $J_{12} = \frac{\Gamma}{2}\sin(k|x_1 - x_2|) \in \mathbb{R}$, which can be inferred by comparing Eqs. (5.6), (5.7) and (5.8). The resulting master equation for this system reads

$$\partial_t \rho = -i\left[J_{12}(S_+^\dagger S_+ - S_-^\dagger S_-), \rho\right] + \Gamma_+ \mathcal{D}[S_+]\rho + \Gamma_- \mathcal{D}[S_-]\rho\,. \tag{5.12}$$

Note that the dynamics for the super- and subradiant states completely decouple, and both states are shifted by J_{12} with respect to each other. This situation is qualitatively similar to a system of two atoms coupled to the electromagnetic continuum in free space as the parameters J_{12} and F_{12} are real and depend on the relative distance between the atoms. The precise form of the coupling parameter and decay rates, however, are much more complicated and also depend on the relative orientation of the two atoms.

The dynamics of the system of two atoms can be calculated analytically for arbitrary positions of the atoms and by defining the elements of the density matrix $\rho_{\alpha\beta} = \langle\alpha|\,\rho\,|\beta\rangle$. The populations of the bright state and dark state for a system initially prepared in the bright state are given by

$$\rho_{WW}(t) = e^{-\Gamma t}\left|\cosh\left(\frac{\Gamma t}{2}\,e^{ik|x_1-x_2|}\right) - \cos(k\,(x_1-x_2))\sinh\left(\frac{\Gamma t}{2}\,e^{ik|x_1-x_2|}\right)\right|^2, \tag{5.13}$$

$$\rho_{DD}(t) = e^{-\Gamma t}\sin^2(k|x_1-x_2|)\left|\sinh\left(\frac{\Gamma t}{2}\,e^{ik|x_1-x_2|}\right)\right|^2. \tag{5.14}$$

For short distances, $k|x_1-x_2| \ll 1$, one can approximate $F_{12} \approx 1$ and $J_{12} \approx 0$ resulting in $\Gamma_+ = 2\Gamma$ and $\Gamma_- = 0$. In addition, the bright and dark state coincide with the super- and subradiant state, respectively (see Fig. 5.2(c)). In this scenario, the bright state decays exponentially with an enhanced decay rate 2Γ known as single-photon superradiance which was already studied by Dicke [3]. The same holds when we go to the experimentally more relevant case where the positions of the atoms might fluctuate for different realizations of the experiment. Assuming that the atoms are distributed according to a density distribution with characteristic length scale σ, single-photon superradiance is also present if $k\sigma \ll 1$, that is if the atoms are much closer than a wavelength. This can be also seen from Eq. (5.13) which reduces to $\rho_{WW}(t) \approx e^{-2\Gamma t}$ in these cases.

In the opposite limit where the extent of the ensemble is much larger than the wavelength, that is $k\sigma \gg 1$, the behaviour for small times $\Gamma t \ll 1$ after averaging over the atomic distribution[1] is

$$\rho_{WW}(t) \approx 1 - \frac{3}{2}\Gamma t + \mathcal{O}((\Gamma t)^2) \approx e^{-\frac{3}{2}\Gamma t}, \tag{5.15}$$

$$\rho_{DD}(t) \approx \frac{1}{8}(\Gamma t)^2 + \mathcal{O}((\Gamma t)^3). \tag{5.16}$$

[1] Note that in the limit $k\sigma \to \infty$, the precise form of the distribution does not matter for the final result. Different distributions only give rise to different corrections for finite $k\sigma$. A Gaussian distribution, for example, leads to exponential corrections in $k\sigma$, while a uniform distribution with width σ gives rise to corrections $\sim 1/(k\sigma)^2$.

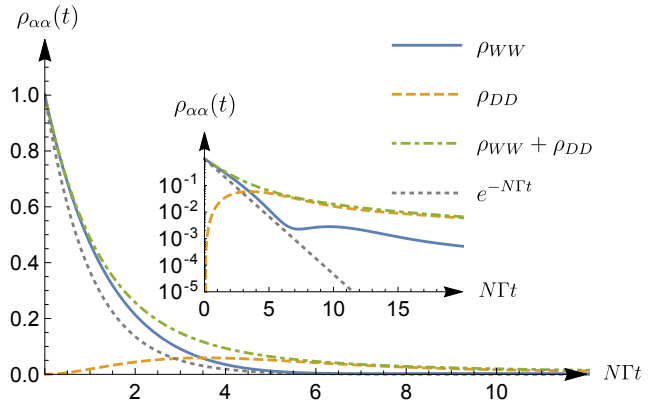

Fig. 5.3.: Time evolution of the population of the bright state (blue solid line), the dark state (orange dashed line) and the total population of excited states (green dash-dotted line) for $N = 2$ atoms coupled to a bidirectional waveguide in the limit $k\sigma \gg 1$. The gray dotted line shows an exponential decay with a collectively enhanced decay rate $N\Gamma = 2N\gamma$ expected in single-photon superradiance which appears for $k\sigma \ll 1$. (Inset): The inset shows the time evolution on a logarithmic scale. For small times $N\Gamma t \ll 1$, the decay can be approximated as $1 - \frac{3}{2}N\Gamma t \approx e^{-\frac{3}{2}N\Gamma t}$. For long times $N\Gamma t \gg 1$, the populations decay much slower compared to an exponential decay with collectively enhanced decay rate $N\Gamma$. The numerical calculations were performed for $k\sigma = 1000$ and the positions of the atoms varied according to a Gaussian density distribution with mean 0 and variance σ^2. The plot shows the average over $M = 1000$ realizations and convergence with respect to M was checked.

Thus, the bright state initially does not decay with a collectively enhanced rate 2Γ, but slightly slower due to the additional decay channel in the backward direction. The full, numerical solution for the time evolution of the bright state, the dark state and the overall population $\rho_{WW} + \rho_{DD}$ of the excited states is shown in Fig. 5.3 alongside with the time evolution for the superradiant case. It can be seen that for longer times, $\Gamma t \gg 1$ the population of the bright state together with the overall population of the excited states decay much slower than expected from a superradiant sample due to the influence of the dipole-dipole interactions.

5.3.2. Chiral Waveguide

Next, we study a chiral waveguide, where each atom only couples to the forward propagating modes of the waveguide and the emission of each atom is directional with rate $\Gamma = \gamma$. The measure of the collective decay is $F_{12} = e^{ik(x_1-x_2)}$ and carries the phase the photon picks up when propagating from one atom to the

other. The exchange coupling parameter reads $J_{12} = \frac{\Gamma}{2i}\text{sign}(x_1 - x_2)e^{ik(x_1-x_2)}$ and is in general complex. Like the correlated decay term, the exchange coupling also carries the phase of the photon due to propagation while the sign term comes from the chiral coupling.

For the chiral system, the definition of the bright (dark) state $|W\rangle$ ($|D\rangle$) coincides with the definition of the superradiant (subradiant) state $|+\rangle$ ($|-\rangle$), see also Fig. 5.2(b). As a matter of fact, neither the precise positions of the atoms nor their relative distance matter for the physics but only their ordering with respect to each other. This is due to the cascaded nature of the system, where the atoms can only emit into the forward direction, which coincides with the direction of propagation of the incoming plane wave. This can also be seen by redefinition of the spin operators to include the propagation phase, i.e., $e^{-ik(x_1-x_2)}\sigma_2^+ \to \sigma_2^+$. The master equation (5.8) for the chiral system expressed in terms of super- and subradiant operators reads

$$\begin{aligned}\partial_t\rho &= -i\left[i\frac{\Gamma}{4}(S_+^\dagger S_- - S_-^\dagger S_+), \rho\right] + \Gamma_+\mathcal{D}[S_+]\rho \\ &= -i\left[i\frac{\Gamma}{4}(S_W^\dagger S_D - S_D^\dagger S_W), \rho\right] + \Gamma_+\mathcal{D}[S_W]\rho\,,\end{aligned} \tag{5.17}$$

where $\Gamma_+ = 2\Gamma = 2\gamma$ and $\Gamma_- = 0$. This means that the super- and subradiant states in this case are perfectly superradiant and subradiant, respectively. In addition, we have assumed $x_1 < x_2$ for simplicity. In contrast to the bidirectional case, the master equation does not decouple into super- and subradiant states but coherently couples them due to the chiral coupling (see also Fig. 5.2). Preparing the system in the bright state (which is equivalent to the superradiant state), the bright state can either decay with enhanced rate $\Gamma_+ = 2\Gamma$ or couple to the dark (subradiant) state that does not decay at all. Since the coupling is a coherent process, the system will decay with Γ_+ in linear order. For later times, the probability to remain in the bright state will no longer follow an exponential decay with enhanced decay rate Γ_+ but should first decay faster due to an additional channel to the dark state with a subsequent revival due to coupling back from the dark state. The time evolution for the population of the bright and dark state of a system initially prepared in the bright state reads

$$\rho_{WW}(t) = \frac{1}{4}e^{-\Gamma t}(\Gamma t - 2)^2\,, \tag{5.18}$$

$$\rho_{DD}(t) = \frac{1}{4}e^{-\Gamma t}(\Gamma t)^2 \tag{5.19}$$

and is shown in Fig. 5.4. As discussed before, for short times, $\Gamma t \ll 1$, the bright state decays as $\rho_{WW}(t) \approx 1 - 2\Gamma t \approx e^{-2\Gamma t}$, while it vanishes for $\Gamma t = 2$, has a

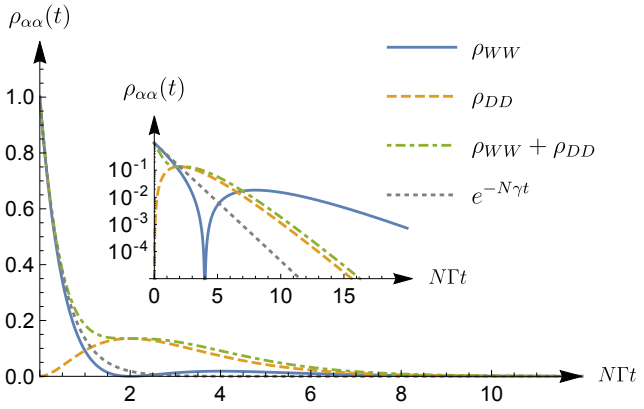

Fig. 5.4.: Time evolution of the population of the bright state (blue solid line), the dark state (orange dashed line) and the total population of the excited states (green dash-dotted line) for $N = 2$ atoms coupled to a chiral waveguide. The gray dotted line shows an exponential decay with collectively enhanced decay rate $N\Gamma$. (Inset): The inset shows a logarithmic plot of the time evolution of the populations. For $N\Gamma t \gg 1$, the decay of the bright state population is slowed down due to the coupling to the dark state.

revival shortly after and then decays again. The rapid decrease of the population of the bright state after some initial time must not be confused with the spontaneous emission of a photon but rather with the transfer of the excitation into the dark state. This can also be seen by looking at the corresponding population of the dark state and the probability to find an excitation in the system, given by $\rho_{WW} + \rho_{DD}$. At $\Gamma t = 2$, all population that has not yet decayed is transferred to the dark state. For longer times, the decay is not exponential with a collectively enhanced decay rate but rather slows down due to the coupling of the bright, superradiant state to the dark, subradiant one.

5.4. N Atoms Coupled to a One-Dimensional Waveguide

After having shown that including the coherent exchange interaction into the dynamics of a two-emitter system can alter the characteristics of the decay dynamics of a single collective excitation, we proceed to a more complex situation where an arbitrary number N of emitters are coupled to a one-dimensional waveguide. At first glance, it is not obvious that we can expect similar dynamics as in the case of only two emitters as we are dealing with many dark states that are also coupled to each other leaving the possibility of an ordinary exponential decay albeit with a

modified decay rate. In the following, we show both numerically and analytically that this is not the case but instead there are oscillations in the population of the bright state with an overall algebraic decay. First, we discuss the case of a chiral coupling, meaning that the photons emitted from the atoms into the waveguide can only propagate in one direction (for example from left to right). Owing to the chiral coupling, it is possible to derive an analytical expression for the population of the bright state. In a second step, we include the emission into the other direction and show that, for an extended sample of atoms, the dynamics reduces to that of a chiral waveguide.

5.4.1. Chiral Waveguide

Since for a chiral setup the atoms can only emit into one direction (say to the right), they form a cascaded open quantum system [108, 109]. The corresponding master equation reads [105, 167, 231]

$$\begin{aligned}\partial_t \rho = &-\frac{i}{\hbar}\left[\frac{\hbar\gamma}{2i}\sum_{j,l}\operatorname{sign}(x_j - x_l)e^{ik(x_j-x_l)}\sigma_j^+\sigma_l^-,\rho\right]\\ &+\gamma\sum_{j,l}e^{ik(x_j-x_l)}\left(\sigma_l^-\rho\sigma_j^+ - \frac{1}{2}\left\{\sigma_j^+\sigma_l^-,\rho\right\}\right),\end{aligned} \tag{5.20}$$

where $\operatorname{sign}(x-y) = \mp 1$ if $x \lessgtr y$ and $\operatorname{sign}(x-y) = 0$ if $x = y$. Again, the specific positions x_i of the atoms do not influence the dynamics as the phase factors could be absorbed into the definition of the operators $\sigma_i^{\pm}$.

Since we are only interested in the dynamics of a single excitation, the time evolution of the system is well described by the effective non-Hermitian Hamiltonian

$$H_{\text{eff}} = \frac{\hbar\gamma}{2i}\sum_{j,l}\left(\operatorname{sign}(x_j - x_l) + 1\right)e^{ik(x_j-x_l)}\sigma_j^+\sigma_l^- \tag{5.21}$$

which includes both the coherent exchange coupling and the collective chiral decay. This description is possible since we do not have any external driving and do not assume initial coherences between the single-excitation subspace and the ground state. In what follows, we focus on the modification of the collectively enhanced decay of the state

$$|W\rangle = \frac{1}{\sqrt{N}}\sum_j e^{ikx_j}\sigma_j^+|G\rangle \tag{5.22}$$

due to the chiral coupling; we consider the quantity

$$P_W(t) = |\langle W| e^{-iH_{\text{eff}}t/\hbar} |W\rangle|^2 , \tag{5.23}$$

which is identical to the population of the state $|W\rangle$. The time evolution of the $|W\rangle$ state can be calculated analytically for the chiral case and the solution reads (see Appendix 5.A for more details)

$$P_W(t) = \frac{1}{N^2} e^{-\gamma t} \left[L_{N-1}^{(1)}(\gamma t) \right]^2 , \tag{5.24}$$

where $L_m^{(n)}(x)$ is the generalized Laguerre polynomial. The decay dynamics of the state $|W\rangle$ is shown in Fig. 5.5.

For short times $\gamma t \ll 1$, one expects the coherent exchange to play no role such that the decay is completely determined by the collective decay given by $N\gamma$. Indeed, for short times $N\gamma t \ll 1$, we find

$$P_W(t \ll 1/N\gamma) \approx 1 - N\gamma t + \mathcal{O}((N\gamma t)^2) \approx e^{-N\gamma t} . \tag{5.25}$$

Equation (5.24) can also be simplified in the limit $N \to \infty$, and we obtain

$$P_W(t) = \frac{\left[J_1(2\sqrt{\kappa t}) \right]^2}{\kappa t} \tag{5.26}$$

where $J_n(x)$ is the Bessel function of the first kind and $\kappa = N\gamma$ with κ fixed for $N \to \infty$. In the limit $N \to \infty$, the initial decay for short times is given by κ, while for long times $\kappa t \gg 1$, we find a characteristic algebraic behavior

$$P_W(\kappa t \gg 1) = \frac{1}{\pi(\kappa t)^{3/2}} \cos^2\left(2\sqrt{\kappa t} - \frac{3\pi}{4} \right) . \tag{5.27}$$

Interestingly, there is no exponential decay for long times but rather an algebraic one with $(\kappa t)^{-3/2}$. This is also shown in the inset of Fig. 5.5. For finite N the algebraic decay is present on intermediate timescales $\kappa t \gg 1$. However, the decay of individual atoms eventually becomes the dominant contribution, which happens on timescales $\kappa t \gg N^2$. This is in stark contrast to the collectively enhanced exponential decay one encounters in single-photon superradiance.

The slowing down of the emission from the bright state can be understood as follows: Also for many atoms, the single-excitation subspace can be divided into a superradiant state and subradiant states. The interaction mediated by photon exchange via the waveguide couples the bright superradiant state to the other subradiant states. Therefore, these subradiant states become populated during the

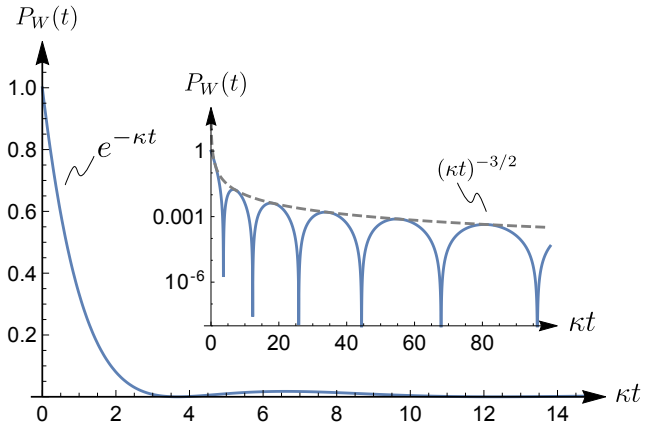

Fig. 5.5.: Decay dynamics of a single collective excitation of a system of N atoms coupled to a chiral waveguide in the limit $N \to \infty$. The collective excitation initially decays exponentially with decay rate κ while for long times the decay is algebraic with $(\kappa t)^{-3/2}$ which is shown in the inset. The dashed line shows the long-time behavior. Note that the dynamics looks qualitatively the same for finite N and $N \gg 1$.

time evolution, and the excitation is less likely to decay if it is "protected" in these subradiant states. This mechanism then provides the slowing down of the decay dynamics.

We want to point out that in the limit of $N \to \infty$, the rotating-wave approximation breaks down and neglecting retardation effects is also no longer justified. As a physically meaningful limit, we require always $\kappa = N\gamma \ll \omega_0$. Typical experiments with ultracold atoms, for example, involve about 10^3 to 10^4 atoms with coupling constant γ in the MHz regime and optical transition frequencies in the THz regime. The above condition is thus well satisfied.

5.4.2. Bidirectional Waveguide: Large and Small Samples

While we have shown above that the dynamics of a single collective excitation in a one-dimensional chiral waveguide undergoes interesting dynamics, we now turn to the case where the waveguide is bidirectional but the positions of the atoms fluctuate with each realization. It turns out that in the limit where the distribution of the positions of the atoms is smooth compared to the wavelength, one recovers the dynamics of a chiral waveguide. In contrast, the case of an ensemble that is confined within a wavelength shows single-photon superradiance with a collectively enhanced exponential decay of the collective excitation.

First, we consider the case where the atoms are randomly distributed along the

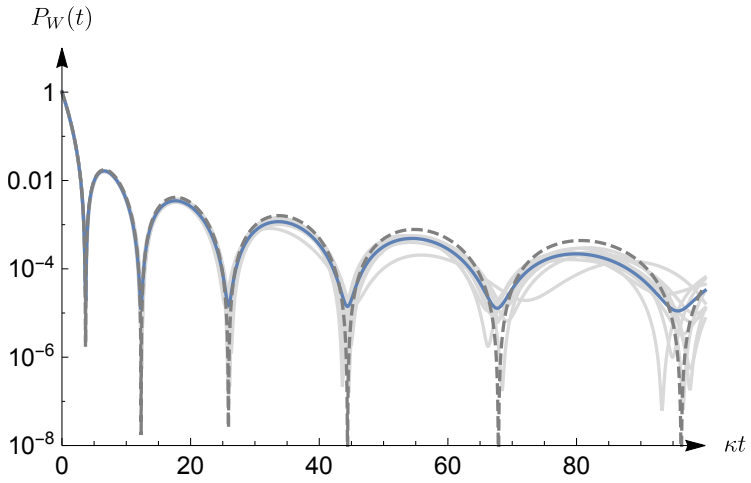

Fig. 5.6.: The blue line shows the time evolution of the bright state in the case of a bidirectional coupling and a normal distribution of the atoms with zero mean and variance σ^2 with $k\sigma = 1000$ for $N = 100$ atoms and averaged over $M = 100$ realizations. The gray dashed line shows the corresponding time evolution for the chiral case for the same number of particles. The light gray curves in the background show trajectories for single realizations.

waveguide with a characteristic length scale σ, which is much larger than the wavelength of the atomic transition, that is $k\sigma \gg 1$. The time evolution of the bright state for $N = 100$ atoms can be determined numerically and is shown in Fig. 5.6. For concreteness, we use a Gaussian density distribution with width σ and $k\sigma = 1000$, the result is averaged over 100 realizations. Interestingly, the dynamics in the bidirectional case are qualitatively similar to the chiral case after averaging over the position of the atoms. Even for single realizations of the system the time evolution of the bidirectional case resembles the dynamics of the chiral system in terms of algebraic decay and period of the oscillations.

To understand this observation, we can go to the continuum limit for $N \to \infty$, and introduce again the effective Hamiltonian

$$H_{\text{eff}} = -i\gamma \int dx\, dy\, \exp(ik|x-y|)\Psi^\dagger(x)\Psi(y) \tag{5.28}$$

with the field creation and annihilation operators $\Psi^\dagger(x)$ and $\Psi(x)$, respectively. Their commutation relations are $[\Psi(x), \Psi^\dagger(y)] = \delta(x-y)$. The time evolution of the state

$$|\psi(t)\rangle = \frac{1}{\sqrt{N}} \int dx\, \psi(x,t)\Psi^\dagger(x)\,|G\rangle \tag{5.29}$$

with the initial condition $\psi(x,0) = e^{ikx}$ is then given by the effective Schrödinger equation

$$\partial_t \psi(x,t) = -\gamma \int dy\, \exp(ik|x-y|)\psi(y,t)n(y)\,, \tag{5.30}$$

where $n(y)$ is the density distribution of the atoms with $\int dx\, n(x) = N$ and a characteristic width σ. In the limit $k\sigma \to \infty$ and assuming that the atoms are uniformly distributed in the interval $[0,\sigma]$, this equation can be solved using the Laplace transform with respect to both t and x. The solution for $\psi(x,t)$ is given by (for more details see Appendix 5.B)

$$\psi(x,t) = e^{ikx} J_0\left(2\sqrt{\kappa t x/\sigma}\right)\,. \tag{5.31}$$

The population of the bright state is then given by

$$P_W(t) = \left|\int_0^1 dx\, J_0\left(2\sqrt{\kappa t x}\right)\right|^2 = \frac{\left[J_1(2\sqrt{\kappa t})\right]^2}{\kappa t}\,. \tag{5.32}$$

Note that this result is actually independent of the precise density distribution as long as $k\sigma \gg 1$ and we have only chosen a uniform distribution to simplify the calculations. Consequently, in the limit $N \to \infty$ and $k\sigma \gg 1$, the dynamics of the bright state exactly reduces to the chiral case given by Eq. (5.26). The same result has already been found in [227, 232], where the authors studied a similar system in three dimensions treating the atoms as point-like emitters and neglecting any polarization effects by taking only the scalar photon propagator. Further, their decay rate is increased by a factor of 2 as they consider an initial excitation of forward- and backward-propagating modes.

The second regime of interested is obtained if we assume that the width of the distribution of the positions is much smaller than the wavelength, i.e., $k\sigma \ll 1$. Then, all atoms are confined within one wavelength; in this limit also $k|x_j - x_l| \ll 1$ for all j and l. Thus, we might expand the sine and cosine term in Eqs. (5.6) and (5.7) leading to $J_{jl} \approx 0$ and $\Gamma_{jl} \approx 2\gamma$, respectively. Clearly, there is no coupling to the dark states while the bright state decays exponentially with a collectively enhanced decay rate $2N\gamma$. The factor of 2 appears because of the bidirectional coupling to the forward and backward-propagating modes. This limit corresponds to the situation Dicke considered originally where the particles are close to each other and single-photon superradiance is restored. This result can also be derived analytically noting that in the limit $k\sigma \ll 1$, the effective Schrödinger equation (5.30) reduces to

$$\partial_t \psi(x,t) = -\gamma \int dy\, n(y)\psi(y,t)\,, \tag{5.33}$$

with the same initial condition. As $\psi(x,t)$ varies only slowly within the range of σ, the differential equation is solved by the function $\psi(x,t) = \psi(x,0)e^{-\kappa t}$. Then, the population of the bright state is given by

$$P_W(t) = \left| \frac{1}{N} \int dx\, n(x) e^{-\kappa t} \right|^2 = e^{-2\kappa t}\,, \tag{5.34}$$

with the collectively enhanced decay rate $\kappa = N\gamma$.

5.5. Conclusion

In this chapter, we have studied the dynamics of a single collective excitation of N two-level atoms influenced by photon-mediated coherent interactions. While one expects a collectively enhanced spontaneous decay if all the atoms are close together (as predicted by Dicke in his seminal work [3]), we demonstrated within an analytical approach for a one-dimensional waveguide that the general long-time behavior is significantly modified due to the coherent exchange of virtual photons. Especially for large numbers of particles this exchange gives rise to a characteristic algebraic behavior $\sim 1/(\kappa t)^{3/2}$. The slowed down decay can be explained by the additional coupling of the superradiant bright state to subradiant states with different, but slower decay rates. While this result is rigorous for a chiral waveguide, we demonstrated that this behavior also emerges in a bidirectional waveguide if the atoms are randomly distributed on a length scale larger than the optical wavelength of the transition. This opens up the possibility to study the peculiar influence of the virtual exchange of photons in systems without requiring a strictly chiral coupling which can be implemented much more easily. Examples of potential applications include, but are not limited to, atoms coupled to optical nanofibers or waveguides [89, 92, 106], quantum dots coupled to photonic crystal waveguides or nanostructures [94, 233], vacancy centers in crystals [195], superconducting qubits [95, 192, 234] and also molecular chains [235]. Even though we focused our analysis on a purely one-dimensional system, we expect similar behavior to also appear in three-dimensional setups in free space where the atoms are coupled to a single focused light mode. Our observations are thus relevant for a broad range of systems with collective excitations as for example quantum memories. In particular, it is of fundamental importance for understanding Rydberg superatoms in free space which have recently attracted a lot of experimental attention [177] (see also Chapter 3). We expect that the influence of this coherent exchange interaction is also relevant for the experimental observation of an oscillatory behavior of the decay rate of such Rydberg superatoms [226, 236], which we also discuss in Chapter 6 in more detail.

Appendix

5.A. Analytical Solution for $P_W(t)$ for N Atoms

In this section, we present the derivation of Eq. (5.24) using the effective (non-Hermitian) Hamiltonian

$$H_{\text{eff}} = \frac{\hbar\gamma}{2i} \sum_{j,l} \left(\text{sign}(x_j - x_l) + 1\right) e^{ik(x_j - x_l)} \sigma_j^+ \sigma_l^- \,. \tag{5.35}$$

Even though the emitter system is described by a master equation, in the absence of driving and assuming the system is initially prepared in the bright state $|W\rangle = \frac{1}{\sqrt{N}} \sum_j e^{ikx_j} \sigma_j^+ |G\rangle$, it is possible to describe the time evolution of $|W\rangle$ with the effective Hamiltonian above.

To simplify the calculations, we absorb all phases into the operators, that is $\sigma_j^+ \to e^{-ikx_j} \sigma_j^+$ and similarly for σ_j^-. The effective Hamiltonian can then be written as

$$H_{\text{eff}} = \frac{\hbar\gamma}{2i} \sum_{j,l} \left(\text{sign}(x_j - x_l) + 1\right) \sigma_j^+ \sigma_l^- \,. \tag{5.36}$$

Note that this transformation is not useful in the case of a bidirectional system and reflects the fact that for a chiral system only the order of the emitters is important but not their relative distance. In the following, we will assume that $x_j < x_l$ if $j < l$.

In the basis $\{|j\rangle = \sigma_j^+ |G\rangle \,,\, j = 1, \ldots, N\}$, we can represent the Hamiltonian in Eq. (5.36) as the sum of the $N \times N$ identity matrix I and a nilpotent matrix M_N for which $(M_N)^n = 0$, $n \geq N$:

$$H_{\text{eff}} = -\frac{i\hbar\gamma}{2}(I + 2M_N) \,, \tag{5.37}$$

where M_N is a strictly lower triangular matrix whose nonzero entries are all 1.

The time evolution of the bright state is then given by

$$|\psi(t)\rangle = e^{-iH_{\text{eff}}t/\hbar}\,|W\rangle = e^{-\frac{\gamma t}{2}I}\sum_{n=0}^{N-1}\frac{(-\gamma t)^n}{n!}(M_N)^n\,|W\rangle\ . \tag{5.38}$$

The probability to remain in the bright state as a function of time can be written as

$$P_W(t) = e^{-\gamma t}\left|\sum_{n=0}^{N-1}\frac{(-\gamma t)^n}{n!}\,\langle W|\,(M_N)^n\,|W\rangle\right|^2\ . \tag{5.39}$$

In the basis given above, $|W\rangle$ is represented by the vector

$$|W\rangle = \frac{1}{\sqrt{N}}\begin{pmatrix}1\\ \vdots\\ 1\end{pmatrix} \tag{5.40}$$

such that the matrix element $\langle W|\,(M_N)^n\,|W\rangle$ can be calculated as

$$\begin{aligned}\langle W|\,(M_N)^n\,|W\rangle &= \sum_{j_1<j_2<\cdots<j_{n+1}}\frac{1}{N}\\ &= \frac{1}{N}\frac{N(N-1)\cdots(N-n)}{(n+1)!}\\ &= \frac{1}{N}\binom{N}{n+1} = \frac{1}{N}\binom{N}{N-(n+1)}\ .\end{aligned} \tag{5.41}$$

Finally, the time evolution of the occupation of the bright state reads

$$\begin{aligned}P_W(t) &= |\,\langle W|\,e^{-iH_{\text{eff}}t/\hbar}\,|W\rangle\,|^2\\ &= \left|\sum_{n=0}^{N-1}\frac{(-\gamma t)^n}{n!}\frac{1}{N}\binom{N}{N-(n+1)}\right|^2 e^{-\gamma t}\\ &= \left[\frac{1}{N}L_{N-1}^{(1)}(\gamma t)\right]^2 e^{-\gamma t}\end{aligned} \tag{5.42}$$

where $L_n^{(\alpha)}(x)$ is the generalized Laguerre polynomial.

In the limit $N\to\infty$, one can approximate the Laguerre polynomial by a Bessel function as

$$L_N^{(\alpha)}(x) \approx \sqrt{N^\alpha}\frac{J_\alpha(2\sqrt{Nx})}{\sqrt{x^\alpha}}e^{\frac{x}{2}} \tag{5.43}$$

such that

$$P_W(t) = \frac{1}{N^2} e^{-\gamma t} \left[L_{N-1}^{(1)}(\gamma t) \right]^2 \approx \frac{[J_1(2\sqrt{\kappa t})]^2}{\kappa t} , \tag{5.44}$$

with $\kappa = N\gamma$ fixed. For long times $\kappa t \gg 1$, the asymptotic behaviour of the Bessel function leads to

$$P_W(\kappa t \gg 1) = \frac{1}{\pi(\kappa t)^{3/2}} \cos^2 \left(2\sqrt{\kappa t} - \frac{3\pi}{4} \right) , \tag{5.45}$$

which gives the characteristic algebraic behaviour $\sim (\kappa t)^{-3/2}$.

5.B. Continuum Limit in the Bidirectional Case

Here, we show that the time evolution of the bright state in the bidirectional waveguide reduces to the time evolution in the chiral case in the limit where $N \to \infty$ and $k\sigma \to \infty$. In contrast to the numerical calculations mentioned in Section 5.4.2 where we used a Gaussian density distribution, here we assume the atoms to be uniformly distributed in an interval $[0, \sigma]$ along the waveguide such that the analytical calculations simplify. The final result, however, does not depend on the details of the distribution as long as $k\sigma \gg 1$.

In the limit $N \to \infty$ and σ finite, we can go over to the continuum limit by keeping $\kappa = N\gamma$ fixed. The effective Hamiltonian in this case reads

$$H = -i\gamma \int dx\, dy\, \exp(ik|x-y|) \Psi^\dagger(x) \Psi(y) \tag{5.46}$$

with the field creation and annihilation operators $\Psi^\dagger(x)$ and $\Psi(x)$, respectively. The have the commutation relations $[\Psi(x), \Psi^\dagger(y)] = \delta(x-y)$. The initial bright state is given by

$$|W\rangle = \frac{1}{\sqrt{N}} \int dx\, e^{ikx} \Psi^\dagger(x) |G\rangle \ . \tag{5.47}$$

In order to calculate the time evolution for the state

$$|\psi(t)\rangle = \frac{1}{\sqrt{N}} \int dx\, \psi(x,t) \Psi^\dagger(x) |G\rangle \ , \tag{5.48}$$

we have to solve the effective Schrödinger equation

$$i\partial_t \psi(x,t) = -i\frac{\kappa}{\sigma} \int_0^\sigma dy\, \exp(ik|x-y|) \psi(y,t) \, . \tag{5.49}$$

In the following, we rescale all lengths by σ and introduce the dimensionless quantity $q = k\sigma$. Further, we rescale all times by the collective rate κ, such that $t \to \tau/\kappa$ with dimensionless τ. Then, the dimensionless Schrödinger equation reads

$$\partial_\tau \psi(x,\tau) = -\int_0^1 dy\, \exp(iq|x-y|)\psi(y,\tau) \tag{5.50}$$

with the initial condition $\psi(x,0) = e^{ikx}$.

To solve this differential equation, we first perform a Laplace transform from the variable τ to the variable s,

$$\begin{aligned} s\,\hat{\psi}(x,s) - \psi(x,0) &= -\int_0^1 dy\, e^{iq|x-y|}\hat{\psi}(y,s) \\ &= -\int_0^x dy\, e^{iq(x-y)}\hat{\psi}(y,s) - \int_x^1 dy\, e^{-iq(x-y)}\hat{\psi}(y,s) \\ &= -\int_0^x dy\, e^{iq(x-y)}\hat{\psi}(y,s) + \int_0^x dy\, e^{-iq(x-y)}\hat{\psi}(y,s) \\ &\quad -\int_0^1 dy\, e^{-iq(x-y)}\hat{\psi}(y,s)\,. \end{aligned} \tag{5.51}$$

As we want to get rid of fast oscillating terms in the end, we make the ansatz $\hat{\psi}(x,s) = e^{iqx}\hat{\phi}(x,s)$, where $\hat{\phi}(x,s)$ is assumed to be a slowly varying function of x. It then follows

$$\begin{aligned} s\,\hat{\phi}(x,s) - 1 &= -\int_0^x dy\, \hat{\phi}(y,s) + \int_0^x dy\, e^{-2iq(x-y)}\hat{\phi}(y,s) \\ &\quad - e^{-2iqx}\int_0^1 dy\, e^{2iqy}\hat{\phi}(y,s)\,. \end{aligned} \tag{5.52}$$

The last integral in this expression vanishes in the limit $q \to \infty$ and we can drop it in the following. Next, we perform a Laplace transform from the variable x to u which leads to

$$s\hat{\hat{\phi}}(u,s) - \frac{1}{u} = -\frac{\hat{\hat{\phi}}(u,s)}{u} + \frac{\hat{\hat{\phi}}(u,s)}{u+2iq}\,, \tag{5.53}$$

where we have made use of the convolution theorem for the Laplace transform. The integral equation is then reduced to an algebraic one whose solution reads

$$\hat{\hat{\phi}}(u,s) = \frac{u+2iq}{su^2 + 2iq(1+su)}\,. \tag{5.54}$$

Now we can take the limit $q \to \infty$ and are left with

$$\hat{\tilde{\phi}}(u,s) \approx \frac{1}{su+1}\,. \tag{5.55}$$

The inverse Laplace transform of this expression back to the variables x and τ is given by

$$\phi(x,\tau) = J_0(2\sqrt{x\tau}) \tag{5.56}$$

with the Bessel function of the first kind $J_0(x)$. Thus, the full solution for the wavefunction reads

$$\psi(x,\tau) = e^{iqx} J_0(2\sqrt{x\tau})\,. \tag{5.57}$$

The time evolution of the bright state is thus given by

$$P_W(t) = \left| \int_0^1 dx\, J_0(2\sqrt{x\tau}) \right|^2 = \left| \frac{J_1(2\sqrt{\tau})}{\sqrt{\tau}} \right|^2 = \frac{\left[J_1(2\sqrt{\kappa t})\right]^2}{\kappa t}\,, \tag{5.58}$$

where $J_1(x)$ is the Bessel function of the first kind. This is the same result as in the chiral case in the limit $N \to \infty$.

The probability of finding an excitation in the system at time t is given by

$$P(t) = \int_0^1 dx\, \left[J_0(2\sqrt{x\tau})\right]^2 = \left[J_0(2\sqrt{\kappa t})\right]^2 + \left[J_1(2\sqrt{\kappa t})\right]^2 \tag{5.59}$$

and is shown in Fig. 5.7 as the green solid line. The initial dynamics resembles the exponential decay for the state $|W\rangle$ with rate κ, while the long-time behaviour for $\kappa t \gg 1$ is again algebraic albeit with an even slower decay $\sim 1/\kappa t$ compared to the $1/(\kappa t)^{3/2}$ scaling for the collective excitation. This comes from the fact that the probability $P(t)$ also includes the dark states to which the initial collective excitation is non-radiatively transferred.

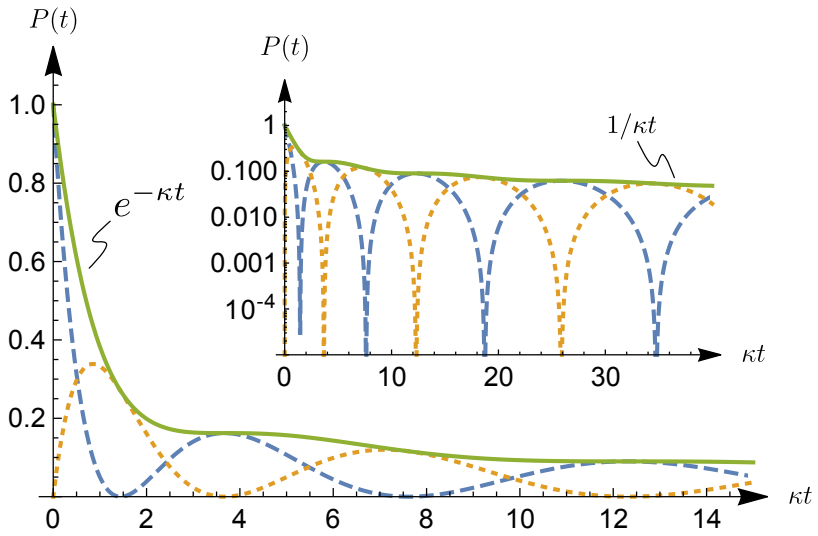

Fig. 5.7.: The green solid line shows the probability $P(t)$ to have an excitation in a bidirectional waveguide with initial state $|W\rangle$ given by Eq. (5.59). Initially, the excitation decays exponentially in agreement with the result obtained for the decay of the collective excitation. In the long time limit, the probability decays algebraically with $1/\kappa t$. The blue dashed line shows the contribution coming from $J_0(2\sqrt{\kappa t})^2$ and the orange dotted line the contribution from $J_1(2\sqrt{\kappa t})^2$. The inset shows the same function for longer times with a log scale on the y-axis.

6

Observation of Collective Decay Dynamics of a Single Rydberg Superatom

In this chapter, we discuss the observation of collective decay dynamics of a single Rydberg superatom [236]. The experimental setup is similar to the one in Chapter 3 but now the intensity of the light emitted after the pulse has ended is studied in more detail and with higher accuracy. The experimental results show that the decay rate of the outgoing intensity changes depending on the internal state of the Rydberg superatom at the end of the pulse. This is a consequence of the internal dynamics due to the resonant dipole-dipole interaction between the individual atoms. This effect can be modelled by adding an additional state to the effective three-level model in Chapter 3 to which the bright state can coherently couple.

In the following, the focus will be on the theoretical contributions but relevant experimental details are also discussed in view of a more coherent story. More details on the experiment can be found in [236].

6.1. Introduction

The collective interaction between an ensemble of emitters and photons is a fundamental topic of quantum optics, which has been extensively studied for over 60 years [3]. Collective enhancement of the emission, known as superradiance, has been observed in a variety of physical systems ranging from atoms [5] and ions [38] over molecules [35], artificial atoms coupled to microwave waveguides

[192], and solid-state systems [12, 13], to ensembles of nuclei [6]. Suppression of emission is more elusive because excitation fields typically do not couple to subradiant states, and was only recently observed for ensembles of more than two emitters [39, 40]. Here, we investigate the collective emission of a single photon from a Rydberg superatom [67] and show that the experimentally observed decay rate depends on the initial state preparation by a few-photon driving field [177]. This effect can be attributed to a coherent population redistribution between collective super- and subradiant states due to coherent excitation exchange between the individual emitters inside the superatom [216, 226] (see also Chapters 4 and 5).

It is already known that a collectively excited ensemble features modifications to the rate and spatial distribution of its spontaneous emission [217, 237–239], and coherent exchange of photons between individual emitters in an ensemble results in a collective Lamb shift [2, 6, 11, 18, 202, 218, 240]. These phenomena can be understood in a semi-classical approach as dipole-dipole interaction between individual emitters [75, 83, 169, 226, 241–243], or quantum-mechanically by treating the emitters as an interacting spin ensemble coupled to an optical mode [167, 174, 216, 244]. The latter approach has been used to study the propagation of quantized light in one-dimensional waveguides, while the semi-classical approach enables investigation of large, weakly driven ensembles in two or three dimensions. In the single-excitation sector and as long as saturation of the medium can be neglected, the two approaches lead to equivalent results [227, 245]. There has recently been strong interest in structured emitter arrays for tailoring optical properties with unprecedented control [75, 83, 85, 246], for example exploiting subradiance to enhance photon storage fidelities [25, 247]. Striking experimental demonstrations of this concept are realizations of highly reflective monolayers with ultracold atoms in optical lattices [84] and solid state systems [248, 249].

6.2. Experimental Setup and Observation

In the experimental setup, an ensemble of ultracold ^{87}Rb atoms is optically trapped and confined such that the excitation volume created by the two counterpropagating lasers is smaller than the blockade volume (see Fig. 6.1)[1]. Each atom is driven by a probe field with variable photon rate $\mathcal{R}_p$ which couples the ground state $|g\rangle = \left|5S_{1/2},\ F = 2,\ m_F = 2\right\rangle$ to the intermediate state $|e\rangle = \left|5P_{1/2},\ F = 3,\ m_F = 3\right\rangle$ with Rabi frequency $g_0\sqrt{\mathcal{R}_p}$, where g_0 is the single-photon-single-atom coupling strength. A strong control field with Rabi frequency Ω_c then couples the interme-

[1] The experimental setup is similar to the one presented in Chapter 3 but will be presented again for the sake of completeness and clarity.

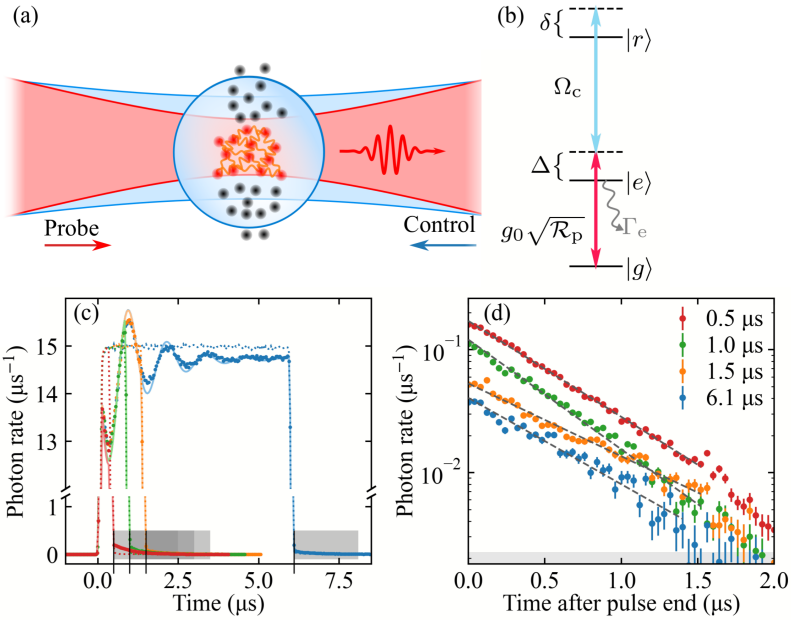

Fig. 6.1.: (a) Sketch of the experimental implementation and (b) single-atom level scheme to create a single Rydberg superatom. (c) Probe pulses of different duration measured on single-photon counters with (solid circles) and without atoms (dashed lines). The solid lines show the solution to the master equation for the model system shown in Fig. 6.3. The shaded areas indicate the parts of the pulses our analysis focuses on. (d) Logarithmic plot of the difference between the signal with and without atoms detected after the driving pulse has ended for different pulse lengths. The time $t = 0$ where the probe field is turned off is extracted from fits to the probe pulse measured without atoms. The dashed lines are fits to the data points as described in the text. The gray area shows the level below which the data are excluded from the fits. The error-bars are standard error of the mean. Figure taken and adapted from [236].

diate state to the Rydberg state $|r\rangle = |111S_{1/2},\, J = 1/2,\, m_J = 1/2\rangle$. For large detuning $\Delta \gg \Gamma_e, \Omega$, the intermediate state $|e\rangle$ can be adiabatically eliminated turning each atom into a two-level system given by $|g\rangle$ and $|r\rangle$ with effective Rabi frequency $\Omega = \sqrt{\mathcal{R}_p} g_0 \Omega_c/(2\Delta)$ and Raman decay $\Gamma = \Gamma_e \left(\Omega_c/2\Delta\right)^2$.

Due to the Rydberg blockade, the whole ensemble can only support a single excitation and its dynamics can be explained in terms of a two-level superatom with ground state $|G\rangle = |g_1, \ldots, g_N\rangle$ and a single excited bright state $|W\rangle = \frac{1}{\sqrt{N}} \sum_{j=1}^{N} |g_1, \ldots, r_j, \ldots, g_N\rangle$ with $N \sim 5000$ atoms overlapping with the probe beam in the experiment. The microscopic description of the bright state in terms of the atomic distribution and the mode wave function was discussed in Chapter 3.

The ground state and the bright state are coupled by the collectively enhanced Rabi frequency $\Omega_{\mathrm{col}} = 2\sqrt{\kappa \mathcal{R}_p}$, where $\sqrt{\kappa} = \sqrt{N} g_0 \Omega_c/(4\Delta)$ is the collective single-photon coupling.

In order to study the decay dynamics, the superatom is first driven by a Tukey-shaped probe pulse of varying length and the light emitted into the forward direction is then measured with very high accuracy after extinguishing the probe pulse on a time scale shorter than the enhanced emission rate κ, while the control field remains on. Analyzing the photon statistics of the forward-emitted light after the driving pulse, one obtains for the background-corrected second-order correlation function $g^{(2)}(\tau = 0) < 0.1$ confirming that the superatom emits one photon at maximum. The presence of a single excitation in the superatom is further confirmed by measuring the ion-counting statistics of the field-ionized ensemble at the end of the probe pulse.

Figure 6.1(d) shows the experimentally observed probe light after the probe pulse has been turned off for four different pulse lengths (shown in Fig. 6.1(c)). Clearly, the exponential decay shows different decay rates depending on how long the superatom has been driven and thus on the internal state of the superatom at the end of the pulse.

The dependence of the decay rate on the parameters of the superatom is systematically studied by repeating the experiment with varying probe pulse lengths for a range of different parameter sets, changing the single-photon coupling strength κ and the probe photon rate $\mathcal{R}_{\mathrm{p}}$. The photon decay rate is quantified assuming an initial exponential decay and fitting the measured photon rates with $I_0 e^{-\gamma t}$ to extract both the photon flux I_0 (measured in photons/μs emitted back into the probe mode) and the decay rate in forward emission γ. The exponential fit takes into account data points up to $1.5\,\mu$s after the pulse ends or up to the first datapoint below the threshold where the uncertainty becomes similar to the absolute value (see [236] for more details). The area used for fitting is illustrated by the shaded region in Fig. 6.1(c).

Figure 6.2 shows the observed decay rates as a function of the pulse length for three different values of the intermediate-state detuning and a probe photon rate $\mathcal{R}_{\mathrm{p}} = 15.0\,\mu\mathrm{s}^{-1}$. Changing Δ varies both the coupling strength κ between the ground state $|G\rangle$ and the bright state $|W\rangle$ as well as the Raman decay Γ as $\kappa, \Gamma \sim 1/\Delta^2$. The initial amplitudes in Fig. 6.2 reflect the collective Rabi oscillations of the superatom during the probe pulse and become slower for increasing Δ, as $\Omega \sim 1/\Delta$. The initial amplitude of the forward emission also decreases over time due to spontaneous Raman decay and dephasing of the collective state. More surprisingly, the decay rates (shown in Fig. 6.2(a)-(c)) depend on the probe pulse length and oscillate out of phase with the oscillations of the initial amplitude. The overall

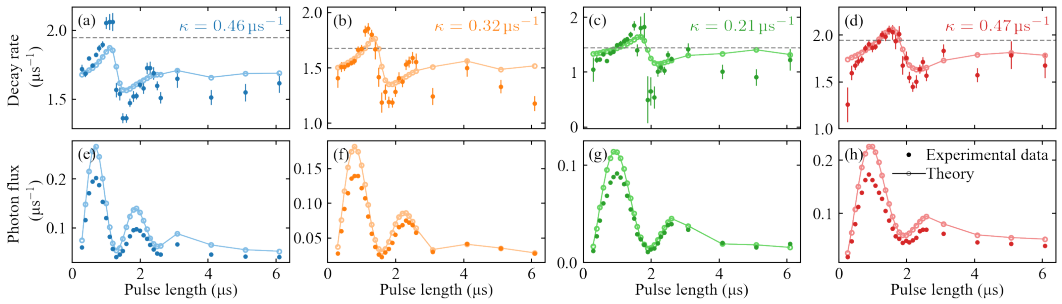

Fig. 6.2.: (a,b,c,d) Observed decay rates and (e,f,g,h) initial amplitudes as a function of pulse length extracted from exponential fits to data as shown in Fig. 6.1 (c,d) for different values of the single-photon coupling strength κ and photon rate $\mathcal{R}_\mathrm{p}$. For figures (a,b,c,e,f,g) $\mathcal{R}_\mathrm{p} = 15.0\,\mu\mathrm{s}^{-1}$, and for (d,h) $\mathcal{R}_\mathrm{p} = 6.7\,\mu\mathrm{s}^{-1}$. In addition to experimental data (dark circles), we show the theoretical results of the extented superatom model discussed in the text and shown in Fig. 6.3 (light diamonds), as well as the constant decay rate of the simple superatom model without internal coherent dynamics (dashed lines). The errorbars shown on the rates are one standard deviation confidence interval of the exponential fits to the data. Figure taken and adapted from [236].

magnitude of the decay rates decreases with higher Δ, which is expected as a higher Δ leads to a reduction of κ and Γ. In the limit of long pulses, the decay rate approaches a constant value since the superatom reaches a steady state due to dephasing.

The effect of changing Ω is investigated in Fig. 6.2(d,h), with a fixed $\Delta = 2\pi \times 100\mathrm{MHz}$ but a lower photon rate, $\mathcal{R}_\mathrm{p} = 6.7\,\mu\mathrm{s}^{-1}$. The reduction of the photon rate leads to a slower oscillation of the decay rate and the initial amplitude while the range of decay rates remains the same. This set of parameters is comparable (in terms of Ω) to the parameters used in Fig. 6.2(b,f) such that the oscillation periods in both cases are similar. Since, however, the coupling strength and the Raman decay are larger, the values of the decay rate increase.

Summarizing, the experimental data convincingly shows that the initial decay rate of the light emitted in the forward direction depends on the internal state of the superatom at the end of the probe pulse. The initial state is in general a superposition of the bright state and subradiant states. The oscillatory behaviour of the decay rates with the pulse length indicates that the internal dynamics are based on a coherent process.

6.3. Effective Model with Coherent Coupling

In the following we will discuss how the experimental observations can be explained in terms of a microscopic theory. First, it is important to note that the varying decay rate of the probe light after turning off the pulse cannot be explained by a fully incoherent dynamics of the superatom. In this case the decay rate would be constant and would be given by the sum of the collective emission rate κ, the Raman decay rate Γ, and a dephasing rate γ_D indicated by the dashed lines in Fig. 6.2. It is thus necessary to include an additional coherent coupling which is provided by the resonant dipole-dipole interaction between the atoms.

As was shown in Chapter 2, the internal dynamics of the Rydberg superatom can be microscopically described in terms of atoms coupled to a one-dimensional chiral waveguide whose dynamics are described in terms of the master equation

$$\partial_t \rho = -\frac{i}{\hbar}[H_0(t) + H_\mathrm{dip}, \rho] + (\kappa + \Gamma)\mathcal{D}[\sigma_\mathrm{GW}]\rho\,, \tag{6.1}$$

where $\mathcal{D}[\sigma]\rho = \sigma\rho\sigma^\dagger - \{\sigma^\dagger\sigma, \rho\}/2$ and $\sigma_\mathrm{GW} = |G\rangle\langle W|$. The coherent dynamics is given by the driving Hamiltonian

$$H_0(t) = 2\hbar\sqrt{\kappa\mathcal{R}_\mathrm{p}}(\sigma_\mathrm{GW} + \sigma_\mathrm{GW}^\dagger)\,, \tag{6.2}$$

where $\mathcal{R}_\mathrm{p}$ is the (time-dependent) photon rate of the probe field. The resonant dipole-dipole interaction is given by the Hamiltonian

$$H_\mathrm{dip} = \frac{\hbar\kappa}{2iN}\sum_{j,l}\mathrm{sign}(x_j - x_l)\sigma_\mathrm{Gj}^\dagger\sigma_\mathrm{Gl}\,, \tag{6.3}$$

where $|l\rangle = |g_1, \ldots, r_l, \ldots, g_N\rangle$. This Hamiltonian can be diagonalized analytically (see Chapter 4) and the bright state can be expressed in terms of only a few of these eigenstates, that is $|W\rangle \approx \sum_\alpha 2i/(\pi\alpha)\,|\alpha\rangle$, where $|\alpha\rangle$ is the eigenstate of H_dip and $-N \leq \alpha < N$ is an odd integer.

Likewise, one can introduce a different set of operators [17, 250]

$$S_m^\dagger = \frac{1}{\sqrt{N}}\sum_{j=0}^{N-1} e^{i\frac{2\pi m}{N}j}\sigma_\mathrm{Gj}^\dagger\,, \tag{6.4}$$

where $-N/2 \leq m < N/2$ is an integer. The states $|\psi_m\rangle = S_m^\dagger|G\rangle$ are orthonormal with $\langle\psi_m|\psi_n\rangle = \delta_{mn}$ and build a basis of the single-excitation subspace. The bright state in this basis is $|W\rangle = |\psi_0\rangle$ while the dark states are build from states with $m \neq 0$. It is important to note that this set of states is only one way to

characterize the dark states but one that will prove useful in what follows. The Hamiltonian (6.3) can be expressed in terms of the operators given in Eq. (6.4) as

$$H_{\mathrm{dip}} = -\frac{\hbar\kappa}{2N}\sum_{m\neq 0}\cot\left(\frac{\pi m}{N}\right)S_m^\dagger S_m + \frac{\hbar\kappa}{2N}\sum_{m\neq 0}\left[i+\cot\left(\frac{\pi m}{N}\right)\right]S_0^\dagger S_m + \mathrm{h.c.}\,. \tag{6.5}$$

The first term accounts for level shifts of the dark states and the second term describes a coupling of the bright state to the dark states. Note that in contrast to the states $|\alpha\rangle$ introduced in Chapter 4, the Hamiltonian does not take a diagonal form but describes a coupling of the bright state to the dark states which themselves are not coupled to each other (see Fig. 6.3(a)). This allows to identify those dark states to which the bright state couples most strongly. The level shifts, for example, are strongest for small m/N and are given by $\hbar\delta_m \approx -\hbar\kappa/2\pi m$ while they vanish for $|m| \sim N/2$ and $N \gg 1$. On the other hand, the couplings between the bright and the dark states are also strongest for small m/N and read $\hbar\kappa_m \approx \hbar\kappa/2\pi m$ and reduce to $i\hbar\kappa/2N$ for $|m| \sim N/2$. In the limit $N \gg 1$, these couplings are negligible compared to those for $m \ll N$. Numerically solving the time evolution of an initial excitation in $|W\rangle$ with the Hamiltonian (6.5) also confirms that only those dark states with small m acquire a significant population.

This result suggests that we can extend the effective model used in Chapter 3 to account for internal coherent dynamics by coherently coupling the bright state $|W\rangle$ to one of the dark states, called $|C\rangle$, which then again can dephase into the manifold of weakly coupled dark states, represented by $|D\rangle$, with rate γ_{D} [70] (see also Fig. 6.3(b)). The full master equation of the effective four-level model then reads

$$\begin{aligned}\partial_t\rho &= -\frac{i}{\hbar}[H_0(t)+H_C,\rho] + (\kappa+\Gamma)\mathcal{D}[\sigma_{\mathrm{GW}}]\rho + \gamma_{\mathrm{D}}\mathcal{D}[\sigma_{\mathrm{DW}}]\rho + \gamma_D\mathcal{D}[\sigma_{\mathrm{DC}}]\rho \\ &\quad + \Gamma\mathcal{D}[\sigma_{\mathrm{GC}}]\rho + \Gamma\mathcal{D}[\sigma_{\mathrm{GD}}]\rho \\ &\equiv \mathcal{L}(t)\rho\,,\end{aligned} \tag{6.6}$$

with $H_C = \hbar\eta(\sigma_{\mathrm{CW}}^\dagger + \sigma_{\mathrm{CW}})$. Here, η denotes the coupling between the bright state $|W\rangle$ and the coherent dark state $|C\rangle$ and from the above analysis one estimates that η is on the order of κ. For the extended effective model, however, it is left as a free parameter, which will serve as a fit parameter when comparing the results of our model to the experimental data.

Before directly comparing with the experiment, we discuss how a variable decay rate arises within the extended model. To this end, we consider the system to be driven by a constant pulse α for some time τ. After the pulse has ended, the time

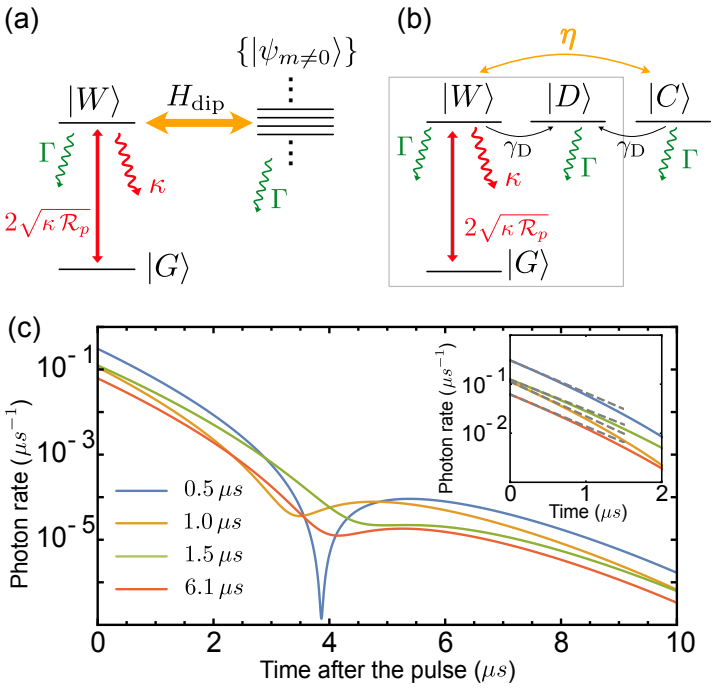

Fig. 6.3.: (a) Level scheme of the ground state and the single-excitation subspace for the internal dynamics of the Rydberg superatom. The probe field couples the collective ground state $|G\rangle$ to the collective bright state $|W\rangle$ with an effective coupling strength $\sqrt{\kappa\mathcal{R}_{\rm p}}$. The bright state decays into the forward direction with rate κ and into other modes with rate Γ. The resonant dipole-dipole interaction couples the bright state to the dark states which are subradiant and decay with single-atom decay rate Γ. (b) Effective four-level model including internal coherent dynamics of the superatom. The bright state $|W\rangle$ dephases with rate $\gamma_{\rm D}$ into a dark state $|D\rangle$ which does not couple to the light. In addition, $|W\rangle$ coherently couples to a single subradiant state $|C\rangle$. This new subradiant state also dephases to $|D\rangle$. All excited states decay via Raman decay Γ to the ground state. (c) Collective emission into the forward direction after the driving pulse has ended as predicted by this model for different pulse length calculated for the same parameters as found for the data shown in Fig. 6.1(c, d). The emission into forward direction shows clear signs of nonexponential decay for longer times. (Inset) Initial emission after the driving pulse for short times shows exponential behavior with varying decay rate but already deviates from pure exponential decay for intermediate times.

evolution is given by Eq. (6.6) with $H_0(t) = 0$. Linearizing the time evolution, one can define an instantaneous decay rate via

$$\frac{\rho(\tau + dt) - \rho(\tau)}{dt} = \mathcal{L}\rho(\tau)\,. \tag{6.7}$$

The decay rate of the intensity is obtained by projecting this equation onto the state $|W\rangle$ to get the component ρ_{WW} which is directly proportional to the intensity after the pulse. Thus, one has

$$\begin{aligned}\frac{\rho_{\mathrm{WW}}(\tau + dt) - \rho_{\mathrm{WW}}(\tau)}{dt} &= \langle W|\,\mathcal{L}\rho(\tau)\,|W\rangle \\ &= -(\gamma_D + \Gamma + \kappa)\rho_{\mathrm{WW}}(\tau) - i\eta(\rho_{\mathrm{CW}}(\tau) - \rho_{\mathrm{WC}}(\tau))\,.\end{aligned} \tag{6.8}$$

This can be brought into a more convenient form given by

$$\begin{aligned}\rho_{\mathrm{WW}}(\tau + dt) &= \rho_{\mathrm{WW}}(\tau)\left[1 - \left(\gamma_D + \Gamma + \kappa + i\eta\frac{\rho_{\mathrm{CW}}(\tau) - \rho_{\mathrm{WC}}(\tau)}{\rho_{\mathrm{WW}}(\tau)}\right)dt\right] \\ &= \rho_{\mathrm{WW}}(\tau)(1 - \gamma_{\mathrm{eff}}dt)\,,\end{aligned} \tag{6.9}$$

where γ_{eff} is the effective decay rate in the presence of the coherent coupling right after the pulse ends. The effective decay rate depends on the coherence between the bright state and the coherently coupled dark state and therefore on the internal state of the superatom at the end of the driving pulse.

In general, this can be calculated numerically by solving the full master equation during the driving and then obtaining the values for $\rho_{\mathrm{CW}}(\tau)$, $\rho_{\mathrm{WC}}(\tau)$, and $\rho_{\mathrm{WW}}(\tau)$. However, we might also obtain analytical results and discuss the effective decay rate in the case where the system is first driven to steady state and then the driving is turned off. The initial effective decay rate then reads

$$\gamma_{\mathrm{eff}}^{\mathrm{ss}} = \gamma_{\mathrm{D}} + \Gamma + \kappa + \frac{4\eta^2(\kappa + 2(\Gamma + \gamma_{\mathrm{D}}))}{(\gamma_{\mathrm{D}} + \Gamma)(\kappa + 2(\Gamma + \gamma_D)) + 4\kappa\mathcal{R}_{\mathrm{p}}} \tag{6.10}$$

and is larger than the sum of the individual decay or dephasing rates. This comes from the fact that the bright state can also transfer population into the dark state which results in a population loss that can be accounted for as an increased decay rate.

The result given in Eq. (6.9) is only valid for short times when the dynamics is approximately exponential. In Chapter 5, we have already seen that the bright state features interesting nonexponential decay dynamics. This can also be seen

when solving the master equation numerically and is shown in Fig. 6.3c) for the experimental parameters used in Fig. 6.1. The forward emission becomes nonexponential and features a drop and revival which are more pronounced for shorter pulses. This can be understood as shelving the excitation in the coherently coupled dark state $|C\rangle$, where the excitation is protected from forward emission. This observation is in agreement with recent predictions [226]. The reduction of this drop for longer pulses is a result of the dynamics becoming dominated by dephasing which also prevents the occurence of a second drop. This striking example of collective decay dynamics can, however, not be directly observed in the experiment as the predicted drop in the emission occurs at photon rates which are well below the noise level in the experiment as indicated in Fig. 6.1d). The inset in Fig. 6.3c) shows the dynamics at short times where the dynamics are approximately exponential but already start to deviate from a purely exponential behavior. The gray dashed lines indicate the effective decay rate calculated using Eq. (6.9).

6.4. Comparison with Experimental Data

To compare the predictions of the theoretical model given in Eq. (6.6) for the initial amplitude and the decay rate with the experimental data, the model including the driving term is fitted to the data. In this procedure, the Raman decay Γ is determined from experimental parameters and γ_{D} is assumed to be the same value for all datasets. Furthermore, the scaling $\kappa \sim 1/\Delta$ is taken into account. More details on the fitting procedure can be found in [236]. For completeness the fitted parameters are shown in Table 6.1.

The predicted decay rates from the theoretical model are then obtained by fitting an exponential decay after the end of the probe pulse. While the nonexponential decay predicted by the model makes this fitting impossible for long times, the initial decay up to $1.5\,\mu\mathrm{s}$ after the probe pulse is turned off is reasonably well approximated by an exponential decay. The exponential fits are shown in Fig. 6.3(c) and the predicted decay rates and initial amplitudes are shown in Fig. 6.2 and agree very well with the experimental data. It is important to point out that the analytical expression Eq. (6.9) leads to smaller values for the decay rate than the one obtained from the fitting. This comes from the nonexponential decay which results in a larger decay rate when fitting the exponential up to longer times. The figure also shows the expected constant decay rate in the absence of the coherent exchange ($\eta = 0$) which is indicated by the gray dashed line in each plot. This confirms that the coherent coupling is crucial in explaining the experimental observations. Note that this model is an extension to the one successfully used in [177, 178] (see

$\mathcal{R}_p\,(\mu s^{-1})$	$\Delta/2\pi\ (\mu s^{-1})$	$\kappa\,(\mu s^{-1})$	$\Gamma\,(\mu s^{-1})$	$\gamma_D\,(\mu s^{-1})$	$\eta\,(\mu s^{-1})$	In Figures
15.0	100	0.46	0.15	0.85 (1.34)	0.31	6.1, 6.2(a,e), 6.3
15.0	125	0.32	0.10	0.85 (1.26)	0.32	6.2(b,f)
15.0	150	0.21	0.064	0.85 (1.18)	0.31	6.2(c,g)
6.7	100	0.47	0.15	0.85 (1.33)	0.34	6.2(d,h)

Table 6.1.: Parameter sets from fitting the theoretical model in Eq. (6.6) to the experimental data. The values for γ_D given in the brackets are the values obtained from fitting the experimental data to the theoretical model with $\eta = 0$.

also Chapter 3) to explain photon correlations mediated by the superatom and in the study of single-photon absorption [70, 71], where the coherent coupling was not included in the model. These observations are still captured by the extended model as the correction coming from the coherent exchange only plays a minor role during the driving of the pulse for the photon rates considered in those experiments. However, the effects of the coherent exchange become more visible for lower photon rates as well as for the coherent population shelving during the emission process after the pulse ends. Finally, the four-level model used above can also be validated by simulating an idealized one-dimensional chiral system which predicts a coherent exchange coupling strength η on the order of κ in agreement with the fit parameters extracted from the experimental data [236, 251].

6.5. Summary and Outlook

In summary, the experimentally observed nontrivial collective emission dynamics of a Rydberg superatom are attributed to coherent exchange interactions between individual atoms and a simple effective model including a single coherently coupled subradiant state well reproduces the experimental observations. The experimental and theoretical work is complementary to recent investigations of weakly excited ensembles [226, 239, 240] and structured emitter arrays [84, 248, 249], but adds a new component through the saturation of the ensemble by a single photon because of the Rydberg blockade, which imposes further challenges for a full theoretical treatment. While the theoretical model is motivated by comparison to simulations of an idealized waveguide system and captures the core aspects of the system, a full understanding of the coherent and incoherent dynamics in a thermal atomic ensemble will ultimately require a full microscopic model. The observations presented here are of immediate consequence for the study and application of Rydberg superatoms and other collective quantum emitters, for example in cascaded emitter systems in waveguide-like geometries, where the internal dy-

namics will significantly alter the behaviour of the full ensemble [216, 223] (see also Chapters 4 and 5). More generally, these dynamics become relevant whenever collective excitations are created or probed on timescales comparable to the coherent photon exchange rates, e.g. in quantum simulation or photon memories. It will be relevant to study to what extent such internal interaction dynamics impose a fundamental limit on applications of collective excitations for single photon sources and quantum gates. At the same time, a better understanding of these dynamics enables precise collective state engineering, for example to efficiently store photons in subradiant collective states [252].

Part II.

Quantum Effects in Dipolar Bose Gases

Introduction

The experimental realization of Bose-Einstein condensation in dilute atomic gases in 1995 [253–255] marked the beginning of a new era of atomic, molecular and optical (AMO) physics and earned Cornell, Wieman and Ketterle the 2001 Nobel Prize in Physics. With the ability of controlling and manipulating this state of matter, an experimental platform became available to study quantum phenomena such as matter-wave interference [256], superfluidity and the appearance of vortices [257], and quantum phase transitions like the superfluid-to-Mott-insulator transition [258].

Due to the diluteness of the atomic gases involved and the ultracold temperatures in the nanokelvin range, the interaction between the particles can be described in terms of an effective contact interaction characterized by the s-wave scattering length which replaces the real, short-range interatomic potential. The strength of the interaction is nowadays routinely controlled by means of Feshbach resonance [134]. Dilute gases of weakly interacting cold bosons at ultracold temperatures are commonly described in terms of a mean-field theory by the Gross-Pitaevskii equation [259, 260].

In recent years, the tremendous experimental progress has added a new component to the ever-growing field of interacting Bose-Einstein condensates: the dipolar Bose-Einstein condensate. After its first experimental realization in an ultracold gas of chromium atoms in the group of Tilman Pfau in Stuttgart [261], Bose-Einstein condensates with even stronger dipolar interaction have been created with dysprosium [262] and erbium [263]. Compared to chromium which has a magnetic moment of $6\mu_{\mathrm{B}}$, erbium has a magentic moment of $7\mu_{\mathrm{B}}$[2]. Due to their electron configuration the bosonic isotopes of dysprosium have a magnetic moment of $10\mu_{\mathrm{B}}$ making it the most magnetic element available[3]. The presence of long-range and anisotropic interactions can strongly affect the properties of the

[2] We always refer to the bosonic isotopes of the elements.

[3] The fermionic isotopes of Dysprosium have the largest magnetic moment overall [262].

gas and brings a number of interesting effects and possible applications [125, 264]. The partly attractive nature of the interaction, for example, can lead the gas to collapse [265], which can be experimentally controlled by tuning the strength of the short-range repulsion relative to the dipolar interaction. Chapter 7 of this thesis will give a more detailed discussion of the interaction properties of ultracold dipolar Bose gases.

Despite the success in describing ultracold gases within mean-field theory for many years, the progress in experimental techniques such as trapping, cooling and imaging made it possible to observe beyond-mean-field effects such as the depletion of the condensate [266], corrections to the excitation spectrum [267, 268], and the ground state energy [269]. One of the striking effects due to quantum fluctuations was discovered in the formation of stable dense droplets for a dipolar gas close to its stability boundary [270] which triggered a huge interest in this field [271–275]. While mean-field theory predicts a collapse of the gas due to the dipolar interaction, the leading beyond-mean-field corrections induce an effective many-body repulsion which stabilizes the gas [276]. These corrections are known as Lee-Huang-Yang (LHY) corrections for contact interactions [277–279] and have also been calculated for dipolar interactions [280]. Even though the beyond-mean-field effects in dilute and weakly interacting gases are typically small, fine-tuning the relative strength of dipolar and contact interaction strength leads to a cancellation of the mean-field contributions making the LHY corrections become dominant [281]. This stabilization mechanism has also been observed in two-component Bose gases [282]. Recently, the behaviour of the beyond-mean-field corrections in the case of a dimensional crossover from three to low dimensions has been studied for contact [283, 284] and dipolar [285] interactions. An introduction into the calculation of beyond-mean-field corrections will be given in Chapter 7.

Moreover, a confined strongly dipolar gas can exhibit a roton-maxon excitation spectrum [286, 287] similar to that proposed for liquid Helium [288]. This excitation spectrum has also been experimentally observed [289]. Increasing the relative contribution of dipolar interactions, the gas undergoes a roton instability and fragments into arrays of droplets [290]. In a series of experiments [290–292] it was shown that different droplets also exhibit phase coherence realizing a long-sought state of matter, the supersolid. It combines the superfluid properties associated with the spontaneous breaking of the continuous global $U(1)$ phase symmetry with the density modulation induced by spontaneously breaking the translational invariance (see also [293] for a recent review on dipolar supersolids).

While the breaking of translational invariance in the dipolar supersolids is induced by intrinsic interactions, it can also be broken by an external periodic po-

tential. Optical lattices offer a versatile platform for manipulation and control of ultracold gases [294, 295] as they allow for creating a perfectly periodic potential for the atoms with tunable depth and geometry. This, for example, enabled the realization of the Bose-Hubbard model [296] and the demonstration of the quantum phase transition between the superfluid and Mott insulator phase [258]. By virtue of the long-range and anisotropic nature of their interaction, dipoles confined to optical lattices defy a description in terms of the standard Bose-Hubbard model [297, 298]. Extended Bose-Hubbard models have been realized experimentally [299] and it has been shown theoretically that they feature rich physics including the realization of exotic quantum phases such as supersolid, striped, and checkerboard phases in the strongly correlated limit [297, 300, 301].

In the superfluid limit, on the other hand, it was shown that the presence of an external periodic potential can increase beyond-mean-field effects in contact-interacting Bose gases [302]. In this work, the authors studied a BEC in a tight two-dimensional periodic potential forming a two-dimensional array of weakly coupled tubes. They showed that the resulting frequency shift due to beyond-mean-field effects in the lowest compressional mode along the axis of the tubes becomes large enough to be measured experimentally. For a trapped dipolar gas, it was shown that superimposing a one-dimensional lattice can lead to a stabilizing effect on the mean-field level [303]. This effect strongly depends on the intersite coupling coming from the long-range dipolar interactions, which is also expected to enhance the roton character in the excitation spectrum [304, 305] influencing the properties of interaction- and lattice-induced supersolids.

Chapter 8 thus studies the influence of an optical lattice on the beyond-mean-field corrections for a dipolar Bose gas. In particular, it will address the question whether and how one can control the strength of quantum fluctuations in this setup.

7

Basic Concepts

In this chapter, we briefly review important concepts for our study of dipolar Bose-Einstein condensates. First, we discuss how the interaction of ultracold Bose gases can be described in terms of an effective contact interaction and how magnetic atoms or polar molecules interact via the dipole-dipole interaction. Second, we present how beyond-mean-field corrections due to quantum fluctuations can be calculated.

Note that there are excellent reviews on the physics of dipolar Bose gases by Lahaye et al. [125] and the theory of dipolar gases by Baranov et al. [264], by which this chapter is inspired.

7.1. Short- and Long-Range Interactions in Ultracold Bose Gases

Even though Bose-Einstein condensation is a purely quantum-statistical phenomenon and does not rely on interactions between the particles, real-life systems almost always posses some interaction between its constituents. In Bose-Einstein condensates these interactions are responsible for phenomena such as superfluidity and are of importance when dealing with strongly correlated systems [295].

In the following, we are only concerned with ultracold and very dilute gases with temperatures in the micro- to nanokelvin regime and densities on the order of $10^{14} - 10^{15}\,\mathrm{cm}^{-3}$. Due to this diluteness, the interaction is governed by two-body interactions whereas interactions involving more particles are suppressed. Typically, this interatomic interaction potential is very complicated at short dis-

tances but falls off as the van der Waals interaction with r^{-6} at longer distances. As the gas is cooled down to ultracold temperatures, the low-energy scattering properties of short-ranged interaction potentials are universally characterized by the s-wave scattering length a_s. It is common to approximate the interaction in this limit by an isotropic contact potential of the form

$$V(\mathbf{r}) = g\delta(\mathbf{r})\,, \tag{7.1}$$

where m is the mass of the particles and g is the interaction strength which is determined to reproduce the correct scattering length a_s. For the δ-potential this can only be achieved within the first Born approximation since all higher contributions diverge. While this form of the interaction potential simplifies calculations, it has to be taken with care, especially when calculating effects beyond the mean-field level (see Section 7.2). A way to properly take into account the full scattering problem beyond the first Born approximation is to use the pseudopotential $V(\mathbf{r}) = g\delta(\mathbf{r})\partial_r r$, where $g = 4\pi\hbar^2 a_s/m$ to all orders in the Born series.

While the scattering length, and therefore g, can be both positive or negative indicating repulsive or attractive interactions, respectively, we only deal with $a_s > 0$ in order to prevent a collapse of the gas. Note, however, that the character of the interaction can be experimentally controlled by tuning the scattering length by means of Feshbach resonances [134]. It is also important to note that the Fourier transform of the pseudopotential is given by the constant g and thus couples all momenta.

Dipolar gases, which, for example, consist of magnetic atoms or polar molecules, interact in addition via the static dipole-dipole interaction

$$V_{dd}(\mathbf{r}) = \frac{C_{dd}}{4\pi}\frac{(\mathbf{e}_1\cdot\mathbf{e}_2)r^2 - 3(\mathbf{e}_1\cdot\mathbf{r})(\mathbf{e}_2\cdot\mathbf{r})}{r^5}\,, \tag{7.2}$$

where C_{dd} is the coupling constant and is $\mu_0\mu^2$ for particles having a permanent magnetic dipole moment μ (e.g. magnetic atoms) with μ_0 being the permeability of the vacuum and d^2/ϵ_0 for particles having a permanent electric dipole moment d (e.g. heteronuclear molecules) with ϵ_0 being the permittivity of the vacuum. The vectors $\mathbf{e}_{1,2}$ give the unit vectors for the orientation of the respective dipole moments and $\mathbf{r}$ is the relative distance of both particles (see also Fig. 7.1a)). In the following, we will only deal with polarized dipolar gases where the dipole moments are aligned by some external field (see Fig. 7.1b)). In this case, Eq. (7.2) takes the simpler form

$$V_{dd}(\mathbf{r}) = \frac{C_{dd}}{4\pi}\frac{1-3\cos^2\theta}{r^3}, \tag{7.3}$$

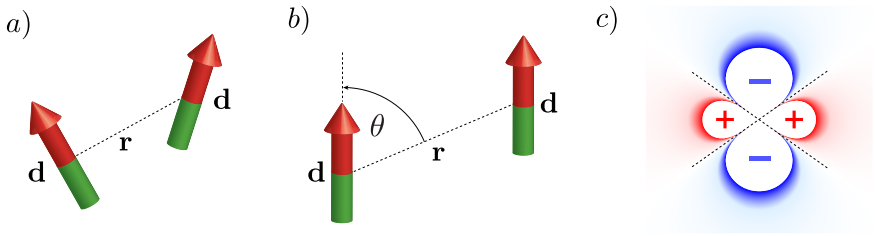

Fig. 7.1.: Sketch of the dipole-dipole interaction. a) Non-polarized dipoles interacting with each other at a relative distance $\mathbf{r}$ and dipole moments $\mathbf{d}$. b) Polarized dipoles interacting with each other. The interaction is now characterized by the relative distance r and the angle θ between the polarization axis and the direction of $\mathbf{r}$. c) Angular dependence of the dipole-dipole interaction for polarized dipoles. The interaction is attractive in a head-to-tail configuration (blue area) and repulsive if they are side by side (red area). The dashed line indicates the "magic angle" $\theta^* \approx 54.7°$ for which the interaction vanishes. Figure adapted from [125].

where $r = |\mathbf{r}|$ is the relative distance between the dipoles and θ is the angle between the relative position $\mathbf{r}$ and the polarization axes of the dipoles. It is important to note that while the contact interaction, Eq. (7.1), is either attractive or repulsive depending on the sign of the s-wave scattering length a_s, the dipole-dipole interaction in Eq. (7.3) has both attractive and repulsive character depending on the orientation of the dipoles (see Fig. 7.1c)). If the dipoles are in a head-to-tail configuration, where $\theta = 0$, the dipole-dipole interaction becomes attractive while it is repulsive for dipoles sitting side by side, that is $\theta = \pi/2$. Interestingly, placing the dipoles at an angle $\theta^* = \arccos(1/\sqrt{3}) \approx 54.7°$, the dipole-dipole interaction vanishes. Note that while the strength and sign of the dipole-dipole interaction are fixed by the magnitude and orientation of the dipoles, it is possible to tune both parameters using a combination of dc and ac electric field for electric dipoles [125].

In contrast to the isotropic and short-range character of the interaction between particles having no dipole moment, the dipole-dipole interaction is both anisotropic and long-range. Since the dipole-dipole interaction is anisotropic, the angular momentum is not conserved during the scattering. In the case of polarized gases, however, the projection of the angular momentum on the polarization axis is still a good quantum number. In addition, the long-range character of the dipole-dipole interaction leads to a contribution of all partial waves to the scattering at low energies and the phase shifts behave as $\delta_l \sim k$ for $l > 0$ and small k. Thus, it is not possible to replace it by a pure contact interaction potential. In fact, the coupling between different scattering channels introduces a contribution to the s-

wave scattering and therefore also modifies the short-range part of the interaction potential, Eq. (7.1). This leads to the appearance of so-called "shape" resonances [306–308]. For the scope of this thesis, we always consider setups where these resonances do not play any role.

The interatomic interaction pseudopotential of two dipolar particles at ultracold temperatures can thus be written as [309–312]

$$V(\mathbf{r}) = \frac{4\pi\hbar^2 a_s(C_{dd})}{m}\delta(\mathbf{r}) + \frac{C_{dd}}{4\pi}\frac{1-3\cos^2\theta}{r^3}. \tag{7.4}$$

Note that the strength of the contact interaction now also depends on the coupling strength of the dipole-dipole interaction and thus on the magnitude of the respective dipole moments. As we only deal with systems where the dipole moments are fixed, we will drop the dependence on the dipole moments and always refer to the s-wave scattering length in the presence of the dipole moment of the respective particle.

Similar to the scattering length a_s in the case of short-range interactions, the strength of the dipole-dipole interaction can be characterized by the dipolar length[1]

$$a_{dd} = \frac{mC_{dd}}{12\pi\hbar^2}\,. \tag{7.5}$$

The behaviour of a dilute dipolar Bose gas at ultracold temperatures is then described in terms of the parameter

$$\varepsilon_{dd} = \frac{a_{dd}}{a_s} \tag{7.6}$$

which gives the relative strength of the dipole-dipole interaction compared to the strength of the contact interaction. For $\varepsilon_{dd} < 1$, the gas is dominated by the isotropic short-range interaction while for $\varepsilon_{dd} \gtrsim 1$, the interaction is dominated by the anisotropic, long-range interaction. Note, however, that a homogeneous dipolar Bose-Einstein condensate in three dimensions is unstable for $\varepsilon_{dd} \geq 1$ [125]. The commonly used atomic species ^{87}Rb, with magnetic moment of $1\mu_B$, has $\varepsilon_{dd} = 0.007$ [313] and can be considered a BEC with pure contact interactions. In turn, for ^{52}Cr, with $\mu = 6\mu_B$, one has $\varepsilon_{dd} = 0.16$ [314] and the recently used lanthanide atoms ^{164}Dy and ^{166}Er have $\varepsilon_{dd} \approx 1.3$ [270, 315] and $\varepsilon_{dd} = 0.97$ [272] at the background scattering length, respectively. Note that polar molecules, which

[1] The dipolar length can be obtained by equating the strength of the dipole-dipole interaction at a length a_{dd}, $C_{dd}/4\pi a_{dd}^3$ with the energy of a particle in a box in three dimensions of the same length, $3\hbar^2/ma_{dd}^2$.

have a permanent electric dipole, can have values of ε_{dd} which can be one or two orders of magnitude larger than those of magnetic atoms [125][2].

7.2. Beyond-Mean-Field Corrections in Dilute Bose Gases

The ground state energy of an ultracold Bose gas below the condensation threshold interacting via short-range interactions in three dimensions is usually well described by the mean-field energy density

$$\frac{E_0^{\mathrm{MF}}}{V} = \frac{2\pi\hbar^2 a_s n^2}{m}\,, \tag{7.7}$$

where $n = N/V$ is the density of the gas. The same expression also holds for a gas that interacts via the long-range and anisotropic dipole-dipole interaction in three dimensions since the angular contribution vanishes when averaging over all angles. Note, however, that for a gas that is confined by an external trapping potential for example, the dipole-dipole interaction also contributes to the mean-field energy [125], which we will also see in Chapter 8 where the external potential is an optical lattice.

Even though the mean-field treatment of a Bose gas below condensation threshold allows for the succesful description in terms of the Gross-Pitaevskii equation explaining dynamical properties of trapped and rotating gases [316], it assumes that all particles occupy the state of lowest energy. In the presence of interactions, even at zero temperatures, quantum fluctuations drive particles to occupy higher-energy states that leads to corrections to the ground state energy. The important parameter here is the so-called "gas parameter" na_s^3. In three dimensions, the corrections can then be derived perturbatively if $na_s^3 \ll 1$ indicating the dilute limit.

7.2.1. Bogoliubov Method

A very common way to calculate the beyond-mean-field corrections is to use the Bogoliubov method [317] which we will briefly outline for the case of short-range interactions in the following. More details can for example be found in [318]. Consider a dilute gas of bosons with mass m at $T = 0$ and density $n = N/V$, where

[2] It is, however, important to mention that the precise background scattering lengths of those molecules are not known yet and values of ε_{dd} are only rough estimates [125].

N is the number of particles and V is the volume. Using the interaction potential in Eq. (7.1), the Hamiltonian of the system in momentum space is

$$H = \sum_{\mathbf{k}} \epsilon_{\mathbf{k}} a^\dagger_{\mathbf{k}} a_{\mathbf{k}} + \frac{g}{2V} \sum_{\mathbf{k}+\mathbf{k}'=\mathbf{q}+\mathbf{q}'} a^\dagger_{\mathbf{q}} a^\dagger_{\mathbf{q}'} a_{\mathbf{k}'} a_{\mathbf{k}} \tag{7.8}$$

where $\epsilon_{\mathbf{k}} = \hbar^2 k^2/2m$ is the dispersion relation of a free particle and the operator $a^{(\dagger)}_{\mathbf{k}}$ describes the annihilation (creation) of a particle with momentum $\mathbf{k}$. At zero temperature, the particles of a noninteracting Bose gas in free space would all occupy the lowest momentum state $\mathbf{k} = 0$, which one calls the condensate mode. In a dilute gas of interacting particles, however, the ground state only differs slightly from that of an ideal gas and modes with $\mathbf{k} \neq 0$ will only be occupied by some small amount of particles. The Bogoliubov approximation now consists of replacing all operators of the mode $\mathbf{k} = 0$ with the c-number $\sqrt{N_0}$ of particles in this mode. In addition to that, all interaction terms involving more than two particles in modes with $\mathbf{k} \neq 0$ are neglected since they are of lower order in N_0. The Hamiltonian then reduces to

$$H = \frac{gn}{2} V + \frac{1}{2} \sum_{\mathbf{k}\neq 0} \left[(\epsilon_{\mathbf{k}} + gn) \left(a^\dagger_{-\mathbf{k}} a_{-\mathbf{k}} + a^\dagger_{\mathbf{k}} a_{\mathbf{k}} \right) + gn (a^\dagger_{\mathbf{k}} a^\dagger_{-\mathbf{k}} + a_{\mathbf{k}} a_{-\mathbf{k}}) \right] , \tag{7.9}$$

where we used that the total number of particles in the system can be written as $N = N_0 + \frac{1}{2} \sum_{\mathbf{k}\neq 0} (a^\dagger_{\mathbf{k}} a_{\mathbf{k}} + a^\dagger_{-\mathbf{k}} a_{-\mathbf{k}})$. Since the Hamiltonian in Eq. (7.9) is quadratic in the operators a and $a^\dagger$, one can use a Bogoliubov-Valatin transformation to diagonalize it and bring it to the form

$$H = \frac{gn}{2} V + \frac{1}{2} \sum_{\mathbf{k}\neq 0} (E_{\mathbf{k}} - \epsilon_{\mathbf{k}} - gn) + \sum_{\mathbf{k}\neq 0} E_{\mathbf{k}} \alpha^\dagger_{\mathbf{k}} \alpha_{\mathbf{k}} \, . \tag{7.10}$$

In this expression, the first term is the mean field energy in Eq. (7.7), while the last term gives the elementary excitations of the Bose gas in the presence of interactions. They are now described by the operators $\alpha^{(\dagger)}_{\mathbf{k}}$ and the excitation spectrum is given by the famous Bogoliubov excitation spectrum

$$E_{\mathbf{k}} = \sqrt{\epsilon_{\mathbf{k}} \left(\epsilon_{\mathbf{k}} + 2gn \right)} \, , \tag{7.11}$$

which for small momenta is phonon-like, that is $E_{\mathbf{k}} \sim |\mathbf{k}|$ and goes over to the energy of a free particle at large momenta, $E_{\mathbf{k}} \sim k^2$.

The second term in Eq. (7.10) gives the correction to the mean-field energy in the presence of interaction-induced quantum fluctuations but diverges for large

momenta as $\sum_{\mathbf{k}} k^{-2}$. This problem arises since the energy corrections cannot be expanded in powers of g but instead the gas parameter na_s^3 has to be small. As already discussed above, the relation $g = 4\pi\hbar^2 a_s/m$ for the potential in Eq. (7.1) is only exact in the first Born approximation and has to be corrected for the calculation of the beyond-mean-field corrections by including the second-order Born approximation as

$$g - \frac{g^2}{V}\sum_{\mathbf{k}\neq 0}\frac{1}{2\epsilon_{\mathbf{k}}} = \frac{4\pi\hbar^2 a_s}{m}\,. \tag{7.12}$$

Note that the second term in this expression shows the same divergence as the energy correction in Eq. (7.10).

Expressing g in terms of a_s in Eq. (7.10), one arrives at the expression for the ground state energy

$$\frac{E_0}{V} = \frac{2\pi\hbar^2 a_s n}{m} + \frac{1}{2V}\sum_{\mathbf{k}\neq 0}\left(E_{\mathbf{k}} - \epsilon_{\mathbf{k}} - \frac{4\pi\hbar^2 a_s}{m}n + \left(\frac{4\pi\hbar^2 a_s}{m}\right)^2\frac{n^2}{2\epsilon_{\mathbf{k}}}\right)\,. \tag{7.13}$$

Evaluating the sum in the limit $V\to\infty$, one gets

$$\frac{E_0}{V} = \frac{2\pi\hbar^2 a_s}{m}n^2\left(1 + \frac{128}{15\sqrt{\pi}}\sqrt{na_s^3}\right) \tag{7.14}$$

with the small expansion parameter $\sqrt{na_s^3} \ll 1$. It is important to note that at this point, the interaction strength g drops out of the problem and the only relevant property is that the gas is dilute. The beyond-mean-field corrections where first derived by Lee, Huang, and Yang in 1957 using the pseudopotential method [277]. The approach outlined above can also be generalized to pseudopotentials with Fourier components $V_{\mathbf{k}}$, where one has

$$\frac{E_0}{V} = \frac{V_0 n^2}{2} + \frac{1}{2V}\sum_{\mathbf{k}\neq 0}\left(E_{\mathbf{k}} - \epsilon_{\mathbf{k}} - V_{\mathbf{k}}n + \frac{(V_{\mathbf{k}}n)^2}{2\epsilon_{\mathbf{k}}}\right)\,. \tag{7.15}$$

This is for example the case for the dipolar pseudopotential in Eq. (7.4) whose Fourier transform is calculated in Appendix 7.A. The derivation of the beyond-mean-field energy for the dipolar pseudopotential is performed in the next section using a different method but we want to point out that it was first calculated using the Bogoliubov method by Lima and Pelster [280].

7.2.2. Field-Theoretic Method

While the Bogoliubov approach is very convenient for calculations, it suffers from artificially removing the divergence in the correction to the ground state energy which occurs due to the improper handling of the interaction potential. A very elegant way around this problem was introduced by Beliaev [279] and Hugenholtz and Pines [278], which relies on including the full scattering problem in the dilute limit and allows for the self-consistent, perturbative calculation of corrections to the ground state energy. In the following, we will outline this approach for the case of a short-ranged interaction potential closely following the derivations of Hugenholtz and Pines [278] and Beliaev [279], where more details can be found. In the end, we will discuss how the result can be extended to dipolar interactions.

For the field-theoretic method, we start with the task to find the ground state of a dilute Bose gas of N interacting particles with mass m in a volume V described by the Hamiltonian

$$\begin{aligned} H &= -\frac{\hbar^2}{2m}\int d^3r\, \Psi^\dagger(\mathbf{r})\nabla^2\Psi(\mathbf{r}) + \frac{1}{2}\int d^3r\, d^3r'\, \Psi^\dagger(\mathbf{r})\Psi^\dagger(\mathbf{r}')V(\mathbf{r}-\mathbf{r}')\Psi(\mathbf{r}')\Psi(\mathbf{r}) \\ &= H_0 + H_{\text{int}}\,, \end{aligned} \tag{7.16}$$

where $\Psi^{(\dagger)}(\mathbf{r})$ are the field operators describing particles at position $\mathbf{r}$ and have commutation relations $\left[\Psi(\mathbf{r}), \Psi^\dagger(\mathbf{r}')\right] = \delta(\mathbf{r}-\mathbf{r}')$. The particles interact via the potential $V(\mathbf{r}-\mathbf{r}')$ which at this point is arbitrary but later is assumed to be either short-ranged or of dipolar nature. Similar to the Bogoliubov method, we assume that the number of particles in the ground state of the noninteracting system is very large and we may separate the contributions from the condensate mode and all the other modes as

$$\Psi(\mathbf{r}) = \sqrt{n_0} + \psi(\mathbf{r})\,. \tag{7.17}$$

Here, the first term describes the condensate mode with density $n_0 = N_0/V$ and $\psi(\mathbf{r})$ is the field operator for particles not in the condensate, that is those with momentum $\mathbf{k} \neq 0$. After the Bogoliubov prescription, Eq. (7.17), the Hamiltonian is a function of n_0, $H(n_0)$, and since it no longer preserves the number of particles, one has to impose the additional condition that

$$N = N_0 + \int d^3r\, \langle\phi_0|\, \psi^\dagger(\mathbf{r})\psi(\mathbf{r})\, |\phi_0\rangle = N_0 + N' \tag{7.18}$$

with the ground state of the interacting system $|\phi_0\rangle$. An alternative formulation of the problem is then not to look for the ground state of this Hamiltonian with the

condition of particle number conservation but instead to look for the same ground state of the grand-canonical Hamiltonian

$$H' = H(n_0) - \mu N' \tag{7.19}$$

without any additional condition. The parameter μ is the chemical potential of the system and plays the role of a Lagrange multiplier. It is fixed by the condition that for fixed density $n = N/V$, one has $n'(n_0, \mu) = n - n_0$. The ground state density is determined by the condition $dE_0/dN_0 = 0$. The chemical potential is also directly related to the ground state energy by the important relation

$$\frac{d}{dn}\left(\frac{E_0}{V}\right) = \mu\,. \tag{7.20}$$

At this point it is important to mention that the condensate mode has been removed from the initial problem of calculating the ground state energy of the Hamiltonian in Eq. (7.16). The new problem now consists of calculating the ground state of a new Hamiltonian

$$H' = \int d^3r\, \psi^\dagger(\mathbf{r}) \left(-\frac{\hbar^2\nabla^2}{2m} - \mu\right) \psi(\mathbf{r}) + H_{\rm int}(n_0) = H_0(n_0) + H_{\rm int}(n_0) \tag{7.21}$$

where μ plays the role of an external potential and $H_{\rm int}(n_0)$ includes all interaction terms where the field operator Ψ has been replaced according to Eq. (7.17). This problem can now be tackled with standard methods from quantum field theory.

In the field-theoretic treatment of the problem, the central quantity is the one-particle Green's function of the Hamiltonian H'

$$G(\mathbf{r} - \mathbf{r}', t - t') = i \left\langle \phi_0 \right| \mathcal{T} \psi(\mathbf{r}, t) \psi^*(\mathbf{r}', t') \left| \phi_0 \right\rangle \,. \tag{7.22}$$

It is important to note that this Green's function only describes particles which are not in the condensate, which has been eliminated from the problem. As we consider particles in free space without any position-dependent potential, we have translational invariance in space and momentum still is a good quantum number such that we define the Green's function in energy-momentum space as

$$G(\mathbf{k}, \epsilon) = \int d^3r \int dt\, e^{i(\epsilon t - \mathbf{k}\cdot\mathbf{r})} G(\mathbf{r}, t) \tag{7.23}$$

It is then possible to relate the ground state energy directly to the Green's function by

$$\frac{E_0}{V} - \frac{n\mu}{2} = \frac{i}{2\pi} \int \frac{d^3k}{(2\pi)^3} \int_{\mathcal{C}} d\epsilon\, \frac{(\epsilon + \epsilon_{\mathbf{k}})}{2} G(\mathbf{k}, \epsilon)\,, \tag{7.24}$$

where the countour $\mathcal{C}$ goes along the real axis from $-\infty$ to $+\infty$ and is closed in the upper-half plane to preserve causality. Note that this constitutes a differential equation where the derivative in the form of μ enters on both sides of the equation. In the dilute limit, it is possible to derive corrections perturbatively using lower orders of μ on the right-hand side to calculate a certain order of $G(\mathbf{k},\epsilon)$ and E_0. The crucial step in calculating the ground state energy is now to calculate the Green's function to a given order.

Using diagrammatic techniques, one can derive a closed form for the Green's function $G(\mathbf{k},\epsilon)$, which is given by

$$G(\mathbf{k},\epsilon) = \frac{\epsilon + \epsilon_{\mathbf{k}} - \mu + \Sigma^{11}_{\mathbf{k}}(-\epsilon)}{\left[\epsilon - \frac{\hbar\Sigma^{11}_{\mathbf{k}}(\epsilon)-\hbar\Sigma^{11}_{\mathbf{k}}(-\epsilon)}{2}\right]^2 - \left[\epsilon_{\mathbf{k}} - \mu + \frac{\hbar\Sigma^{11}_{\mathbf{k}}(\epsilon)+\hbar\Sigma^{11}_{\mathbf{k}}(-\epsilon)}{2}\right]^2 + \left|\hbar\Sigma^{02}_{\mathbf{k}}(\epsilon)\right|^2} . \tag{7.25}$$

In this expression, $\hbar\Sigma^{11}_{\mathbf{k}}(\epsilon)$ is the self-energy due to the scattering of a particle with momentum $\mathbf{k}$ off the condensate and $\hbar\Sigma^{02}_{\mathbf{k}}(\epsilon)$ denotes the self-energy coming from the scattering of two particles in the condensate resulting in two particles out of the condensate with opposite momenta.

In the dilute regime, the self-energies can be calculated perturbatively in orders of the ground state density n_0. Within this treatment, the repeated scattering of particles is taken into account to all orders in the interaction strength. To lowest order in the density, it is sufficient to keep the repeated scattering of two particles, so-called ladder diagrams in the language of quantum field theory, and the self-energies are directly proportional to the scattering amplitude

$$f(\mathbf{k}',\mathbf{k}) = \int d^3r\, V(\mathbf{r}) e^{-i\mathbf{k}'\cdot\mathbf{r}} \psi_{\mathbf{k}}(\mathbf{r}) \,, \tag{7.26}$$

where $\psi_{\mathbf{k}}(\mathbf{r})$ is the solution to the Lippman-Schwinger equation of a particle scattering off the potential $V(\mathbf{r})$ with incoming momentum $\mathbf{k}$. The self-energies to first order read

$$\hbar\Sigma^{02}_{\mathbf{k}}(\epsilon) = n_0 f(0,\mathbf{k}) \,, \tag{7.27}$$

$$\hbar\Sigma^{11}_{\mathbf{k}}(\epsilon) = 2n_0 \frac{f(\mathbf{k}/2,\mathbf{k}/2) + f(-\mathbf{k}/2,\mathbf{k}/2)}{2} \,. \tag{7.28}$$

Note that while $f(\mathbf{k}/2,\mathbf{k}/2)$ and $f(-\mathbf{k}/2,\mathbf{k}/2)$ account for forward and backward scattering of a particle, respectively, the scattering amplitude $f(0,\mathbf{k})$ describes a process which is forbidden for two particles in vacuum. This is reminiscent of the fact that the self-energy $\hbar\Sigma^{02}_{\mathbf{k}}$ accounts for the scattering of two particles in the condensate, which we eliminated in the problem, into two particles out of the condensate.

First Order: Mean-Field Energy

In the lowest order in the density, we need the zeroth-order Green's function, which is the one of a free particle, that is $G^{(0)}(\mathbf{k},\epsilon) = 1/(\epsilon - \epsilon_{\mathbf{k}} + i\delta)$, since both the chemical potential and the self-energies vanish to zeroth order. On the other hand, we need the first-order chemical potential for the left-hand side of Eq. (7.24). The chemical potential is given by the Hugenholtz-Pines relation $\mu = \hbar\Sigma_0^{11}(0) - \hbar\Sigma_0^{02}(0)$ which in fact is exact to all order in perturbation theory. To first order, one has $\mu^{(1)} = n_0 f(0,0) \equiv n_0 f_0$. As the Green's function $G^{(0)}(\mathbf{k},\epsilon)$ has no poles in the upper-half plane, the right hand side of Eq. (7.24) vanishes and we are left with the mean-field energy

$$\frac{E_0^{(1)}}{V} = \frac{n_0 n f_0}{2} = \frac{2\pi\hbar^2 a_s}{m} n^2 \,, \tag{7.29}$$

where we used $f_0 = 4\pi\hbar^2 a_s/m$ for short-ranged potentials characterized by the s-wave scattering a_s and replaced n_0 by n which is correct to this order.

Second Order: Beyond-Mean-Field Corrections

In order to calculate the second order in the energy, which gives the beyond-mean-field corrections, we need the first-order Green's function, which involves both the first-order chemical potential already calculated in the previous paragraph as well as the first-order self-energies calculated in Eqs. (7.27) and (7.28). The Green's function then reads

$$G^{(1)}(\mathbf{k},\epsilon) = \frac{\epsilon + \epsilon_{\mathbf{k}} - n_0 f_0}{\epsilon^2 + E_{\mathbf{k}}^2 + i\delta} \,, \tag{7.30}$$

where $E_{\mathbf{k}}^2 = (\epsilon_{\mathbf{k}} - n_0 f_0 + \hbar\Sigma_{\mathbf{k}}^{11})^2 - |\hbar\Sigma_{\mathbf{k}}^{02}|^2$ is the generalized Bogoliubov excitation spectrum and $\delta > 0$ is used to shift the poles correctly. Using the Green's function to first order, the integral over ϵ in Eq. (7.24) can be performed and leads to

$$\frac{E_0^{(2)}}{V} - \frac{n\mu^{(2)}}{2} = \frac{1}{2}\int \frac{d^3k}{(2\pi)^3} \frac{(\epsilon_{\mathbf{k}} + n_0 f_0 - E_{\mathbf{k}})(\epsilon_{\mathbf{k}} - E_{\mathbf{k}})}{2E_{\mathbf{k}}} \,. \tag{7.31}$$

The integration of the momentum on the right-hand side can be performed once the momentum dependence of the scattering amplitudes is known which depends on the interaction potential at hand. For simplicity, we restrict ourselves to short-ranged potentials with small momentum transfers and later generalize this to the long-ranged dipolar interactions. For momenta small compared to the characteristic size of the interaction, that is $ka_s < 1$, one can approximate the scattering amplitudes in Eqs. (7.27) and (7.28) as being constant with their value at zero

momentum, that is $f(0,\mathbf{k}) \approx f(0,0) = f_0$ and similarly for $f(\mathbf{k}/2,\mathbf{k}/2)$ and $f(-\mathbf{k}/2,\mathbf{k}/2)$. The excitation spectrum then reduces to Eq. (7.11) and the integral in Eq. (7.31) can be calculated leading to

$$\frac{E_0^{(2)}}{V} - \frac{n\mu^{(2)}}{2} = -\frac{\sqrt{2}}{15\pi^2}(n_0 f_0)^{5/2}\left(\frac{2m}{\hbar^2}\right)^{3/2} . \tag{7.32}$$

In the last expression, we can replace n_0 by n as corrections will only contribute to higher-order corrections to the ground state energy. Recalling that the chemical potential is related to the energy density by $\mu = \frac{\mathrm{d}(E_0/V)}{\mathrm{d}n}$, we then have to solve a differential equation in n. The homogeneous part of this differential equation is solved by an energy density which is proportional to n^2 which is the same order as the mean-field energy we have already calculated in Eq. (7.7). The correction to the mean-field energy provided by Eq. (7.31) then reads

$$\frac{E_0^{(2)}}{V} = -n^2 \int_0^n dy\, \frac{2f(y)}{y^3} \tag{7.33}$$

with $f(n) = -\frac{\sqrt{2}}{15\pi^2}(nf_0)^{5/2}\left(\frac{2m}{\hbar^2}\right)^{3/2}$. The lower boundary of the integral derives from the constraint that for weak interactions, the mean-field result provides the dominant contribution. In three dimensions, a Bose gas is weakly interacting in the dilute regime, given by the condition $na_s^3 \ll 1$, and the contribution from the beyond-mean-field energy has to vanish faster than n^2 in the limit $n \to 0$. The integral can be solved analytically and the ground state energy after setting $f_0 = 4\pi\hbar^2/m$ reads

$$\frac{E_0}{V} = \frac{2\pi\hbar^2 a_s}{m} n^2 \left(1 + \frac{128}{15\sqrt{\pi}}\sqrt{na_s^3}\right) \tag{7.34}$$

which is the same result that was obtained in Eq. (7.14) using the Bogoliubov method. Note that even though both the Bogoliubov approach and the field-theoretic approach by Hugenholtz and Pines and Beliaev give the same result, the field-theoretic method offers the advantage of circumventing unphysical divergences arising due to a necessary renormalization of the scattering length which occurs in the Bogoliubov method [319]. Using the field-theoretic approach it is also possible to calculate higher-order corrections to the ground state energy and the next-order term has the form $(na_s^3)\ln(na_s^3)$ [278].

Dipolar Interaction

In contrast to short-ranged interactions, which are well characterized by the s-wave scattering length a_s at low energies and where the scattering amplitude can

be approximated as being constant, the long-range character does not necessarily allow for such a simplification. However, it turns out that for low energies and away from shape resonances, the scattering amplitude of dipolar particles is well approximated by the Fourier transform of the pseudopotential Eq. (7.4) [309–311, 320] given by

$$V_{\mathbf{k}} = \frac{4\pi\hbar^2 a_s}{m} + C_{dd}\left(\cos^2\alpha - \frac{1}{3}\right) , \tag{7.35}$$

where α is the angle between the polarization axis and $\mathbf{k}$. The calculation of the Fourier transform is presented in Appendix 7.A. Note that for $\mathbf{k} \to 0$ there is a discontinuity in the second part depending on which direction we take the limit from . Calculating the value V_0 directly, one obtains $V_0 = 4\pi\hbar^2 a_s/m$ which we will use in the following.

The corresponding self-energies to first order can then be written as

$$\hbar\Sigma^{02}_{\mathbf{k}} = n_0 V_{\mathbf{k}} , \tag{7.36}$$

$$\hbar\Sigma^{11}_{\mathbf{k}} = n_0(V_0 + V_{\mathbf{k}}) . \tag{7.37}$$

The evaluation of the integral in Eq. (7.31) then follows along the same lines as above and solving the remaining differential equation, we get

$$\frac{E_0}{V} = \frac{2\pi\hbar^2 a_s}{m} n^2 \left(1 + \frac{128}{15\sqrt{\pi}}\sqrt{n a_s^3} F(\varepsilon_{dd})\right) , \tag{7.38}$$

where $F(\varepsilon_{dd}) = \frac{1}{2}\int_{-1}^{1} \mathrm{d}u\, (1 + \varepsilon_{dd}(3u^2 - 1))^{5/2}$ accounts for the influence of the dipole-dipole interaction and $F(0) = 1$ in the absence of the dipole-dipole interaction. It is interesting to note that the contribution from the dipolar part is merely a factor which depends only on the parameter ε_{dd} and does not introduce an additional density dependence. This comes from the fact that the Fourier transform of the dipole-dipole interaction only depends on the angle between $\mathbf{k}$ and the dipole moment but not on $|\mathbf{k}|$ itself. Another peculiarity of this additional factor is that it becomes complex for $\varepsilon_{dd} > 1$ which is reminiscent of the stability properties of the dipolar Bose gas. The theory itself can no longer be applied in this case as the original assumption of a stable ground state is no longer satisfied. The beyond-mean-field correction to the ground state energy of a dipolar Bose gas was first calculated by Lima and Pelster in [280] using the Bogoliubov method.

Appendix

7.A. Fourier Transform of the Dipole-Dipole Interaction

In this appendix, we calculate the Fourier transform of the dipole-dipole interaction in Eq. (7.3) in three dimensions. For the derivation we closely follow [125].

Formally, the Fourier transform is given by

$$\tilde{V}_{dd}(\mathbf{k}) = \frac{C_{dd}}{4\pi} \int \mathrm{d}^3 r \, e^{-i\mathbf{kr}} \frac{1 - 3(z/|\mathbf{r}|)^2}{|\mathbf{r}|^3} \,. \tag{7.39}$$

This expression is simplified by transforming to spherical coordinates (r, θ, ϕ) and aligning the polar axis along the direction of $\mathbf{k}$. The dipole moment is assumed to be in the $y = 0$ plane and makes an angle α with $\mathbf{k}$. The Fourier transform then reads

$$\begin{aligned}
\tilde{V}_{dd}(\mathbf{k}) &= \frac{C_{dd}}{4\pi} \int \mathrm{d}r \, \mathrm{d}\theta \, \mathrm{d}\phi \, \sin\theta e^{-ikr\cos\theta} \frac{1 - 3(\sin\alpha \, \sin\theta \, \cos\phi + \cos\alpha \, \cos\phi)^2}{r} \\
&= \frac{C_{dd}}{4\pi} \int_{r_c}^{\infty} \frac{\mathrm{d}r}{r} \int_0^{\pi} \mathrm{d}\theta \, \sin\theta e^{-ikr\cos\theta} \pi (3\cos^2\alpha - 1)(1 - 3cos^2\theta) \\
&= C_{dd}(1 - 3\cos^2\alpha) \int_{r_c}^{\infty} \mathrm{d}r \, \left(\frac{\sin(kr)}{(kr)^2} + \frac{3\cos(kr)}{(kr)^3} - \frac{3\sin(kr)}{(kr)^4} \right) \\
&= C_{dd}(1 - 3\cos^2\alpha) \frac{kr_c \, \cos(kr_c) - \sin(kr_c)}{(kr_c)^3} \,.
\end{aligned} \tag{7.40}$$

In the second line, we have introduced the cutoff r_c at small distances in order to avoid divergences. As our result should not include the cutoff, we can now let r_c go to zero and obtain

$$\tilde{V}_{dd}(\mathbf{k}) = \frac{C_{dd}}{3}(3\cos^2\alpha - 1) \,. \tag{7.41}$$

Note that the Fourier transform does not depend on the magnitude of $\mathbf{k}$ but only on its orientation with respect to the polarization axis, that is the axis along which the dipole is oriented.

8

Beyond Mean-Field Corrections for Dipolar Bosons in an Optical Lattice

In this chapter, we study the influence of an optical lattice on the beyond-mean-field (LHY) corrections for a dipolar Bose gas. In particular, we investigate whether and how one can control the strength of the quantum fluctuations in a suitable way. In Section 8.1, we first consider the case of a deep three-dimensional cubic lattice. In this setup, we calculate the LHY correction to the ground state energy of an interacting Bose gas for contact (on-site) interactions, as well as for dipolar density-density interactions neglecting the interaction-induced tunneling effects. In the limit of a large healing length, an effective mass emerges and we also calculate the corrections that arise for larger interaction strengths. After that, in Section 8.2, we turn to the case of a weak one-dimensional lattice and show that by manipulating the orientation of the lattice with respect to the dipole orientation axis it is possible to control and tune the magnitude of the LHY corrections. This chapter is based on Ref. [321].

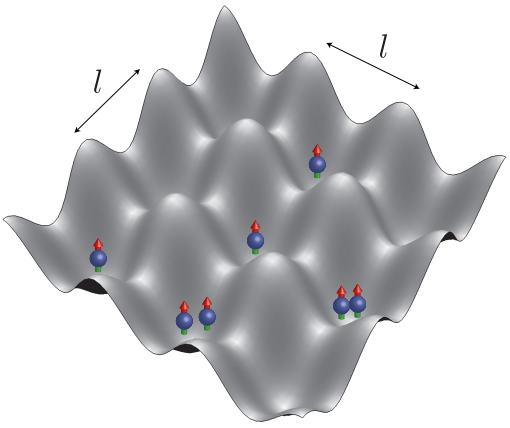

Fig. 8.1.: Schematic illustration of the deep optical lattice. The dipoles are trapped in a deep three-dimensional optical lattice with lattice spacing l, but are in the weakly interacting regime and remain superfluid.

8.1. Deep Optical Lattice

We start our considerations with the general many-body Hamiltonian of an interacting Bose gas at zero temperature in second quantized form,

$$H = \int d^3r\, \Psi^\dagger(\mathbf{r}) \left(-\frac{\hbar^2\nabla^2}{2m} + U(\mathbf{r}) \right) \Psi(\mathbf{r}) + \frac{1}{2} \int d^3r \int d^3r'\, \Psi^\dagger(\mathbf{r}) \Psi^\dagger(\mathbf{r}') V(\mathbf{r}-\mathbf{r}') \Psi(\mathbf{r}') \Psi(\mathbf{r})\,. \tag{8.1}$$

In this Hamiltonian, $U(\mathbf{r})$ describes an external potential, e.g. a trapping potential or an optical lattice, while $V(\mathbf{r})$ describes the interaction potential. For dipolar particles which are polarized along one direction, the interaction potential can be represented in terms of a pseudopotential [310]

$$V(\mathbf{r}) = g_0 \delta(\mathbf{r}) + \frac{C_{dd}}{4\pi} \frac{1 - 3\cos^2\theta}{r^3}\,, \tag{8.2}$$

where θ is the angle between the direction of the polarization of the dipoles and their relative position. The first term of this pseudopotential accounts for the s-wave interactions which result from the short-ranged van der Waals interactions but contains also the contribution of the dipolar part of the potential. The second part stands for the higher partial waves, which are dominated by the long-range

and anisotropic dipolar interaction. The coupling constant g_0 is related to the s-wave scattering length a_s via $g_0 = 4\pi\hbar^2 a_s/m$. The dipolar coupling constant C_{dd} is $\mu_0\mu^2$ for particles having a magnetic dipole moment with μ_0 being the permeability of the vacuum, and d^2/ϵ_0 for particles having an electric dipole moment d with ϵ_0 being the permittivity of the vacuum. In free space, the relative strength of the contact and the dipolar interaction is determined by the dimensionless parameter $\varepsilon_{dd}^0 = a_{dd}/a_s$ with the so-called dipolar length $a_{dd} = mC_{dd}/12\pi\hbar^2$.

Now, we consider the particles to be trapped in a deep three-dimensional simple cubic optical lattice described by the trapping potential $U(\mathbf{r}) = U_L \sum_i \sin^2(q_L r_i)$, where $i \in \{x, y, z\}$, U_L is the lattice depth and $q_L = 2\pi/\lambda$ is the lattice vector with λ being the laser wavelength and the lattice period is given by $l = \lambda/2$. The typical energy scale of a particle in a lattice is the recoil energy $E_R = \hbar^2 q_L^2/2m$ and the strength of the lattice can be characterized by the dimensionless parameter $s = U_L/E_R$. In the case of a deep lattice, we have $s \gg 1$. In this regime, one can assume that only the lowest Bloch band is occupied (in practice this is a good approximation already for $s \sim 10$ [295]) and we can rewrite the field operators $\Psi(\mathbf{r})$ and $\Psi^\dagger(\mathbf{r})$ in terms of the Wannier functions $w(\mathbf{r} - \mathbf{r}_i)$ localized around the lattice site i at position $\mathbf{r}_i$

$$\Psi(\mathbf{r}) = \sum_i w(\mathbf{r} - \mathbf{r}_i) a_i \tag{8.3}$$

with the bosonic annihilation operator a_i at lattice site i. The annihilation operators in real and quasi-momentum space are connected via a discrete Fourier transform

$$a_i = \frac{1}{\sqrt{N_L}} \sum_{\mathbf{k}\in K} a_{\mathbf{k}} e^{-i\mathbf{k}\mathbf{r}_i} , \tag{8.4}$$

where N_L denotes the number of lattice sites and the summation over $\mathbf{k}$ is restricted to the first Brillouin zone K. Using these transformations, the single-particle term of the Hamiltonian becomes diagonal and the total Hamiltonian can be written as

$$H = \sum_{\mathbf{k}} \epsilon_{\mathbf{k}} a_{\mathbf{k}}^\dagger a_{\mathbf{k}} + \frac{1}{2} \sum_{i,j,l,m} V_{ijlm} a_i^\dagger a_j^\dagger a_l a_m . \tag{8.5}$$

The dispersion relation of a particle in a deep lattice is given by

$$\epsilon_{\mathbf{k}} = -2t \left(\sum_{i=x,y,z} \cos(k_i l) - 3 \right) , \tag{8.6}$$

where the hopping amplitude t is related to the lattice depth U_L, the recoil energy E_R and the lattice spacing l [296]. Note that the zero of energy is shifted such that $\epsilon_0 = 0$. In the interaction part of Eq. (8.5), the matrix elements V_{ijlm} are given in terms of the Wannier functions

$$V_{ijlm} = \int d^3r \int d^3r'\, w^*(\mathbf{r}-\mathbf{r}_i)w^*(\mathbf{r}'-\mathbf{r}_j)V(\mathbf{r}-\mathbf{r}')w(\mathbf{r}'-\mathbf{r}_l)w(\mathbf{r}-\mathbf{r}_m)\,. \tag{8.7}$$

For deep lattices, the Wannier functions are well localized and the contribution due to the contact interaction is only significant if $i = j = l = m$, such that we may write

$$V_{ij}^{\text{contact}} = \delta_{ij}\, g_0 \int d^3r\, |w(\mathbf{r})|^4 \equiv g\delta_{ij}\,. \tag{8.8}$$

Approximating the Wannier function at a given lattice site by the ground state wavefunction of an harmonic oscillator, g can be calculated explicitly as [296]

$$g = g_0 \frac{(2\pi)^{3/2}}{l^3} s^{3/4}\,. \tag{8.9}$$

For the dipolar part, we replace the Wannier functions by δ-functions,

$$w^*(\mathbf{r}-\mathbf{r}_i)w(\mathbf{r}-\mathbf{r}_m) \approx \delta_{im}\delta(\mathbf{r}-\mathbf{r}_i)\,. \tag{8.10}$$

The matrix elements now only depend on sites i and j and are given by

$$V_{ij} = g\delta_{ij} + \frac{C_{dd}}{4\pi}\frac{1-3\cos^2\theta_{ij}}{|\mathbf{r}_i-\mathbf{r}_j|^3}\,, \tag{8.11}$$

with θ_{ij} being the angle between sites i and j. Note that the on-site contribution from the dipolar part is zero for an isotropic confinement at each lattice site. The Hamiltonian in Eq. (8.5) then reduces to

$$H = \sum_{\mathbf{k}} \epsilon_{\mathbf{k}} a_{\mathbf{k}}^\dagger a_{\mathbf{k}} + \frac{1}{2}\sum_{i,j} V_{ij} n_i n_j\,. \tag{8.12}$$

Taking into account the spatial structure of the Wannier states and computing the matrix elements in Eq. (8.7) explicitly gives rise to additional processes such as density-assisted and correlated tunneling [322, 323]. These processes are strongly suppressed for deep lattices due to the exponential decay of the Wannier functions,

but can lead to additional corrections for moderate lattice depths. The role of these terms is discussed in Appendix 8.A.2.

For what follows, we also need to transform the interaction part of Eq. (8.5) into momentum space which requires the discrete Fourier transform of the interaction potential and might be written as

$$V(\mathbf{k}) \equiv V_{\mathbf{k}} = g\left(1 + \varepsilon_{dd}\frac{3}{4\pi}\sum_j e^{i\mathbf{k}\mathbf{r}_j}\frac{1-3\cos^2\theta_j}{|\mathbf{j}|^3}\right), \tag{8.13}$$

where the parameter ε_{dd} is renormalized by the lattice and related to its free space variant by

$$\varepsilon_{dd} = \frac{\varepsilon_{dd}^0}{l^3\int d^3r\,|w(\mathbf{r})|^4} = \frac{\varepsilon_{dd}^0}{(2\pi)^{3/2}s^{3/4}}. \tag{8.14}$$

The last result was obtained using Eq. (8.9). The exact form of $V_{\mathbf{k}}$ can be obtained analytically under our approximations (see Appendix 8.A.1) and leads to noticeable differences with respect to the free space Fourier transform in which $V_{\mathbf{k}}$ only depends on the angle between $\mathbf{k}$ and the direction of the polarization of the dipoles but not on the magnitude of $\mathbf{k}$.

8.1.1. Beyond-Mean-Field Corrections

In order to calculate the beyond-mean-field energy corrections, we restrict ourselves to the case where the system is in the superfluid phase and the mean-field approach correctly describes its properties. The correction to the mean-field energy is then given by [278]

$$\frac{E_0^{(2)}}{V} - \frac{1}{2}n\mu^{(2)} = \frac{1}{2}\int_K \frac{d^3k}{(2\pi)^3}\frac{(\epsilon_{\mathbf{k}} + nV_{\mathbf{k}} - E_{\mathbf{k}})(\epsilon_{\mathbf{k}} - E_{\mathbf{k}})}{2E_{\mathbf{k}}}, \tag{8.15}$$

where $V = N_L l^3$ is the volume of the system, $n = N/V$ the density, and $\mu^{(2)}$ denotes the second-order correction to the chemical potential, which is related to the energy by $\mu = d(E/V)/dn$. The Bogoliubov dispersion relation $E_{\mathbf{k}}$ is given by $E_{\mathbf{k}} = \sqrt{\epsilon_{\mathbf{k}}(\epsilon_{\mathbf{k}} + 2nV_{\mathbf{k}})}$ with the noninteracting single-particle dispersion $\epsilon_{\mathbf{k}}$ in Eq. (8.6) and the (discrete) Fourier transform of the dipolar potential $V_{\mathbf{k}}$. We note that as the integration is restricted to the first Brillouin zone, the result is in principle always convergent and no renormalization is needed. We will now study the structure of the correction for different cases, starting for simplicity with the contact interactions.

Contact Interaction

For a purely contact interacting Bose gas, we have $V_{\mathbf{k}} = g$ and thus no momentum dependence of the interaction potential. In order to simplify the integral on the right-hand side of Eq. (8.15) and to make it dimensionless, we introduce the effective mass $m^* = \hbar^2/(2tl^2)$ and the healing length $\xi^2 = \hbar^2/(2m^*ng)$. We further introduce the dimensionless parameter $\alpha = \xi^2/l^2 = t/ng$, which parametrizes the relative strength of the interaction. Staying in the superfluid phase requires $\alpha \gg 1$. Using the substitution $k_i l = u_i l/\xi = u_i/\sqrt{\alpha}$, the integral in Eq. (8.15) reduces to

$$\frac{1}{2}ng\frac{1}{l^3\alpha^{3/2}}\int_{-\pi\sqrt{\alpha}}^{\pi\sqrt{\alpha}}\frac{d^3u}{(2\pi)^3}\frac{(\epsilon_{\mathbf{u}}+1-E_{\mathbf{u}})(\epsilon_{\mathbf{u}}-E_{\mathbf{u}})}{2E_{\mathbf{u}}} \tag{8.16}$$

with $\epsilon_{\mathbf{u}} = -2\alpha\left(\sum_{i=x,y,z}\cos(u_i/\sqrt{\alpha}) - 3\right)$ and $E_{\mathbf{u}} = \sqrt{\epsilon_{\mathbf{u}}(\epsilon_{\mathbf{u}}+2)}$. The prefactor $ng/(\alpha^{3/2}l^3)$ in front of the integral can equivalently be written as

$$\frac{ng}{l^3\alpha^{3/2}} = \frac{(ng)^{5/2}(2m^*)^{3/2}}{\hbar^3}\,. \tag{8.17}$$

This is, up to a constant numerical factor, exactly the form of the LHY correction in the absence of the optical lattice such that its effects are contained solely in the integral

$$I(\alpha) = \frac{1}{2}\int_{-\pi/\sqrt{\alpha}}^{\pi/\sqrt{\alpha}}\frac{d^3u}{(2\pi)^3}\frac{(\epsilon_{\mathbf{u}}+1-E_{\mathbf{u}})(\epsilon_{\mathbf{u}}-E_{\mathbf{u}})}{2E_{\mathbf{u}}}\,. \tag{8.18}$$

In the limit $\alpha \to \infty$, which corresponds to free space, the integral $I(\alpha)$ can be calculated analytically and approaches the constant $I(\alpha \to \infty) = -1/15\sqrt{2}\pi^2$ such that

$$\frac{E_0^{(2)}}{V} - \frac{1}{2}n\mu^{(2)} = \frac{(ng)^{5/2}(2m^*)^{3/2}}{\hbar^3}\left(-\frac{1}{15\sqrt{2}\pi^2}\right)\,. \tag{8.19}$$

Solving the differential equation with the initial condition $E_0^{(2)}(n=0) = 0$ ensuring the correct mean-field result, one recovers the well-known free space LHY term

$$\frac{E_0^{(2)}}{V} = \frac{8}{15\pi^2}\frac{(m^*)^{3/2}(ng)^{5/2}}{\hbar^3} \tag{8.20}$$

with an effective mass accounting for the underlying lattice structure. For finite α, one can compute the integral numerically and the result is shown in Fig. 8.2. As expected, there are corrections to the free space value at finite α which introduces an additional density dependence to the right hand side of Eq. (8.15). We discuss this additional density dependence and its influence on the beyond-mean-field energy corrections below

Dipolar Interaction

We now turn to the case of dipolar interactions. It is interesting to study both the differences which arise with respect to the contact interaction case as well as the effect of the lattice on the dipolar gas. In order to achieve better understanding of the role of the lattice, we first approximate the lattice Fourier transform of the dipolar interaction which is derived in Appendix 8.A.1 by the free space Fourier transform

$$V_{dd}^{\text{free}}(\mathbf{k}) = g\varepsilon_{dd}\left(3\frac{k_z^2}{k_x^2+k_y^2+k_z^2}-1\right), \tag{8.21}$$

which only depends on the angle between $\mathbf{k}$ and the direction of polarization of the dipoles (which is assumed to be the z-axis). The integral $I(\alpha)$ can only be calculated numerically for finite α and the results for different values of ε_{dd} are shown in Fig. 8.2. The asymptotic value for $\alpha \to \infty$ can again be calculated analytically and reads

$$I(\alpha\to\infty) = -\frac{1}{15\sqrt{2}\pi^2}F(\varepsilon_{dd}) \tag{8.22}$$

with $F(\varepsilon_{dd}) = \frac{1}{2}\int_{-1}^{1} du\,(1+\varepsilon_{dd}(3u^2-1))^{5/2}$ accounting for the anisotropic nature of the dipolar interaction (see also [280]). In the absence of dipolar interactions, it reduces to $F(0)=1$. In the case of finite α, the integral $I(\alpha)$ leads to corrections qualitatively similar as in the case of contact interaction, while their magnitude increases with increasing ε_{dd}.

The effect of the dipolar interaction is even more enhanced when taking the full lattice Fourier transform of the dipolar interaction as derived in Sec. 8.A.1. For $\alpha \to \infty$, $I(\alpha)$ also approaches the free space result and is equivalent to taking the free space Fourier transform in Eq. (8.21), whereas the deviations with respect to the case of contact interaction are more prominent for finite α. This can be understood by comparing the lattice Fourier transform and the free space Fourier transform as shown in Fig. 8.3. In contrast to free space, the lattice Fourier transform of the dipolar potential also depends on the absolute value of the momentum. For large

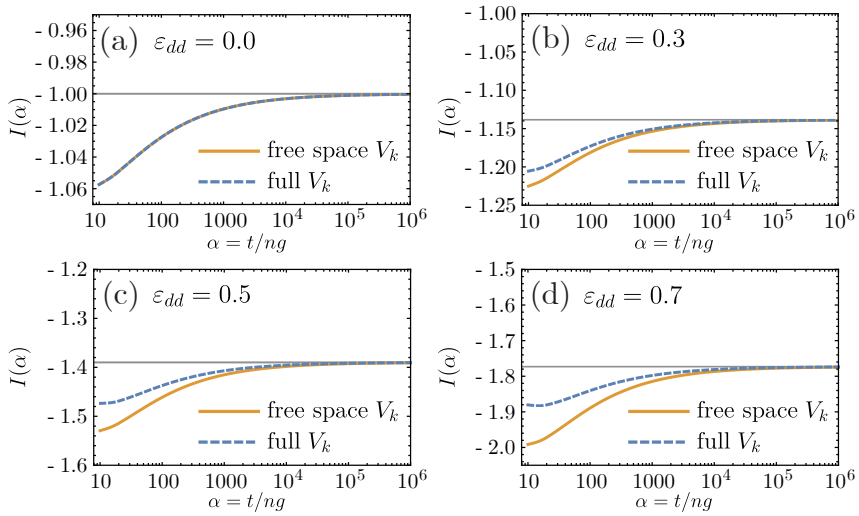

Fig. 8.2.: $I(\alpha)$ coefficient for full (orange solid line) lattice dipolar interaction compared with the free space one (blue dashed line) for several different values of (a) $\varepsilon_{dd} = 0.0$, (b) $\varepsilon_{dd} = 0.3$, (c) $\varepsilon_{dd} = 0.5$ and (d) $\varepsilon_{dd} = 0.7$. For the contact interaction (a), there is no difference between both cases as the interaction potential is constant in momentum space.

values of α, the integral in Eq. (8.15) only gives a contribution near $\mathbf{k} = 0$ where there is little difference between both cases, while for decreasing values of α, the integral also probes higher momenta where the lattice enhances the effect of the dipolar potential.

General Structure of the Energy Correction

In the previous sections, we have seen that in the presence of a deep lattice, corrections to the usual free space behavior arise. These corrections lead to a modified scaling in the density which is discussed in this section. In order to do so, we rewrite Eq. (8.15) expressing the energy density $E_0^{(2)}/V$ in terms of t/l^3, that is $E_0^{(2)}/V = (t/l^3)e_0^{(2)}$. Substituting $n \to t/\alpha g$ and noting that $\frac{d}{dn} = -(\alpha^2 t/g)\frac{d}{d\alpha}$, we end up with the dimensionless differential equation

$$e_0^{(2)} + \frac{1}{2}\alpha\frac{de_0^{(2)}}{d\alpha} = \alpha^{-5/2}I(\alpha) = -\frac{F(\varepsilon_{dd})}{15\sqrt{2}\pi^2}\alpha^{-5/2}(1 + f(\alpha)) \equiv P(\alpha)\,. \quad (8.23)$$

Note that in this expression, all contributions reminiscent of the free space result are written explicitly and the function $f(\alpha)$ provides all the corrections coming from the lattice and $f(\alpha \to \infty) = 0$. The differential equation can formally be

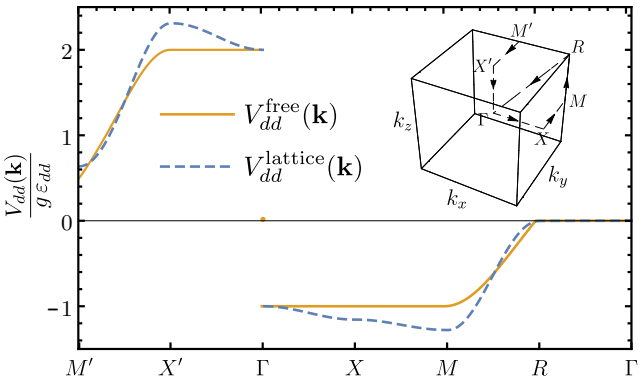

Fig. 8.3.: Comparison between free space (orange solid line) and lattice (blue dashed line) dipolar Fourier transform plotted over the first Brillouin zone.

solved and using the initial condition $e_0^{(2)}(\infty) = 0$ such that we obtain the correct mean-field result, the solution reads

$$e_0^{(2)} = -\frac{1}{\alpha^{-2}} \int_\alpha^\infty dy\, 2P(y)y\,. \tag{8.24}$$

This is the particular solution of Eq. (8.23), while the homogeneous solution would only affect the mean-field energy in which we are not interested right now. From another point of view, one can also solve Eq. (8.15) with an inhomogeneity $G(n)$ which leads to the solution

$$\frac{E_0^{(2)}}{V} = -n^2 \int_0^n dy\, \frac{2G(y)}{y^3}\,. \tag{8.25}$$

Substituting $\alpha = t/ng$ and expressing the energy density in terms of t/l^3 leads to the solution of Eq. (8.24). For the rest of the discussion, we return to the dimensionless form of the solution given in Eq. (8.24). In the presence of the lattice[1], we can split the inhomogeneous term on the right hand side of the differential equation into one part containing the free space result and one part containing the corrections arising from the lattice,

$$P(\alpha) = P_0(\alpha) + \Delta P(\alpha) = -\frac{F(\varepsilon_{dd})}{15\sqrt{2}\pi^2}\alpha^{-5/2}(1 + f(\alpha))\,. \tag{8.26}$$

[1]The following discussion is essentially more general provided that there exists a dimensionless parameter such that the inhomogeneity has the same scaling as in free space in some limit of this parameter.

The first term gives rise to the standard result in free space $e_0^{(2)} = \frac{4\,F(\varepsilon_{dd})}{15\sqrt{2}\pi^2}\alpha^{-5/2}$ which leads to the beyond-mean-field correction

$$\frac{E_0^{(2)}}{V} = \frac{4F(\varepsilon_{dd})}{15\sqrt{2}\pi^2}\frac{(2m^*)^{3/2}(ng)^{5/2}}{\hbar^3}\,. \tag{8.27}$$

For the second part, we see from Fig. 8.2 that we can describe the corrections due to the lattice by a function $f(\alpha) = c\alpha^{-\gamma}$ for $\alpha \gg 1$. The parameters c and γ will in general depend on the relative dipolar interaction strength ε_{dd} and will later be determined by fitting the expression to the numerically calculated $I(\alpha)$. Note that $\gamma > 0$ as $f(\alpha \to \infty) = 0$. Thus, the energy correction due to the second part reads

$$\Delta e_0^{(2)} = \frac{F(\varepsilon_{dd})}{15\sqrt{2}\pi^2}\frac{2c}{\alpha^3}\int_\alpha^\infty dy\, y^{-3/2-\gamma} = \frac{4F(\varepsilon_{dd})}{15\sqrt{2}\pi^2}\frac{c}{1+2\gamma}\alpha^{-5/2-\gamma}\,. \tag{8.28}$$

Finally, the complete beyond-mean-field energy correction reads

$$\frac{E_0^{(2)}}{V} = \frac{8}{15\pi^2}\frac{(m^*)^{3/2}(ng)^{5/2}}{\hbar^3}F(\varepsilon_{dd})\left(1 + \frac{c}{1+2\gamma}\left(\frac{ng}{t}\right)^\gamma\right)\,. \tag{8.29}$$

Since $\gamma > 0$, the correction to the beyond-mean-field correction to the ground state energy due to the lattice increases with increasing density. In the limit $t \gg ng$, Eq. (8.29) reduces to the free space result with a renormalized mass as discussed before. For the present setup of a three-dimensional simple cubic lattice, we determine the coefficients c and γ by fitting to the results obtained using numerical integration. For the scaling coefficients, we get $\gamma \approx 1/2$ independent of ε_{dd} and valid also for contact interactions, whereas the coefficient c ranges from $c \approx 0.3$ for $\varepsilon_{dd} = 0$ to $c \approx 0.76$ for $\varepsilon_{dd} = 0.7$.

8.2. Weak One-Dimensional Lattice

Up to now, we have considered a three-dimensional optical lattice. However, an additional intriguing possibility is to restrict the lattice to one dimension and play with the relative orientation of the dipoles and the wave vector of the lattice. In this section, we demonstrate that this generates additional corrections to the usual beyond-mean-field corrections that can be enhanced or diminished depending on the relative orientation between the lattice and the dipoles. The basic assumption of our analysis is that the lattice is weak and can be treated as a perturbation to the free space case and we do not restrict ourselves to the lowest Bloch band.

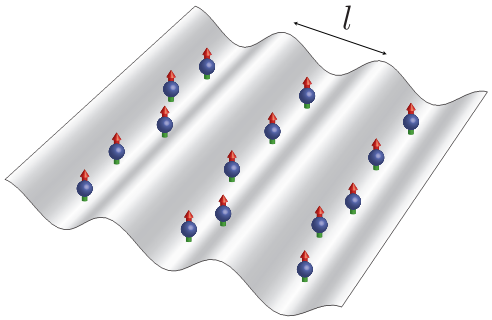

Fig. 8.4.: Schematic illustration of particles in a weak one-dimensional optical lattice with lattice spacing l. The dipoles are only very weakly trapped along one dimension.

8.2.1. Model

The one-dimensional lattice potential is given as

$$U(\mathbf{r}) = U_L \sin^2(\mathbf{q}_L \mathbf{r})\,, \tag{8.30}$$

where, as before, $q_L = \pi/l$ is the lattice vector and l is the lattice period (see also Fig. 8.4). The orientation of the lattice relative to the dipole axis, which we assume to be parallel to the z-axis, can be varied by varying the direction of the lattice vector $\mathbf{q}_L$. In the presence of this lattice, the eigenfunctions of the noninteracting problem are given in terms of a product of plane waves (in those directions where no lattice is present) and Bloch functions (in the direction of the lattice),

$$\psi_{\mathbf{k}}(\mathbf{r}) = e^{i\mathbf{k}_\perp \mathbf{r}} \phi_{k_\parallel}(\mathbf{r}_\parallel)\,. \tag{8.31}$$

In this basis, the single-particle part of the Hamiltonian is diagonal with $H_0 = \sum_{\mathbf{k}} \epsilon_{\mathbf{k}} a^\dagger_{\mathbf{k}} a_{\mathbf{k}}$, where $\epsilon_{\mathbf{k}} = \hbar^2 \mathbf{k}_\perp^2/2m + \tilde{\epsilon}_k$. The components of $\mathbf{k}$ that are parallel to the lattice are restricted to the first Brillouin zone, $k \in [-\pi/l, \pi/l]$. In general, the lattice dispersion $\tilde{\epsilon}_k$ cannot be written down in closed form for arbitrary lattice depth while for weak lattices there are approximations (see Appendix 8.B). As for the deep lattice, we introduce the recoil energy $E_R = \hbar^2 q_L^2/2m$ and the dimensionless lattice depth $s = U_L/E_R$ which for a weak lattice is assumed to be much smaller than one, that is $s \ll 1$.

8.2.2. Contact Interaction

We proceed as in the previous section and start with the contact interaction where the interaction part of the Hamiltonian takes the form

$$H_{int} = \frac{g}{2V} \sum_{\mathbf{k},\mathbf{k}',\mathbf{q}} a^\dagger_{\mathbf{k}+\mathbf{q}} a^\dagger_{\mathbf{k}'-\mathbf{q}} a_{\mathbf{k}} a_{\mathbf{k}'} \,. \tag{8.32}$$

We now apply the Bogoliubov theory following e.g. [318], which leads to the excitation spectrum

$$E_{\mathbf{k}} = \sqrt{\epsilon_{\mathbf{k}}(\epsilon_{\mathbf{k}} + 2ng)} \tag{8.33}$$

as well as the beyond-mean-field contributions to the ground state energy per volume

$$\frac{\Delta E_0}{V} = \frac{1}{2V} \sum_{\mathbf{k}} (E_{\mathbf{k}} - (\epsilon_{\mathbf{k}} + ng)) \,. \tag{8.34}$$

Since the lattice is assumed to be weak, the dispersion $\epsilon_{\mathbf{k}}$ will only have small deviations from the dispersion in free space such that we can split the result into a term corresponding to the free space result, the well-known LHY term, and one additional term which includes all the corrections to it. The free space result diverges which can be cured by a proper renormalization of the coupling constant g (see e.g. [318]). We focus here on the remaining corrections to the LHY term due to the lattice which can be expressed as

$$\frac{\Delta E^s_0}{V} = \frac{1}{2} \int \frac{d^3k}{(2\pi)^3} (E^s_{\mathbf{k}} - E^0_{\mathbf{k}} - (\epsilon^s_{\mathbf{k}} - \epsilon^0_{\mathbf{k}})) \,, \tag{8.35}$$

where $E^s_{\mathbf{k}}$ ($\epsilon^s_{\mathbf{k}}$) and $E^0_{\mathbf{k}}$ ($\epsilon^0_{\mathbf{k}}$) denote the Bogoliubov excitation spectrum (single-particle dispersion) in the presence of the lattice and in free space, respectively.

Similarily to the case of a deep lattice, we introduce a dimensionless quantity

$$\beta^2 = \frac{E_R}{ng} = \pi^2 \frac{\xi^2}{l^2} = \pi^2 \alpha \tag{8.36}$$

which compares the healing length ξ with the optical lattice period l.

As we are only interested in a weak lattice, we calculate the beyond-mean-field corrections due to the lattice given in Eq. (8.35) to leading order in s, for which analytical results can be obtained (see Appendix 8.B for further details). The general dependence of the beyond-mean-field corrections on the parameter β in the

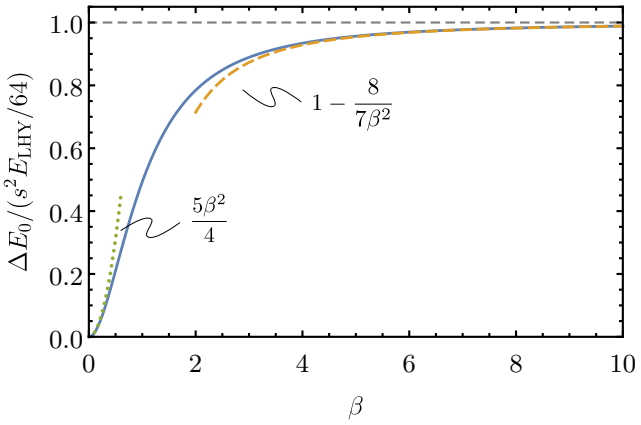

Fig. 8.5.: (Blue solid): General dependence of the beyond-mean-field correction to the energy on the parameter β. (Green dotted): Asymptotic behaviour for $\beta \to 0$. (Orange dashed): Asymptotic behaviour for $\beta \to \infty$.

case of a contact-interacting Bose gas is shown in Fig. 8.5 (blue/solid line) and also includes the leading behaviour in the limits $\beta \ll 1$ (green/dash-dotted line) and $\beta \gg 1$ (orange/dashed line) which are discussed below.

In the limit of $\beta \to 0$, which corresponds to $l/\xi \gg 1$, the leading behaviour of Eq. 8.96 is given by

$$\frac{\Delta E_0^2}{V} = \frac{E_{\mathrm{LHY}}}{V} s^2 \beta^2 \frac{5}{256} \to 0 \tag{8.37}$$

with the usual LHY correction

$$\frac{E_{\mathrm{LHY}}}{V} = \frac{8}{15\pi^2} \frac{m^{3/2}(ng)^{5/2}}{\hbar^3} \,. \tag{8.38}$$

The vanishing influence of the lattice in this case is intuitively clear as the limit $l/\xi \gg 1$ indeed should correspond to free space.

In the opposite limit, $\beta \to \infty$ ($l/\xi \ll 1$), the correction instead approaches a constant and reads

$$\frac{\Delta E_0^s}{V} = \frac{E_{\mathrm{LHY}}}{V} \frac{s^2}{64} \,. \tag{8.39}$$

Combing this with the mean-field energy, the ground state energy per volume is given by

$$\frac{E_0}{V} = \left(\frac{n^2 g}{2} + \frac{E_{\mathrm{LHY}}}{V} \right) \left(1 + \frac{s^2}{64} \right) \,. \tag{8.40}$$

Both the mean-field term and the beyond-mean-field term are enhanced by the presence of the lattice in the same way in the leading order. The correction to the mean-field term comes from the correction to the $k = 0$ mode due to the coupling to modes with $k = \pm q_L$ in the presence of the lattice.

Interestingly, this result can also be obtained when assuming that the bosons are in free space but acquire an anisotropic effective mass along the direction of the lattice (say in z-direction) with $m_z = m/(1 - s^2/32) = m/\gamma^2$ to leading order in s. This immediately leads to

$$E_{\mathrm{LHY}} \to \gamma^{-1} E_{\mathrm{LHY}} \approx \left(1 + \frac{s^2}{64}\right) E_{\mathrm{LHY}} \,. \tag{8.41}$$

Figure 8.5 shows that the asymptotic value for $\beta \gg 1$ is already approached for β on the order of 10. This suggests that describing the system as a free space gas with an effective anisotropic mass should be adequate already at values of β on the order of 10 which corresponds to $\xi \approx 3l$. Typically, the lattice period is on the order of a few hundred nanometers while the healing length is on the order of micrometers for standard cold atom experiments [295] such that this approximation can be used in typical experiments.

8.2.3. Dipolar Interactions

After having discussed the case of a contact-interacting gas, we turn to the case where the particles interact via dipolar interactions given by the interaction potential

$$V_{dd}(\mathbf{r}) = g\epsilon_{dd} \frac{1 - 3\cos^2\theta}{r^3} \,, \tag{8.42}$$

where θ is the angle between the direction of the dipole moment, which is assumed to be parallel to the z-axis and the relative position of the two particles given by $\mathbf{r}$. As we are only concerned about the leading-order corrections for small values of s, we can consistently neglect the weak lattice effect on the interaction potential and use the free space formula

$$V_{\mathbf{k}} = g\left(1 + \varepsilon_{dd}\left(3\frac{k_z^2}{k_x^2 + k_y^2 + k_z^2} - 1\right)\right) \equiv g\tilde{V}_{\mathbf{k}} \,. \tag{8.43}$$

In contrast to the contact-interacting case, the integrals cannot be solved analytically for arbitrary β. However, the previous analysis suggested to view the limit $\beta \to \infty$, or equivalently $l/\xi \ll 1$, as nothing else but a gas in free space with

an anisotropic effective mass. In the following, we make use of this simplification and derive the corrections due to the weak lattice potential along an arbitrary direction. In the end, we discuss two special limits when the lattice is parallel and perpendicular to the polarization axis of the dipoles.

Since the dipole potential is invariant under rotation around the z-axis, the final results can only depend on the angle η between the direction of the polarization of the dipoles, which is assumed to be the z-axis, and the lattice vector $\mathbf{q}_L$. For simplicity, we choose the lattice wave vector to be in the yz-plane. Introducing the effective mass $m_{\text{eff}} = m/\gamma^2$ with $\gamma^2 = 1 - s^2/32$, the dispersion relation reads

$$\epsilon_{\mathbf{k}} = \frac{\hbar^2}{2m}\left(k_x^2 + (k_y\cos\eta + k_z\sin\eta)^2 + \gamma^2(k_z\cos\eta - k_y\sin\eta)^2\right) . \tag{8.44}$$

The correction to the ground state energy can now be calculated according to Eq. (8.15) with the difference that we integrate over the whole momentum space and use Eqs. (8.44) and (8.43) for the single-particle dispersion and interaction potential, respectively. The integrals are most conveniently performed in spherical coordinates and the beyond-mean-field corrections for a dipolar Bose gas in the presence of a weak one-dimensional lattice read (see Appendix 8.B for details)

$$\frac{E_0^{(2)}}{V} = \frac{8}{15\pi^2}\frac{(ng)^{5/2}m^{3/2}}{\hbar^3}\left\{F(\varepsilon_{dd}) + \frac{s^2}{64}\left[F(\varepsilon_{dd}) + \frac{1}{2}(3\cos^2\eta - 1)H(\varepsilon_{dd})\right]\right\} \tag{8.45}$$

with $F(\varepsilon_{dd}) = \frac{1}{2}\int_{-1}^{1} du\,(1+\varepsilon_{dd}(3u^2-1))^{5/2}$ and $H(\varepsilon_{dd}) = \frac{1}{2}\int_{-1}^{1} du\,(1+\varepsilon_{dd}(3u^2-1))^{5/2}(3u^2-1)$.

The energy correction thus has the following form: The first term inside the curly brackets is the usual LHY correction in the case of a dipolar gas in free space [280]. The second term accounts for the influence of the lattice and has two parts. The first term is isotropic, has the same structure as in free space and can be explained by an effective mass in one direction. The other part proportional to $H(\varepsilon_{dd})$ is clearly anisotropic in the sense that it depends on the orientation of the lattice with respect to the dipoles. In Fig. 8.6, we plot the function $F(\varepsilon_{dd}) + 1/2(3\cos^2\eta - 1)H(\varepsilon_{dd})$ for different values of the tilting angle η between lattice wave vector and polarization of the dipoles. When the lattice is oriented parallel to the dipoles ($\eta = 0$, blue/solid line), the corrections are enhanced and monotonically increase with increasing ε_{dd}. In this setup, the dipoles are directed by the trapping potential to arrange in a side-by-side configuration so that the fluctuations have mainly repulsive character. On the other hand, when the lattice is orientated perpendicular to the dipoles ($\eta = \pi/2$, red/dotted line), the correction

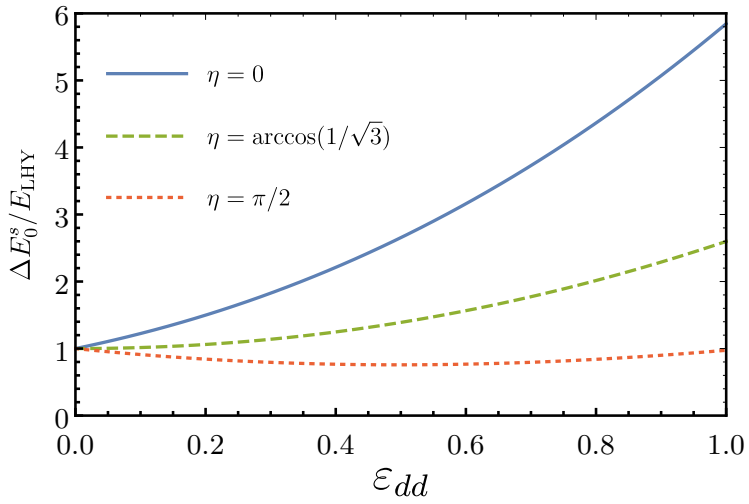

Fig. 8.6.: Leading-order correction to the beyond-mean-field contribution of the ground state energy as a function of the relative dipole interaction strength ε_{dd} for different tilting angles η between the polarization axis of the dipoles and the wave vector of the lattice. The angle $\eta = 0$ (blue solid line) corresponds to the case where the lattice wave vector is parallel to the dipoles, the angle $\eta = \pi/2$ (red dotted line) corresponds to the case where the lattice is applied perpendicular to the dipoles. At $\eta = \arccos(1/\sqrt{3}) \approx 54.7\,^\circ$, the anisotropic correction vanishes and only the isotropic correction contributes (green dashed line).

first decreases for small ε_{dd}, reaches a minimum and finally increases for larger ε_{dd}. In contrast to the parallel orientation, the dipoles are now dragged to the head-tail configuration such that the attractive character of the fluctuations is enhanced. In this case, the correction is also much smaller than in the case where the lattice is oriented parallel to the dipoles. At the 'magic angle' $\eta = \arccos(1/\sqrt{3}) \approx 54.7\,^\circ$, the anisotropic correction vanishes and only the isotropic correction contributes (green/dashed line).

8.2.4. Mean-Field Terms

In the above discussion, we have so far neglected the contributions coming from the mean field terms which also have an isotropic and anisotropic part where the latter comes from the orientation of the lattice relative to the dipoles. The mean field terms can be written as

$$\frac{E_{MF}}{V} = \frac{1}{2} n^2 g + \frac{s^2}{64} \left(\frac{n^2 g}{2} (1 + \varepsilon_{dd}(3\cos^2\eta - 1)) \right) . \tag{8.46}$$

The first term is the usual contribution from the chemical potential in free space in the absence of any lattice. The second part is the leading-order correction to the mean field energy in the presence of a weak lattice and provides an anisotropic correction. The anisotropic correction has the same functional dependence on the angle between the lattice wave vector and the polarization axis of the dipoles but, apart from the different scaling in the density, a different functional dependence on the relative dipole interaction strength ε_{dd}. While the mean field term goes linearly with ε_{dd} for all values, the function $H(\varepsilon_{dd}) \approx 2\varepsilon_{dd} + 6/7\varepsilon_{dd}^2$ is linear only for small values of ε_{dd}.

8.3. Conclusions

In this chapter, we studied the effects of an optical lattice on the beyond-mean-field corrections for a dipolar Bose gas with emphasis on the ability to control and manipulate the strength of these corrections with respect to the depth and the orientation of the lattice. In the case of a deep three-dimensional lattice, the presence of the lattice introduces a nontrivial density dependence of the beyond-mean-field terms whose form is independent of the strength of the dipolar interaction but whose strength can be enhanced by increasing the dipolar interaction strength. For a weak one-dimensional lattice, we find that the strength of the beyond-mean-field corrections can be controlled by manipulating the relative orientation of the lattice and the dipole axis. In view of the current experiments on dipolar quantum droplets, we would like to point out that our results of the study of the deep optical lattice are not directly applicable to these droplets due to the missing cancellation of the mean-field contributions. However, our results for the weak one-dimensional case might be of importance for future experiments with droplets in weak lattices.

Appendix

8.A. Dipolar Interactions in a Deep Lattice

8.A.1. Lattice Fourier Transform

In this section, we present the calculation of the discrete Fourier transform of the dipolar potential as given in Eq. (8.13). The calculation is based on the analogous one performed in two dimensions [324] extended to three dimensions. Note that in this section, we denote the summation over lattice sites by $\sum_{\mathbf{R}}$ and measure all lengths and momenta in terms of the lattice spacing and the inverse lattice spacing, respectively.

The lattice Fourier transformation of the dipolar interaction can be written as

$$V_{dd}(\mathbf{k}) = g\,\varepsilon_{dd}\frac{3}{4\pi}\sum_{\mathbf{R}\neq 0}\frac{R^2-3z^2}{R^5}e^{i\mathbf{k}\mathbf{R}}\,, \tag{8.47}$$

which we may rewrite as

$$V_{dd}(\mathbf{k}) = g\,\varepsilon_{dd}\frac{3}{4\pi}\left(\chi^3(\mathbf{k})+3\frac{\partial^2}{\partial k_z^2}\chi^5(\mathbf{k})\right)\,, \tag{8.48}$$

with

$$\chi^n(\mathbf{k}) = \sum_{\mathbf{R}\neq 0}\frac{1}{R^n}e^{i\mathbf{k}\mathbf{R}}\,. \tag{8.49}$$

Note that in three dimensions, both $\chi^3(\mathbf{k})$ as well as $\frac{\partial^2}{\partial k_z^2}\chi^5(\mathbf{k})$ are divergent for $\mathbf{k}\to 0$. However, as will be shown, the sum of both contributions leads to a finite result which is nonanalytic for $\mathbf{k}\to 0$.

Calculation of χ^n

In order to calculate χ^n, we note the following identity

$$\frac{1}{R^n} = \frac{1}{\Gamma(n/2)} \int_0^\infty du\, e^{-uR^2} u^{\frac{n}{2}-1}, \quad n > 0\,, \tag{8.50}$$

where $\Gamma(m)$ denotes the Gamma function. In the end, we will be interested in $n = 3$ and $n = 5$. Using the above identity and splitting the integral into regions from 0 to η and η to ∞, we arrive at

$$\begin{aligned}\sum_{\mathbf{R}\neq 0} \frac{1}{R^n} e^{i\mathbf{k}\mathbf{R}} &= \frac{1}{\Gamma(n/2)} \sum_{\mathbf{R}\neq 0} \left(\int_0^\eta + \int_\eta^\infty \right) du\, e^{-uR^2} u^{\frac{n}{2}-1} e^{i\mathbf{k}\mathbf{R}} \\ &= \frac{\eta^{n/2}}{\Gamma(n/2)} \sum_{\mathbf{R}\neq 0} \left(\int_1^\infty du\, e^{-\frac{\eta R^2}{u}} u^{-\frac{n}{2}-1} + \int_1^\infty du\, e^{-\eta u R^2} u^{\frac{n}{2}-1} \right) e^{i\mathbf{k}\mathbf{R}}\,.\end{aligned} \tag{8.51}$$

In the second step, we have rescaled u by η/u for the first integral and by ηu in the second one. The parameter η is the so-called Ewald parameter and determines the boundary between the summation in real space and the summation in the momentum space. In the end, this parameter should be chosen such that convergence is achieved rapidly for both sums. However, the result is independent of the choice of η.

Next, we use Poisson's summation formula to turn the sum of the first part in Eq. (8.51) into a sum in momentum space. In d dimensions, Poisson's summation formula applied to our case reads

$$\sum_{\mathbf{R}\neq 0} e^{-aR^2} e^{i\mathbf{k}\mathbf{R}} = \sum_{\mathbf{R}} e^{-aR^2} e^{i\mathbf{k}\mathbf{R}} - 1 = \frac{\pi^{d/2}}{a^{d/2}} \sum_{\mathbf{q}} e^{-\frac{|\mathbf{q}+\mathbf{k}|^2}{4a}} - 1\,. \tag{8.52}$$

With $a = \eta/u$ and $d = 3$, we arrive at

$$\begin{aligned}\chi^n(\mathbf{k}) &= \frac{\eta^{n/2}}{\Gamma(n/2)} \left(\frac{\pi^{3/2}}{\eta^{3/2}} \sum_{\mathbf{q}} \int_1^\infty du\, u^{-\frac{n}{2}+\frac{1}{2}} e^{-\frac{u}{4\eta}|\mathbf{q}+\mathbf{k}|^2} - \frac{2}{n} \right. \\ &\quad \left. + \sum_{\mathbf{R}\neq 0} \int_1^\infty du\, e^{-\eta u R^2} u^{\frac{n}{2}-1} e^{i\mathbf{k}\mathbf{R}} \right) \\ &= \frac{\eta^{n/2}}{\Gamma(n/2)} \left(\frac{\pi^{3/2}}{\eta^{3/2}} \sum_{\mathbf{q}} E_{\frac{n-1}{2}} \left(\frac{|\mathbf{q}+\mathbf{k}|^2}{4\eta} \right) - \frac{2}{n} + \sum_{\mathbf{R}\neq 0} E_{\frac{2-n}{2}}(\pi R^2) e^{i\mathbf{k}\mathbf{R}} \right)\end{aligned} \tag{8.53}$$

with the exponential integral function

$$E_m(x) = \int_1^\infty \frac{e^{-xt}}{t^m}\,. \tag{8.54}$$

Setting $n = 3$ and choosing $\eta = \pi$, we get

$$\chi^3(\mathbf{k}) = 2\pi \left(\sum_{\mathbf{q}} E_1 \left(\frac{|\mathbf{q}+\mathbf{k}|^2}{4\pi} \right) - \frac{2}{3} + \sum_{\mathbf{R}\neq 0} E_{-1/2}(\pi R^2) e^{i\mathbf{k}\mathbf{R}} \right)\,. \tag{8.55}$$

Note that the function $E_1(x)$ diverges logarithmically for $x \to \infty$. This is expected as the sum $\sum_{\mathbf{R}\neq 0} 1/R^3$ diverges logarithmically in three dimensions.

Calculation of the Anisotropic Part

Now we turn to the anisotropic part given by $\frac{\partial^2}{\partial k_z^2}\chi^5(\mathbf{k})$. For $\eta = \pi$ and $n = 5$, we get

$$\chi^5(\mathbf{k}) = \frac{4\pi^2}{3} \left(\sum_{\mathbf{q}} E_2 \left(\frac{|\mathbf{q}+\mathbf{k}|^2}{4\pi} \right) - \frac{2}{5} + \sum_{\mathbf{R}\neq 0} E_{-3/2}(\pi R^2) e^{i\mathbf{k}\mathbf{R}} \right)\,. \tag{8.56}$$

Differentiating the last term twice with respect to k_z, we obtain

$$\frac{\partial^2}{\partial k_z^2} \sum_{\mathbf{R}\neq 0} E_{-3/2}(\pi R^2) e^{i\mathbf{k}\mathbf{R}} = -\sum_{\mathbf{R}\neq 0} z^2\, E_{-3/2}(\pi R^2) e^{i\mathbf{k}\mathbf{R}}\,. \tag{8.57}$$

For the first term, we note the relation

$$E_n'(x) = -E_{n-1}(x) \tag{8.58}$$

and thus have

$$\frac{\partial^2}{\partial k_z^2} \sum_{\mathbf{q}} E_2\left(\frac{|\mathbf{q}+\mathbf{k}|^2}{4\pi}\right) = \sum_{\mathbf{q}} E_0\left(\frac{|\mathbf{q}+\mathbf{k}|^2}{4\pi}\right) \frac{(k_z+q_z)^2}{4\pi^2} - E_1\left(\frac{|\mathbf{q}+\mathbf{k}|^2}{4\pi}\right)\frac{1}{2\pi}\,. \tag{8.59}$$

Finally, we end up with

$$\begin{aligned}\frac{\partial^2}{\partial k_z^2}\chi^5(\mathbf{k}) = \frac{4\pi^2}{3}\Bigg(&\sum_{\mathbf{q}} E_0\left(\frac{|\mathbf{q}+\mathbf{k}|^2}{4\pi}\right)\frac{(k_z+q_z)^2}{4\pi^2} \\ &- E_1\left(\frac{|\mathbf{q}+\mathbf{k}|^2}{4\pi}\right)\frac{1}{2\pi} - \sum_{\mathbf{R}\neq 0} z^2\, E_{-3/2}(\pi R^2) e^{i\mathbf{k}\mathbf{R}}\Bigg)\,.\end{aligned} \tag{8.60}$$

In this expression, we again encounter the diverging part $E_1(x)$ with exactly the prefactor needed in order to cancel the contribution from the isotropic $1/R^3$ part.

Combining everything and using the explicit form of $E_0(x) = e^{-x}/x$, the final result reads

$$\begin{aligned}V_{dd}(\mathbf{k}) = g\,\varepsilon_{dd}\Bigg(&\left(3e^{-\frac{k^2}{4\pi}}\frac{k_z^2}{k^2} - 1\right) + \frac{3}{2}\sum_{\mathbf{R}\neq 0} E_{-1/2}(\pi R^2) \\ &- 2\pi z^2 E_{-3/2}(\pi R^2) e^{i\mathbf{k}\mathbf{R}} + 3\sum_{\mathbf{q}\neq 0} e^{-\frac{|\mathbf{q}+\mathbf{k}|^2}{4\pi}}\frac{(k_z+q_z)^2}{|\mathbf{k}+\mathbf{q}|^2}\Bigg)\,.\end{aligned} \tag{8.61}$$

The first part exactly reproduces the continuous Fourier transform of $V_{dd}(\mathbf{k})$ in the limit $\mathbf{k} \to 0$, while the second part, including the sums, vanishes in this limit as is shown in the next paragraph. Note in addition that this expression can be evaluated numerically very efficiently since the summations converge very quickly. For numerical purposes, it is useful to replace $\mathbf{q} = 2\pi\mathbf{R}$ in the second summation such that convergence is achieved using only a few lattice sites.

In Figures 8.7 and 8.8, the angular dependence of Eq. (8.61) is plotted for different values of k and one can see that in contrast to the free space result, the Fourier transform also depends on the absolute value of $\mathbf{k}$. The corrections to the free space Fourier transform become even more apparent when plotting both functions over the first Brillouin zone of a simple cubic lattice along paths of high symmetry as shown in Fig. 8.3. Around $\mathbf{k} = 0$, there is little difference between both functions, whereas for finite momenta, deviations become clearly visible since the anisotropic structure of the lattice is probed.

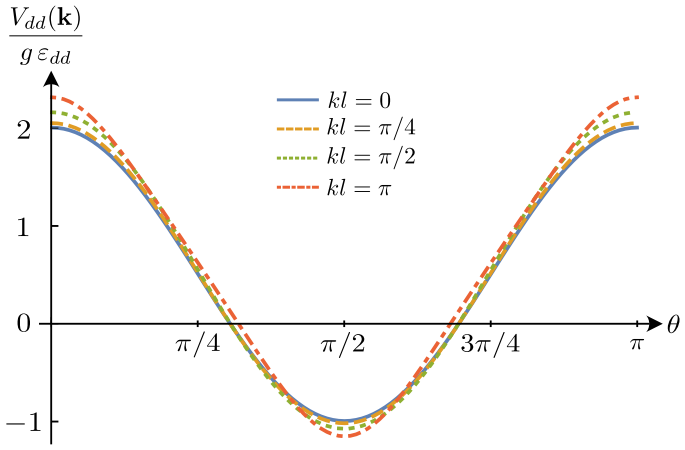

Fig. 8.7.: Angular dependence of the lattice Fourier transform V_k for $kl = 0$ (blue solid), which corresponds to the result in free space, $kl = \pi/4$ (orange dashed), $kl = \pi/2$ (green dotted), and $kl = \pi$ (red dash-dotted).

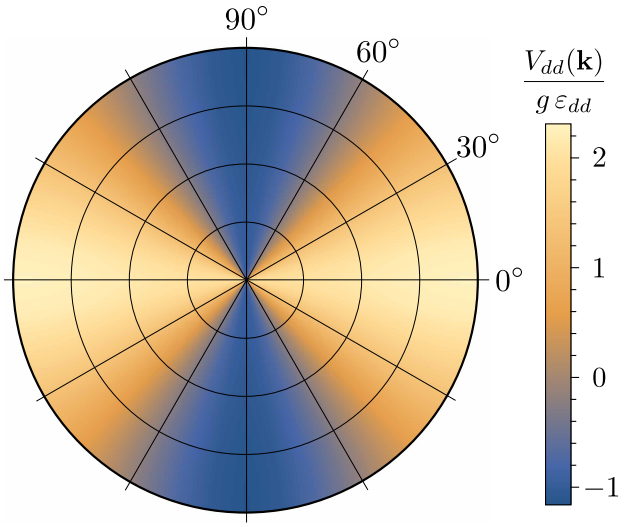

Fig. 8.8.: Polar plot of $V_{dd}(k, \theta, \phi = 0)$ for $kl \in [0, \pi]$. The boundary circle corresponds to $kl = \pi$ while the inner circles correspond to $kl = \pi/4,\ \pi/2,\ 3\pi/4$ (from innermost circle towards to edge).

Continuous Limit $\mathbf{k} \to 0$ and Nonanalytic Behaviour

In the long wavelength limit $\mathbf{k} \to 0$, the first term in Eq. (8.61) reduces to the continuous Fourier transform $V_{dd}(\mathbf{k}) = g\,\varepsilon_{dd}(3\cos^2\theta - 1)$, where θ is the angle between $\mathbf{k}$ and the z-axis, which is assumed to be the axis along which the dipoles are polarized.

The other terms in Eq. (8.61) for $\mathbf{k} \to 0$ read

$$\begin{aligned}\frac{3}{2}\sum_{\mathbf{R}\neq 0}\left(E_{-1/2}(\pi R^2) - 2\pi z^2 E_{-3/2}(\pi R^2)\right) + 3\sum_{\mathbf{q}\neq 0} e^{-\frac{q^2}{4\pi}}\frac{q_z^2}{q^2} \\ = \frac{3}{2}\sum_{\mathbf{R}\neq 0}\left(E_{-1/2}(\pi R^2) - 2\pi z^2 E_{-3/2}(\pi R^2)\right) + 3\pi\sum_{\mathbf{R}\neq 0} z^2\, E_0(\pi R^2)\,, \end{aligned} \tag{8.62}$$

where we replaced $\mathbf{q} = 2\pi\mathbf{R}$. In order to simplify this expression further, we make use of the recurrence relation

$$E_0(x) = E_m(x) + \frac{m}{x}E_{m+1}(x)\,. \tag{8.63}$$

Choosing $m = 3/2$, we get

$$\frac{3}{2}\sum_{\mathbf{R}\neq 0} E_{-1/2}(\pi R^2)\left(1 - 3\frac{z^2}{R^2}\right) = 0 \tag{8.64}$$

due to the symmetry of the lattice. Thus, we end up with

$$V_{dd}(\mathbf{k}\to 0) = g\,\varepsilon_{dd}\left(3\frac{k_z^2}{k^2} - 1\right) = g\,\varepsilon_{dd}\left(3\cos^2\theta - 1\right)\,. \tag{8.65}$$

This is exactly the same result as in free space and is nonanalytic for $\mathbf{k} \to 0$.

8.A.2. Role of the Next-Order Terms

For the analysis of the beyond-mean-field terms in Section 8.1, we only included the density-density interactions. However, dipolar interaction gives rise to terms like density-induced tunneling or pair hopping. Including the interaction-induced nearest-neighbour couplings results in [298, 322, 323]

$$\begin{aligned}H = -t\sum_{\langle i,j\rangle} b_i^\dagger b_j + \frac{U}{2}\sum_i n_i(n_i-1) + \frac{V}{2}\sum_{\langle i,j\rangle} n_i n_j \\ - T\sum_{\langle i,j\rangle} b_i^\dagger(n_i + n_j)b_j + \frac{P}{2}\sum_{\langle i,j\rangle} b_i^{\dagger 2} b_j^2\,. \end{aligned} \tag{8.66}$$

Transforming this to the quasi-momentum space, one obtains

$$H = \sum_{\mathbf{k}} \epsilon_{\mathbf{k}} b^\dagger_{\mathbf{k}} b_{\mathbf{k}} + \frac{1}{N_L} \sum_{\mathbf{k},\mathbf{k}',\mathbf{q},\mathbf{q}'} \delta_{\mathbf{k}-\mathbf{k}'+\mathbf{q}-\mathbf{q}',\mathbf{K}_m} f(\mathbf{q},\mathbf{q}',\mathbf{k}') b^\dagger_{\mathbf{k}} b^\dagger_{\mathbf{q}} b_{\mathbf{k}'} b_{\mathbf{q}'} \tag{8.67}$$

with

$$\begin{aligned} f(\mathbf{q},\mathbf{q}',\mathbf{k}') = \frac{U}{2} + \frac{V}{2} \sum_{\boldsymbol{\delta}} e^{-i\boldsymbol{\delta}(\mathbf{q}-\mathbf{q}')} - T \sum_{\boldsymbol{\delta}} \left(e^{i\boldsymbol{\delta}\mathbf{q}'} + e^{-i\boldsymbol{\delta}(\mathbf{q}-\mathbf{q}'-k')} \right) \\ + \frac{P}{2} \sum_{\boldsymbol{\delta}} e^{i\boldsymbol{\delta}(\mathbf{k}'+\mathbf{q}')}. \end{aligned} \tag{8.68}$$

Here, the sums over $\boldsymbol{\delta}$ are performed over nearest neighbors only. This Hamiltonian has the same structure as the one without additional terms but with modified effective interaction $f(\mathbf{q},\mathbf{q}',\mathbf{k}')$. We can thus perform the Bogoliubov approximation, assuming the presence of the condensate at zero momentum and replacing $b_0 \to \sqrt{N_0}$, where N_0 is the number of particles in the condensate with $N = N_0 + \frac{1}{2}\sum'_{\mathbf{p}} b^\dagger_{\mathbf{p}} b_{\mathbf{p}} + b^\dagger_{-\mathbf{p}} b_{-\mathbf{p}}$ and the prime denotes omitting the zero-momentum mode. For the case of a three-dimensional cubic lattice this gives

$$\begin{aligned} H = \frac{N^2}{N_L} f(0,0,0) + \frac{1}{2} \sum_{\mathbf{p}}{}' \Bigg\{ \Bigg[\epsilon_{\mathbf{p}} - 2\frac{N}{N_L} f(0,0,0) + \frac{N}{N_L} \Big(f(\mathbf{p},\mathbf{p},0) \\ + f(\mathbf{p},0,\mathbf{p}) + f(0,\mathbf{p},0) + f(0,0,\mathbf{p}) \Big) \Bigg] \left(b^\dagger_{\mathbf{p}} b_{\mathbf{p}} + b^\dagger_{-\mathbf{p}} b_{-\mathbf{p}} \right) \\ + 2\frac{N}{N_L} \left(f(0,-\mathbf{p},\mathbf{p}) b_{\mathbf{p}} b_{-\mathbf{p}} + f(-\mathbf{p},0,0) b^\dagger_{\mathbf{p}} b^\dagger_{-\mathbf{p}} \right) \Bigg\}. \end{aligned} \tag{8.69}$$

The relevant values for a cubic lattice in three dimensions are

$$f(0,0,0) = \frac{U}{2} + 3V - 12T + 3P\,, \tag{8.70}$$

$$f(\mathbf{p},\mathbf{p},0) = \frac{U}{2} + 3V - T(2c_{\mathbf{p}} + 6) + Pc_{\mathbf{p}}\,, \tag{8.71}$$

$$f(\mathbf{p},0,\mathbf{p}) = \frac{U}{2} + Vc_{\mathbf{p}} - 12T + Pc_{\mathbf{p}}\,, \tag{8.72}$$

$$f(0,0,\mathbf{p}) = \frac{U}{2} + 3V - T(2c_{\mathbf{p}} + 6) + Pc_{\mathbf{p}}\,, \tag{8.73}$$

$$f(0,\mathbf{p},0) = \frac{U}{2} + Vc_{\mathbf{p}} - 4Tc_{\mathbf{p}} + Pc_{\mathbf{p}}\,, \tag{8.74}$$

$$f(0,-\mathbf{p},\mathbf{p}) = \frac{U}{2} + Vc_{\mathbf{p}} - T(2c_{\mathbf{p}} + 6) + 3P\,, \tag{8.75}$$

$$f(-\mathbf{p},0,0) = \frac{U}{2} + Vc_{\mathbf{p}} - T(2c_{\mathbf{p}} + 6) + 3P\,. \tag{8.76}$$

Here, we defined $\sum_{\boldsymbol{\delta}} e^{i\boldsymbol{\delta}\mathbf{p}} \equiv c_{\mathbf{p}}$ and $c_{-\mathbf{p}} = c_{\mathbf{p}}$ for a cubic lattice.

Now we perform the Bogoliubov transformation and arrive at the formula for the ground state energy

$$E_0 = E_{\text{MF}} + \sum_{\mathbf{p}}{}' (E_{\mathbf{p}} - \alpha_{\mathbf{p}}) \,. \tag{8.77}$$

with

$$E_{\mathbf{p}} \equiv \sqrt{\alpha_{\mathbf{p}}^2 - \beta_{\mathbf{p}}^2} \tag{8.78}$$

and

$$\alpha_{\mathbf{p}} = c_{\mathbf{p}}(-2t - 8nT + 4nP + 2nV) + 6t + nU - 6nP \,, \tag{8.79}$$
$$\beta_{\mathbf{p}} = nU + 2nc_{\mathbf{p}}(V - 2T) - 12nT + 6nP \,. \tag{8.80}$$

Defining

$$\tilde{U}_{\mathbf{p}} = U - 12T + 6P + 2c_{\mathbf{p}}(V - 2T) \,, \tag{8.81}$$
$$\tilde{\epsilon}_{\mathbf{p}} = -2(t + 2nT - nP)(c_{\mathbf{p}} - 3) \,, \tag{8.82}$$

the Bogoliubov spectrum takes the form

$$E_{\mathbf{p}} = \sqrt{\tilde{\epsilon}_{\mathbf{p}}(\tilde{\epsilon}_{\mathbf{p}} + n\tilde{U}_{\mathbf{p}})} \tag{8.83}$$

similar to the standard Bose-Hubbard model, where $\tilde{\epsilon}_{\mathbf{p}} = -2t(c_{\mathbf{p}} - 3)$ and $\tilde{U}_{\mathbf{p}} = U$. One can also see that the spectrum is gapless and linear for small momenta

$$E_{\mathbf{p}} = \sqrt{2\tilde{t}\tilde{U}_0}|\mathbf{p}| \tag{8.84}$$

with the renormalized hopping amplitude $\tilde{t} = t + 2nT - nP$ which is now density dependent. The sound velocity is given by $c = \sqrt{2\tilde{t}\tilde{U}_0}$. The renormalized hopping amplitude also renormalizes the effective mass which is now given by $m_{\text{eff}} = \hbar^2/2l^2\tilde{t}$. We see that the modifications resulting from additional terms do not fundamentally change the properties of the superfluid. In our case the lattice is assumed to be deep and the role of tunnelling terms in the interaction is perturbative.

8.B. Dispersion in the Presence of a Weak Optical Lattice

In this section, we first state some important results from the physics of a single particle with mass m in the presence of a weak optical lattice. We restrict our discussion to the case of a one-dimensional lattice along the z-axis of the form

$$U_L(z) = U \sin^2(q_L z) = \frac{U}{2}(1 + \cos(2q_L z)) \,, \tag{8.85}$$

where $q_L = \pi/l$ is the lattice vector and l is the lattice period. The energy scale of the lattice is given by the recoil energy $E_R = \hbar^2 q_L^2/2m$. The full spectrum of the resulting single-particle Hamiltonian can be obtained by diagonalization which is in general only possible numerically. However, since we are interested only in weak lattices with $s = U/E_R \ll 1$, we can calculate the spectrum analytically using perturbation theory in the parameter s. In second order, the correction to the free space energy is given by

$$\epsilon_k^s = \epsilon_{k-K}^0 + \sum_{K'} \frac{|U_{K'-K}|^2}{\epsilon_{k-K}^0 - \epsilon_{k-K'}^0} + \mathcal{O}(U^3) \,, \tag{8.86}$$

where K is a vector of the reciprocal lattice, $K = 2nq_L$ with integer n, the free space dispersion $\epsilon_k^0 = \hbar^2 k^2/2m$ and the Fourier transform of the lattice potential, $U_K = U/2(\delta_{K,2q_L} + \delta_{K,-2q_L})$. Note that we omit the constant shift $U/2$ which leads to a shift in the chemical potential and in the end, we choose the dispersion such that $\epsilon_{k=0}^s = 0$. Setting $k = zq_L$, $z \in [-1, 1]$, we can write

$$\begin{aligned} \epsilon_z^s = E_R \Bigg[(z - 2n)^2 + \frac{s^2}{16} \Bigg(& \frac{1}{(z-2n)^2 - (z - 2(n+1))^2} \\ & + \frac{1}{(z-2n)^2 - (z - 2(n-1))^2} \Bigg) \Bigg] + \mathcal{O}(s^3) \,, \end{aligned} \tag{8.87}$$

where n denotes the index of the Bloch band.

Note that Eq. (8.86) only holds for nondegenerate energies away from the edges and the center of the Brillouin zone and in a region of energies where $|\epsilon_{k-K}^0 - \epsilon_{k-K'}^0| \gg U_K$. Close to the edges of the Brillouin zone, $k = \pm q_L$, energies are degenerate and nondegenerate perturbation theory cannot be applied. The dis-

persion relation in this case reads

$$\epsilon_k^s = \frac{\epsilon_k^0 - \epsilon_{k-K}^0}{2} \pm \sqrt{\left(\frac{\epsilon_k^0 - \epsilon_{k-K}^0}{2}\right)^2 + \frac{|U_K|^2}{4}} \tag{8.88}$$

$$= E_R \left(\frac{z^2 - (z-2n)^2}{2} \pm \sqrt{\left(\frac{z^2 - (z-2n)^2}{2}\right)^2 + \frac{s^2}{4}} \right) . \tag{8.89}$$

The above results suggest a splitting into a degenerate and nondegenerate region for the lowest two bands where the border of both regions is determined by the condition $\epsilon_{k-K}^0 - \epsilon_{k-K'}^0 = U_K$ leading to $z = 1 - s/8$. In the following, we will assume that z is positive but not restricted to values smaller than 1 as indicated above. Thus, the integration has to be split into three regions. The two nondegenerate regions are from $z = 0$ to $z = 1 - s/8$ and from $z = 1 + s/8$ to $z = \infty$ [2]. The degenerate region extends from $z = 1 - s/8$ to $z = 1 + s/8$.

8.B.1. Contribution from the Degenerate Region

Here, we argue that the contribution from the degenerate region will not contribute in leading order in s. In order to see that, we expand Eq. (8.89) for $z^2 - (z - 2n)^2 \ll s^2$ which leads to

$$\epsilon_k^s = \frac{E_R}{2} \left[(z^2 + (z-2)^2) - \frac{s}{8} - \frac{16(z-1)^2}{s} \right] \tag{8.90}$$

for $1 - s/8 \leq z \leq 1$, and

$$\epsilon_k^s = \frac{E_R}{2} \left[(z^2 + (z-2)^2) + \frac{s}{8} + \frac{16(z-1)^2}{s} \right] \tag{8.91}$$

for $1 \leq z \leq 1 + s/8$.

One can now show that the contribution to the integral in Eq. (8.95) coming from the degenerate region is of order s^3. Next, we show that the leading-order corrections are indeed of order s^2 and come exclusively from the nondegenerate region.

[2] Note that to leading order we only consider a splitting between the lowest and the second lowest Bloch band at $k = \pm q_L$ ($z = \pm 1$) while all other splittings are ignored.

8.B.2. Contributions from the Nondegenerate Region

For the nondegenerate region which ranges from $z = 0$ to $z = 1 - s/8$ and from $z = 1 + s/8$ to $z = \infty$, we have to consider an integral of the form

$$I(s) = \int_0^{1-s/8} dz\, h(z,s) + \int_{1+s/8}^{\infty} dz\, h(z,s)\,, \tag{8.92}$$

where $h(z,0) = 0$. For small s, we can expand the integral

$$I(s) \approx I(0) + s\,\partial_s I(s)|_{s=0} + \frac{1}{2}s^2\,\partial_s^2 I(s)|_{s=0}\,. \tag{8.93}$$

The constant term $I(0)$ as well as the linear term vanish due to the structure of $h(z,s)$. The quadratic term, using again that $h(z,0) = 0$, yields

$$\partial_s^2 I(s)|_{s=0} = \text{P.V.} \int_0^{\infty} dz\, \partial_s^2 h(z,s)|_{s=0}\,, \tag{8.94}$$

where P.V. denotes the Cauchy principal value. When evaluating the integral, divergences will arise in the vicinity of $z = 1$ since the nondegenerate approach is no longer valid. However, the divergences for $z > 1$ and $z < 1$ will cancel each other.

8.B.3. Beyond-Mean-Field Corrections in a Weak Lattice

Contact Interaction

In a next step, we present the details on how to calculate the beyond-mean-field corrections for a contact-interacting gas in a weak lattice. For this purpose, we consider Eq. (8.35) and, in what follows, we set $\tilde{\epsilon}_k = E_R f(kl)$, where $f(kl)$ is a dimensionless function of the quasi-momentum along the direction of the lattice. Using this form of the lattice dispersion and changing to dimensionless variables $k_\perp \xi = u$ and $kl = z$, we can transform Eq. (8.35) into

$$\begin{aligned}\frac{\Delta E_0^s}{V} = \frac{4\pi(2m)^{3/2}(ng)^{5/2}}{2(2\pi)^3\hbar^3} \int_0^{\infty} du\, u \int_0^{\infty} dz\, \sqrt{(u^2 + \beta^2 f(z/\beta))(u^2 + \beta^2 f(z/\beta) + 2)} \\ - \sqrt{(u^2+z^2)(u^2+z^2+2)} - \left(\beta^2 f(z/\beta) - z^2\right)\,.\end{aligned} \tag{8.95}$$

The factor in front of the integral is proportional to the usual LHY term, that is $m^{3/2}(ng)^{5/2}/\hbar^3$, while the remaining part accounts for the influence of the lattice.

As we are now interested in a weak lattice, we calculate the integrals in leading order in s. It turns out that the leading order is proportional to s^2 and the corrections read

$$\begin{aligned}\frac{\Delta E_0^s}{V} &= \frac{(2m)^{3/2}(ng)^{5/2}}{2(2\pi)^3\hbar^3}\frac{\pi s^2\beta^2}{96}\Big[2\sqrt{2}(2+3\beta^2) \\ &\quad + 3\beta^2\sqrt{2+\beta^2}\left(\ln(2\beta^2) - 2\ln(2+\sqrt{2}\sqrt{2+\beta^2})\right)\Big] \\ &= \frac{E_{\mathrm{LHY}}}{V}\frac{s^2}{64}\frac{5\beta^2}{32}\Big[8+12\beta^2+3\beta^2\sqrt{4+2\beta^2} \\ &\quad \times\left(\ln(2\beta^2) - 2\ln(2+\sqrt{4+2\beta^2})\right)\Big]\,. \end{aligned} \tag{8.96}$$

Since we are also interested in the limit $\beta \to \infty$ and claim that this corresponds to essentially having an effective mass in the direction of the lattice, we look for an expansion of Eq. (8.95) for $\beta \to \infty$ or, to be more rigorous, for $z \ll \beta$. The function f in the integrand plays the role of our lattice dispersion. For small arguments, we can expand Eq. (8.87) around $z = 0$ for the lowest band, $n = 0$:

$$\begin{aligned}\epsilon_k^s &= E_R\left[z^2 + \frac{s^2}{16}\left(\frac{1}{z^2-(z-2)^2} + \frac{1}{z^2-(z+2)^2}\right)\right] \\ &\approx E_R\left[-\frac{s^2}{32} + \left(1-\frac{s^2}{32}\right)z^2\right]\,. \end{aligned} \tag{8.97}$$

The first term is just the constant shift that will be subtracted by an additional chemical potential. The second term gives the leading behaviour and corresponds to having an effective mass in the z-direction, $m_z = m/(1-s^2/32)$.

Dipolar Interaction

In this part, we present the details of the derivation of Eq. (8.45). First, we express the dispersion relation for an anisotropic effective mass in spherical coordinates, that is

$$\begin{aligned}\epsilon_k &= \frac{\hbar^2k^2}{2m}(\cos^2\theta\sin^2\eta + \sin^2\theta(\cos^2\phi + \gamma^2\sin^2\eta\sin^2\phi) \\ &\quad + \cos^2\eta(\gamma^2\cos^2\theta + \sin^2\phi\sin^2\theta) + (\gamma^2-1)\cos\eta\sin\eta\sin\phi\sin 2\theta) \\ &= \frac{\hbar^2k^2}{2m}f(\theta,\phi,\gamma,\eta)\,. \end{aligned} \tag{8.98}$$

The correction to the ground state energy can now be calculated using Eq. (8.15) according to which

$$\frac{E_0^{(2)}}{V} - \frac{1}{2} n\mu^{(2)} = \frac{1}{2(2\pi)^3} \int_0^\infty dk\, k^2 \int d\Omega\, \frac{\left(\frac{\hbar^2 k^2}{2m} f + nV_k - E_k\right)\left(\frac{\hbar^2 k^2}{2m} f - E_k\right)}{2E_k}\,, \tag{8.99}$$

where $E_k = \sqrt{\epsilon_k(\epsilon_k + 2nV_k)}$ is the Bogoliubov spectrum and $\int d\Omega = \int_0^\pi d\theta\, \sin\theta \times \int_0^{2\pi} d\phi$ denotes the integration over the solid angle .

The integral on the right-hand side can be simplified and made dimensionless by pulling out the factor ng and using the healing length $\xi^2 = \hbar^2/2mng$. Making the substitution $(k\xi)^2 f = x^2$ and performing the integral over k leads to

$$\frac{1}{16\pi^3} \frac{ng}{\xi^3} \left(-\frac{2\sqrt{2}}{15}\right) \int d\Omega\, \frac{\tilde{V}^{5/2}}{f^{3/2}}\,. \tag{8.100}$$

The remaining integrals cannot be solved analytically in general. However, we are only interested in the lowest-order corrections which are due to the lattice such that we can expand the function under the integral to the lowest order in s, which leads to

$$\frac{1}{16\pi^3} \frac{ng}{\xi^3} \left(-\frac{2\sqrt{2}}{15}\right) \int d\Omega\, \tilde{V}^{5/2} \left(1 + \frac{3s^2}{64}(\cos\eta\cos\theta - \sin\eta\sin\phi\sin\theta)^2\right). \tag{8.101}$$

Bibliography

[1] J. D. Jackson. *Classical Electrodynamics*. Third Edition. John Wiley & Sons, Inc., 1999.

[2] R. H. Lehmberg. "Radiation from an N-Atom System. I. General Formalism". Physical Review A **2** (1970), 883.

[3] R. H. Dicke. "Coherence in Spontaneous Radiation Processes". Physical Review **93** (1954), 99.

[4] F. Andreoli, M. J. Gullans, A. A. High, A. Browaeys, and D. E. Chang. "Maximum Refractive Index of an Atomic Medium". Physical Review X **11** (2021), 011026.

[5] M. Gross and S. Haroche. "Superradiance: An essay on the theory of collective spontaneous emission". Physics Reports **93** (1982), 301.

[6] R. Röhlsberger, K. Schlage, B. Sahoo, S. Couet, and R. Ruffer. "Collective Lamb Shift in Single-Photon Superradiance". Science **328** (2010), 1248.

[7] J. Keaveney, A. Sargsyan, U. Krohn, I. G. Hughes, D. Sarkisyan, and C. S. Adams. "Cooperative Lamb Shift in an Atomic Vapor Layer of Nanometer Thickness". Physical Review Letters **108** (2012), 173601.

[8] J. Pellegrino, R. Bourgain, S. Jennewein, Y. R. P. Sortais, A. Browaeys, S. D. Jenkins, and J. Ruostekoski. "Observation of Suppression of Light Scattering Induced by Dipole-Dipole Interactions in a Cold-Atom Ensemble". Physical Review Letters **113** (2014), 133602.

[9] S. Jennewein, M. Besbes, N. J. Schilder, S. D. Jenkins, C. Sauvan, J. Ruostekoski, J.-J. Greffet, Y. R. P. Sortais, and A. Browaeys. "Coherent Scattering of Near-Resonant Light by a Dense Microscopic Cold Atomic Cloud". Physical Review Letters **116** (2016), 233601.

[10] A. Glicenstein, G. Ferioli, N. Šibalić, L. Brossard, I. Ferrier-Barbut, and A. Browaeys. "Collective Shift in Resonant Light Scattering by a One-Dimensional Atomic Chain". Physical Review Letters **124** (2020), 253602.

[11] Z. Meir, O. Schwartz, E. Shahmoon, D. Oron, and R. Ozeri. "Cooperative Lamb Shift in a Mesoscopic Atomic Array". Physical Review Letters **113** (2014), 193002.

[12] M. Scheibner, T. Schmidt, L. Worschech, A. Forchel, G. Bacher, T. Passow, and D. Hommel. "Superradiance of quantum dots". Nature Physics **3** (2007), 106.

[13] P. Tighineanu, R. S. Daveau, T. B. Lehmann, H. E. Beere, D. A. Ritchie, P. Lodahl, and S. Stobbe. "Single-Photon Superradiance from a Quantum Dot". Physical Review Letters **116** (2016), 163604.

[14] J. A. Mlynek, A. A. Abdumalikov, C. Eichler, and A. Wallraff. "Observation of Dicke superradiance for two artificial atoms in a cavity with high decay rate". Nature Communications **5** (2014), 5186.

[15] A. Goban, C.-L. Hung, S.-P. Yu, J. Hood, J. Muniz, J. Lee, M. Martin, A. McClung, K. Choi, D. E. Chang, O. Painter, and H. Kimble. "Atom–light interactions in photonic crystals". Nature Communications **5** (2014).

[16] M. O. Scully, E. S. Fry, C. H. R. Ooi, and K. Wódkiewicz. "Directed Spontaneous Emission from an Extended Ensemble of N Atoms: Timing Is Everything". Physical Review Letters **96** (2006), 010501.

[17] P. A. Vetter, L. Wang, D.-W. Wang, and M. O. Scully. "Single photon subradiance and superradiance revisited: a group theoretic analysis of subradiant states". Physica Scripta **91** (2016), 023007.

[18] M. O. Scully and A. A. Svidzinsky. "The Super of Superradiance". Science **325** (2009), 1510.

[19] M. O. Scully. "Collective Lamb Shift in Single Photon Dicke Superradiance". Physical Review Letters **102** (2009), 143601.

[20] A. A. Svidzinsky, J.-T. Chang, and M. O. Scully. "Dynamical Evolution of Correlated Spontaneous Emission of a Single Photon from a Uniformly Excited Cloud of N Atoms". Physical Review Letters **100** (2008), 160504.

[21] I. E. Mazets and G. Kurizki. "Multiatom cooperative emission following single-photon absorption: Dicke-state dynamics". Journal of Physics B: Atomic, Molecular and Optical Physics **40** (2007), F105.

[22] R. Friedberg and J. T. Manassah. "Effects of including the counterrotating term and virtual photons on the eigenfunctions and eigenvalues of a scalar photon collective emission theory". Physics Letters A **372** (2008), 2514.

[23] J. T. Manassah. "The single photon superradiance from the eigenmode analysis". Laser Physics **19** (2009), 2102.

[24] I. M. Mirza and T. Begzjav. "Fano-Agarwal couplings and non-rotating wave approximation in single-photon timed Dicke subradiance". EPL (Europhysics Letters) **114** (2016), 24004.

[25] A. Asenjo-Garcia, M. Moreno-Cardoner, A. Albrecht, H. J. Kimble, and D. E. Chang. "Exponential Improvement in Photon Storage Fidelities Using Subradiance and "Selective Radiance" in Atomic Arrays". Physical Review X **7** (2017), 031024.

[26] L. Henriet, J. S. Douglas, D. E. Chang, and A. Albrecht. "Critical open-system dynamics in a one-dimensional optical-lattice clock". Physical Review A **99** (2019), 023802.

[27] S. J. Masson and A. Asenjo-Garcia. "Atomic-waveguide quantum electrodynamics". Physical Review Research **2** (2020), 043213.

[28] J. H. Eberly. "Superradiance Revisited". American Journal of Physics **40** (1972), 1374.

[29] A. Crubellier, S. Liberman, D. Pavolini, and P. Pillet. "Superradiance and subradiance. I. Interatomic interference and symmetry properties in three-level systems". Journal of Physics B: Atomic and Molecular Physics **18** (1985), 3811.

[30] A. Crubellier and D. Pavolini. "Superradiance and subradiance. II. Atomic systems with degenerate transitions". Journal of Physics B: Atomic and Molecular Physics **19** (1986), 2109.

[31] A. Crubellier and D. Pavolini. "Superradiance and subradiance. IV. Atomic cascades between degenerate levels". Journal of Physics B: Atomic and Molecular Physics **20** (1987), 1451.

[32] A. Crubellier. "Superradiance and subradiance. III. Small samples". Journal of Physics B: Atomic and Molecular Physics **20** (1987), 971.

[33] T. Bienaimé, N. Piovella, and R. Kaiser. "Controlled Dicke Subradiance from a Large Cloud of Two-Level Systems". Physical Review Letters **108** (2012), 123602.

[34] R. T. Sutherland and F. Robicheaux. "Collective dipole-dipole interactions in an atomic array". Physical Review A **94** (2016), 013847.

[35] C. Hettich. "Nanometer Resolution and Coherent Optical Dipole Coupling of Two Individual Molecules". Science **298** (2002), 385.

[36] Y. Takasu, Y. Saito, Y. Takahashi, M. Borkowski, R. Ciuryło, and P. S. Julienne. "Controlled Production of Subradiant States of a Diatomic Molecule in an Optical Lattice". Physical Review Letters **108** (2012), 173002.

[37] B. H. McGuyer, M. McDonald, G. Z. Iwata, M. G. Tarallo, W. Skomorowski, R. Moszynski, and T. Zelevinsky. "Precise study of asymptotic physics with subradiant ultracold molecules". Nature Physics **11** (2015), 32.

[38] R. G. DeVoe and R. G. Brewer. "Observation of Superradiant and Subradiant Spontaneous Emission of Two Trapped Ions". Physical Review Letters **76** (1996), 2049.

[39] W. Guerin, M. O. Araújo, and R. Kaiser. "Subradiance in a Large Cloud of Cold Atoms". Physical Review Letters **116** (2016), 083601.

[40] S. D. Jenkins, J. Ruostekoski, N. Papasimakis, S. Savo, and N. I. Zheludev. "Many-Body Subradiant Excitations in Metamaterial Arrays: Experiment and Theory". Physical Review Letters **119** (2017), 053901.

[41] D. Das, B. Lemberger, and D. D. Yavuz. "Subradiance and superradiance-to-subradiance transition in dilute atomic clouds". Physical Review A **102** (2020), 043708.

[42] A. Cipris, N. A. Moreira, T. S. do Espirito Santo, P. Weiss, C. J. Villas-Boas, R. Kaiser, W. Guerin, and R. Bachelard. "Subradiance with Saturated Atoms: Population Enhancement of the Long-Lived States". Physical Review Letters **126** (2021), 103604.

[43] M. O. Scully. "Single Photon Subradiance: Quantum Control of Spontaneous Emission and Ultrafast Readout". Physical Review Letters **115** (2015), 243602.

[44] H. Cai, D.-W. Wang, A. A. Svidzinsky, S.-Y. Zhu, and M. O. Scully. "Symmetry-protected single-photon subradiance". Physical Review A **93** (2016), 053804.

[45] J. A. Needham, I. Lesanovsky, and B. Olmos. "Subradiance-protected excitation transport". New Journal of Physics **21** (2019), 073061.

[46] D. Petrosyan and G. Kurizki. "Scalable Solid-State Quantum Processor Using Subradiant Two-Atom States". Physical Review Letters **89** (2002), 207902.

[47] K. Hammerer, A. S. Sørensen, and E. S. Polzik. "Quantum interface between light and atomic ensembles". Reviews of Modern Physics **82** (2010), 1041.

[48] J. D. Pritchard, K. J. Weatherill, and C. S. Adams. "Nonlinear optics using cold Rydberg atoms". *Annual Review of Cold Atoms and Molecules*, 301.

[49] O. Firstenberg, C. S. Adams, and S. Hofferberth. "Nonlinear quantum optics mediated by Rydberg interactions". Journal of Physics B: Atomic, Molecular and Optical Physics **49** (2016), 152003.

[50] C. Murray and T. Pohl. "Chapter Seven - Quantum and Nonlinear Optics in Strongly Interacting Atomic Ensembles". Ed. by E. Arimondo, C. C. Lin, and S. F. Yelin. **65**. Advances In Atomic, Molecular, and Optical Physics. Academic Press, 2016, 321.

[51] D. Jaksch, J. I. Cirac, P. Zoller, S. L. Rolston, R. Côté, and M. D. Lukin. "Fast Quantum Gates for Neutral Atoms". Physical Review Letters **85** (2000), 2208.

[52] M. D. Lukin, M. Fleischhauer, R. Cote, L. M. Duan, D. Jaksch, J. I. Cirac, and P. Zoller. "Dipole Blockade and Quantum Information Processing in Mesoscopic Atomic Ensembles". Physical Review Letters **87** (2001), 037901.

[53] M. Fleischhauer, A. Imamoglu, and P. J. Marangos. "Electromagnetically induced transparency". Reviews of Modern Physics **77** (2005), 633.

[54] I. Friedler, D. Petrosyan, M. Fleischhauer, and G. Kurizki. "Long-range interactions and entanglement of slow single-photon pulses". Physical Review A **72** (2005), 043803.

[55] A. K. Mohapatra, T. R. Jackson, and C. S. Adams. "Coherent Optical Detection of Highly Excited Rydberg States Using Electromagnetically Induced Transparency". Physical Review Letters **98** (2007), 113003.

[56] J. D. Pritchard, D. Maxwell, A. Gauguet, K. J. Weatherill, M. P. A. Jones, and C. S. Adams. "Cooperative Atom-Light Interaction in a Blockaded Rydberg Ensemble". Physical Review Letters **105** (2010), 193603.

[57] A. V. Gorshkov, J. Otterbach, M. Fleischhauer, T. Pohl, and M. D. Lukin. "Photon-photon interactions via Rydberg blockade". Physical Review Letters **107** (2011), 133602.

[58] T. Peyronel, O. Firstenberg, Q. Y. Liang, S. Hofferberth, A. V. Gorshkov, T. Pohl, M. D. Lukin, and V. Vuletić. "Quantum nonlinear optics with single photons enabled by strongly interacting atoms". Nature **488** (2012), 57.

[59] O. Firstenberg, T. Peyronel, Q.-Y. Liang, A. V. Gorshkov, M. D. Lukin, and V. Vuletić. "Attractive photons in a quantum nonlinear medium". Nature **502** (2013), 71.

[60] S. H. Cantu, A. V. Venkatramani, W. Xu, L. Zhou, B. Jelenković, M. D. Lukin, and V. Vuletić. "Repulsive photons in a quantum nonlinear medium". Nature Physics **16** (2020), 921.

[61] S. Baur, D. Tiarks, G. Rempe, and S. Dürr. "Single-Photon Switch Based on Rydberg Blockade". Physical Review Letters **112** (2014), 073901.

[62] H. Gorniaczyk, C. Tresp, J. Schmidt, H. Fedder, and S. Hofferberth. "Single-Photon Transistor Mediated by Interstate Rydberg Interactions". Physical Review Letters **113** (2014), 053601.

[63] D. Tiarks, S. Baur, K. Schneider, S. Dürr, and G. Rempe. "Single-Photon Transistor Using a Förster Resonance". Physical Review Letters **113** (2014), 053602.

[64] D. Tiarks, S. Schmidt, G. Rempe, and S. Dürr. "Optical π phase shift created with a single-photon pulse". Science Advances **2** (2016), e1600036.

[65] D. Tiarks, S. Schmidt-Eberle, T. Stolz, G. Rempe, and S. Dürr. "A photon–photon quantum gate based on Rydberg interactions". Nature Physics **15** (2019), 124.

[66] D. E. Chang, J. S. Douglas, A. González-Tudela, C. L. Hung, and H. J. Kimble. "Colloquium: Quantum matter built from nanoscopic lattices of atoms and photons". Reviews of Modern Physics **90** (2018), 031002.

[67] Y. O. Dudin, L. Li, F. Bariani, and A. Kuzmich. "Observation of coherent many-body Rabi oscillations". Nature Physics **8** (2012), 790.

[68] Y. O. Dudin and A. Kuzmich. "Strongly Interacting Rydberg Excitations of a Cold Atomic Gas". Science **336** (2012), 887.

[69] F. Ripka, H. Kübler, R. Löw, and T. Pfau. "A room-temperature single-photon source based on strongly interacting Rydberg atoms". Science **362** (2018), 446.

[70] J. Honer, R. Löw, H. Weimer, T. Pfau, and H. P. Büchler. "Artificial Atoms Can Do More Than Atoms: Deterministic Single Photon Subtraction from Arbitrary Light Fields". Physical Review Letters **107** (2011), 093601.

[71] C. Tresp, C. Zimmer, I. Mirgorodskiy, H. Gorniaczyk, A. Paris-Mandoki, and S. Hofferberth. "Single-Photon Absorber Based on Strongly Interacting Rydberg Atoms". Physical Review Letters **117** (2016), 223001.

[72] N. Stiesdal, H. Busche, K. Kleinbeck, J. Kumlin, M. G. Hansen, H. P. Büchler, and S. Hofferberth. "Controlled multi-photon subtraction with cascaded Rydberg superatoms as single-photon absorbers". arXiv:2103.15738 (2021).

[73] F. J. García de Abajo. "Colloquium : Light scattering by particle and hole arrays". Reviews of Modern Physics **79** (2007), 1267.

[74] S. D. Jenkins and J. Ruostekoski. "Metamaterial Transparency Induced by Cooperative Electromagnetic Interactions". Physical Review Letters **111** (2013), 147401.

[75] R. J. Bettles, S. A. Gardiner, and C. S. Adams. "Enhanced Optical Cross Section via Collective Coupling of Atomic Dipoles in a 2D Array". Physical Review Letters **116** (2016), 103602.

[76] J. Perczel, J. Borregaard, D. E. Chang, H. Pichler, S. F. Yelin, P. Zoller, and M. D. Lukin. "Topological Quantum Optics in Two-Dimensional Atomic Arrays". Physical Review Letters **119** (2017), 023603.

[77] D. S. Wild, E. Shahmoon, S. F. Yelin, and M. D. Lukin. "Quantum Nonlinear Optics in Atomically Thin Materials". Physical Review Letters **121** (2018), 123606.

[78] I. Bloch. "Ultracold quantum gases in optical lattices". Nature Physics **1** (2005), 23.

[79] D. Barredo, S. de Léséleuc, V. Lienhard, T. Lahaye, and A. Browaeys. "An atom-by-atom assembler of defect-free arbitrary two-dimensional atomic arrays". Science **354** (2016), 1021.

[80] M. Endres, H. Bernien, A. Keesling, H. Levine, E. R. Anschuetz, A. Krajenbrink, C. Senko, V. Vuletić, M. Greiner, and M. D. Lukin. "Atom-by-atom assembly of defect-free one-dimensional cold atom arrays". Science **354** (2016), 1024.

[81] D. Barredo, V. Lienhard, S. de Léséleuc, T. Lahaye, and A. Browaeys. "Synthetic three-dimensional atomic structures assembled atom by atom". Nature **561** (2018), 79.

[82] R. J. Bettles, S. A. Gardiner, and C. S. Adams. "Cooperative eigenmodes and scattering in one-dimensional atomic arrays". Physical Review A **94** (2016), 043844.

[83] E. Shahmoon, D. S. Wild, M. D. Lukin, and S. F. Yelin. "Cooperative Resonances in Light Scattering from Two-Dimensional Atomic Arrays". Physical Review Letters **118** (2017), 113601.

[84] J. Rui, D. Wei, A. Rubio-Abadal, S. Hollerith, J. Zeiher, D. M. Stamper-Kurn, C. Gross, and I. Bloch. "A subradiant optical mirror formed by a single structured atomic layer". Nature **583** (2020), 369.

[85] R. Bekenstein, I. Pikovski, H. Pichler, E. Shahmoon, S. F. Yelin, and M. D. Lukin. "Quantum metasurfaces with atom arrays". Nature Physics **16** (2020), 676.

[86] D. Roy, C. M. Wilson, and O. Firstenberg. "Colloquium: Strongly interacting photons in one-dimensional continuum". Reviews of Modern Physics **89** (2017), 021001.

[87] P. Türschmann, H. Le Jeannic, S. F. Simonsen, H. R. Haakh, S. Götzinger, V. Sandoghdar, P. Lodahl, and N. Rotenberg. "Coherent nonlinear optics of quantum emitters in nanophotonic waveguides". Nanophotonics **8** (2019), 1641.

[88] A. S. Sheremet, M. I. Petrov, I. V. Iorsh, A. V. Poshakinskiy, and A. N. Poddubny. "Waveguide quantum electrodynamics: collective radiance and photon-photon correlations". arXiv:2103.06824v2 (2021).

[89] E. Vetsch, D. Reitz, G. Sagué, R. Schmidt, S. T. Dawkins, and A. Rauschenbeutel. "Optical Interface Created by Laser-Cooled Atoms Trapped in the Evanescent Field Surrounding an Optical Nanofiber". Physical Review Letters **104** (2010), 203603.

[90] P. Solano, P. Barberis-Blostein, F. K. Fatemi, L. A. Orozco, and S. L. Rolston. "Super-radiance reveals infinite-range dipole interactions through a nanofiber". Nature Communications **8** (2017), 1857.

[91] N. V. Corzo, J. Raskop, A. Chandra, A. S. Sheremet, B. Gouraud, and J. Laurat. "Waveguide-coupled single collective excitation of atomic arrays". Nature **566** (2019), 359.

[92] J. D. Hood, A. Goban, A. Asenjo-Garcia, M. Lu, S.-P. Yu, D. E. Chang, and H. J. Kimble. "Atom–atom interactions around the band edge of a photonic crystal waveguide". Proceedings of the National Academy of Sciences **113** (2016), 10507.

[93] M. Arcari, I. Söllner, A. Javadi, S. Lindskov Hansen, S. Mahmoodian, J. Liu, H. Thyrrestrup, E. H. Lee, J. D. Song, S. Stobbe, and P. Lodahl. "Near-Unity Coupling Efficiency of a Quantum Emitter to a Photonic Crystal Waveguide". Physical Review Letters **113** (2014), 093603.

[94] P. Lodahl, S. Mahmoodian, and S. Stobbe. "Interfacing single photons and single quantum dots with photonic nanostructures". Reviews of Modern Physics **87** (2015), 347.

[95] M. Mirhosseini, E. Kim, X. Zhang, A. Sipahigil, P. B. Dieterle, A. J. Keller, A. Asenjo-Garcia, D. E. Chang, and O. Painter. "Cavity quantum electrodynamics with atom-like mirrors". Nature **569** (2019), 692.

[96] F. Le Kien and A. Rauschenbeutel. "Nanofiber-mediated chiral radiative coupling between two atoms". Physical Review A **95** (2017), 023838.

[97] J. S. Douglas, H. Habibian, C.-L. Hung, A. V. Gorshkov, H. J. Kimble, and D. E. Chang. "Quantum many-body models with cold atoms coupled to photonic crystals". Nature Photonics **9** (2015), 326.

[98] J.-T. Shen and S. Fan. "Strongly Correlated Two-Photon Transport in a One-Dimensional Waveguide Coupled to a Two-Level System". Physical Review Letters **98** (2007), 153003.

[99] S. Mahmoodian, M. Čepulkovskis, S. Das, P. Lodahl, K. Hammerer, and A. S. Sørensen. "Strongly Correlated Photon Transport in Waveguide Quantum Electrodynamics with Weakly Coupled Emitters". Physical Review Letters **121** (2018), 143601.

[100] A. S. Prasad, J. Hinney, S. Mahmoodian, K. Hammerer, S. Rind, P. Schneeweiss, A. S. Sørensen, J. Volz, and A. Rauschenbeutel. "Correlating photons using the collective nonlinear response of atoms weakly coupled to an optical mode". Nature Photonics **14** (2020), 719.

[101] K. Stannigel, P. Rabl, and P. Zoller. "Driven-dissipative preparation of entangled states in cascaded quantum-optical networks". New Journal of Physics **14** (2012), 063014.

[102] O. A. Iversen and T. Pohl. "Strongly Correlated States of Light and Repulsive Photons in Chiral Chains of Three-Level Quantum Emitters". Physical Review Letters **126** (2021), 083605.

[103] S. Mahmoodian, G. Calajó, D. E. Chang, K. Hammerer, and A. S. Sørensen. "Dynamics of Many-Body Photon Bound States in Chiral Waveguide QED". Physical Review X **10** (2020), 031011.

[104] B. Olmos, G. Buonaiuto, P. Schneeweiss, and I. Lesanovsky. "Interaction signatures and non-Gaussian photon states from a strongly driven atomic ensemble coupled to a nanophotonic waveguide". Physical Review A **102** (2020), 043711.

[105] P. Lodahl, S. Mahmoodian, S. Stobbe, A. Rauschenbeutel, P. Schneeweiss, J. Volz, H. Pichler, and P. Zoller. "Chiral quantum optics". Nature **541** (2017), 473.

[106] J. Petersen, J. Volz, and A. Rauschenbeutel. "Chiral nanophotonic waveguide interface based on spin-orbit interaction of light". Science **346** (2014), 67.

[107] K. Y. Bliokh and F. Nori. "Transverse and longitudinal angular momenta of light". Physics Reports **592** (2015), 1.

[108] H. J. Carmichael. "Quantum trajectory theory for cascaded open systems". Physical Review Letters **70** (1993), 2273.

[109] C. W. Gardiner. "Driving a quantum system with the output field from another driven quantum system". Physical Review Letters **70** (1993), 2269.

[110] J. I. Cirac, P. Zoller, H. J. Kimble, and H. Mabuchi. "Quantum State Transfer and Entanglement Distribution among Distant Nodes in a Quantum Network". Physical Review Letters **78** (1997), 3221.

[111] C. Gonzalez-Ballestero, A. Gonzalez-Tudela, F. J. Garcia-Vidal, and E. Moreno. "Chiral route to spontaneous entanglement generation". Physical Review B **92** (2015), 155304.

[112] A. B. Young, A. C. Thijssen, D. M. Beggs, P. Androvitsaneas, L. Kuipers, J. G. Rarity, S. Hughes, and R. Oulton. "Polarization Engineering in Photonic Crystal Waveguides for Spin-Photon Entanglers". Physical Review Letters **115** (2015), 153901.

[113] S. Mahmoodian, P. Lodahl, and A. S. Sørensen. "Quantum Networks with Chiral-Light-Matter Interaction in Waveguides". Physical Review Letters **117** (2016), 240501.

[114] K. A. Safinya, J. F. Delpech, F. Gounand, W. Sandner, and T. F. Gallagher. "Resonant Rydberg-Atom-Rydberg-Atom Collisions". Physical Review Letters **47** (1981), 405.

[115] I. Beigman and V. Lebedev. "Collision theory of Rydberg atoms with neutral and charged particles". Physics Reports **250** (1995), 95.

[116] T. F. Gallagher and P. Pillet. "Dipole–Dipole Interactions of Rydberg Atoms". *Advances in Atomic, Molecular and Optical Physics*. **56**. Academic Press, 2008, 161.

[117] H. Weimer, M. Müller, I. Lesanovsky, P. Zoller, and H. P. Büchler. "A Rydberg quantum simulator". Nature Physics **6** (2010), 382.

[118] H. Labuhn, D. Barredo, S. Ravets, S. de Léséleuc, T. Macrì, T. Lahaye, and A. Browaeys. "Tunable two-dimensional arrays of single Rydberg atoms for realizing quantum Ising models". Nature **534** (2016), 667.

[119] H. Bernien, S. Schwartz, A. Keesling, H. Levine, A. Omran, H. Pichler, S. Choi, A. S. Zibrov, M. Endres, M. Greiner, V. Vuletić, and M. D. Lukin. "Probing many-body dynamics on a 51-atom quantum simulator". Nature **551** (2017), 579.

[120] P. Schauss. "Quantum simulation of transverse Ising models with Rydberg atoms". Quantum Science and Technology **3** (2018), 023001.

[121] A. Browaeys and T. Lahaye. "Many-body physics with individually controlled Rydberg atoms". Nature Physics **16** (2020), 132.

[122] R. Löw, H. Weimer, J. Nipper, J. B. Balewski, B. Butscher, H. P. Büchler, and T. Pfau. "An experimental and theoretical guide to strongly interacting Rydberg gases". Journal of Physics B: Atomic, Molecular and Optical Physics **45** (2012), 113001.

[123] M. Saffman, T. G. Walker, and K. Mølmer. "Quantum information with Rydberg atoms". Reviews of Modern Physics **82** (2010), 2313.

[124] T. F. Gallagher. *Rydberg Atoms*. Cambridge University Press, 1994.

[125] T. Lahaye, C. Menotti, L. Santos, M. Lewenstein, and T. Pfau. "The physics of dipolar bosonic quantum gases". Reports on Progress in Physics **72** (2009), 126401.

[126] E. Brion, L. H. Pedersen, and K. Mølmer. "Adiabatic elimination in a lambda system". Journal of Physics A: Mathematical and Theoretical **40** (2007), 1033.

[127] R. J. Le Roy. "Long-Range Potential Coefficients From RKR Turning Points: C_6 and C_8 for $B(3\Pi_{Ou}^+)$-State Cl_2, Br_2, and I_2". Canadian Journal of Physics **52** (1974), 246.

[128] S. Weber, C. Tresp, H. Menke, A. Urvoy, O. Firstenberg, H. P. Büchler, and S. Hofferberth. "Calculation of Rydberg interaction potentials". Journal of Physics B: Atomic, Molecular and Optical Physics **50** (2017), 133001.

[129] T. Förster. "Zwischenmolekulare Energiewanderung und Fluoreszenz". Annalen der Physik **437** (1948), 55.

[130] S. Ravets, H. Labuhn, D. Barredo, T. Lahaye, and A. Browaeys. "Measurement of the angular dependence of the dipole-dipole interaction between two individual Rydberg atoms at a Förster resonance". Physical Review A **92** (2015), 020701.

[131] S. Ravets, H. Labuhn, D. Barredo, L. Béguin, T. Lahaye, and A. Browaeys. "Coherent dipole–dipole coupling between two single Rydberg atoms at an electrically-tuned Förster resonance". Nature Physics **10** (2014), 914.

[132] H. Gorniaczyk, C. Tresp, P. Bienias, A. Paris-Mandoki, W. Li, I. Mirgorodskiy, H. P. Büchler, I. Lesanovsky, and S. Hofferberth. "Enhancement of Rydberg-mediated single-photon nonlinearities by electrically tuned Förster resonances". Nature Communications **7** (2016), 12480.

[133] V. Lienhard, P. Scholl, S. Weber, D. Barredo, S. de Léséleuc, R. Bai, N. Lang, M. Fleischhauer, H. P. Büchler, T. Lahaye, and A. Browaeys. "Realization of a Density-Dependent Peierls Phase in a Synthetic, Spin-Orbit Coupled Rydberg System". Physical Review X **10** (2020), 021031.

[134] C. Chin, R. Grimm, P. Julienne, and E. Tiesinga. "Feshbach resonances in ultracold gases". Reviews of Modern Physics **82** (2010), 1225.

[135] M. Şener, J. Strümpfer, J. Hsin, D. Chandler, S. Scheuring, C. N. Hunter, and K. Schulten. "Förster Energy Transfer Theory as Reflected in the Structures of Photosynthetic Light-Harvesting Systems". ChemPhysChem **12** (2011), 518.

[136] E. Collini. "Spectroscopic signatures of quantum-coherent energy transfer". Chemical Society Reviews **42** (2013), 4932.

[137] G. Günter, H. Schempp, M. Robert-de-Saint-Vincent, V. Gavryusev, S. Helmrich, C. S. Hofmann, S. Whitlock, and M. Weidemüller. "Observing the Dynamics of Dipole-Mediated Energy Transport by Interaction-Enhanced Imaging". Science **342** (2013), 954.

[138] H. Levine, A. Keesling, A. Omran, H. Bernien, S. Schwartz, A. S. Zibrov, M. Endres, M. Greiner, V. Vuletić, and M. D. Lukin. "High-Fidelity Control and Entanglement of Rydberg-Atom Qubits". Physical Review Letters **121** (2018), 123603.

[139] T. M. Graham, M. Kwon, B. Grinkemeyer, Z. Marra, X. Jiang, M. T. Lichtman, Y. Sun, M. Ebert, and M. Saffman. "Rydberg-Mediated Entanglement in a Two-Dimensional Neutral Atom Qubit Array". Physical Review Letters **123** (2019), 230501.

[140] M. Saffman, I. I. Beterov, A. Dalal, E. J. Páez, and B. C. Sanders. "Symmetric Rydberg controlled-Z gates with adiabatic pulses". Physical Review A **101** (2020), 062309.

[141] L. Li, Y. O. Dudin, and A. Kuzmich. "Entanglement between light and an optical atomic excitation". Nature **498** (2013), 466.

[142] K. M. Birnbaum, A. Boca, R. Miller, A. D. Boozer, T. E. Northup, and H. J. Kimble. "Photon blockade in an optical cavity with one trapped atom". Nature **436** (2005), 87.

[143] A. Cidrim, T. S. do Espirito Santo, J. Schachenmayer, R. Kaiser, and R. Bachelard. "Photon Blockade with Ground-State Neutral Atoms". Physical Review Letters **125** (2020), 073601.

[144] R. Heidemann, U. Raitzsch, V. Bendkowsky, B. Butscher, R. Löw, L. Santos, and T. Pfau. "Evidence for Coherent Collective Rydberg Excitation in the Strong Blockade Regime". Physical Review Letters **99** (2007), 163601.

[145] J. Zeiher, P. Schauß, S. Hild, T. Macrì, I. Bloch, and C. Gross. "Microscopic Characterization of Scalable Coherent Rydberg Superatoms". Physical Review X **5** (2015), 031015.

[146] D. Braun, P. Jian, O. Pinel, and N. Treps. "Precision measurements with photon-subtracted or photon-added Gaussian states". Physical Review A **90** (2014), 013821.

[147] P. Solano, J. A. Grover, J. E. Hoffman, S. Ravets, F. K. Fatemi, L. A. Orozco, and S. L. Rolston. "Optical Nanofibers". *Advances in Atomic, Molecular and Optical Physics*. **66**. Academic Press Inc., 2017, 439.

[148] X. Gu, A. F. Kockum, A. Miranowicz, Y.-x. Liu, and F. Nori. "Microwave photonics with superconducting quantum circuits". Physics Reports **718-719** (2017), 1.

[149] J. D. Joannopoulos, S. G. Johnson, J. N. Winn, and R. D. Meade. *Photonic Crystals: Molding the Flow of Light*. Princeton University Press, 2008.

[150] J. D. Brehm, A. N. Poddubny, A. Stehli, T. Wolz, H. Rotzinger, and A. V. Ustinov. "Waveguide bandgap engineering with an array of superconducting qubits". npj Quantum Materials **6** (2021), 10.

[151] E. Kim, X. Zhang, V. S. Ferreira, J. Banker, J. K. Iverson, A. Sipahigil, M. Bello, A. González-Tudela, M. Mirhosseini, and O. Painter. "Quantum Electrodynamics in a Topological Waveguide". Physical Review X **11** (2021), 011015.

[152] K. Baumann, C. Guerlin, F. Brennecke, and T. Esslinger. "Dicke quantum phase transition with a superfluid gas in an optical cavity". Nature **464** (2010), 1301.

[153] S. John and J. Wang. "Quantum electrodynamics near a photonic band gap: Photon bound states and dressed atoms". Physical Review Letters **64** (1990), 2418.

[154] P. Kristensen, A. F. Koenderink, P. Lodahl, B. Tromborg, and J. Mørk. "Fractional decay of quantum dots in real photonic crystals". Optics Letters **33** (2008), 1557.

[155] G. Kurizki. "Two-atom resonant radiative coupling in photonic band structures". Physical Review A **42** (1990), 2915.

[156] A. González-Tudela and J. I. Cirac. "Markovian and non-Markovian dynamics of quantum emitters coupled to two-dimensional structured reservoirs". Physical Review A **96** (2017), 043811.

[157] G. Calajó, F. Ciccarello, D. Chang, and P. Rabl. "Atom-field dressed states in slow-light waveguide QED". Physical Review A **93** (2016), 033833.

[158] E. Sánchez-Burillo, D. Zueco, L. Martín-Moreno, and J. J. García-Ripoll. "Dynamical signatures of bound states in waveguide QED". Physical Review A **96** (2017), 023831.

[159] H. Z. Shen, S. Xu, H. T. Cui, and X. X. Yi. "Non-Markovian dynamics of a system of two-level atoms coupled to a structured environment". Physical Review A **99** (2019), 032101.

[160] F. Dinc and A. M. Brańczyk. "Non-Markovian super-superradiance in a linear chain of up to 100 qubits". Physical Review Research **1** (2019), 032042.

[161] K. Sinha, P. Meystre, E. A. Goldschmidt, F. K. Fatemi, S. L. Rolston, and P. Solano. "Non-Markovian Collective Emission from Macroscopically Separated Emitters". Physical Review Letters **124** (2020), 043603.

[162] M. Neugebauer, J. S. Eismann, T. Bauer, and P. Banzer. "Magnetic and Electric Transverse Spin Density of Spatially Confined Light". Physical Review X **8** (2018), 021042.

[163] K. Y. Bliokh, A. Y. Bekshaev, and F. Nori. "Extraordinary momentum and spin in evanescent waves". Nature Communications **5** (2014), 3300.

[164] I. Söllner, S. Mahmoodian, S. L. Hansen, L. Midolo, A. Javadi, G. Kiršanskė, T. Pregnolato, H. El-Ella, E. H. Lee, J. D. Song, S. Stobbe, and P. Lodahl. "Deterministic photon–emitter coupling in chiral photonic circuits". Nature Nanotechnology **10** (2015), 775.

[165] D. E. Chang, L. Jiang, A. V. Gorshkov, and H. J. Kimble. "Cavity QED with atomic mirrors". New Journal of Physics **14** (2012), 063003.

[166] T. Shi, D. E. Chang, and J. I. Cirac. "Multiphoton-scattering theory and generalized master equations". Physical Review A **92** (2015), 053834.

[167] H. Pichler, T. Ramos, A. J. Daley, and P. Zoller. "Quantum optics of chiral spin networks". Physical Review A **91** (2015), 042116.

[168] J. Ruostekoski and J. Javanainen. "Emergence of correlated optics in one-dimensional waveguides for classical and quantum atomic gases". Physical Review Letters **117** (2016), 143602.

[169] A. Asenjo-Garcia, J. D. Hood, D. E. Chang, and H. J. Kimble. "Atom-light interactions in quasi-one-dimensional nanostructures: A Green's-function perspective". Physical Review A **95** (2017), 033818.

[170] B. R. Mollow. "Pure-state analysis of resonant light scattering: Radiative damping, saturation, and multiphoton effects". Physical Review A **12** (1975), 1919.

[171] V. Weisskopf and E. Wigner. "Berechnung der natürlichen Linienbreite auf Grund der Diracschen Lichttheorie". Zeitschrift für Physik **63** (1930), 54.

[172] C. Gardiner and P. Zoller. *Quantum Noise: A handbook of Markovian and Non-Markovian Quantum Stochastic Methods with Applications to Quantum Optics*. Berlin: Springer, 2004.

[173] M. Fleischhauer and M. D. Lukin. "Quantum memory for photons: Dark-state polaritons". Physical Review A **65** (2002), 022314.

[174] T. Caneva, M. T. Manzoni, T. Shi, J. S. Douglas, J. I. Cirac, and D. E. Chang. "Quantum dynamics of propagating photons with strong interactions: a generalized input–output formalism". New Journal of Physics **17** (2015), 113001.

[175] L. Vestergaard Hau, S. E. Harris, Z. Dutton, and C. H. Behroozi. "Light speed reduction to 17 metres per second in an ultracold atomic gas". Nature **397** (1999), 594.

[176] N. S. Ginsberg, S. R. Garner, and L. V. Hau. "Coherent control of optical information with matter wave dynamics". Nature **445** (2007), 623.

[177] A. Paris-Mandoki, C. Braun, J. Kumlin, C. Tresp, I. Mirgorodskiy, F. Christaller, H. P. Büchler, and S. Hofferberth. "Free-Space Quantum Electrodynamics with a Single Rydberg Superatom". Physical Review X **7** (2017), 041010.

[178] N. Stiesdal, J. Kumlin, K. Kleinbeck, P. Lunt, C. Braun, A. Paris-Mandoki, C. Tresp, H. P. Büchler, and S. Hofferberth. "Observation of Three-Body Correlations for Photons Coupled to a Rydberg Superatom". Physical Review Letters **121** (2018), 103601.

[179] C. Cohen-Tannoudji, J. Dupont-Roc, and G. Grynberg. *Photons and Atoms*. New York: Wiley-VCH, 1997.

[180] H. J. Kimble. "The quantum internet". Nature **453** (2008), 1023.

[181] A. Reiserer and G. Rempe. "Cavity-based quantum networks with single atoms and optical photons". Reviews of Modern Physics **87** (2015), 1379.

[182] B. Hacker, S. Welte, G. Rempe, and S. Ritter. "A photon–photon quantum gate based on a single atom in an optical resonator". Nature **536** (2016), 193.

[183] I. Shomroni, S. Rosenblum, Y. Lovsky, O. Bechler, G. Guendelman, and B. Dayan. "All-optical routing of single photons by a one-atom switch controlled by a single photon". Science **345** (2014), 903.

[184] T. G. Tiecke, J. D. Thompson, N. P. de Leon, L. R. Liu, V. Vuletić, and M. D. Lukin. "Nanophotonic quantum phase switch with a single atom". Nature **508** (2014), 241.

[185] B. W. Shore and P. L. Knight. "The Jaynes-Cummings Model". Journal of Modern Optics **40** (1993), 1195.

[186] J. M. Raimond, M. Brune, and S. Haroche. "Manipulating quantum entanglement with atoms and photons in a cavity". Reviews of Modern Physics **73** (2001), 565.

[187] A. Wallraff, D. I. Schuster, A. Blais, L. Frunzio, R.-S. Huang, J. Majer, S. Kumar, S. M. Girvin, and R. J. Schoelkopf. "Strong coupling of a single photon to a superconducting qubit using circuit quantum electrodynamics". Nature **431** (2004), 162.

[188] R. J. Schoelkopf and S. M. Girvin. "Wiring up quantum systems". Nature **451** (2008), 664.

[189] A. N. Vamivakas, M. Atatüre, J. Dreiser, S. T. Yilmaz, A. Badolato, A. K. Swan, B. B. Goldberg, A. Imamoğlu, and M. S. Ünlü. "Strong Extinction of a Far-Field Laser Beam by a Single Quantum Dot". Nano Letters **7** (2007), 2892.

[190] M. K. Tey, Z. Chen, S. A. Aljunid, B. Chng, F. Huber, G. Maslennikov, and C. Kurtsiefer. "Strong interaction between light and a single trapped atom without the need for a cavity". Nature Physics **4** (2008), 924.

[191] A. Maser, B. Gmeiner, T. Utikal, S. Götzinger, and V. Sandoghdar. "Few-photon coherent nonlinear optics with a single molecule". Nature Photonics **10** (2016), 450.

[192] A. F. van Loo, A. Fedorov, K. Lalumiere, B. C. Sanders, A. Blais, and A. Wallraff. "Photon-Mediated Interactions Between Distant Artificial Atoms". Science **342** (2013), 1494.

[193] S. Faez, P. Türschmann, H. R. Haakh, S. Götzinger, and V. Sandoghdar. "Coherent Interaction of Light and Single Molecules in a Dielectric Nanoguide". Physical Review Letters **113** (2014), 213601.

[194] A. Goban, C.-L. Hung, J. D. Hood, S.-P. Yu, J. A. Muniz, O. Painter, and H. J. Kimble. "Superradiance for Atoms Trapped along a Photonic Crystal Waveguide". Physical Review Letters **115** (2015), 063601.

[195] A. Sipahigil et al. "An integrated diamond nanophotonics platform for quantum-optical networks". Science **354** (2016), 847.

[196] M. K. Bhaskar et al. "Quantum Nonlinear Optics with a Germanium-Vacancy Color Center in a Nanoscale Diamond Waveguide". Physical Review Letters **118** (2017), 223603.

[197] E. Urban, T. A. Johnson, T. Henage, L. Isenhower, D. D. Yavuz, T. G. Walker, and M. Saffman. "Observation of Rydberg blockade between two atoms". Nature Physics **5** (2009), 110.

[198] A. Gaëtan, Y. Miroshnychenko, T. Wilk, A. Chotia, M. Viteau, D. Comparat, P. Pillet, A. Browaeys, and P. Grangier. "Observation of collective excitation of two individual atoms in the Rydberg blockade regime". Nature Physics **5** (2009), 115.

[199] D. Porras and J. I. Cirac. "Collective generation of quantum states of light by entangled atoms". Physical Review A **78** (2008), 053816.

[200] Y. Miroshnychenko, U. V. Poulsen, and K. Mølmer. "Directional emission of single photons from small atomic samples". Physical Review A **87** (2013), 023821.

[201] M. O. Araújo, I. Krešić, R. Kaiser, and W. Guerin. "Superradiance in a Large and Dilute Cloud of Cold Atoms in the Linear-Optics Regime". Physical Review Letters **117** (2016), 073002.

[202] S. J. Roof, K. J. Kemp, M. D. Havey, and I. M. Sokolov. "Observation of Single-Photon Superradiance and the Cooperative Lamb Shift in an Extended Sample of Cold Atoms". Physical Review Letters **117** (2016), 073003.

[203] G. Leuchs and M. Sondermann. "Light–matter interaction in free space". Journal of Modern Optics **60** (2013), 36.

[204] Y. Wang, J. Minář, L. Sheridan, and V. Scarani. "Efficient excitation of a two-level atom by a single photon in a propagating mode". Physical Review A **83** (2011), 063842.

[205] V. Leong, M. A. Seidler, M. Steiner, A. Cerè, and C. Kurtsiefer. "Time-resolved scattering of a single photon by a single atom". Nature Communications **7** (2016), 13716.

[206] M. Lax. "Quantum Noise. XI. Multitime Correspondence between Quantum and Classical Stochastic Processes". Physical Review **172** (1968), 350.

[207] A. Grankin, E. Brion, R. Boddeda, S. Ćuk, I. Usmani, A. Ourjoumtsev, and P. Grangier. "Inelastic Photon Scattering via the Intracavity Rydberg Blockade". Physical Review Letters **117** (2016), 253602.

[208] E. Rephaeli and S. Fan. "Stimulated Emission from a Single Excited Atom in a Waveguide". Physical Review Letters **108** (2012), 143602.

[209] M. Assmann, F. Veit, M. Bayer, M. van der Poel, and J. M. Hvam. "Higher-Order Photon Bunching in a Semiconductor Microcavity". Science **325** (2009), 297.

[210] M. Koch, C. Sames, M. Balbach, H. Chibani, A. Kubanek, K. Murr, T. Wilk, and G. Rempe. "Three-Photon Correlations in a Strongly Driven Atom-Cavity System". Physical Review Letters **107** (2011), 023601.

[211] Q.-Y. Liang, A. V. Venkatramani, S. H. Cantu, T. L. Nicholson, M. J. Gullans, A. V. Gorshkov, J. D. Thompson, C. Chin, M. D. Lukin, and V. Vuletić. "Observation of three-photon bound states in a quantum nonlinear medium". Science **359** (2018), 783.

[212] V. I. Yudson. "Dynamics of integrable quantum systems". Sov. Phys. JETP **61** (1985), 1043.

[213] K. Kleinbeck. "Quantum Light Interaction with Superatoms". MSc thesis. University of Stuttgart, 2017.

[214] A. E. Siegman. *Lasers*. University Science Books, 1986.

[215] S. Swain. "Master equation derivation of quantum regression theorem". Journal of Physics A: Mathematical and General **14** (1981), 2577.

[216] J. Kumlin, S. Hofferberth, and H. P. Büchler. "Emergent Universal Dynamics for an Atomic Cloud Coupled to an Optical Waveguide". Physical Review Letters **121** (2018), 013601.

[217] S. L. Bromley, B. Zhu, M. Bishof, X. Zhang, T. Bothwell, J. Schachenmayer, T. L. Nicholson, R. Kaiser, S. F. Yelin, M. D. Lukin, A. M. Rey, and J. Ye. "Collective atomic scattering and motional effects in a dense coherent medium". Nature Communications **7** (2016), 11039.

[218] R. Friedberg, S. Hartmann, and J. Manassah. "Frequency shifts in emission and absorption by resonant systems ot two-level atoms". Physics Reports **7** (1973), 101.

[219] J. Javanainen, J. Ruostekoski, Y. Li, and S.-M. Yoo. "Shifts of a Resonance Line in a Dense Atomic Sample". Physical Review Letters **112** (2014), 113603.

[220] M. Ebert, A. Gill, M. Gibbons, X. Zhang, M. Saffman, and T. G. Walker. "Atomic Fock State Preparation Using Rydberg Blockade". Physical Review Letters **112** (2014), 043602.

[221] G. Meltz, W. W. Morey, and W. H. Glenn. "Formation of Bragg gratings in optical fibers by a transverse holographic method". Optics Letters **14** (1989), 823.

[222] S. P. Yu, J. D. Hood, J. A. Muniz, M. J. Martin, R. Norte, C. L. Hung, S. M. Meenehan, J. D. Cohen, O. Painter, and H. J. Kimble. "Nanowire photonic crystal waveguides for single-atom trapping and strong light-matter interactions". Applied Physics Letters **104** (2014), 111103.

[223] J. Kumlin, K. Kleinbeck, N. Stiesdal, H. Busche, S. Hofferberth, and H. P. Büchler. "Nonexponential decay of a collective excitation in an atomic ensemble coupled to a one-dimensional waveguide". Physical Review A **102** (2020), 063703.

[224] W. Guerin, M. Rouabah, and R. Kaiser. "Light interacting with atomic ensembles: collective, cooperative and mesoscopic effects". Journal of Modern Optics **64** (2017), 895.

[225] N. Lambert, Y. Matsuzaki, K. Kakuyanagi, N. Ishida, S. Saito, and F. Nori. "Superradiance with an ensemble of superconducting flux qubits". Physical Review B **94** (2016), 224510.

[226] R. J. Bettles, T. Ilieva, H. Busche, P. Huillery, S. W. Ball, N. L. R. Spong, and C. S. Adams. "Collective Mode Interferences in Light–Matter Interactions". arXiv:1808.08415v4 (2018).

[227] A. A. Svidzinsky, J.-T. Chang, and M. O. Scully. "Cooperative spontaneous emission of N atoms: Many-body eigenstates, the effect of virtual Lamb shift processes, and analogy with radiation of N classical oscillators". Physical Review A **81** (2010), 053821.

[228] A. Grankin, P. O. Guimond, D. V. Vasilyev, B. Vermersch, and P. Zoller. "Free-space photonic quantum link and chiral quantum optics". Physical Review A **98** (2018), 043825.

[229] P. R. Berman. "Theory of two atoms in a chiral waveguide". Physical Review A **101** (2020), 013830.

[230] H. H. Jen, M.-S. Chang, G.-D. Lin, and Y.-C. Chen. "Subradiance dynamics in a singly excited chirally coupled atomic chain". Physical Review A **101** (2020), 023830.

[231] K. Stannigel, P. Rabl, A. S. Sørensen, P. Zoller, and M. D. Lukin. "Optomechanical Transducers for Long-Distance Quantum Communication". Physical Review Letters **105** (2010), 220501.

[232] R. Röhlsberger. "Cooperative emission from nuclei: The collective Lamb shift and electromagnetically induced transparency". Fortschritte der Physik **61** (2013), 360.

[233] P. Lodahl, A. Floris van Driel, I. S. Nikolaev, A. Irman, K. Overgaag, D. Vanmaekelbergh, and W. L. Vos. "Controlling the dynamics of spontaneous emission from quantum dots by photonic crystals". Nature **430** (2004), 654.

[234] B. Kannan et al. "Waveguide quantum electrodynamics with superconducting artificial giant atoms". Nature **583** (2020), 775.

[235] Y. Luo et al. "Electrically Driven Single-Photon Superradiance from Molecular Chains in a Plasmonic Nanocavity". Physical Review Letters **122** (2019), 233901.

[236] N. Stiesdal, H. Busche, J. Kumlin, K. Kleinbeck, H. P. Büchler, and S. Hofferberth. "Observation of collective decay dynamics of a single Rydberg superatom". Physical Review Research **2** (2020), 043339.

[237] M. Chalony, R. Pierrat, D. Delande, and D. Wilkowski. "Coherent flash of light emitted by a cold atomic cloud". Physical Review A **84** (2011), 011401.

[238] C. C. Kwong, T. Yang, M. S. Pramod, K. Pandey, D. Delande, R. Pierrat, and D. Wilkowski. "Cooperative Emission of a Coherent Superflash of Light". Physical Review Letters **113** (2014), 223601.

[239] S. Jennewein, L. Brossard, Y. R. P. Sortais, A. Browaeys, P. Cheinet, J. Robert, and P. Pillet. "Coherent scattering of near-resonant light by a dense, microscopic cloud of cold two-level atoms: Experiment versus theory". Physical Review A **97** (2018), 053816.

[240] T. Peyrot, Y. R. P. Sortais, A. Browaeys, A. Sargsyan, D. Sarkisyan, J. Keaveney, I. G. Hughes, and C. S. Adams. "Collective Lamb Shift of a Nanoscale Atomic Vapor Layer within a Sapphire Cavity". Physical Review Letters **120** (2018), 243401.

[241] B. Hopkins, A. N. Poddubny, A. E. Miroshnichenko, and Y. S. Kivshar. "Revisiting the physics of Fano resonances for nanoparticle oligomers". Physical Review A **88** (2013), 053819.

[242] R. J. Bettles, S. A. Gardiner, and C. S. Adams. "Cooperative ordering in lattices of interacting two-level dipoles". Physical Review A **92** (2015), 063822.

[243] W. Guerin and R. Kaiser. "Population of collective modes in light scattering by many atoms". Physical Review A **95** (2017), 053865.

[244] B. Zhu, J. Cooper, J. Ye, and A. M. Rey. "Light scattering from dense cold atomic media". Physical Review A **94** (2016), 023612.

[245] E. Shahmoon and G. Kurizki. "Nonlinear theory of laser-induced dipolar interactions in arbitrary geometry". Physical Review A **89** (2014), 043419.

[246] S. D. Jenkins and J. Ruostekoski. "Controlled manipulation of light by cooperative response of atoms in an optical lattice". Physical Review A **86** (2012), 031602.

[247] G. Facchinetti, S. D. Jenkins, and J. Ruostekoski. "Storing Light with Subradiant Correlations in Arrays of Atoms". Physical Review Letters **117** (2016), 243601.

[248] P. Back, S. Zeytinoglu, A. Ijaz, M. Kroner, and A. Imamoğlu. "Realization of an Electrically Tunable Narrow-Bandwidth Atomically Thin Mirror Using Monolayer $MoSe_2$". Physical Review Letters **120** (2018), 037401.

[249] G. Scuri, Y. Zhou, A. A. High, D. S. Wild, C. Shu, K. De Greve, L. A. Jauregui, T. Taniguchi, K. Watanabe, P. Kim, M. D. Lukin, and H. Park. "Large Excitonic Reflectivity of Monolayer $MoSe_2$ Encapsulated in Hexagonal Boron Nitride". Physical Review Letters **120** (2018), 037402.

[250] H. H. Jen, M.-S. Chang, and Y.-C. Chen. "Cooperative single-photon subradiant states". Physical Review A **94** (2016), 013803.

[251] K. Kleinbeck. "(In preparation)". PhD thesis. University of Stuttgart.

[252] M. T. Manzoni, M. Moreno-Cardoner, A. Asenjo-Garcia, J. V. Porto, A. V. Gorshkov, and D. E. Chang. "Optimization of photon storage fidelity in ordered atomic arrays". New Journal of Physics **20** (2018), 083048.

[253] K. B. Davis, M.-O. Mewes, M. R. Andrews, N. J. van Druten, D. S. Durfee, D. M. Kurn, and W. Ketterle. "Bose-Einstein Condensation in a Gas of Sodium Atoms". Physical Review Letters **75** (1995), 3969.

[254] M. H. Anderson, J. R. Ensher, M. R. Matthews, C. E. Wieman, and E. A. Cornell. "Observation of Bose-Einstein Condensation in a Dilute Atomic Vapor". Science **269** (1995), 198.

[255] C. C. Bradley, C. A. Sackett, J. J. Tollett, and R. G. Hulet. "Evidence of Bose-Einstein Condensation in an Atomic Gas with Attractive Interactions". Physical Review Letters **75** (1995), 1687.

[256] M. Greiner, O. Mandel, T. W. Hänsch, and I. Bloch. "Collapse and revival of the matter wave field of a Bose–Einstein condensate". Nature **419** (2002), 51.

[257] K. W. Madison, F. Chevy, W. Wohlleben, and J. Dalibard. "Vortex Formation in a Stirred Bose-Einstein Condensate". Physical Review Letters **84** (2000), 806.

[258] M. Greiner, O. Mandel, T. Esslinger, T. W. Hänsch, and I. Bloch. "Quantum phase transition from a superfluid to a Mott insulator in a gas of ultracold atoms". Nature **415** (2002), 39.

[259] E. P. Gross. "Structure of a quantized vortex in boson systems". Il Nuovo Cimento **20** (1961), 454.

[260] L. P. Pitaevskii. "Vortex lines in an imperfect Bose gas". Sov. Phys. JETP **13** (1961), 451.

[261] A. Griesmaier, J. Werner, S. Hensler, J. Stuhler, and T. Pfau. "Bose-Einstein Condensation of Chromium". Physical Review Letters **94** (2005), 160401.

[262] M. Lu, N. Q. Burdick, S. H. Youn, and B. L. Lev. "Strongly Dipolar Bose-Einstein Condensate of Dysprosium". Physical Review Letters **107** (2011), 190401.

[263] K. Aikawa, A. Frisch, M. Mark, S. Baier, A. Rietzler, R. Grimm, and F. Ferlaino. "Bose-Einstein Condensation of Erbium". Physical Review Letters **108** (2012), 210401.

[264] M. A. Baranov, M. Dalmonte, G. Pupillo, and P. Zoller. "Condensed Matter Theory of Dipolar Quantum Gases". Chemical Reviews **112** (2012), 5012.

[265] T. Lahaye, J. Metz, B. Fröhlich, T. Koch, M. Meister, A. Griesmaier, T. Pfau, H. Saito, Y. Kawaguchi, and M. Ueda. "d-Wave Collapse and Explosion of a Dipolar Bose-Einstein Condensate". Physical Review Letters **101** (2008), 080401.

[266] R. Lopes, C. Eigen, N. Navon, D. Clément, R. P. Smith, and Z. Hadzibabic. "Quantum Depletion of a Homogeneous Bose-Einstein Condensate". Physical Review Letters **119** (2017), 190404.

[267] J. Steinhauer, R. Ozeri, N. Katz, and N. Davidson. "Excitation Spectrum of a Bose-Einstein Condensate". Physical Review Letters **88** (2002), 120407.

[268] R. Lopes, C. Eigen, A. Barker, K. G. H. Viebahn, M. Robert-de-Saint-Vincent, N. Navon, Z. Hadzibabic, and R. P. Smith. "Quasiparticle Energy in a Strongly Interacting Homogeneous Bose-Einstein Condensate". Physical Review Letters **118** (2017), 210401.

[269] N. Navon, S. Piatecki, K. Günter, B. Rem, T. C. Nguyen, F. Chevy, W. Krauth, and C. Salomon. "Dynamics and Thermodynamics of the Low-Temperature Strongly Interacting Bose Gas". Physical Review Letters **107** (2011), 135301.

[270] H. Kadau, M. Schmitt, M. Wenzel, C. Wink, T. Maier, I. Ferrier-Barbut, and T. Pfau. "Observing the Rosensweig instability of a quantum ferrofluid". Nature **530** (2016), 194.

[271] M. Schmitt, M. Wenzel, F. Böttcher, I. Ferrier-Barbut, and T. Pfau. "Self-bound droplets of a dilute magnetic quantum liquid". Nature **539** (2016), 259.

[272] L. Chomaz, S. Baier, D. Petter, M. J. Mark, F. Wächtler, L. Santos, and F. Ferlaino. "Quantum-Fluctuation-Driven Crossover from a Dilute Bose-Einstein Condensate to a Macrodroplet in a Dipolar Quantum Fluid". Physical Review X **6** (2016), 041039.

[273] I. Ferrier-Barbut, M. Wenzel, F. Böttcher, T. Langen, M. Isoard, S. Stringari, and T. Pfau. "Scissors Mode of Dipolar Quantum Droplets of Dysprosium Atoms". Physical Review Letters **120** (2018), 160402.

[274] F. Böttcher, M. Wenzel, J.-N. Schmidt, M. Guo, T. Langen, I. Ferrier-Barbut, T. Pfau, R. Bombín, J. Sánchez-Baena, J. Boronat, and F. Mazzanti. "Dilute dipolar quantum droplets beyond the extended Gross-Pitaevskii equation". Physical Review Research **1** (2019), 033088.

[275] M. Guo, F. Böttcher, J. Hertkorn, J.-N. Schmidt, M. Wenzel, H. P. Büchler, T. Langen, and T. Pfau. "The low-energy Goldstone mode in a trapped dipolar supersolid". Nature **574** (2019), 386.

[276] D. S. Petrov. "Quantum Mechanical Stabilization of a Collapsing Bose-Bose Mixture". Physical Review Letters **115** (2015), 155302.

[277] T. D. Lee, K. Huang, and C. N. Yang. "Eigenvalues and Eigenfunctions of a Bose System of Hard Spheres and Its Low-Temperature Properties". Physical Review **106** (1957), 1135.

[278] N. M. Hugenholtz and D. Pines. "Ground-State Energy and Excitation Spectrum of a System of Interacting Bosons". Physical Review **116** (1959), 489.

[279] S. T. Beliaev. "Energy Spectrum of a Non-Ideal Bose Gas". Sov. Phys. JETP **7** (1958), 299.

[280] A. R. P. Lima and A. Pelster. "Beyond mean-field low-lying excitations of dipolar Bose gases". Physical Review A **86** (2012), 063609.

[281] I. Ferrier-Barbut, H. Kadau, M. Schmitt, M. Wenzel, and T. Pfau. "Observation of Quantum Droplets in a Strongly Dipolar Bose Gas". Physical Review Letters **116** (2016), 215301.

[282] C. R. Cabrera, L. Tanzi, J. Sanz, B. Naylor, P. Thomas, P. Cheiney, and L. Tarruell. "Quantum liquid droplets in a mixture of Bose-Einstein condensates". Science **359** (2018), 301.

[283] T. Ilg, J. Kumlin, L. Santos, D. S. Petrov, and H. P. Büchler. "Dimensional crossover for the beyond-mean-field correction in Bose gases". Physical Review A **98** (2018), 051604.

[284] P. Zin, M. Pylak, T. Wasak, M. Gajda, and Z. Idziaszek. "Quantum Bose-Bose droplets at a dimensional crossover". Physical Review A **98** (2018), 051603.

[285] D. Edler, C. Mishra, F. Wächtler, R. Nath, S. Sinha, and L. Santos. "Quantum Fluctuations in Quasi-One-Dimensional Dipolar Bose-Einstein Condensates". Physical Review Letters **119** (2017), 050403.

[286] L. Santos, G. V. Shlyapnikov, and M. Lewenstein. "Roton-Maxon Spectrum and Stability of Trapped Dipolar Bose-Einstein Condensates". Physical Review Letters **90** (2003), 250403.

[287] S. Ronen, D. C. E. Bortolotti, and J. L. Bohn. "Radial and Angular Rotons in Trapped Dipolar Gases". Physical Review Letters **98** (2007), 030406.

[288] L. Landau. "On the Theory of Superfluidity of Helium II". J. Phys **11** (1941), 592.

[289] L. Chomaz, R. M. W. van Bijnen, D. Petter, G. Faraoni, S. Baier, J. H. Becher, M. J. Mark, F. Wächtler, L. Santos, and F. Ferlaino. "Observation of roton mode population in a dipolar quantum gas". Nature Physics **14** (2018), 442.

[290] F. Böttcher, J.-N. Schmidt, M. Wenzel, J. Hertkorn, M. Guo, T. Langen, and T. Pfau. "Transient Supersolid Properties in an Array of Dipolar Quantum Droplets". Physical Review X **9** (2019), 011051.

[291] L. Chomaz, D. Petter, P. Ilzhöfer, G. Natale, A. Trautmann, C. Politi, G. Durastante, R. M. W. van Bijnen, A. Patscheider, M. Sohmen, M. J. Mark, and F. Ferlaino. "Long-Lived and Transient Supersolid Behaviors in Dipolar Quantum Gases". Physical Review X **9** (2019), 021012.

[292] L. Tanzi, E. Lucioni, F. Famà, J. Catani, A. Fioretti, C. Gabbanini, R. N. Bisset, L. Santos, and G. Modugno. "Observation of a Dipolar Quantum Gas with Metastable Supersolid Properties". Physical Review Letters **122** (2019), 130405.

[293] F. Böttcher, J.-N. Schmidt, J. Hertkorn, K. S. H. Ng, S. D. Graham, M. Guo, T. Langen, and T. Pfau. "New states of matter with fine-tuned interactions: quantum droplets and dipolar supersolids". Reports on Progress in Physics **84** (2021), 012403.

[294] M. Lewenstein, A. Sanpera, V. Ahufinger, B. Damski, A. Sen(De), and U. Sen. "Ultracold atomic gases in optical lattices: mimicking condensed matter physics and beyond". Advances in Physics **56** (2007), 243.

[295] I. Bloch, J. Dalibard, and W. Zwerger. "Many-body physics with ultracold gases". Reviews of Modern Physics **80** (2008), 885.

[296] D. Jaksch, C. Bruder, J. I. Cirac, C. W. Gardiner, and P. Zoller. "Cold Bosonic Atoms in Optical Lattices". Physical Review Letters **81** (1998), 3108.

[297] C. Trefzger, C. Menotti, B. Capogrosso-Sansone, and M. Lewenstein. "Ultracold dipolar gases in optical lattices". Journal of Physics B: Atomic, Molecular and Optical Physics **44** (2011), 193001.

[298] O. Dutta, M. Gajda, P. Hauke, M. Lewenstein, D.-S. Lühmann, B. A. Malomed, T. Sowiński, and J. Zakrzewski. "Non-standard Hubbard models in optical lattices: a review". Reports on Progress in Physics **78** (2015), 066001.

[299] S. Baier, M. J. Mark, D. Petter, K. Aikawa, L. Chomaz, Z. Cai, M. Baranov, P. Zoller, and F. Ferlaino. "Extended Bose-Hubbard models with ultracold magnetic atoms". Science **352** (2016), 201.

[300] H. P. Büchler, E. Demler, M. Lukin, A. Micheli, N. Prokof'ev, G. Pupillo, and P. Zoller. "Strongly Correlated 2D Quantum Phases with Cold Polar Molecules: Controlling the Shape of the Interaction Potential". Physical Review Letters **98** (2007), 060404.

[301] B. Capogrosso-Sansone, C. Trefzger, M. Lewenstein, P. Zoller, and G. Pupillo. "Quantum Phases of Cold Polar Molecules in 2D Optical Lattices". Physical Review Letters **104** (2010), 125301.

[302] G. Orso, C. Menotti, and S. Stringari. "Quantum fluctuations and Collective Oscillations of a Bose-Einstein Condensate in a 2D Optical Lattice". Physical Review Letters **97** (2006), 190408.

[303] S. Müller, J. Billy, E. A. L. Henn, H. Kadau, A. Griesmaier, M. Jona-Lasinio, L. Santos, and T. Pfau. "Stability of a dipolar Bose-Einstein condensate in a one-dimensional lattice". Physical Review A **84** (2011), 053601.

[304] M. Klawunn and L. Santos. "Hybrid multisite excitations in dipolar condensates in optical lattices". Physical Review A **80** (2009), 013611.

[305] D.-W. Wang and E. Demler. "Collective excitations and instabilities in multi-layer stacks of dipolar condensates". arXiv:0812.1838v1 (2008).

[306] M. Marinescu and L. You. "Controlling Atom-Atom Interaction at Ultralow Temperatures by dc Electric Fields". Physical Review Letters **81** (1998), 4596.

[307] B. Deb and L. You. "Low-energy atomic collision with dipole interactions". Physical Review A **64** (2001), 022717.

[308] C. Ticknor and J. L. Bohn. "Long-range scattering resonances in strong-field-seeking states of polar molecules". Physical Review A **72** (2005), 032717.

[309] S. Yi and L. You. "Trapped atomic condensates with anisotropic interactions". Physical Review A **61** (2000), 041604.

[310] S. Yi and L. You. "Trapped condensates of atoms with dipole interactions". Physical Review A **63** (2001), 053607.

[311] A. Derevianko. "Anisotropic pseudopotential for polarized dilute quantum gases". Physical Review A **67** (2003), 033607.

[312] A. Derevianko. "Erratum: Anisotropic pseudopotential for polarized dilute quantum gases [Phys. Rev. A 67 , 033607 (2003)]". Physical Review A **72** (2005), 039901.

[313] D. M. Stamper-Kurn and M. Ueda. "Spinor Bose gases: Symmetries, magnetism, and quantum dynamics". Reviews of Modern Physics **85** (2013), 1191.

[314] B. Pasquiou, G. Bismut, Q. Beaufils, A. Crubellier, E. Maréchal, P. Pedri, L. Vernac, O. Gorceix, and B. Laburthe-Tolra. "Control of dipolar relaxation in external fields". Physical Review A **81** (2010), 042716.

[315] Y. Tang, A. Sykes, N. Q. Burdick, J. L. Bohn, and B. L. Lev. "s-wave scattering lengths of the strongly dipolar bosons ^{162}Dy and ^{164}Dy". Physical Review A **92** (2015), 022703.

[316] L. Pitaevskii and S. Stringari. *Bose-Einstein Condensation*. Oxford: Oxford University Press, 2003.

[317] N. Bogoliubov. "On the theory of superfluidity". Journal of Physics **11** (1947), 23.

[318] A. A. Abrikosov, L. P. Gorkov, and I. E. Dzyaloshinski. *Methods of Quantum Field Theory in Statistical Physics*. Ed. by R. A. Silverman. New York: Dover Publications, Inc., 1963.

[319] T. Ilg. "Quantum Corrections in Cold Dipolar Gases". MSc thesis. University of Stuttgart, 2017.

[320] R. Ołdziejewski and K. Jachymski. "Properties of strongly dipolar Bose gases beyond the Born approximation". Physical Review A **94** (2016), 063638.

[321] J. Kumlin, K. Jachymski, and H. P. Büchler. "Beyond-mean-field corrections for dipolar bosons in an optical lattice". Physical Review A **99** (2019), 033622.

[322] T. Sowiński, O. Dutta, P. Hauke, L. Tagliacozzo, and M. Lewenstein. "Dipolar Molecules in Optical Lattices". Physical Review Letters **108** (2012), 115301.

[323] M. L. Wall and L. D. Carr. "Dipole–dipole interactions in optical lattices do not follow an inverse cube power law". New Journal of Physics **15** (2013), 123005.

[324] D. Peter. "Quantum states with topological properties via dipolar interaction". PhD thesis. University of Stuttgart, 2015.

Ausführliche Zusammenfassung in deutscher Sprache

Kollektive Effekte der Licht-Materie-Wechselwirkung in Rydberg-Superatomen

Die Wechselwirkung von Licht und Materie ist eine wichtige Grundlage für viele Vorgänge in der Natur. Durch sie können Menschen und Tiere sehen und Pflanzen durch Photosynthese Energie gewinnen. Auch viele Anwendungen in unserer modernen Welt wie bildgebende Verfahren in der Medizin, spektroskopische Verfahren in verschiedensten Bereichen der Forschung, aber auch Anwendungen in der optischen Informationsverarbeitung wären ohne ein Verständnis der fundamentalen Prozesse der Licht-Materie-Wechselwirkung nicht möglich.

Aus Sicht der klassischen Physik kann diese Wechselwirkung verstanden werden, indem die Emitter als oszillierende Dipole behandelt werden, die Energie in der Form elektromagnetischer Wellen aussenden [1]. Die ausgesendete Strahlung kann wiederum andere Dipole in der Nähe anregen und so eine dynamische Dipol-Dipol-Wechselwirkung induzieren. Auf der quantenmechanischen Ebene werden die Emitter oft als Zwei-Niveau-Systeme modelliert, in denen der Dipol durch das Übergangsdipolmoment zwischen beiden Niveaus gegeben ist. Haben alle Emitter die gleiche Resonanfrequenz, ist das ausgestrahlte Licht eines Emitters resonant mit anderen Emittern, weshalb diese Wechselwirkungen auch als *resonante Dipol-Dipol-Wechselwirkungen* bezeichnet werden. Diese Wechselwirkungen sind aus zwei Gründen interessant: Zum einen sind sie langreichweitig, wodurch ein Emitter mit vielen anderen gleichzeitig wechselwirken kann. Zum anderen haben sie sowohl eine dispersive als auch eine dissipative Komponente. Die dispersive Komponente entsteht durch das Treiben eines Dipols durch das ausgesendete Licht eines anderen und die dissipative Komponente rührt von der Tatsache her, dass ein

einzelner Dipol in den freien Raum abstrahlen kann [2].

Darüber hinaus können resonante Dipol-Dipol-Wechselwirkungen die optischen Eigenschaften eines Ensembles von Emittern verändern. In einer wegweisenden Arbeit zeigte Dicke, dass Emitter, deren Abstand kleiner ist als ihre Resonanzwellenlänge, nicht unabhängig strahlen, sondern kooperatives Verhalten zeigen, da sie an ein gemeinsames Strahlungsfeld gekoppelt sind [3]. Die Strahlungseigenschaften eines Emitters hängen dann aufgrund der resonanten Dipol-Dipol-Wechselwirkungen stark vom Zustand anderer in der Nähe ab. Dieses kooperative Verhalten in dichten Gasen führt zu enormen Verschiebungen der Energieniveaus und korrelierter spontaner Emission. Während die Verschiebungen der Energieniveaus eine Sättigung des Brechungsindex in dichten Gasen und Festkörpern zur Folge hat [4], führt die korrelierte spontane Emission zum Phänomen der *Superradianz* [3, 5]. Superradianz beschreibt eine stark verstärkte Emission aus einem dichten Ensemble von Atomen aufgrund von selbststimulierter Emission. Sind alle Emitter angeregt, skaliert die emittierte Intensität quadratisch mit der Anzahl der Emitter (statt linear wie bei unabhängiger Emission). Außerdem variiert auch die Emissionsrate während des Emissionsprozesses und skaliert quadratisch, wenn die Hälfte des Ensembles angeregt ist [5]. Superradiante Eigenschaften, einschließlich der Verschiebung der Energieniveaus aufgrund kooperativer Effekte, wurden in einem breiten Spektrum physikalischer Systeme beobachtet, die von Ensembles von Kernen [6] über kalte Atome [7–10], Ionen [11] und Festkörpersysteme [12, 13] bis hin zu künstlichen und hybriden Licht-Materie-Systemen wie supraleitenden Qubits [14] und an nanophotonische Strukturen gekoppelte Atome [15] reichen.

Während Superradianz ursprünglich für dichte Ensembles diskutiert wurde, deren Ausdehnung kleiner ist als die Resonanzwellenlänge, tritt auch in Ensembles mit größeren Längenskalen kollektives Verhalten auf. In diesem Regime wird eine stark verstärkte und sogar stark direktionale Emission von Photonen aus dem Ensemble durch konstruktive Interferenz für Zustände erreicht, in denen die Phaseninformation des einfallenden Photons in einer kollektiven Anregung des Ensemble gespeichert ist. Diese werden daher auch als „timed“ Dicke-Zustände[3] [16] bezeichnet. Im Gegensatz zu dichten und nicht ausgedehnten Ensembles, bei denen Superradianz auch im Falle mehrerer Anregungen untersucht wurde, beschränkte sich die theoretische Untersuchung der Superradianz in ausgedehnten Ensembles, mit wenigen Ausnahmen [25–27], bisher meist auf eine einzelne Anregung [16–24], was den Begriff *Einzel-Photonen-Superradianz* [18] geprägt hat. Obwohl viele Aspekte der Superradianz - wie die quadratische Skalierung der emittierten Intensität oder die stark direktionale Emission von Strahlung - klassisch als in Pha-

[3] An dieser Stelle wird der englische Begriff verwendet, da eine griffige deutsche Übersetzung nur schwer zu finden ist.

se schwingende Dipole (analog zu phasenkohärenten Antennen-Arrays) verstanden werden können, ist eine quantenmechanische Behandlung der Licht-Materie-Wechselwirkung für ein vollständiges Verständnis superradianter Phänomene notwendig [28].

Eng verbunden mit dem Phänomen der Superradianz ist die *Subradianz*, die eine *unterdrückte* spontane Emission aufgrund destruktiver Interferenz beschreibt. Genauso wie die Superradianz hat die Subradianz im Laufe der Jahre viel Aufmerksamkeit im Rahmen von theoretischen Betrachtungen erhalten [5, 25, 29–34]. Durch die nur schwache Kopplung von subradianten Zuständen an das elektromagnetische Feld entzog sie sich jedoch lange Zeit der experimentellen Beobachtung. Die meisten Experimente in dieser Richtung konzentrierten sich auf zwei Emitter in Molekül- [35–37] und Ionensystemen [38] und Subradianz wurde erst kürzlich in atomaren Ensembles beobachtet [39–42]. Aus praktischer Sicht sind subradiante Zustände attraktiv für die Photonenspeicherung [43–45] und den Einsatz in Quantencomputern [46], da sie weniger anfällig für spontane Emission sind, und es wurde vorhergesagt, dass subradiante Zustände in geordneten Systemen von Atomen zu einer drastischen Verbesserung der Speicherung von Photonen führen können [25].

Kollektive und kooperative Phänomene treten in verschiedenen Systemen auf und es wurde gezeigt, dass die Kopplung von Licht mit atomaren Ensembles viele nützliche Anwendungen hat [47]. Ensembles aus Rydberg-Atomen bieten jedoch ein besonders interessantes System, um die kollektive Antwort eines mit Licht wechselwirkenden atomaren Ensembles zu nutzen, was das Gebiet der *Rydberg-Quantenoptik* [48–50] inspiriert hat. Die starke Van-der-Waals-Wechselwirkung zwischen Rydberg-Atomen führt zu dem Phänomen der *Dipol-* oder *Rydberg-Blockade*, welche erstmals im Kontext der Quanteninformationsverarbeitung diskutiert wurde [51, 52]. Aufgrund der Rydberg-Blockade kann innerhalb eines bestimmten Volumens nur eine einzige Anregung vorhanden sein, wodurch die optische Antwort auf einfallende Photonen nichtlinear wird. Mithilfe von elektromagnetisch induzierter Transparenz [53] können die starken Wechselwirkungen zwischen den Rydberg-Atomen auf die Photonen [54, 55] abgebildet werden, wodurch kooperative optische Nichtlinearitäten [56] und eine effektive Photon-Photon-Wechselwirkung realisiert werden [57–60]. Anwendungen von Photon-Photonen-Wechselwirkungen, die durch Rydberg-Atome vermittelt werden, sind Einzelphotonenschalter [61] oder -transistoren [62, 63] sowie die Realisierung von Quantengattern [64, 65].

Besonders interessant ist das Konzept eines *Rydberg-Superatoms*, bei dem alle Bestandteile des Ensembles innerhalb des blockierten Volumens eingeschlossen sind und ein einzelnes Photon ausreicht, um das Medium zu sättigen und die

größtmögliche nichtlineare Antwort zu erzielen [66]. Das gesamte Ensemble verhält sich dann ähnlich einem Zwei-Niveau-System mit kollektiv erhöhter Kopplungsstärke, das kollektiv verstärkte Vielteilchen-Rabi-Oszillationen [67] hervorruft. Da die Phaseninformation des einfallenden Lichts in die kollektive Anregung des Ensembles übertragen wird, erfolgt eine stark gerichtete Emission der Anregung in Richtung der sich ausbreitenden Photonen. Die starke Kopplung eines Rydberg-Superatoms an die propagierende Mode eines Lasers und die daraus resultierende Vorwärtsemission werden in Kapitel 3 dieser Arbeit diskutiert. Die emittierten Photonen können analysiert und als Folge der effektiven Photon-Photon-Wechselwirkung, die durch das Rydberg-Superatom vermittelt wird, sowohl Zwei- als auch Drei-Photonen-Korrelationen beobachtet werden. Die stark gerichtete Emission in Kombination mit der Blockade ermöglicht beispielsweise die Realisierung einer Einzelphotonenquelle in einem kalten Ensemble [68] sowie in einer Dampfzelle bei Raumtemperatur [69], wobei eine Vier-Wellen-Mischung („four-wave mixing“) verwendet wird, um die Emission der kollektiven Anregung zuerst im Medium zu speichern und anschließend über den kollektiven Emissionsprozess wieder abzurufen.

Obwohl die Beschreibung des Rydberg-Superatoms als Atom mit zwei Energieniveaus eine gute Intuition vermittelt, hat das Superatom immer noch eine innere Struktur, da es aus vielen Emittern besteht, die über die resonante Dipol-Dipol-Wechselwirkung, die durch das sich ausbreitende Lichtfeld vermittelt wird, wechselwirken können. In Kapitel 6 wird der Einfluss solcher kollektiver Effekte auf die Zerfallsdynamik eines Rydberg-Superatoms aufgrund der resonanten Dipol-Dipol-Wechselwirkung diskutiert. In Fällen, in denen der Einfluss resonanter Dipol-Dipol-Wechselwirkungen durch inkohärente Effekte verschleiert wird (wie zum Beispiel einer Dephasierung aufgrund der thermischen Bewegung der Atome), können einzelne Photonen durch einen irreversiblen Transfer der kollektiven Anregung in Zustände, die nicht mehr an das Lichtfeld koppeln, deterministisch aus dem Lichtpuls entfernt werden [70–72].

Ergänzend zu ungeordneten Ensembles im freien Raum hat in den letzten Jahren auch das Interesse an der Licht-Materie-Wechselwirkung in niedrigdimensionalen und synthetischen Atomstrukturen rasch zugenommen [73–77]. Die Entwicklung von experimentellen Techniken wie optischen Gittern [78] und optischen Pinzetten [79–81] hat die Realisierung periodischer Atomanordnungen in einer, zwei und sogar drei Dimensionen ermöglicht. Die Kontrolle der Positionen der Atome ermöglicht eine Feinabstimmung der optischen Antwort des Ensembles [82, 83], was zu beeindruckenden Ergebnissen wie einem Spiegel, der aus einer einzigen Atomschicht aufgebaut ist [84], führt und mithilfe der Rydberg-Blockade zur Erzeugung stark verschränkter photonischer Zustände [85] verwendet werden kann.

Neben periodischen Anordnungen von Atomen hat der experimentelle Fortschritt bei der Herstellung von Nanostrukturen und optischen Nanofasern den Weg zum Paradigma der *Wellenleiter-Quantenelektrodynamik* geebnet, bei dem Quantenemitter, modelliert als Zwei-Niveau-Systeme, stark an ein eindimensionales Kontinuum geführter Moden gekoppelt sind [66, 86–88]. Eine kurze Einführung in die Wellenleiter-Quantenelektrodynamik wird in Kapitel 1 gegeben. Die Wellenleiter-Quantenelektrodynamik wird unter anderem durch Atome realisiert, die an das evaneszente Feld einer optischen Nanofaser [89–91] oder eines photonischen Kristallwellenleiters [15, 92] gekoppelt sind sowie durch an photonische Nanostrukturen gekoppelte Quantenpunkte [93, 94] und an die Transmissionlinie eines Mikrowellenresonators gekoppelte supraleitende Qubits [95]. Kürzlich wurde auch vorgeschlagen, die Wellenleiter-Quantenelektrodynamik mit den geführten Moden eines geordneten Atomarrays zu realisieren [27].

Eindimensionale photonische Strukturen und Nanofasern bieten die Möglichkeit, nicht nur langreichweitige, sondern sogar Wechselwirkungen mit *unendlicher* Reichweite zu realisieren, die durch Photonen vermittelt werden, die sich nur entlang einer Raumdimension ausbreiten können [90, 96]. Darüber hinaus können andere Arten von Wechselwirkungen konstruiert werden, indem, beispielsweise unter Verwendung photonischer Kristalle, die Umgebung, in der sich die Photonen bewegen, angepasst wird, wodurch die Untersuchung durchstimmbarer und kontrollierter Quanten-Vielteilchensysteme realisert wird [97]. Diese Systeme ermöglichen zum Beispiel die Untersuchung des stark korrelierten Photonentransports [98–100] und der Physik niedrigdimensionaler dissipativer Systeme [101] und ermöglichen die Erzeugung nichtklassischer Lichtzustände [102–104].

Die Eingrenzung des Lichts in nanophotonischen Strukturen wie photonischen Wellenleitern und Nanofasern auf Längenskalen unterhalb der Wellenlänge eröffnet zudem die Möglichkeit, exotische *chirale* Wechselwirkungen zwischen den Emittern zu realisieren [105]. In einer solchen Struktur ist die Ausbreitungsrichtung des Lichts mit der Polarisation des Übergangsdipolmoments des Emitters verknüpft, so dass die Wechselwirkung zwischen den Atomen und Photonen nichtreziprok wird [106, 107]. Im Extremfall werden Absorption und Emission von Photonen sogar unidirektional. Diese besondere Art der Wechselwirkung ermöglicht die Implementierung von kaskadierten Quantensystemen [108, 109], bei denen die Photonen ohne Rückfluss von Information von einem Emitter zum nächsten gesendet werden und als Vermittler für die deterministische Übertragung von Quanteninformation zwischen entfernten Qubits fungieren können [110]. Weitere Anwendungen sind die robustere Erzeugung einer Atom-Atom-Verschränkung [101, 111], das optische Auslesen des Spinzustands eines einzelnen Elektrons in einem Quantenpunkt in nur einer Messung [112] und die Implementierung skalierbarer

Quantennetzwerke [113]. In dieser Arbeit werden in den Kapiteln 4 und 5 kollektive Effekte durch chirale und nicht-chirale Licht-Materie-Wechselwirkungen in eindimensionalen Wellenleitern untersucht. Die Ergebnisse dieser Kapitel verbessern auch das Verständnis der internen Dynamik des Rydberg-Superatoms, die in Kapitel 6 diskutiert wird. Das in Kapiteln 3 und 6 vorgestellte Rydberg-Superatom, das an eine propagierende Lasermode gekoppelt ist, bietet darüber hinaus ebenfalls die Möglichkeit durch die stark direktionale Emission chirale Wechselwirkungen zwischen mehreren Superatomen zu realisieren [72].

Im Folgenden werden die einzelnen Kapitel vorgestellt und auf ihren Inhalt eingegangen. Kapitel 1 führt zunächst die wichtigsten Konzepte, wie Rydberg-Atome und ihre Wechselwirkung, das Rydberg-Superatom und resonante Dipol-Dipol-Wechselwirkungen ein, die für das Verständnis dieser Arbeit relevant sind. Darüber hinaus wird eine kurze Einführung in die Wellenleiter-Quantenelektrodynamik und chirale Licht-Materie-Wechselwirkungen gegeben, die im Rahmen von Modellsystemen in dieser Arbeit verwendet werden.

In Kapitel 2 werden dann die theoretischen Grundlagen für die Beschreibung der mikroskopischen Wechselwirkung zwischen Licht und Materie gelegt. Dies führt auf ein effektives Spin-Model für die einzelnen Atome, das sich durch Ausintegrieren der Freiheitsgrade des elektromagnetischen Feldes erhalten lässt. Durch die Kopplung an ein gemeinsames Feld verhalten sich die Atome nicht mehr unabhängig, sondern es kommt zu einer korrelierten spontanen Emission von Photonen. Zudem tritt eine Austauschwechselwirkung zwischen den Atomen auf, die durch das elektromagnetische Feld vermittelt wird. Im Rahmen dieser Dissertation werden Modellsysteme betrachtet, in denen die Atome an eine einzelne propagierende Mode eines Lasers gekoppelt sind, die sich analog zu einem eindimensionalen Wellenleiter verhält. Insbesondere werden chirale und nicht-chirale Wellenleiter diskutiert und es wird auf die Unterschiede der Wechselwirkungen eingegangen. Um eine Anwendung des hergeleiteten Spin-Modells zu illustrieren, wird die Lichtausbreitung in einem Ensemble von Drei-Niveau-Atomen mit elektromagnetisch induzierter Transparenz diskutiert und die Verbindung mit bisherigen Kontinuumsmodellen hergestellt.

Als experimentell relevantes System wird in Kapitel 3 dann das Rydberg-Superatom betrachtet, das an ein propagierendes Lichtfeld gekoppelt ist. Das Experiment wurde von der Gruppe von Sebastian Hofferberth an der Universität Stuttgart und der Syddansk Universitet in Odense, Dänemark, durchgeführt. Aufgrund des kollektiven Charakters der Anregung im Superatom und der resultierenden verstärkten Emission in die anregende Lasermode ist die Kopplung des Systems an die Lasermode im Vergleich zu einem einzelnen Atom extrem verstärkt. Das System lässt sich dann auf ein einzelnes effektives Zwei-Niveau-System in einem

eindimensionalen Wellenleiter reduzieren und kann nach dem Ausintegrieren des elektromagnetischen Feldes durch die Mastergleichung eines Atoms mit verstärkter Kopplung an das Lichtfeld sowie der daraus resultierenden verstärkten Emission von Photonen beschrieben werden. Die Dynamik des Systems ist durch die Anzahl der einfallenden Photonen und die kollektive Kopplung sowie die daraus resultierende verstärkte Emission charakterisert. Dies führt zu einem dynamischen Phasendiagramm mit drei verschiedenen Phasen. Ist die Anzahl der einfallenden Photonen, die das System treiben, sowie die Kopplung an das Lichtfeld für eine gegebene Pulslänge zu klein, befindet sich das System in einem schwach getriebenen Zustand. Ist hingegen die Kopplung und damit die Emission zu stark, geht das System in einen überdämpften Zustand über. Zwischen diesen beiden Bereichen gibt es einen Parameterbereich, in dem intrinsisch gedämpfte Rabi-Oszillationen beobachtet werden können. Dies steht im starken Kontrast zu Systemen, in denen Atome in optischen Resonatoren gehalten werden und die Kopplung sowie die Emission dadurch unabhängig voneinander verändert werden können. Die effektive Wechselwirkung zwischen den Photonen, die durch das Superatom vermittelt wird, kann durch Zwei- und Drei-Photonen-Korrelationen quantifiziert werden und es wird gezeigt, dass nicht-triviale Drei-Photonen-Korrelationen auftreten. Da das Superatom auch eine interne Dynamik hat, ist es notwendig, das Zwei-Niveau-Modell phänomenologisch um einen dritten Zustand zu erweitern, an den die kollektive Anregung dissipativ koppeln kann. Dadurch lässt sich eine sehr gute Übereinstimmung zwischen den theoretischen Berechnungen und den experimentellen Beobachtungen herstellen.

Die interne Dynamik wird in Kapitel 4 näher untersucht, das sich mit Effekten beschäftigt, die durch die kohärente Austauschwechselwirkung zwischen den einzelnen Atomen des Superatoms aufgrund der resonante Dipol-Dipol-Wechselwirkung entstehen. Dafür wird die Dynamik eines kollektiv angeregten Zustandes in einem Ensemble von Atomen, die an einen eindimensionalen Wellenleiter gekoppelt sind, in Gegenwart der Austauschwechselwirkung betrachtet. Es wird analytisch gezeigt, dass diese für einen chiralen Wellenleiter, in dem Photonen nur in eine Richtung propagieren können, universell ist und keine Dephasierung auftritt. Mithilfe einer Störungstheorie kann auch der Einfluss von Rückstreuung verstanden werden. Die Dynamik wird dann von der Zeitskala der kohärenten und universellen Dynamik eines chiralen Wellenleiters sowie der Zeitskala der Dephasierung aufgrund der Rückstreuung und der zufälligen Positionen der Emitter beinflusst. Da beide Zeitskalen unterschiedlich von der Anzahl der Atome im System abhängen, tritt die universelle Dynamik für eine größer werdende Zahl an Atomen immer stärker hervor. Darüber hinaus kann gezeigt werden, dass sich die dephasierte kollektive Anregung nicht auf alle Emitter gleichmäßig verteilt und die

Wahrscheinlichkeit in der ursprünglichen Anregung zu sein auf einen konstanten, nichtverschwindenden Wert abfällt, der unabhängig von der Zahl der Atome im System ist. Die analytischen Ergebnisse zeigen eine sehr gute Übereinstimmung mit einer numerischen Simulation der Dynamik. Diese Beobachtungen setzen damit eine fundamentale Grenze für die Dephasierung in solch einem System.

In Kapitel 5 wird dann die Zerfallsdynamik einer kollektiven Anregung genauer untersucht, wobei nun das Hauptaugenmerk auf dem Zusammenspiel zwischen der, im vorherigen Kapitel diskutierten, kohärenten Austauschwechselwirkung und der korrelierten spontanen Emission liegt. Die dissipative Dynamik eines strahlenden Ensembles kann durch superradiante und subradiante Zustände beschrieben werden, die eine verstärkte beziehungsweise reduzierte Zerfallsrate haben. Die kohärente Dynamik wiederum sorgt für eine Kopplung zwischen beiden Arten von Zuständen. Dieser Mechanismus wird zuerst anhand des einfachen Beispiels von nur zwei Atomen illustriert und anschließend auf eine beliebige Anzahl erweitert. Für einen chiralen Wellenleiter gibt es nur einen superradianten Zustand, der der kollektiven Anregung entspricht, die von einem einfallenden Lichtfeld erzeugt wird. Alle anderen Zustände sind perfekt subradiant und zerfallen nicht. Interessanterweise zeigt sich nun, dass die kollektive Anregung zwar zu Beginn mit der zu erwartenden kollektiv verstärkten Rate exponentiell zerfällt, durch die Kopplung an subradiante Zustände jedoch eine Verlangsamung des Zerfalls einsetzt und in einen algebraischen Zerfall übergeht. Dieses Verhalten lässt sich auf einen bidirektionalen Wellenleiter und zufällige Positionen der Atome verallgemeinern. Außerdem wird analytisch, unter der Verwendung eines Kontinuumsmodells, gezeigt, dass sich im Falle von vielen Atomen ein bidirektionaler und ein chiraler Wellenleiter für die untersuchte kollektive Anregung gleich verhalten, was die experimentelle Beobachtung von chiralen Effekten auch in bidirektionalen Wellenleitern ermöglicht.

Abschließend spannt Kapitel 6 wieder den Bogen zum Rydberg-Superatom, wobei nun die experimentelle und theoretische Untersuchung der Zerfallsdynamik der kollektiven Anregung im Superatom im Vordergrund steht. Dafür wird das Licht, das vom Superatom ausgetrahlt wird, nachdem es für eine gewisse Zeit durch einen Laserpuls angeregt wurde, mit hoher Genauigkeit untersucht. Anstatt einer konstante Zerfallsrate, die durch die kollektive Kopplung an die Lasermode und andere, unabhängige dissipative Prozesse gegeben ist, lässt sich eine variable Zerfallsrate beobachten, die von der Dynamik des Superatoms vor dem Zerfall abhängt. Diese zustandsabhängige Zerfallsrate kann durch den Einfluss der resonanten Dipol-Dipol-Wechselwirkung erklärt werden. Zu diesem Zweck wird das Drei-Niveau-Modell zur Beschreibung des Rydberg-Superatoms aus Kapitel 3 um einen Zustand, der kohärent an die kollektive Anregung gekoppelt ist, erweitert,

was durch die Ergebnisse aus den Kapiteln 4 und 5 motiviert werden kann. Eine Analyse der Mastergleichung zeigt, dass die Zerfallsrate am Ende eines einfallenden Pulses vom internen Zustand des Superatoms abhängt und eine numerische Berechnung der vollen Dynamik liefert eine sehr gute Übereinstimmung zwischen Theorie und Experiment.

Quanteneffekte in dipolaren Bose-Gasen

Die experimentelle Beobachtung der Bose-Einstein-Kondensation in verdünnten Atomgasen im Jahr 1995 [253–255] markierte den Anfang einer neuen Zeitrechnung der Atom-, Molekül- und optischen (AMO) Physik und brachte Eric Cornell, Carl Wieman und Wolfang Ketterle 2001 den Nobelpreis in Physik ein. Durch die Möglichkeit diesen Materiezustand zu kontrollieren wurde eine experimentelle Plattform verfügbar, um Phänomene wie die Interferenz von Materiewellen [256], Suprafluidität und das Auftreten von Vortices [257], sowie Quanten-Phasenübergänge wie den Übergang von einem Suprafluid zu einem Mott-Isolator [258] zu untersuchen.

Aufgrund der geringen Dichte der Gase sowie der extrem kalten Temperaturen im Nanokelvin-Bereich kann die Wechselwirkung zwischen den Teilchen durch eine effektive Kontaktwechselwirkung beschrieben werden, die das echte, kurzreichweitige Wechselwirkungspotential zwischen den Atomen ersetzt und durch die s-Wellenstreulänge charakterisiert ist. Die Stärke der Wechselwirkung kann heutzutage in Experimenten routinemäßig durch Feshbach-Resonanzen kontrolliert und verändert werden [134]. Die kalten, verdünnten und schwach wechselwirkenden Bose-Gase werden für gewöhnlich durch eine Molekularfeldnäherung und die Gross-Pitaevskii-Gleichung beschrieben [259, 260].

In den letzten Jahren hat der enorme experimentelle Fortschritt eine neue Komponente zum immer weiter wachsenden Forschungsfeld der wechselwirkenden Bose-Einstein-Kondensate hinzugefügt: die dipolaren Bose-Einstein-Kondensate. Nach der ersten experimentellen Realisierung in einem ultrakalten Gas aus Chrom-Atomen durch die Gruppe von Tilman Pfau an der Universität Stuttgart [261] wurden auch Bose-Einstein-Kondensate mit stärkerer dipolarer Wechselwirkung in Dysprosium- [262] und Erbium-Atomen [263] erzeugt. Im Vergleich zu Chrom, das ein magnetisches Moment von $6\mu_\mathrm{B}$ besitzt, hat Erbium ein magnetisches Moment von $7\mu_\mathrm{B}$. Die bosonischen Isotope von Dysprosium haben aufgrund ihrer Elektronenkonfiguration mit $10\mu_\mathrm{B}$ das stärkste magnetische Moment aller bosonischen Isotope der Elemente. Das Vorhandensein von langreichweitigen und anisotropen Wechselwirkungen kann die Eigenschaften des Gases stark beeinflussen und führt

zu einer Vielzahl an interessanten Effekten und möglichen Anwendungen [125, 264]. So kann beispielsweise die Stabilität eines dipolaren Gases durch die experimentelle Kontrolle des Verhältnisses zwischen der rein repulsiven Kontakt- und der teilweise attraktiven dipolaren Wechselwirkung beeinflusst werden [265].

Trotz der erfolgreichen Beschreibung ultrakalter Gase durch die Molekularfeldnäherung machten es experimentelle Fortschritte im Bereich der Atomfallen, der Kühlung von Atomen und der Bildgebung möglich, Effekte zu beobachten, die sich der Beschreibung durch die Molekularfeldnährung entziehen. Solche „*beyond-mean-field*"-Effekte[4] (BMF-Effekte) sind zum Beispiel die Verringerung der Anzahl von Teilchen im Kondensat durch Anregung in höhere Moden aufgrund von Quantenfluktuationen [266] und Korrekturen zum Anregungsspektrum [267, 268] sowie der Grundzustandsenergie [269]. Einer der bemerkenswertesten Effekte der Quantenfluktuationen, der darüber hinaus ein großes Interesse an diesem Forschungsfeld in Gang gesetzt hat [271–275], war die Beobachtung von stabilen Quantentröpfchen in einem dipolaren Gas nahe an der Instabilität [270]. Während die Molekularfeldnäherung einen Kollaps des Gases durch die dipolare Wechselwirkung vorhersagt, haben die führenden Korrekturen zur Molekularfeldnäherung eine effektive repulsive Wechselwirkung zur Folge, die das Gas stabilisiert [276]. Diese Korrekturen sind auch als Lee-Huang-Yang-Korrekturen (LHY-Korrekturen) für Kontaktwechselwirkungen bekannt [277–279] und wurden ebenfalls für eine dipolare Wechselwirkung berechnet [280]. Obwohl die BMF-Effekte in schwach wechselwirkenden Gasen typischerweise klein sind, kann eine Feinabstimmung zwischen dipolarer und Kontaktwechselwirkung zu einer Aufhebung der Beiträge der Molekularfeldnäherung führen, so dass die LHY-Korrekturen dominieren [281]. Dieser Mechanismus zur Stabilisierung wurde ebenfalls in zweikomponentigen Bose-Gasen beobachtet [282]. Vor kurzem wurde das Verhalten der BMF-Korrekturen für den Fall des Übergangs von drei Raumdimensionen auf eine Raumdimension für Kontakt- [283, 284] und dipolare [285] Wechselwirkungen untersucht.

Darüber hinaus kann ein in einer Falle eingesperrtes stark dipolares Gas ein Roton-Maxon-Spektrum zeigen [286, 287], das ähnlich zu dem ist, welches für flüssiges Helium vorgeschlagen wurde [288]. Dieses Anregungsspektrum wurde ebenfalls experimentell beobachtet [289]. Eine Erhöhung des relativen Beitrags der dipolaren Wechselwirkung führt zu einer Roton-Instabilität, wodurch sich das Gas in mehrere Quantentröpfchen aufteilt [290]. In einer Reihe von Experimenten [290–292] wurde gezeigt, dass die verschiedenen Quantentröpfchen zueinander phasen-

[4] Dieser Ausdruck lässt sich am besten mit „Effekte, die über die Beschreibung durch die Molekularfeldnäherung hinausgehen" übersetzen. Der Einfachheit halber wird jedoch im Folgenden ausschließlich der englische Begriff beziehungsweise die Abkürzung BMF-Effekte verwendet.

kohärent sind, wodurch sich der lange gesuchte suprasolide Materiezustand realisieren ließ. Dieser Zustand kombiniert die suprafluiden Eigenschaften, die mit der spontanen Brechung der globalen $U(1)$-Phasensymmetrie einhergehen, mit der Dichtemodulation durch die spontane Brechung der Translationssymmetrie.

Während die Brechung der kontinuierlichen Translationsinvarianz in einem dipolaren Supersolid durch die intrinisische Wechselwirkung hervorgerufen wird, kann sie ebenso durch ein externes periodisches Potentiale erreicht werden. Optische Gitter im Allgemeinen bieten durch die Möglichkeit perfekt periodische Potential für Atome mit einer veränderlichen Gittertiefe und Geometrie zu erzeugen eine vielseitige Plattform zur Manipulation und Kontrolle ultrakalter Gase [294, 295]. Das führte beispielsweise zur Implementierung des Bose-Hubbard-Modells [296] und der Beobachtung des Quantenphasenübergangs eines Suprafluids zu einem Mott-Isolator [258]. Durch ihre langreichweitige und anisotrope Wechselwirkung entziehen sich Dipole, die in einem optischen Gitter gefangen sind, jedoch der Beschreibung durch das übliche Bose-Hubbard-Modell [297, 298]. Um diese Wechselwirkungen erweiterte Modelle wurden experimentell implementiert [299] und es wurde vorhergesagt, dass diese zu vielseitigen physikalischen Effekten wie der Realisierung exotischer Quantenphasen für stark korrelierte Systeme führen [297, 300, 301].

Demgegenüber wurde im Grenzfall eines Suprafluids gezeigt, dass das Vorhandensein eines externen periodischen Potentials die BMF-Effekte in Bose-Gasen mit Kontaktwechselwirkung verstärken kann [302]. Ebenfalls wurde gezeigt, dass ein überlagertes eindimensionales Gitter auf dem Level der Molekularfeldnäherung einen stabilisierenden Effekt auf ein gefangenes dipolares Gas hat [303]. Dieser Effekt hängt stark von der Kopplung zwischen den Gitterplätzen aufgrund der langreichweitigen Dipol-Dipol-Wechselwirkung ab. Es wird auch vermutet, dass diese Kopplung den Roton-Charakter im Anregungsspektrums verstärkt [304, 305] und so die Eigenschaften von suprasoliden Zuständen beeinflusst.

Der zweite Teil dieser Arbeit untersucht daher den Einfluss eines optischen Gitters auf die BMF-Korrekturen in einem dipolaren Bose-Gas. Insbesondere geht es um die Frage, ob und wie die Quantenfluktuationen in solch einem Setup kontrolliert werden können. Dafür werden in Kapitel 7 zunächst die Grundlagen der Wechselwirkung von dipolaren Bose-Gasen diskutiert. Ebenfalls werden zwei Methoden zur Berechnung der BMF-Korrekturen vorgestellt: Zum einen eine von Bogoliubov [317] entwickelte Methode, in der das Streuproblem zweier Teilchen störungstheoretisch mithilfe der Born-Näherung gelöst wird. Obwohl sich diese Methode sehr gut eignet, um BMF-Korrekturen zu berechnen, ist bei der Behandlung des Streuproblems zweier Bosonen Vorsicht geboten, um unphysikalische Divergenzen zu verhindern. Zum anderen wird eine feldtheoretische Methode vorge-

stellt, die unter anderem von Beliaev [279] und Hugenholtz und Pines [278] entwickelt wurde. Im Gegensatz zur Bogoliubov-Methode wird hier das Streuproblem mithilfe eines diagrammatischen Ansatzes für ein verdünntes Gas exakt gelöst. Die BMF-Korrekturen können selbstkonsistent mit einer Differentialgleichung berechnet werden.

In Kapitel 8 wird dann ein polarisiertes, dipolares Bose-Gas in einem dreidimensionalen, tiefen optischen Gitter betrachtet, für das die BMF-Korrekturen ausgerechnet werden. Es wird gezeigt, dass das Gitter die Quantenfluktuationen verstärkt und eine nichttriviale Abhängigkeit von der Dichte des Gases auftritt, die über die bisher bekannte Abhängigkeit der Korrekturen zur Molekularfeldnäherung hinausgeht. Ergänzend dazu wird der Fall eines schwachen eindimensionalen Gitters untersucht. Die Orientierung des Gitters im Vergleich zur Polarisation der Dipole kann hierbei variiert werden und so die Dipole wahlweise in eine Konfiguration bringen, in der sich die Pole hauptsächlich Kopf an Fuß oder Seite an Seite befinden. Während im ersten Fall die Quantenfluktuationen aufgrund der vorwiegend attraktiven Wechselwirkung abgeschwächt werden, sind sie im zweiten Fall verstärkt. Beide Fälle lassen sich durch eine anisotrope effektive Masse der Teilchen entlang des Gitters beschreiben.

Acknowledgements

In den vergangenen gut fünfeinhalb Jahren, während denen diese Dissertation entstanden ist, haben mich viele Menschen auf diesem Weg begleitet und damit in der einen oder anderen Form zu dieser Arbeit beigetragen:

Zu allererst möchte ich mich bei Hans Peter Büchler bedanken. Die interessanten und inspirierenden Diskussionen mit Dir haben mir immer weitergeholfen und ich habe von Deiner Herangehensweise an Probleme sehr viel gelernt. Danke für das Vertrauen, die Unterstützung und die vielen Freiheiten, die Du nicht nur mir sondern allen am Institut gibst, sowie für die Möglichkeit meine Forschung auf Konferenzen vorstellen zu können.

Ein großer Dank geht auch an Jörg Main für die schnelle und unkomplizierte Übernahme des Mitberichts. Bei Tilman Pfau bedanke ich mich ebenfalls für die schnelle und unkomplizierte Übernahme des Prüfungsvorsitzes sowie für die Fortgeschrittene-Atomphysik-Vorlesung, die mein Interesse an der Welt der kalten Rydberg-Gase und der Quantenoptik geweckt hat.

Auch wenn ein nicht unerheblicher Teil der Arbeit eines theoretischen Physikers alleine im Büro stattfindet, ist es wichtig Kollegen und andere Doktoranden zu haben, mit denen man sich über Physik und andere Dinge austauschen kann. Dabei möchte ich mich vor allem bei Sebastian Weber bedanken. Wir kennen uns nun schon fast seit der ersten Woche des Studiums und ich schätze die langen Diskussionen, die wir über Physik, aber auch über das Leben allgemein, hatten. Deine Leidenschaft für die Physik bewundere ich immer wieder und wünsche Dir alles Gute für die Zukunft! Außerdem geht ein großer Dank an Nicolai Lang, mit dem ich einige Zeit ein Büro teilen durfte. Vielen Dank für unsere interessanten Diskussionen, bei denen ich immer viel gelernt habe und für die vielen Antworten, die ich stets auf meine Fragen bekommen habe.

Bei Tobias Ilg und Kevin Kleinbeck bedanke ich mich für viele interessante Diskussionen und Gespräche sowie die gute Zusammenarbeit bei spannenden Projekten. Ich werde auch unsere Ausflüge zu den DPG-Tagungen (mit Sebastian) in

guter Erinnerung behalten.

Außerdem geht ein großer Dank an Rukmani Bai, Nastasia Makki, Felix Roser, Katharina Brechtelsbauer, Disha Gupta, Chris Bühler, Alice Pagano und Johannes Mögerle für die tolle Atmosphäre am Institut sowie viele spannende Aktivitäten auch außerhalb des Arbeitsalltags. Ich bin mir sicher, irgendwann wird auch das ITP3 mal das Volleyballturnier gewinnen...

Ein ganz besonderer Dank geht an Oliver Nagel, ohne den vieles am Institut sicherlich nicht so glatt laufen würde. Vielen Dank, dass Du dich so gut um alle administrativen und bürokratischen Dinge kümmerst, damit wir uns auf unsere Forschung konzentrieren können!

Ebenso möchte ich mich bei den ehemaligen Institutsmitgliedern Luka Jibuti, Stephan Humeniuk, Adam Bühler, Przemek Bienias, Krzysiek Jachymski, Daniel Huerga und David Peter für viele interessante Gespräche und die produktive Zusammenarbeit bedanken.

Während meiner Promotionszeit hatte ich das Glück mit der Gruppe von Sebastian Hofferberth an spannenden Experimenten zu Rydberg-Superatomen zusammenarbeiten zu dürfen. Ein großer Teil dieser Arbeit wäre ohne ihn, Nina Stiesdal, Hannes Busche, Asaf Paris-Mandoki, Christoph Braun, Philipp Lunt und Christoph Tresp nicht möglich gewesen. Dank ihnen war es auch mir als Theoretiker vergönnt im Labor (sogar zwei!) Rydberg-Superatome zu erzeugen. Danke Euch allen für die tolle Zusammenarbeit, die interessanten Diskussionen und Eure Gastfreundschaft in Dänemark. Ich wünsche Euch alles Gute und viel Erfolg in Bonn!

Bei Hadiseh Alaeian bedanke ich mich für viele interessante Diskussionen zu Rydberg-Polaritonen in optischen Resonatoren.

Bei Alexey Gorshkov und Przemek Bienias bedanke ich mich für ihre Gastfreundschaft und die spannenden Diskussionen während meines (Corona-bedingt) leider viel zu kurzen Aufenthalts am JQI an der University of Maryland.

Da die wissenschaftliche Arbeit und das Verfassen dieser Dissertation (zumindest in meinem Fall) immer auch mit Höhen und Tiefen verbunden war, geht ein großer Dank an meine Familie und Freunde, die mich während dieser Zeit immer unterstützt und wenn nötig auch abgelenkt haben, um mich auf andere Gedanken zu bringen. Meinen Eltern möchte ich besonders dafür danken, dass sie immer an mich geglaubt haben und mir das Vertrauen entgegengebracht haben, das Richtige im Leben zu tun. Zu guter Letzt danke ich Aleksandra für ihre Liebe, ihr Verständnis und ihre bedingungslose Unterstützung egal in welcher Situation. Volim te!